

Aus dem Fachbereich Medizinische Biochemie und Molekularbiologie
Theoretische Medizin und Biowissenschaften
der Medizinischen Fakultät
der Universität des Saarlandes, Homburg/Saar

**Evaluation of anti-metastatic therapeutics targeting
SEC62 in head and neck cancer using newly established
murine *in vivo* metastasis models and functional
characterization of stable *SEC62* knock-out head and neck
cancer cell lines generated by CRISPR/Cas9**

DISSERTATION

zur Erlangung des akademischen Grades eines Doktors der Naturwissenschaften
der Medizinischen Fakultät
der UNIVERSITÄT DES SAARLANDES

2022

vorgelegt von Sandrina Fabienne Körner
geboren am 20.05.1992 in Ludwigshafen am Rhein

Tag der Promotion: 27.03.2023
Dekan: Univ.-Prof. Dr. med. Michael D. Menger
Berichterstatter: Univ.-Prof. Dr. rer. nat. Martin Jung
Univ.-Prof. Dr. med. Bernhard Schick
Univ.-Prof. Dr. med. Chia-Jung Busch

Eidesstattliche Erklärung

Erklärung gemäß § 7 Abs. 1 Nr. 2

Ich erkläre hiermit an Eides statt, dass ich die vorliegende Arbeit ohne unzulässige Hilfe Dritter und ohne Benutzung anderer als der angegebenen Hilfsmittel angefertigt habe. Die aus anderen Quellen direkt oder indirekt übernommenen Daten und Konzepte sind unter Angabe der Quelle gekennzeichnet.

Bei der Auswahl und Auswertung folgenden Materials haben mir die nachstehend aufgeführten Personen in der jeweils beschriebenen Weise unentgeltlich geholfen:

1. Die Tierversuche wurden in Kooperation des Instituts für Klinische und Experimentelle Chirurgie unter der Leitung von Prof. Michael D. Menger (Universität des Saarlandes, Homburg/Saar) durchgeführt.
2. Die μ CT-Aufnahmen wurden zunächst bis zum Erlernen der Methode von Dr. Christina Körbel im Labor von Prof. Michael D. Menger (Institut für Klinische und Experimentelle Chirurgie, Universität des Saarlandes, Homburg/Saar) durchgeführt.
3. Die MRT-Aufnahmen wurden zusammen mit Dr. Andreas Müller im Labor von Prof. Michael D. Menger (Institut für Klinische und Experimentelle Chirurgie, Universität des Saarlandes, Homburg/Saar) durchgeführt.
4. Bei wissenschaftlichen Fragestellungen wurde Dr. Florian Bochen (Klinik für Hals-Nasen- und Ohrenheilkunde, Universitätsklinikum des Saarlandes, Homburg/Saar) um Rat gebeten.
5. Das *Next Generation Sequencing* erfolgte in Zusammenarbeit mit Dr. Sascha Tierling im Labor von Prof. Dr. Jörn Walter (Genetik/Epigenetik, Universität des Saarlandes, Saarbrücken).
6. Die *live-cell Ca²⁺-Imaging* Experimente wurden von Dr. Tillman Pick im Labor von Prof. Dr. Adolfo Cavalié (Experimentelle und Klinische Pharmakologie und Toxikologie, Präklinisches Zentrum für Molekulare Signalverarbeitung (PSMZ), Universität des Saarlandes, Homburg/Saar) durchgeführt.
7. Die CD31/LYVE-1 Immunfluoreszenzfärbungen wurden von Janine Becker im Institut für Klinische und Experimentelle Chirurgie unter der Leitung von Prof. Michael D. Menger (Universität des Saarlandes, Homburg/Saar) durchgeführt.

Weitere Personen waren an der inhaltlich-materiellen Erstellung der vorliegenden Arbeit nicht beteiligt. Insbesondere habe ich nicht die entgeltliche Hilfe von Vermittlungs- bzw. Beratungsdiensten (Promotionsberater/innen oder anderer Personen) in Anspruch genommen.

Außer den Angegebenen hat niemand von mir unmittelbar oder mittelbar geldwerte Leistungen für Arbeiten erhalten, die im Zusammenhang mit dem Inhalt der vorgelegten Dissertation stehen.

Die Arbeit wurde bisher weder im Inland noch im Ausland in gleicher oder ähnlicher Form in einem anderen Verfahren zur Erlangung des Doktorgrades einer anderen Prüfungsbehörde vorgelegt.

Ich versichere an Eides statt, dass ich nach bestem Wissen die Wahrheit gesagt und nichts verschwiegen habe.

Die Bedeutung der eidesstattlichen Versicherung und die strafrechtlichen Folgen einer unrichtigen oder unvollständigen eidesstattlichen Erklärung sind mir bekannt.

Homburg,

(Unterschrift der/des Promovierenden)

(Unterschrift der die Versicherung an Eides statt aufnehmenden Beamtin bzw. des aufnehmenden Beamten)

Dedicated to my beloved parents

Fabian

Abstract

For several years, research has been concerned with the clinical and molecular role of SEC62, a protein located in the ER membrane, which has been considered as a potential oncogene. Over time, significant overexpression of the SEC62 protein has been shown in various human tumour entities, including squamous cell carcinoma of the head and neck (HNSCC) which display a SEC62 overexpression in approximately 86% of cases. In general, head and neck tumours are among the seventh most common tumour entities worldwide with a mostly consistent and poor 5-year survival rate for affected patients of about 50 to 60 %. Head and neck tumours are often diagnosed at an advanced stage of disease and about 50 % of all patients already display lymph node metastases of the neck at the time of diagnosis. About 10% of patients even have distant metastases. Studies have shown that the ER membrane protein SEC62 is not only overexpressed in the majority of HNSCC patients but is also associated with a significantly worse prognosis and an advanced TNM status. In functional *in vitro* studies of the SEC62 protein, significant changes in migration were found, depending on an artificially altered SEC62 expression. Thus, plasmid-mediated overexpression of SEC62 led to a significantly increased migration. A transient knock-down of SEC62 via siRNA significantly decreased the ability of migration in HNSCC cells. Based on these properties, SEC62 was considered as a potential new target for directed therapy of SEC62-overexpressing HNSCC tumours. Since a direct transfer from those *in vitro* experiments to human is not possible, this work aimed at a functional knock-down of SEC62 by the administration of TFP and TG. TFP leads to an increased cytosolic Ca²⁺ content by blocking CaM, which would close the protein translocation channel SEC61 in the ER membrane. A strong concentration gradient causes a flow of Ca²⁺ from the ER Ca²⁺-store into the cytosol. Moreover, the simultaneous administration of TG irreversibly inhibits SERCA so that no Ca²⁺ can be actively transported back into the ER. These two compounds in combination are thought to significantly upset Ca²⁺ homeostasis in SEC62-overexpressing cancer cells, causing the cells to undergo apoptosis. Since these effects could be proven *in vitro*, two murine xenograft metastasis models were established within this thesis in order to be able to test the efficacy of both substances *in vivo* on the metastasis of HNSCC cells. Therefore, on the one hand tumour cells were injected orthotopically into the tongue of mice to test the anti-metastatic ability of TFP and TG. Here, TFP treatment resulted in a reduction of the number of cervical lymph node metastases, whereas TG treatment was able to reduce the size of detectable metastases. On the other hand, tumour cells were injected i.v. into the tail vein of the animals to investigate the impact of both substances on haematogenous metastasis. Here, the evaluation of the combinatory treatment on haematogenous metastasis achieved a reduction in metastatic burden in the lung. In addition to the main aspect of the effects of TFP and TG on metastasis, various imaging techniques and their

evaluations including MRI, micro-CT, and histology were also established for monitoring the emerging metastases.

In a second part of this work stable *SEC62*-knockout clones of an immortalized HNSCC cell line were generated using CRISPR-Cas9 technology, which should provide deeper insights into the role of *SEC62* and the *SEC62*-associated processes inside the cell. These *SEC62*-ko clones were validated using various methods such as immunofluorescence, Western blot and next generation sequencing (NGS), and were also characterised based on whole-RNA-sequencing. Furthermore, first functional studies with *SEC62*-ko clones and their tolerance to TFP and TG were applied.

In summary, two murine xenograft models for lymphatic and haematogenous metastasis of head and neck cancer were successfully established, on which first investigations on the efficacy of two potential new compounds for a targeted therapy of metastatic *SEC62*-overexpressing head and neck tumours could be performed. Herein, TG and TFP showed promising effects on lymphatic and haematogenous metastasis *in vivo* motivating for further investigations. Furthermore, two stable *SEC62*-ko HNSCC cell lines could be generated, validated and characterised using CRISPR-Cas9. Further analyses to understand the influence and function of *SEC62* in more detail are the subject of future research.

Zusammenfassung

Die Forschung beschäftigt sich bereits seit mehreren Jahren mit der klinischen als auch molekularen Rolle von SEC62, einem Protein, das sich in der ER Membran befindet und als potentielles Onkogen gehandelt wird. In den letzten ca. 15 Jahren konnte in verschiedenen Tumorentitäten eine signifikante Überexpression des SEC62-Proteins nachgewiesen werden, so auch in ca. 86% aller Plattenepithelkarzinome des Kopf-Hals-Bereiches (head and neck squamous cell carcinoma, HNSCC). Im Allgemeinen zählen Kopf-Hals Tumore zu den sieben häufigsten Tumorerkrankungen weltweit mit einer weitestgehend gleichbleibenden, schlechten 5-Jahres Überlebensrate für betroffene Patienten von etwa 50-60%. In der Mehrzahl der Fälle werden Kopf-Hals-Tumore erst in einem späten Stadium der Erkrankung diagnostiziert. Daher weisen zum Diagnosezeitpunkt bereits ca. 50% aller HNSCC-Patienten Hals-Lymphknotenmetastasen auf, ca. 10% der Patienten zeigen sogar bereits Fernmetastasen. In Studien konnte nachgewiesen werden, dass das ER-membranständige Protein SEC62 nicht nur von einem Großteil aller HNSCC Patienten überexprimiert wird, sondern auch mit einer deutlich schlechteren Prognose, sowie mit einem fortgeschrittenen TNM-Stadium assoziiert ist. In funktionellen *in vitro* Untersuchungen des SEC62 Proteins konnten signifikante Veränderungen in der Migrationsfähigkeit festgestellt werden, je nach artifiziell veränderter SEC62-Expression. So führte eine Plasmid-vermittelte Überexpression von SEC62 zu einer deutlich gesteigerten Migration, bzw. ein transients knock-down zu einer signifikanten Abnahme der Migrationsfähigkeit in HNSCC Zellen. Aufgrund dieser Eigenschaften bietet sich SEC62 als mögliches neues Target für eine zielgerichtete Therapie von SEC62-überexprimierenden HNSCCs an. Da ein direkter Transfer der genannten *in vitro* Experimente auf den Menschen nicht möglich ist, wurde in dieser Arbeit ein funktioneller knock-down von SEC62 durch die Gabe von TFP und TG angestrebt. TFP führt zu einem gesteigerten zytosolischen Ca^{2+} -Gehalt durch die Blockade von CaM, das normalerweise den Proteintranslokationskanal SEC61 in der ER-Membran verschließen würde. Durch ein starkes Konzentrationsgefälle von Ca^{2+} strömen die Ionen aus dem ER Ca^{2+} -Speicher ins Zytosol. Durch die gleichzeitige Gabe von TG wird zudem auch die SERCA irreversibel inhibiert, sodass kein Ca^{2+} energieabhängig ins ER zurückgepumpt werden kann. Diese beiden Substanzen in Kombination bringen die Ca^{2+} -Homöostase in SEC62-überexprimierenden Krebszellen signifikant aus dem Gleichgewicht, sodass eine Apoptose der Tumorzellen erreicht werden kann. Da *in vitro* diese Effekte gezeigt werden konnten, wurden in dieser Arbeit zwei murine Xenograft Metastasierungs-Modelle etabliert, um die Wirksamkeit der beiden Substanzen auch *in vivo* auf die Metastasierung von HNSCC Zellen testen zu können. Eine TFP-Behandlung orthotop injizierter Tiere zur Analyse der Auswirkungen beider Substanzen auf die lymphogene Metastasierung, führte zu einer Reduktion der Metastasenanzahl. Eine Behandlung mit TG konnte eine Verkleinerung der detektierten

Metastasen erzeugen. Die Auswertung der Kombinationsbehandlung auf die hämatogene Metastasierung im zweiten etablierten Tiermodell erzielte eine Reduktion der Metastasenlast in der Lunge. Neben dem Hauptaspekt der Auswirkungen von TFP und TG auf die Metastasierung wurden auch verschiedene Bildgebungsverfahren und deren Auswertungen (Kleintier-MRT, micro-CT, Histologie) zum Monitoring der entstehenden Metastasen etabliert.

In einem zweiten Teil dieser Arbeit wurden stabile *SEC62*-knockout Klone einer immortalisierten HNSCC-Zelllinie mittels CRISPR-Cas9 generiert, die tiefere Erkenntnisse über Rolle von *SEC62* und die mit *SEC62*-assoziierten Prozesse in der Zelle liefern sollten. Diese *SEC62*-ko Klone wurden mittels verschiedenster Methoden wie Immunfluoreszenz, Western Blot und next generation sequencing (NGS) validiert, sowie basierend auf einer whole-RNA-Sequenzierung charakterisiert. Des Weiteren wurden erste funktionelle Untersuchungen mit den *SEC62*-ko Klonen und ihre Toleranz gegenüber TFP und TG durchgeführt.

Zusammenfassend konnten zwei murine Xenograft Modelle zur lymphogenen und hämatogenen Metastasierung von Kopf-Hals-Tumoren erfolgreich etabliert werden, an denen erste Untersuchungen zur Wirksamkeit zweier potentieller neuer Substanzen zur Therapie von metastasierenden, *SEC62*-überexprimierenden Kopf-Hals-Tumoren durchgeführt werden konnten. Hierbei zeigten sich die beiden Substanzen TG und TFP als vielversprechende metastasierungshemmende Wirkstoffe, was zu weiteren Untersuchungen motiviert. Zudem konnten zwei stabile *SEC62*-ko Zelllinien mittels CRISPR-Cas9 generiert, validiert und charakterisiert werden. Weitere Analysen, um den Einfluss und die Funktion von *SEC62* genauer verstehen zu können sind Gegenstand zukünftiger Forschung.

Table of Contents

Abstract	VI
Zusammenfassung	VIII
List of Abbreviations	XIII
1. Introduction.....	1
1.1. Epidemiology of cancer	1
1.2. Head and Neck cancer	2
1.3. Genetic variations in human cancer	6
1.4. SEC62	9
1.5. Thapsigargin and Trifluoperazine as potential oncological therapeutics	12
1.6. Motivation	17
2. Materials and methods.....	19
2.1. Materials	19
2.1.1. Chemicals	19
2.1.2. Buffers and solutions	22
2.1.3. Technical equipment and disposables	25
2.1.4. Antibodies	30
2.1.5. Rough microsomes	32
2.1.6. Oligonucleotide primers	32
2.1.7. Bacterial strain	33
2.1.8. Cell lines	33
2.1.9. Kits	33
2.1.10. Software	34
2.2. Animal Experiments.....	35
2.2.1. Animals.....	35
2.2.2. Orthotopic, lymphatic metastasis xenograft model	35
2.2.3. Haematogenous metastasis xenograft model	36
2.3. Histological methods.....	40
2.3.1. Fixation and embedding of histological specimens.....	40
2.3.2. Production of histological sections	41
2.3.3. Haematoxylin and eosin stain	41
2.3.4. Microscopic evaluation.....	42

2.4. Biochemical Methods	43
2.4.1. Protein isolation.....	43
2.4.2. SDS-polyacrylamide gel electrophoresis (SDS-Page)	43
2.4.3. Western Blotting and detection.....	45
2.5. Molecular biology and nucleic acid chemistry.....	48
2.5.1. Strategies for targeted mutagenesis	48
2.5.2. Transformation of bacterial cells.....	48
2.5.3. Cultivation of bacterial cells	49
2.5.4. Plasmid and genomic DNA extraction and quantification.....	49
2.5.5. Sequencing of plasmid DNA and amplification	49
2.5.6. RNA isolation	50
2.5.7. Reverse transcription of RNA into cDNA	50
2.5.8. Quantitative real-time PCR.....	50
2.6. Cell culture and cell manipulation.....	51
2.6.1. Cultivation of mammalian cells	51
2.6.2. Cell counting and harvesting	51
2.6.3. CRISPR/Cas9 technology	52
2.6.4. Clone characterisation.....	56
2.7. Statistics	64
3. Results	65
3.1. Impaired migration of HNSCC cells by TG and TFP application	65
3.2. Establishment of a murine orthotopic lymphatic metastasis model	66
3.2.1. Tumour cell injection into the base of the tongue led to shorten overall survival .	67
3.2.2. Tongue tip has second most lymphatic vessels - decision for injection side	68
3.2.3. Tumour cell injection into the tongue tip led to prolonged overall survival.....	70
3.2.4. Impact of injection side within the tongue tip on tumour growth and metastatic spread	71
3.2.5. Increasing cell amount led to 100 % primary tumour growth in combination with 60 % metastatic spread	73
3.2.6. Doubling cell amount has no impact on metastasis formation in cervical lymph nodes	73
3.2.7. Reproducibility of the new established model with another mouse strain.....	74
3.2.8. Conclusion for establishing a murine orthotopic xenograft model for lymphatic metastatic spread	75
3.3. Establishment of a murine haematogenous metastasis model	78
3.3.1. Frist steps towards model establishment.....	79
3.3.2. Establishment of metastasis formatting cell amount	80

3.3.3. Establishment of histological analysis of lung tissue	82
3.3.4. Comparison of different imaging techniques and evaluation of metastatic burden	83
3.4. TFP and TG administration show a trend towards anti-metastatic effects	97
3.4.1. Tolerance of applied substances.....	98
3.4.2. Impact of TFP/TG administration on lymphatic metastasis.....	99
3.4.3. Impact of TFP/TG administration on haematogenous metastasis	106
3.5. Generation and analysis of SEC62 knockout cells.....	114
3.5.1. Descriptive validation of CRISPR clones.....	115
3.5.2. Functional analysis of generated SEC62 knockouts.....	129
4. Discussion	135
4.1. Establishment of different murine metastasis models	136
4.1.1. Do's and Don'ts for lymphatic metastasis model establishment.....	136
4.1.2. Do's and Don'ts for haematogenous metastasis model establishment	138
4.1.3. The usage of different imaging techniques compared to the histological gold standard for lung volume evaluation.....	141
4.2. Impact of TG/TFP treatment on different murine metastasis models.....	143
4.2.1. Tolerability/toxicity of TG and TFP i.p. administration.....	146
4.2.2. TG/TFP treatment and its consequences on murine lymphatic metastasis	148
4.2.3. TG/TFP treatment and its consequences on murine haematogenous metastasis	152
4.3. Generation of SEC62-knockout by CRISPR/Cas9 and its functional consequences for HNSCC	155
4.4. Summary and perspectives	162
5. References	165
6. Publications and congress contribution	188
Original research articles	188
Planned publications	189
Congress contributions (only first author)	190
Experimentally supervised MD candidates	190
7. Acknowledgement.....	191
8. Supplement.....	192
9. Curriculum vitae	204

List of Abbreviations

%	percent
°C	degree Celsius
μCT	micro computer tomography
μg, μm, μl	microgramme, micrometre, microlitre
4',6-Diamidin-2-phenylindol	DAPI
AKT	serine/threonine protein kinase
Al	aluminium
ANOVA	analysis of variance
Aqua dest.	purified water
ATF3	cyclic AMP-dependent transcription factor
ATP6V1B1	V-type proton ATPase subunit B
auto	automatically
B2M	β-2-Microglobulin
Balb/c nu	Balb/c nude
BiP	Binding immunoglobulin protein
bp	basepair
Ca ²⁺	calcium
CaM	calmodulin
Cas	CRISPR-associated sequence
CCD-camera	charge-coupled device camera
CCDN1	encoding cyclin D1
CD31	Platelet And Endothelial Cell Adhesion Molecule 1
CDKN2A	encoding p16 ^{INK4A}
cDNA	complementary desoxyribonucleic acid
CI	cell index
CLIC3	chloride intracellular channel 3
cmH ₂ O	centimeter water column
CO ₂	carbin dioxide
CRC	colorectal carcinoma
CRISPR	Clustered Regularly Interspaced Short Palindromic Repeats
crRNA	CRISPR-RNA
crRNA	CRISPR ribonucleid acid
CT	computer tomography
CYP4F11	cytochrome P450 4F11
DAVID	Database for Annotation, Visualization and Integrated Discovery
DE	differential expression
DMEM	Dulbecco's Modified Eagle's Medium
DMSO	Dimethyl sulfoxide
DNA	desoxyribonucleic acid
dNTP	deoxyribonucleoside triphosphate
DPBS	Dulbecco's phosphate buffered saline
DSB	double strand break
DUSP	dual-specificity phosphatase
EBV	Epstein-Barr virus
ECL	Electrochemiluminescence
EDTA	Ethylenediaminetetraacetic acid
EEF1A2	elongation factor 1-alpha 2

EGR3	early growth response protein 3
EGTA	ethylene glycol-bis(β -aminoethyl ether)-N,N,N',N'-tetraacetic acid)
EMA	European Medicines Agency
EMT	epithelial-mesenchymal transition
eq	equivalents
ER	endoplasmatic reticulum
et al.	and other
FaDu	
FARP1	FERM, ARH/RhoGEF And Pleckstrin Domain Protein 1
FC	fold change
FCS	fetal calf serum
FDR	false discovery rate
FFPE	formalin fixed and paraffine embedded
FOXO3	Forkhead box protein O3
g	gramme
GAL	galanin
gDNA	genomic desoxyribonucleic acid
GO	gene ontology
h	hour
H ₂ O	water
HDR	homology-directed repair
HE	haematoxylin/eosin
HEPES	2-[4-(2-hydroxyethyl)piperazin-1-yl]ethanesulfonic acid
HIST1H3H	histone H3.1
histo	histology
HNSCC	Head and Neck squamous cell carcinoma
HPV	Human papillomavirus
i.p.	intraperitoneal
i.v.	intravenously
IF	immunofluorescence
indel	insertion- and/or deletion-mutations
IONO	ionomycin
IP ₃ R	Inositol 1,4,5-Trisphosphate Receptor
IRE-1	Inositol-requiring Enzyme 1
ITPR	Inositol 1,4,5-Trisphosphate Receptor Type
IU	international unit
KEGG	Kyoto Encyclopedia of Genes and Genomes
kg	kilogramme
L	litre
L	length
LC3	microtubule-associated proteins 1A/1B light chain 3
LIR	LC3-interacting region
LN	lymph node
LYVE1	Lymphatic Vessel Endothelial Hyaluronan Receptor 1
manu	manually
MAPK	mitogen-activated protein kinase
MEM	Minimal Essential Medium
Met	metastasis
mg, mm, ml	milligramme, millimetre millilitre

min	minute
mIRS	modified immunoreactive score
mM, M	milli-, molarity
MRI	Magnetic resonance imaging
mRNA	messenger ribonucleic acid
n.s.	not significant
NDRG1	N-myc downstream-regulated gene 1 protein
ng, nm	nanogramme, nanometre
NGS	next generation sequencing
NHEJ	non-homologous end joining
nM	nanomolar
no RT control	no reverse transcriptase control
NOD-Scid	Non-Obese Diabetic - Severe Combined Immunodeficiency
nt	nucleotide
OD	optical density
p	statistical significance
PADI2	peptidylarginine deiminase 1
PAM	protospacer adjacent motif
PASMC	pulmonary arteries smooth muscle cells
PBS	Phosphate buffered saline
PCA	principal component analysis
PCR	Polymerase Chain reaction
PET	polyethylene terephthalate
PFA	paraformaldehyde
pH	negative decadic logarithm of the concentration of hydrogen ions
PMCA	plasma membrane Ca ²⁺ ATPase
polyethylene terephthalate	PET
Primer fwd.	Primer forward
Primer rev.	Primer reverse
PSMA	Prostate specific membrane antigen
qRT-PCR	quantitative real-time polymerase chain reaction
R/M-HNSCC	recurrent and/or metastatic HNSCC
REVIGO	reduce and visualize gene ontology
RIN	RNA integrity number
RM	rough microsomes
R _{min}	minimal fluorescent ratio
RNA-seq	RNA-sequencing
ROC	receptor operated Ca ²⁺ channel
ROI	region of interest
RT	Room temperature
RTCA	real-time cell analysis
s	second
SD	standard deviation
SDS-page	Sodium-Dodecylsulfate polyacrylamid-gelelectrophoresis
sgRNA	single guide ribonucleic acid
sgRNA	single guide ribonucleic acid
SLC12A8	Solute Carrier Family 12 Member 8
SMPD3	Sphingomyelin Phosphodiesterase 3
SOCE	store operated Ca ²⁺ entry

List of Abbreviations

SOX18	transcription factor SOX-18
SP	<i>Streptococcus pyogenes</i>
SPNS2	sphingosine-1-phosphate transporter
TBE	TRIS-Borat-EDTA
TBS	Tris-buffered saline
TFP	Trifluoperazine
TG	Thapsigargin
TGFBR3L	transforming growth factor-beta receptor type 3-like
TIDE	tracking of indels by decomposition
TMM	trimmed mean of M-values
TNM	tumour, node, metastasis
TPM	transcripts per kilobase million
tracrRNA	trans-activating crRNA
treat	treatment
UdS	Saarland University
UPR	unfolded protein response
UV	ultraviolet
V	volt
V	volume
v/v	volume per volume
W	width
w/v	weight per volume
WB	western blot
wt	wild type
ZC3H12C	Zinc Finger CCCH-Type Containing 12C
β -ME	β -mercaptoethanol

1. Introduction

1.1. Epidemiology of cancer

Current statistics show that around 630,000 new cancer cases were diagnosed in Germany, worldwide about 19.3 million new cases were registered in 2020. To set these numbers in a relation to the total population – there are 0.8 % new cancer cases in Germany and 2.5 % new cases worldwide in 2020 (Ferlay et al., 2020). These numbers seem to be low at the first glance, but worldwide around 10 Mio people died due to cancer. In Germany more than a quarter of all registered deaths were caused by cancer, even despite the beginning of the COVID-19 pandemic (Ferlay et al., 2020; Federal Bureau of Statistics Germany – Destatis; <https://www.destatis.de/>; data query: 03.02.2022).

In Germany malignant neoplasms are the second most common cause of death with 23.5 % followed by diseases of the respiratory system with 6.2 % at the third place. At the top of the death cause list are diseases of the cardiovascular system (34.3 %) (Federal Bureau of Statistics Germany – Destatis; <https://www.destatis.de/>; data query: 03.02.2022). Even worldwide the ranking of death causes is the same as in Germany. Cancer is the second leading cause of death (17.1 %) and follows directly diseases of the cardiovascular system which are the most common reasons for deaths (31.8 %) (GBD 2017 Risk Factor Collaborators, 2018). In the international comparison the cancer death rate in Germany is around 23.5 % and is obviously higher than the cancer death rate worldwide (17.0 %) (GBD 2017 Causes of Death Collaborators, 2018; Ferlay et al., 2020). When comparing the main reasons for death between different regions over the world there is a remarkable discrepancy between low- and high-income countries. More than 50 % of all deaths in low-income countries result from so called communicable diseases, e.g. diarrhoeal diseases, Human Immunodeficiency Virus (HIV)/Acquired Immune Deficiency Syndrome (AIDS), malaria and tuberculosis (World Health Organization, 2018). Also the average age of death (e.g. 64.5 years in Africa) is noticeable lower compared to high-income countries like the USA (77.2 years) and Germany (81.7 years) (World Health Organization, 2021). Because of this discrepancy of causes for deaths between high- and low-income countries the overall rate of deaths due to cancer is worldwide lower than in Germany (worldwide – 17.1 %; Germany – 23.5 %).

Nevertheless, non-communicable diseases like cancer and cardiovascular diseases are responsible for about 85 % of all deaths in high-income countries (World Health Organization, 2021). Due to the fight against infectious diseases, one might expect that non-communicable diseases will become even more dominant and will cause a significant decrease in the number of communicable diseases. A linked effect of the limitation of infectious diseases is also the increasing age. Between 2000 and 2019 the global average of life expectancy increased by 6.5

years (World Health Organization, 2021). As a result, the risk for developing cancer increased remarkably. In Germany the risk of developing cancer before the age of 75 years is about 30.1 % (both sexes) (Ferlay et al., 2021). The risk of dying from cancer before the age of 75 years in Germany is about 10.8 %, whereby the risk of dying due to cancer for men is nearly 4 % higher compared to women (12.7 % men; 9.0 % women) (Ferlay et al., 2021). About 87 % of all patients dying from cancer are older than 50 years (Roser and Ritchie, 2020). Nevertheless – cancer affects us all and can pertain to anyone even younger people.

In general, men (54.8 %) have a higher risk to develop cancer than women (45.2 %) in Germany and also worldwide (men: 52.2 %; women: 47.8 %). However, for some cancer entities women are more affected than men like for example breast cancer, whereas men are more affected by lung and colorectal cancer (Ferlay et al., 2021). The incidences of most cancer entities are further increasing including a high body mass index due to physical inactivity, unhealthy diet and of course tobacco and alcohol consumption (World Health Organization, 2020). These mostly avoidable factors harbour also the main risks for developing other non-communicable diseases. In addition, also viral infections causing cancer become more prominent in the last years including Human papillomavirus (HPV), Epstein-Barr virus (EBV), Hepatitis B and C virus as well as *Helicobacter pylori* (Plummer et al., 2016; Bray et al., 2018). However, much effort has been spent into research to develop better procedures and tests for diagnosis, screening methods and new approaches in therapy (Bray and Soerjomataram, 2015; Bray et al., 2018; Bernard and Christopher, 2020). As a result of these improvements mortality rates are continuously decreasing (Zentrum für Krebsregisterdaten im Robert Koch-Institut, 2016). Especially consequent screenings for cervical and colorectal cancer allows early detection of precancerous lesions and developing or early-stage cancer can be nipped in the bud (Colombo et al., 2012; Issa and Nouredine, 2017).

1.2. Head and Neck cancer

Head and neck cancer is the seventh most common cancer entity worldwide in 2020 (880.000 new cases), accounting for 4.5 % of all cancer deaths in the world (440.000 deaths). As many as 16,558 new head and neck cancer cases were registered in Germany, which lists head and neck cancer at the eleventh place of the most common cancers (International Agency for Research on Cancer (IARC) and Global Cancer Observatory, 2020).

The term head and neck cancer (HNSCC) summarises various malignant tumours of the lips and the oral cavity, the nasopharynx, oropharynx, hypopharynx and the larynx (Figure 1) (Johnson et al., 2020). Most of the detected HNSCCs of the upper aerodigestive tract are squamous cell carcinoma (Wild et al., 2020). This type of cancer originates from mucosal epithelial cells at the aforementioned anatomical sites (Chow, 2020; Johnson et al., 2020).

Despite huge effort in research mortality rates are just slightly decreasing in the last years. Comparing the 5-year survival rate from 1992-1996 (55 %) with the rate from 2002-2006 (66 %) there is only an increase of 11 % (Johnson et al., 2020). Invasive neoplasms which display various degrees of differentiation, often represent early and extensive lymph node metastases (Magnano et al., 1999). Nearly 50 % of patients introducing themselves in clinic already show lymph node metastases at the time point of diagnosis. Distant metastases are observed in 10 % of patients, which significantly worsen their prognosis (Wiegand et al., 2015). Large tumours with local invasion and the evidence of local or distant metastases display a significant lower 5-year overall survival (>50 %) (Magnano et al., 1999; Braakhuis et al., 2012).

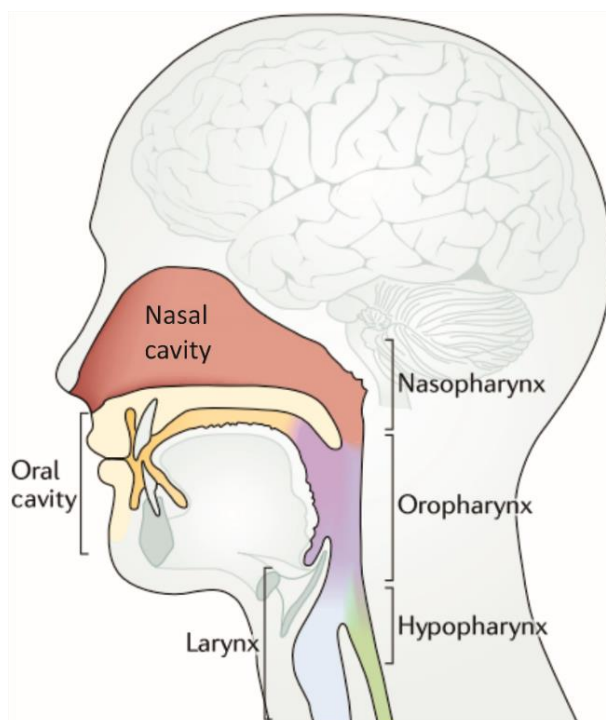


Figure 1 Schematic representation of the anatomical sites of the head and neck region. Figure modified of (Cramer et al., 2019).

The development of malignant tumours in the head and neck region is promoted by a range of factors. Main factors which account for 75 % of tumour burden for the development of HNSCC as well as for other cancer entities of the upper aerodigestive tract, are the tobacco and alcohol consumption as well as environmental pollutants (Hashibe et al., 2007; Pezzuto et al., 2015; Johnson et al., 2020). Especially the combination of tobacco and alcohol abuse has not only an additive effect but results even in a multiplicative effect (Hashibe et al., 2007). Mostly men in the 6th decades of life were affected due to their heavier indulgence in both tobacco and alcohol (Johnson et al., 2020). The incidence for HNSCC diagnosis for women is only one third as compared to men (Wild et al., 2020).

Regarding the last 15 years broad hints were noticeable that an infection with specific human papilloma virus (HPV) types (HPV type 16/18) which are already known for causing cervical

cancers are etiologically involved in the development of oropharyngeal carcinoma (Wild et al., 2020). The virus itself does not trigger directly the carcinoma development, but it is an important co-factor. Viral oncoproteins like E6 and E7 propagate the carcinogenesis due to disruption of two important tumour suppressing pathways involving p53 and the retinoblastoma protein (Rampias et al., 2009; Wild et al., 2020). These differently induced types of HNSCCs differ in terms of epidemiology, clinical and molecular characteristics, which overall results in a better survival of HPV-positive HNSCC patients (Ang et al., 2010; Wild et al., 2020). First of all, affected patients are predominantly younger (~53 years) than patients which were diagnosed for HNSCC because of tobacco- and alcohol abuse (Marur et al., 2010; Windon et al., 2018). Better prognosis of HPV-positive patients is amongst others related to their younger age of diagnosis and therefore a better physical constitution, which may also contribute to the observed positive effect of HPV associated disease on responses to chemotherapy and radiotherapy (Chow, 2020; Kühn et al., 2021).

Beside these main risk factors, HNSCC can also occur due to exposition to ultraviolet (UV) light, chemical and physical noxa like asbestos, or infection by EBV (Gallagher et al., 2010; Langevin et al., 2013; Fung et al., 2016; Broccolo et al., 2018).

Dependent on their localisation, malignant neoplasms of the head and neck region cause a broad range of symptoms e.g., painful but also painless cervical swellings. Often there are tumescence or discolouration as well as longer lasting ulcers at the mucosa. Depending on their size and localisation these changes could limit the mobility of the tongue, cause swelling and/or difficulties in swallowing. Symptoms indicating a larynx carcinoma are often chronic hoarseness, persistent prickle in the throat connected with a constant urge to clear one's throat (Deutsche Krebshilfe, 2017). The most common pre-malignant lesions are the leuko- and erythroplakia, defined as white and red plaques in the mucosal lining (van der Waal, 2009; Johnson et al., 2020) though they are only found in a low percentage of HNSCC patients as a precursor lesion.

After a detailed medical history with an evaluation of potential risk factors and a physical examination an appropriate imaging with ultrasound, computed tomography or magnetic resonance imaging should be performed for a precise evaluation of the primary tumour and possible metastases. Before biopsy specimens are obtained, imaging should be completed to avoid possible anatomical distortions due to biopsy (Chow, 2020).

Usually the tumour, node, metastasis (TNM) staging is applied. A second staging is applied on the basis of the Union for International Cancer Control (UICC; Chow, 2020) dependent on tumour size, involvement of lymph nodes, the existence of metastases and the HPV-status tumours are classified, which helps to determine the best therapy strategy.

The overall modalities for a curative therapy approach are surgical resection (cold steel resection vs. CO₂ laser resection vs. transoral robotic surgery), radiation, and systemic therapy. The decision is made for a therapy which suits best for the individual patient and carries the best

curative approach combined with an optimizing preservation of function (Johnson et al., 2020). Dependent on several aspects like the tumour staging, the anatomical site, and the surgical accessibility, as well as the general state of health of the individual patient, therapy approaches are discussed in involved multispecialty teams like otorhinolaryngology, maxillofacial surgery, and radiation oncology in an interdisciplinary tumour board to discuss the best-suited therapy for each patient. The overall aim is the full excision or destruction of the tumour and its metastases under structural and functional preservation and thereby the morbidity improvement. If curative treatment is not possible, the tumour should be impaired in its growth to enable a long-term maintenance of life quality. Early-stage disease which consists of a small primary cancer without any nodal involvement is usually curable by surgery or definitive radiotherapy (Chow, 2020; Johnson et al., 2020). Robotic surgery and minimal invasive laser microsurgery increase the probability of organ- and function-preservation whereas radiotherapy reduce morbidity because of intensity-modulated and image-guided therapy (Moore et al., 2012; Weiss et al., 2017; Gupta et al., 2018). Locally advanced tumours which occur in >60 % of all HNSCC patients, are mostly treated by multimodal approaches (Braakhuis et al., 2012; Brana and Siu, 2012). In addition, more than 65 % of HNSCC patients will develop a recurrent or metastatic disease (Argiris et al., 2008). Especially for these groups new immunomodulatory approaches are available. First, a monoclonal antibody against a receptor-tyrosine kinase, the epidermal growth factor receptor (EGFR), was established as a therapy against recurrent or metastatic diseases (Bonner et al., 2006). In more than 90 % of all HNSCC specimens an increased EGFR expression is detected, which is strongly associated with a decreased overall survival as well as a poor progression-free survival (Dassonville et al., 1993; Kian Ang et al., 2002). The inhibition of EGFR is able to sensitise HNSCC cells to ionizing radiation (Shintani et al., 2003; Bonner et al., 2006). Cetuximab directly targets EGFR, which leads to an inhibition of the EGFR signalling pathway (Li et al., 2005). In current therapy protocols Cetuximab is combined with radiotherapy and given either in a first-line palliative setting for recurrent/metastatic disease or as adjuvant treatment after tumour resection in patients unfit for platinum-based chemoradiation. Additionally, there are two immunomodulators approved to treat recurrent and/or metastatic disease (R/M-HNSCC). Pembrolizumab and Nivolumab are programmed cell death 1 (PD-1) directed immune-checkpoint inhibitors which show stable responses and survival improvements in HNSCC patients (Ferris et al., 2016; Seiwert et al., 2016). These two monoclonal antibodies show highest response rates in PD-L1 expressing or microsatellite instable tumours (Johnson et al., 2020). Nivolumab is approved by the EMA (European Medicines Agency) for second-line treatment of R/M-HNSCC patients with a failure during or within six months after platinum-based therapy independent of tumour PD-L1 expression (Ferris et al., 2016). Pembrolizumab is approved by the EMA for treating R/M-HNSCC patients either in a second-line setting with failure during or within six months after platinum-based therapy with a tumour proportion PD-L1 score >50 % (TPS) or

additionally in a first-line setting for tumours with a combined positivity score >1 (CPS) as monotherapy or in combination with cisplatin and 5-Fluorouracil. (Burtneess et al., 2019; Cohen et al., 2019). Another immunomodulator which is in active clinical development is ipilimumab (CTLA-4). However, this monoclonal antibody is associated with more toxicity compared to the well tolerated PD1 and PD-L1 inhibitors. The combination of both antibodies is in ongoing clinical trials (Wang et al., 2019). Furthermore, numerous clinical trials evaluate the potential benefit of using checkpoint-inhibitors in a neoadjuvant and/or adjuvant setting as well as in combination with radiation or chemoradiation as primary tumour treatment.

1.3. Genetic variations in human cancer

The development of cancer is a complex process which combines an involvement of multiple panel of pathway mechanisms (Hanahan, 2022). Years can pass between the development of an individual cancer cell and the appearance of a detectable cancer disease.

The origin of cancer lies within the genome, but in general it is an interaction of various dysregulations on different levels of cell biology and the whole body (Hanahan, 2022). Over the time alterations occur within the nucleotide sequence of genes which are normally repaired. Due to several environmental effects like radiation, carcinogenic substances, a viral infection or by epigenetic events these alterations accumulate and cannot be repaired anymore. Normally, cells are able to deal with such mutation accumulations and activate several rescue mechanisms like apoptosis to eliminate those cells. In this context, three gene groups are of particular importance: proto-oncogenes, tumour-suppressor genes and genes of the repair machinery (Vogelstein and Kinzler, 2004). All these gene sets exist in normal and healthy cells and are regulating processes like proliferation and differentiation. There is a balance of proto-oncogenes that are responsible for cell proliferation and tumour-suppressor genes that inhibit the proliferation process (Lee and Muller, 2010). Moreover, in case of genetic alterations within these two groups, the third important group, the genes of the repair machinery will start their work and are able to repair the genetic alterations within the proto-onco- and/or tumour-suppressor genes. However, there is the opportunity of repair failure which leads to an imbalance between proto-onco- and tumour-suppressor genes (Friedberg, 2003). Usually, cells are able to handle such a single stray by utilizing a sophisticated program that serves to operate imbalanced cells into a programmed cell death. Otherwise this imbalance implicates an uncontrolled proliferation and is able to cause an uncontrolled tissue growth (Cory and Adams, 2002). The mutations which lead to variations in the genome can be divided into two groups: hereditary mutations and acquired (or somatic) mutations (Rahner and Steinke, 2008). In this work, the focus will rather be on somatic mutations that occur spontaneously during person's life driven by the aforementioned triggers. According to somatic

mutations only certain cells are affected, instead of each cell of the body (Vogelstein and Kinzler, 2004).

The reason for cancer development is mainly a plethora of genetic events leading to activated proto-oncogenes and the inactivation of tumour-suppressor genes (Balmain et al., 1993). This accumulation of gains of functions of oncogenes and recessive loss of function of tumour-suppressor genes drives for a dysregulation and acquires a succession of the hallmarks of cancer which were postulated by Hanahan and Weinberg (Hanahan and Weinberg, 2000, 2011; Hanahan, 2022). Cancer-related phenotypes include autonomy in growth signals, insensitivity to anti-growth signals and consequential unlimited replicative potential, ability to evade apoptosis, ability of angiogenesis, invasion and metastasis were acquired through the accumulation of mutations in genes acting in cancer-associated signalling pathways (Hanahan and Weinberg, 2000, 2011; Hanahan, 2022). All current hallmarks of cancer are shown in Figure 2. The multistep process of tumorigenesis drives genetic alterations which cause the transformation of a normal cell into a malignant descendent. These alterations of genetic and epigenetic changes accumulate during life time, which is one reason why cancers are often diagnosed in an age-dependant incidence (Sarkar et al., 2013). Mutations could happen in a wide range, from point mutations in which single nucleotides are altered through to changes in the whole chromosome structure (Vogelstein et al., 1988). Most common subgroups of HNSCCs are aneuploid (Bockmühl and Petersen, 2002; Jin et al., 2006). In 1996, Califano et al. postulated the first genetic multi-step progression model in areas of modified histopathologies (Califano et al., 1996). They discovered different loss of heterozygosity patterns dependent on the stage of the carcinogenesis.

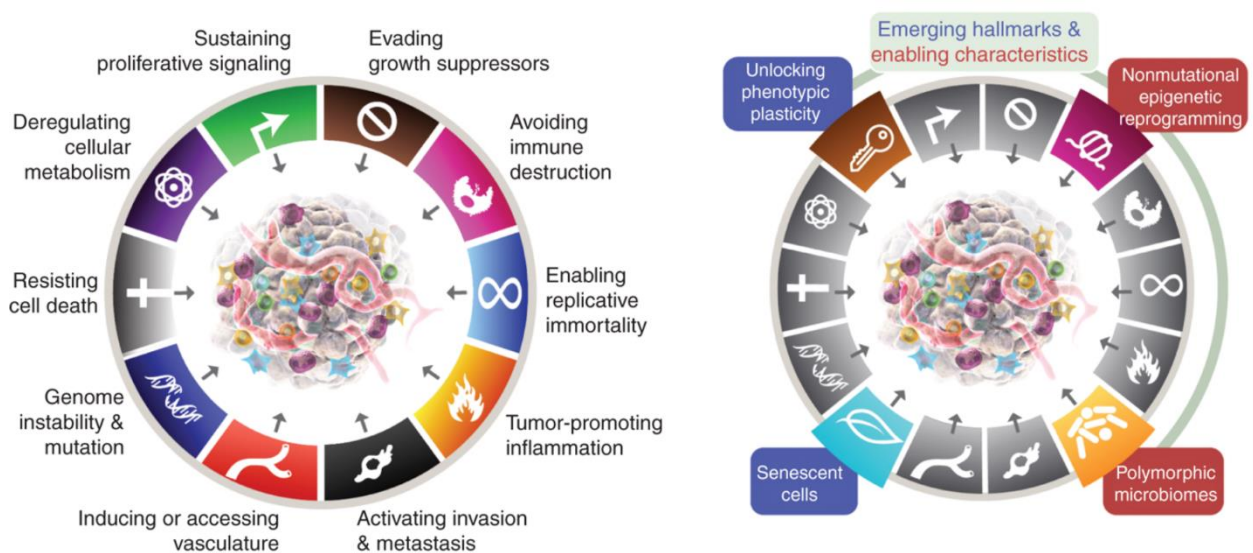


Figure 2 Current Hallmarks of Cancer by Hanahan (2022). The figure is modified of Hanahan, 2022.

One of the most prominent genes which is somatically mutated in 60-80 % of HNSCC is *TP53* (van Houten et al., 2002; Poeta et al., 2007). Its tumour-suppressor protein p53 plays a key role in an early stage of carcinogenesis to overcome senescence and to get in a limitless replicative cycle (Kastan and Bartek, 2004). Other highly mutated genes for early-stage mutations that push cells into an immortalised status are *CDKN2A* (encoding p16^{INK4A}) and *CCND1* (encoding cyclin D1) (Reed et al., 1996; Smeets et al., 2006; Pickering et al., 2013). Both genes belong to the group of tumour-suppressor- and oncogenes and are important regulators in the cell cycle. Johnson et al. published an overview of most of the known genetic events in the process of HNSCC development (Figure 3) (Johnson et al., 2020). Nevertheless, mutation landscape of

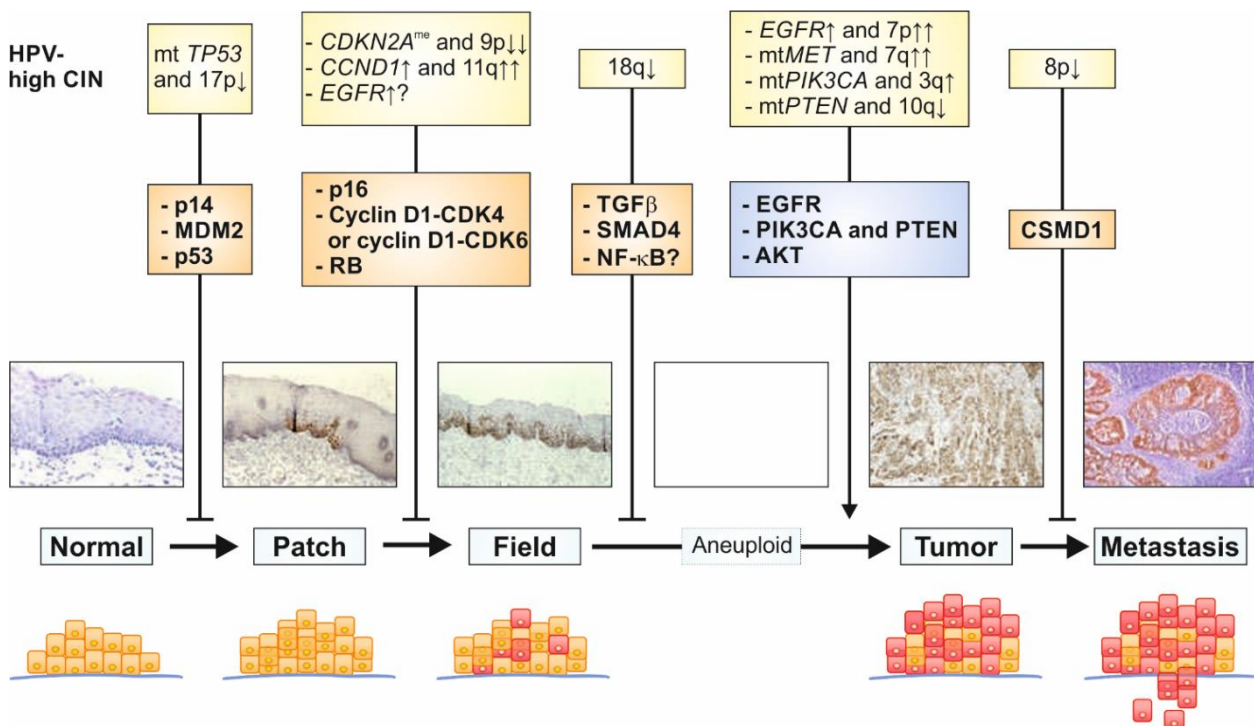


Figure 3 Molecular carcinogenesis model for HNSCC: Graphical overview of the hypothetical development of HPV-negative HNSCC with high chromosomal instability (CIN). In the initial step for carcinogenesis a progenitor cell or adult stem cell acquires one or more mutations that will lead to a patch formation. While the normal growth control is modified the patch will expand into a field. Due to further accumulation of genetic alterations the field will turn into a carcinoma in situ which then is potentially able to perform the epithelial mesenchymal transition (EMT) to start migration and lead to metastasis formation. The yellow boxes indicate genetic and chromosomal alterations associated during different processes within the HNSCC development. The blue box indicates oncogenic pathways as well orange boxes are dedicated to tumour-suppressive pathways. The figure is modified of (Leemans et al., 2011).

HNSCCs differs significantly between noxa- and HPV-induced HNSCC. Thus, mutation in *TP53* is rarely found in HPV-positive HNSCC (Leemans et al., 2011).

HNSCC is a very heterogeneous disease with several subclasses identified at least at the molecular and clinical level. Besides the main somatic mutations mentioned above, also characteristic chromosomal changes have been identified in invasive HNSCC (Bauer et al., 2008). Prognostic relevant chromosomal changes are gains of 11q and 12q, combined with losses of 5q, 6q, 8p 21q and 22q (Bockmühl et al., 1996; Bauer et al., 2008). Several groups also found an amplification on the long arm of chromosome 3 (3q) independent of the HPV status but

significantly associated with an advanced tumour stage (Ell et al., 2002; Abou-Elhamd and Habib, 2008; Bochen et al., 2017).

This significant 3q-amplification was also discovered in other cancer entities like non-small-cell lung cancer, cervical cancer as well as oesophageal cancer, which implies a potential oncogenic role for genes that were encoded on this chromosomal segment (Chujo et al., 2002; Rao et al., 2004; Yen et al., 2005). While searching for possible oncogenes which are encoded on 3q revealed several potential target genes like for example *PIK3CA*, *p63* and *CLAPM1*, but an impact in tumour biology was finally not be determined (Massion et al., 2004; Comtesse et al., 2007; Yamamoto et al., 2008).

1.4. SEC62

Furthermore, another gene encoded and amplified on 3q – *SEC62* - was identified as a potential candidate and further analysed in HNSCC (Wemmert et al., 2016; Bochen et al., 2017). Multiple studies identified *SEC62* in prostate, thyroid, and also non-small-cell lung cancer as the most common overexpressed gene locus on the 3q region (Sicking et al., 2021). This correlated with an increased messenger ribonucleic acid (RNA) amount and elevated protein levels compared with tumour-free tissue samples of the same patients (Jung et al., 2006; Greiner et al., 2011a; Linxweiler et al., 2012). Moreover, a high *SEC62* protein amount in lung cancer correlates significantly with the occurrence of lymph node metastases and is also associated with a significantly shorter overall survival (Linxweiler et al., 2012, 2013). Comparable results were also found in the examination of HNSCC tissue samples. Here, overexpression of *SEC62* compared to tumour-free mucosa was significantly correlated in 86 % with the occurrence of cervical lymph node metastases and a significantly shortened overall survival (Wemmert et al., 2016; Bochen et al., 2017) (Figure 4). Investigations over the last years revealed involvement of amplified *SEC62* in various other cancer entities like hepatocellular carcinoma, melanoma, cervical cancer,

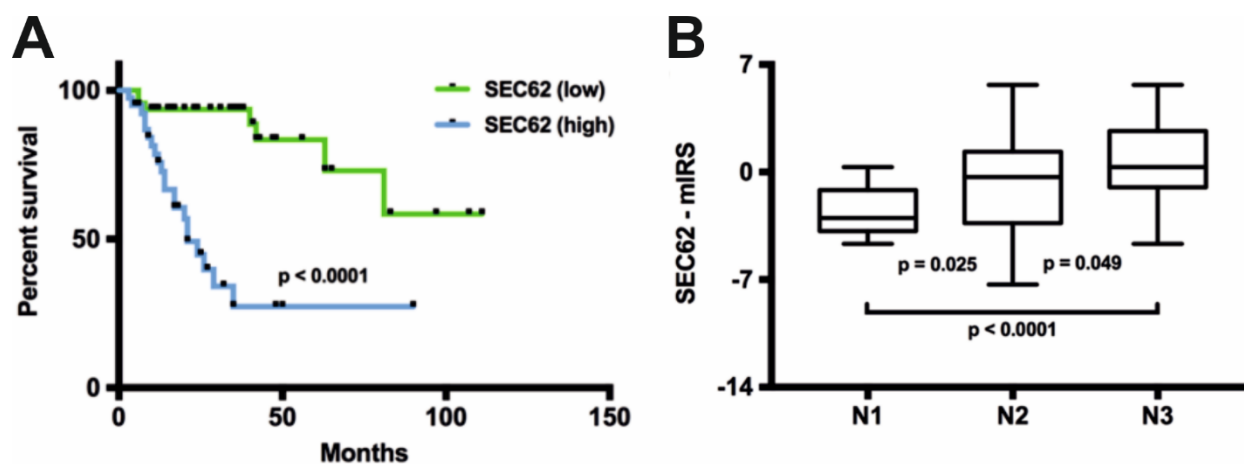


Figure 4 HNSCC prognosis dependent on SEC62 protein amount: (A) Patients with high SEC62 amount show significant shorter survival. **(B)** The SEC62 protein amount correlates significantly with increasing metastasis staging. The figure is modified of (Bochen et al., 2017).

prostate cancer and breast cancer (Bockmühl et al., 1996; Allen et al., 2000; Haverty et al., 2009; Sheu et al., 2009; Takacs et al., 2019; Casper et al., 2021; Müller et al., 2021).

Based on the results obtained in the aforementioned studies, SEC62 seems to play a significant role in tumorigenesis. However, the question of the functional role of SEC62 in the eukaryotic cell remained unanswered for many years.

Sec62p was first discovered in *Saccharomyces cerevisiae*. By structural and functional analysis its location and role in the protein translocation machinery in the membrane of the endoplasmic reticulum (ER) was revealed (Deshaies and Schekman, 1989, 1990; Rothblatt et al., 1989). In the following years, a SEC62 homologue was also discovered in *Drosophila melanogaster* (Drosophila translocation protein 1 – Dtrp1) (Noël and Cartwright, 1994). The mammalian SEC62 was first discovered in 1997 (Daimon et al., 1997; Tyedmers et al., 2000). SEC62 codes for a transmembrane protein of the ER and is part of the dimeric SEC62/SEC63 complex (Meyer et al., 2000). Together with the heterotrimeric SEC61 complex both complexes play an essential role in the translocation of nascent and newly synthesised precursors of polypeptides into and across the ER membrane (Linxweiler et al., 2017b). At its cytosolic N terminus SEC62 obtains two conserved peptide domains that allow ribosome binding, which is one hint for affiliation in the translocation process (Mü et al., 2010). There is additional evidence that posttranslational transported precursor proteins of different length depend on SEC62 in case of an efficient translocation. Nevertheless, the main function of SEC62 is still unknown (Lakkaraju et al., 2012; Lang et al., 2012).

Normally, precursor proteins translocate into the ER for further processing through the SEC61 channel (Linxweiler et al., 2017b). Apart from its channel properties there is a passive Ca^{2+} efflux from the ER lumen into the cytosol driven by a Ca^{2+} gradient (Van Coppenolle et al., 2004). In general, the ER serves as the largest intracellular Ca^{2+} store (Pozzan et al., 1994). Because Ca^{2+} is the most important second messenger and involved in a plenty of cellular pathways, homeostasis of Ca^{2+} concentrations between cytosol and ER lumen is indispensable (Clapham, 1995; Newton et al., 2016; Bagur and Hajnóczky, 2017). Therefore, regulators of this passive efflux are mandatory especially because cytosolic Ca^{2+} levels play a crucial role in cellular processes like migration and apoptosis (Scorrano et al., 2003; Huang et al., 2004). To date, three potential regulatory processes were identified to decrease the passive efflux of Ca^{2+} from the ER lumen into the cytosol. One of these regulatory mechanisms is calmodulin (CaM – calcium-modulated protein) dependent. CaM, a highly conserved target of the main intracellular second-messenger molecule, is able to bind Ca^{2+} -dependent to the SEC61 channel at the cytosolic site and thereby closes the channel and inhibits the ionic leakage (Chin and Means, 2000; Erdmann et al., 2011). In 2012, Schäuble et al. postulated the closure of the SEC61 channel from the ER luminal side through the binding of heatshock protein 70 (Hsp70, BiP, binding immunoglobuline protein). BiP is an ER luminal chaperone whose main function is protein folding assistance of

newly synthesised proteins during their translocation into the ER as well as the regulation of the inositol-requiring enzyme 1 (IRE1)-dependent unfolded protein response (UPR) (Bertolotti et al., 2000; Schäuble et al., 2012; Kopp et al., 2019; Pobre et al., 2019). The third mechanism to regulate the Ca^{2+} leakage through SEC61 channel is mediated through SEC62. Silencing experiments of *SEC62* showed an increased Ca^{2+} leakage from the ER lumen suggesting its regulatory role potentially by inducing conformational changes of its direct interaction partner SEC61, which alters the binding affinity of SEC61 to CaM and thereby causing Ca^{2+} leakage (Linxweiler et al., 2013).

Another crucial role of SEC62 - besides its function in protein translocation and the maintenance of calcium homeostasis - is in the recovery of mammalian cells after ER stress (Fumagalli et al., 2016). In regard of differently induced ER stress, the synthesis of proteins, their folding as well as their translocation are strongly disturbed and has to be recovered. Here, eukaryotic cells are able to decide dependent on the stress level, which destiny they would prefer – initiation of compensatory mechanisms or undergoing programmed cell death (Walter and Ron, 2011).

Because SEC proteins are involved in crucial processes of the protein-synthesis, -folding and -transport machinery there are many opportunities of malfunction as a result of mutations, amplification or overexpression (Linxweiler et al., 2017b). Some of these malfunctions may also play a role in cancer diseases. As already mentioned above, some gene loci are frequently amplified in various cancer entities. Linxweiler et al. (2017) show an overview of so far known mutations affecting SEC proteins and their impact in cancerous lesions (Linxweiler et al., 2017b). Of all known SEC genes, *SEC62* seems to be the most frequently affected gene in human cancer. In 2006, the first study suggesting that SEC62 plays a crucial role in prostate cancer due to gains of *SEC62* leading to increased messenger RNA (mRNA) levels was published (Jung et al., 2006). Beside evidences in tumour tissues, there are also studies investigating SEC62 mRNA and protein levels in peripheral blood mononuclear cells predicting SEC62 as a potential biomarker for recurrence in hepatocellular carcinoma (Weng et al., 2012).

In order to obtain further information about the impact of *SEC62* overexpression on tumour cell biology, several functional studies were performed based on *in vitro* experiments. These functional analyses focus on the investigation of the proliferation- and migration-behaviour of various human cancerous cell lines like prostate cancer, cervix carcinoma, lung cancer, B-cell lymphoma as well as squamous cell carcinoma by an artificially induced decrease or increase of the *SEC62* expression levels (Greiner et al., 2011a; Linxweiler et al., 2012, 2013, 2016; Bochen et al., 2017). Elevated protein levels of SEC62 led to a significant migration stimulation but influenced only slightly the proliferation behaviour of the investigated cell lines (Linxweiler et al., 2012, 2013, 2016; Bochen et al., 2017). Conversely, these results also showed, that a reduction in the SEC62 protein amount mediated by small interfering RNA (siRNA) caused a significant

reduction in the ability of tumour cells to migrate (Linxweiler et al., 2012, 2013, 2016; Bochen et al., 2017).

In summary, an important role of SEC62 in the pathogenesis of several malignant diseases was described in these studies, and implies a potential oncogenic function of SEC62 (Linxweiler et al., 2017b).

1.5. Thapsigargin and Trifluoperazine as potential oncological therapeutics

Although the migration and thus potentially the ability for metastasis could be reduced in HNSCC cells due to siRNA-transfection directed against SEC62 by *in vitro* experiments, a direct transfer of this technology as a therapeutic approach to treat HNSCC patients is not feasible so far. Despite the new and rapidly developed mRNA-based vaccines against the SARS-CoV-2 (severe acute respiratory syndrome corona virus-2), it is still a major challenge to treat tumour entities using RNA interfering (RNAi) technology. The main challenges in this technology are still based in the tumour-specific delivery without affecting non-cancerous cells by severe side effects, the minor stability of RNA molecules as well as the urgently need of an adequate concentration at the tumour site (Burnett and Rossi, 2012; Tian et al., 2021). Therefore, a functional knockdown of SEC62 is discussed as a promising new therapeutic approach without the need of a siRNA-based transient knockdown. Greiner et al. investigated the role of thapsigargin which was already discussed for prostate cancer therapy (Greiner et al., 2011b). Thapsigargin, a potent cytotoxin, is able to induce ER-stress by an irreversible inhibition of the sarcoplasmic/endoplasmic reticulum Ca²⁺-ATPase (SERCA) which will be introduced in detail later (Jaskulska et al., 2021). In the aforementioned study, Greiner et al. found evidence for a SEC62-dependent sensitivity concerning thapsigargin-induced ER-stress. However, SEC62 overproducing prostate cancer cell lines showed an increased resistance against the induction of ER-stress compared to cancer cell lines with a normal level of SEC62. These data suggest a correlation between the SEC62 protein amount and the Ca²⁺ homeostasis regulation (Greiner et al., 2011b). Hereafter, Linxweiler et al. notified a protective effect of elevated SEC62 protein amounts in non-small-cell lung carcinoma against thapsigargin-induced ER-stress (Linxweiler et al., 2012). Due to these benefits of various tumour entities to avoid the initiation of apoptosis and to show an invasive growth behaviour based on SEC62 overexpression this protein seems to be a key player in these processes as well as Ca²⁺ especially as a second messenger. As a consequence of this rescuing effect of SEC62 overexpression thapsigargin seems to be inappropriate as monotherapy against cancer. Here, the role of SEC62 as a regulator of the SEC61 channel closure becomes important and how this function can be evaded. There is evidence that SEC62 recruits Ca²⁺-bound calmodulin (CaM), which in consequence blocks the SEC61 channel at the cytosolic site and inhibits a further Ca²⁺ leakage due to the concentration gradient (Erdmann et al., 2011; Linxweiler et al., 2013). Thus,

CaM displays another attackable target to inhibit the functional role of SEC62. *In vitro* experiments of various human cancer cell lines showed that the treatment with the calmodulin antagonist trifluoperazine was able to create the same phenotypic effect regarding cell migration like a transient siRNA-mediated *SEC62* knockdown (Linxweiler et al., 2013). The combined treatment with trifluoperazine and thapsigargin of siRNA-based *SEC62*-depleted PC3 cells showed an even greater sensitivity towards the proliferation-inhibiting effect *in vitro* (Linxweiler et al., 2013). This combinatory treatment approach which blocks CaM and irreversibly inhibits the SERCA enables a functional *SEC62* knockdown *in vitro* in order to impair the ability of cancer cells to migrate and metastasise, and dose dependently, the ability to proliferate. It cannot be proven that the inhibition of tumour cell migration and proliferation by trifluoperazine or a combined therapy using thapsigargin together with trifluoperazine is mediated solely by influencing the SEC62-based regulation of Ca^{2+} homeostasis at the ER. This effect could also be based on so far unknown additional molecular events. Nevertheless, both substances seem to be powerful candidates as potential therapeutics for SEC62-overexpressing tumours like HNSCC. Figure 5 gives an overview about the suspected molecular mechanisms of a functional SEC62-knockdown by a targeted treatment of human cell line cells using trifluoperazine and thapsigargin. However, the exact molecular mechanisms how SEC62-mediated reduction of the cytosolic Ca^{2+} concentration leads to a stimulation of cell migration are still unknown and are intensively investigated by several groups.

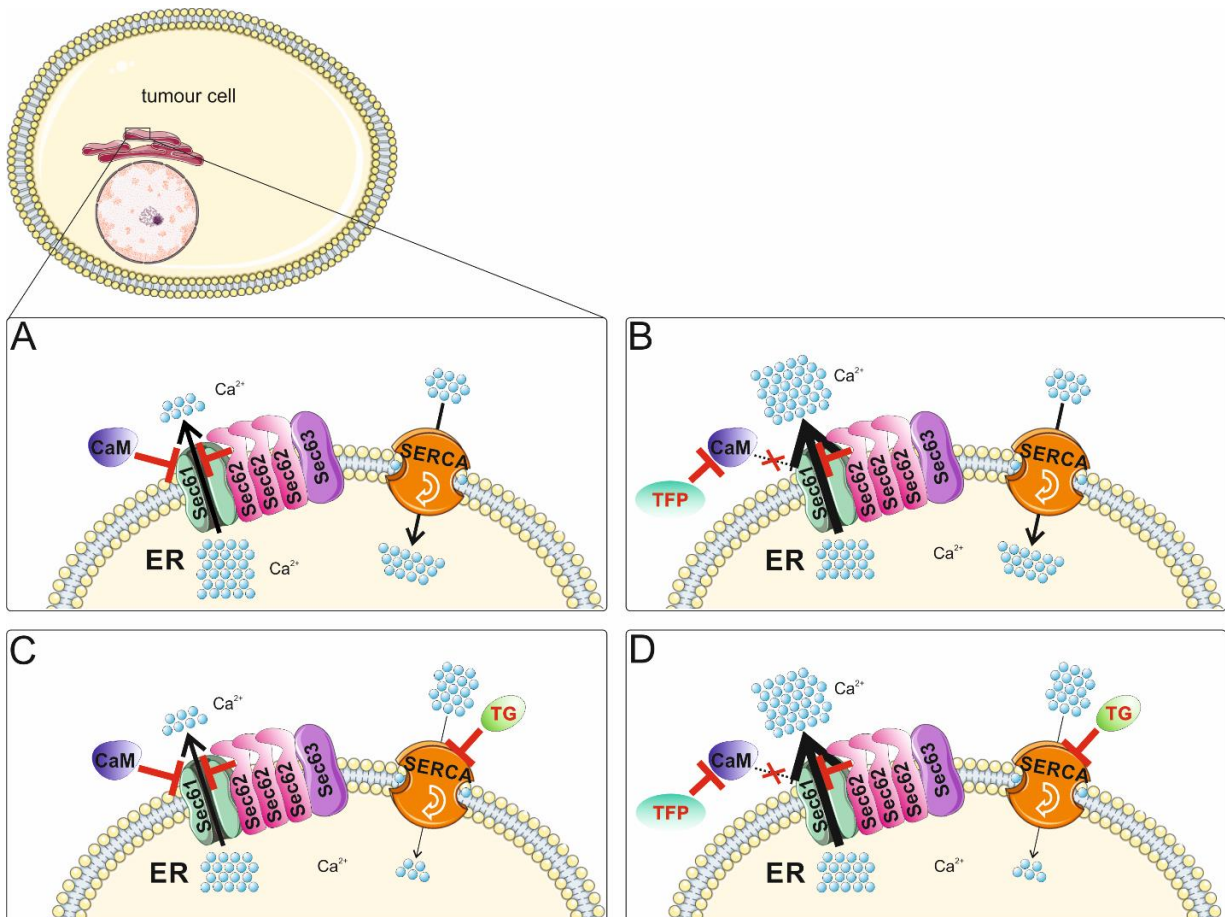


Figure 5 Overview of a functional SEC62 knockdown by TFP and TG administration: Major key components involved in the Ca^{2+} homeostasis within a tumour cell. **(A)** Role of SEC62 overexpression in a tumour cell during a physiological condition. **(B)** Variances in the Ca^{2+} efflux of the ER during TFP administration which leads to an enhanced Ca^{2+} efflux out of the ER due to no CaM binding at the SEC61 channel. CaM is blocked by TFP. **(C)** Variances in the Ca^{2+} regulation while TG administration. TG blocks irreversibly the SERCA which leads to an inhibited Ca^{2+} back haul of Ca^{2+} into the ER and in consequence an increase of cytosolic Ca^{2+} levels. **(D)** Theoretical description of a functional SEC62 knockdown by TFP and TG administration which leads to a huge increase of cytosolic Ca^{2+} levels and therefore leads to ER-stress induction and in consequence to apoptosis. Red bars indicate an inhibition or channel closure. Thickness of the arrows indicate the strength of the Ca^{2+} efflux as well as the amount of Ca^{2+} ions that were transported via SERCA.

Now, let's have a closer look at both promising new therapeutics. Thapsigargin has already been used in the traditional medicine and was known as the "death carrot" (Denmeade and Isaacs, 2005). This chemical substance belongs to the group of sesquiterpene lactones and was first isolated in 1970 (Rasmussen et al., 1978). It is extracted from the roots and resin of an umbelliferas plant which belongs to the family of the *Apiaceae*, the *Thapsia garganica* (Rasmussen et al., 1978). In the traditional medicine thapsigargin was used to treat pulmonary diseases and catarrh, but skin irritations were frequently reported after its clinical use (Quynh Doan and Christensen, 2015). Hakii et al. reported in 1986 that thapsigargin functions also as a cocarcinogen in skin cancer development (Hakii et al., 1986). Other effects of thapsigargin in the human body are the release of histamine from mast cells and the activation of cells of the inflammatory response (Patkar et al., 1979; Ali et al., 1985; Norup et al., 1986). However, the main function of thapsigargin is the irreversible inhibition of the SERCA (Quynh Doan and Christensen, 2015). Therefore, thapsigargin is used as a drug for positive controls for *in vitro* experiments of Ca^{2+} homeostasis as it induces a massive and durable increase of cytosolic Ca^{2+} . Based on its lipophilic properties thapsigargin is able to easily penetrate the cell membrane and bind to the SERCA located in the ER membrane (Doan et al., 2015). Here it binds to the transmembrane segments of the pump and inhibits the conformational change that is needed for a proper pump function. In consequence the SERCA is inhibited and no longer able to pump ATP-dependent Ca^{2+} ions back into the ER lumen to maintain the cytosolic Ca^{2+} homeostasis (Periasamy and Kalyanasundaram, 2007).

Under physiological cellular conditions, the concentration of Ca^{2+} ions in the cytosol is in a low range of about 100 nM. As already mentioned previously in this chapter, the ER acts as a Ca^{2+} store inside the cell (Pozzan et al., 1994). Here, the concentration is much higher with a physiological level of about 0.5 mM (Pozzan et al., 1994; Denmeade and Isaacs, 2005). Under normal circumstances the SERCA simultaneously pumps two Ca^{2+} ions ATP-dependent from the cytosol back into the ER against the concentration gradient to maintain this important homeostasis (Periasamy and Kalyanasundaram, 2007). If thapsigargin inhibits the SERCA function, the Ca^{2+} concentration within the cytosol strongly increases within a few minutes after the thapsigargin application. This fast increase is among others mediated by the passive leakage over the SEC61 channel (Van Coppenolle et al., 2004; Gamayun et al., 2019). Additionally, the ER Ca^{2+} pool depletion induces changes in the cell membrane permeability for Ca^{2+} , which also leads to a Ca^{2+}

ion influx from the extracellular space (Ca^{2+} concentration in extracellular space: 1 – 3 mM) (Mason et al., 1991). Therefore, the intracellular Ca^{2+} concentration rises 100-fold from 20-40 nM up to 200-400 nM (Denmeade and Isaacs, 2005). During the following 6 hours, the initial cytosolic Ca^{2+} ion increase flattens again to a low nanomolar range near the baseline. Within the initial rise several new genes are transcribed, and intracellular Ca^{2+} buffers are induced. The cytosolic Ca^{2+} ion decrease is mainly caused by a calmodulin-dependent calcium pump in the plasma membrane that is now activated (Tombal et al., 2000). One of the newly synthesised proteins during the initial Ca^{2+} increase is Inositol 1,4,5-triphosphate IP3 type 3 receptor which moves to the plasma membrane and results in a formation of a Ca^{2+} channel (Denmeade and Isaacs, 2005). In consequence this leads to a second rise in Ca^{2+} concentration in the cytosol, 18 hours after the initial thapsigargin application. As a result, there is another protein translocation - annexin-V proteins move to the plasma membrane to form homohexamers and build an additional channel which form an open gate for an enhanced Ca^{2+} influx. Both mechanisms lead to an extreme elevation of the intracellular Ca^{2+} to a level of up to 20 μM (Tombal et al., 2002).

These repeated high Ca^{2+} amounts inside the cytosol within less than 24 hours finally lead to morphological changes that are associated with the activation of the apoptotic machinery (Tombal et al., 1999; Quynh Doan and Christensen, 2015). The apoptotic machinery can be activated either directly through the release of special ER proteins or indirectly through exposition of proapoptotic factors from mitochondria (Denmeade and Isaacs, 2005). Instead of other cytotoxic antiproliferative substances like doxorubicin or 5-fluorouracil thapsigargin acts independent from cell proliferation (Denmeade and Isaacs, 2005).

Because the SERCA pump is mandatory in almost all kind of cells, thapsigargin exerts toxic effects on almost every human cell. This is the reason why it is difficult to use this highly potent substance as a targetable drug in the fight against cancer cells. Due to its high potency several prodrugs have been designed which were targetable to the specific tumour site (Denmeade et al., 2012; Mahalingam et al., 2016). Prodrugs in general are designed to have no pharmacological effect within the body until they are delivered to their target, where they are transformed into an active therapeutic (Rautio et al., 2008). The most common approach is to couple the drugs to peptides or other proteins which target the drug to the malignant tissue site (Doan et al., 2015). In case of thapsigargin there are several prodrug-designs available and already in the phase of clinical trials. Prostate specific membrane antigen (PSMA) is a proteolytic enzyme that is expressed in neovascular tissues in a wide range of different tumour entities like hepatocellular-, breast- or glioblastoma cancer. The PSMA, expressed in tumour sites, cleaves the prodrug called Mipsagargin (G202) and activates the SERCA inhibiting function, which will further lead to tumour cell apoptosis. A first phase-I clinical trial including patients with refractory, advanced or metastatic solid tumours resulted in a stabilisation of the disease. Also, minor side effects were observed (“Dose-escalation phase 1 study of G-202 (Mipsagargin) in patients with advanced solid tumours”,

ClinicalTrial.gov, identifier NCT01056029) (Mahalingam et al., 2016). Mipsagargin was also tested in a phase-II study for progressive advanced hepatocellular carcinoma. In this additional study Mipsagargin was well tolerated and resulted in prolonged disease stabilisation (“Study of G-202 (Mipsagargin) as second-line therapy following sorafenib in hepatocellular carcinoma”, ClinicalTrial.gov, identifier NCT01777594) (Mahalingam et al., 2019).

Another promising substance for mimicking a functional *SEC62* knockdown is trifluoperazine. Trifluoperazine belongs to the phenothiazine derivatives, which are the most prescribed and the oldest synthetic antipsychotic drugs worldwide (Sudeshna and Parimal, 2010; Jaszczyszyn et al., 2012). Usually phenothiazine derivatives are used as treatment in schizophrenia and bipolar disorder patients (Wu et al., 2016). For this purpose its mode of action is the blockade of dopaminergic receptors in mesocortical and mesolimbic pathways, but also antimicrobial as well as antitumoral activities were figured out in the last years (Sudeshna and Parimal, 2010; Tardy et al., 2014). Jiang et al. (2017) reported several direct anti-tumour effects by trifluoperazine treatment *in vitro* and *in vivo*. In *in vitro* experiments trifluoperazine inhibited cell vitality by induction of cell cycle arrest at G0/G1, additionally due to increased apoptosis rate also migration- and invasion-potential was impaired. *In vivo* experiments were able to show a restriction in angiogenesis as well as in tumour growth (Jiang et al., 2017). Another study from 2019 postulated that pancreatic ductal adenocarcinoma cells that were treated with trifluoperazine underwent cell death by a metabolic-driven induction of apoptosis and necroptosis, which is a consequence of a coupled stress of the mitochondria and the ER (Huang et al., 2019). In this study, trifluoperazine treatment led to a dramatically decreased ATP content due to a strong decrease in oxidative phosphorylation (OXPHOS) metabolism by mitochondrial stress. This ATP deficiency was accompanied by a compensatory increase in anaerobic glycolysis, but this was less efficient and not able to completely compensate the ATP production by OXPHOS. Cancer cells were not able to overcome energy depletion due to mitochondrial-ER coupled stress and induced different programmed cell death pathways (Huang et al., 2019).

Apart from these apoptosis inducing properties of trifluoperazine several studies show that trifluoperazine is able to be a potential anti-tumorous drug due to its ability to improve tumour cell sensitivity for several anti-cancerous drugs like cisplatin and bleomycin (Yeh et al., 2012; Kuo et al., 2019). The exact molecular mechanism how trifluoperazine can achieve this sensitivity enhancement against several chemotherapeutics remains unclear (Polischouk et al., 2007). Moreover, in combination with ionizing radiation trifluoperazine is able to induce apoptosis (Gangopadhyay et al., 2007). One possibility of trifluoperazine to sensitise cancerous cells for treatment is the involvement in the modulation of several DNA repair pathways like the inhibition of DNA double strand breaks (DSB) repair, which consequently leads to a reduction in cell survival (Perez et al., 1992; Gangopadhyay et al., 2007; Polischouk et al., 2007). An additional mechanism of trifluoperazine to induce apoptotic cell death is the supportive role in suppression of specific

oncogenes (Park et al., 2016). Treatment of prostate cancer and fibrosarcoma cell lines leads to an inhibition of angiogenesis and a significant reduction of tumour cell invasion. These results indicate a suitability of trifluoperazine as an antimetastatic therapeutic (Pulkoski-Gross et al., 2015).

Apart from the above-mentioned facts about trifluoperazine, phenothiazines in general are known to inhibit calmodulin in its function by binding to calmodulin, when it is in interaction with two bound Ca^{2+} ions. Therefore, phenothiazines block calmodulin dependent cellular events (Sudeshna and Parimal, 2010). Further on, ER stress was already mentioned as a potential result of trifluoperazine treatment. One typical feature of ER stress is a massive Ca^{2+} release from the main Ca^{2+} storage in the cell – the ER (Huang et al., 2019). In normally situated cells calmodulin will close the main Ca^{2+} -release SEC61-channel, but under treatment with trifluoperazine calmodulin is inhibited. Consequently, cytosolic Ca^{2+} levels will increase and worsen the cellular stress level. Regarding the antimetastatic efficiency of trifluoperazine (TFP) in humans, a retrospective analysis including only a small number of patients (n=19) with advanced lung- or colon-carcinoma showed a significant prolonged overall survival of two patients treated with the calmodulin-antagonist TFP due to an additional disease (Zacharski et al., 1990).

Taken together, there is the suggestion that the application of trifluoperazine will lead to increased cytosolic Ca^{2+} concentrations due to a blockade of calmodulin which is not able anymore to be recruited by SEC62 for SEC61-channel closure. The TFP application could be combined with the administration of thapsigargin that forces an irreversible inhibition of the SERCA and leads for itself to an increasing cytosolic Ca^{2+} level. The combination of both substances should be able to force SEC62 overexpressing tumour cells into apoptosis due to enormous ER-stress reactions by high cytosolic Ca^{2+} levels and overcome the protective effect of high SEC62 expression levels (Figure 5D).

1.6. Motivation

In the last decade cancer researchers were able to identify characteristic variances on the genomic level, especially the amplification of the long arm of chromosome 3 in various cancer entities. Several genes are encoded on this chromosomal section whereby this work focusses on SEC62, encoded on 3q26.2. Examination of HNSCC tissue samples in which SEC62 overexpression was compared with tumour-free mucosa showed a significant correlation of SEC62 expression level with the occurrence of cervical lymph node metastases in 86 % of the investigated tumours. In addition, a significantly shorter overall survival correlated with a high SEC62 expression level in the tumour. Within the framework of functional analyses to investigate the proliferation and migration behaviour of cell lines with artificially reduced or increased SEC62 expression, a siRNA-mediated reduction of the SEC62 protein content led to a significant

reduction in the migration ability of the used tumour cell lines. In contrast, plasmid induced *SEC62* overexpression led to a stimulation of the migration ability of cells, whereby their proliferation ability was not significantly influenced. Although *in vitro* studies showed a significantly reduced migration and thus potentially also impair the metastatic ability of HNSCC cells, a direct transfer of this technology as a therapeutic approach in humans is not possible so far. Therefore, the task for the present work is divided into three main objectives

- (I) Establishment of an orthotopic HNSCC murine xenograft model to investigate lymphatic metastasis
- (II) Establishment of an HNSCC murine xenograft model to investigate haematogenous metastasis
- (III) Generation of a stable *SEC62*-knockout of an HNSCC cell line via CRISPR-Cas9 technology

The overall aim of this work is to investigate for the first time *in vivo* the metastasis- and proliferation-inhibiting effect of a functional *SEC62*-knockdown based on two promising new therapeutics, TG and TFP. For this purpose, suitable animal models were established for the two main forms of tumour metastasis - haematogenous and lymphatic metastasis (objective I and II). For a better understanding of the role of the transmembrane protein *SEC62* in HNSCC a CRISPR/Cas9 based *SEC62* knockout cell line was generated and functionally characterized as a basis for further *in vivo* testing.

2. Materials and methods

2.1. Materials

2.1.1. Chemicals

Table 1 List of all used chemicals in this study

Product	Product number	Company
2-mercaptoethanol	21985-023	Life technologies corporation, Carlsbad, CA, USA
4',6-Diamidin-2-phenylindol	MBD0015-5ML	Sigma-Aldrich Chemie GmbH, Taufkirchen, Germany
Acrylamide 4X	10677.01	Serva Electrophoresis GmbH, Heidelberg, Germany
Agar-Agar	6494.3	Carl Roth GmbH & Co. KG, Karlsruhe, Germany
Ammonium persulfate	13376.02	Serva Electrophoresis GmbH, Heidelberg, Germany
ampicilin	A5354	Sigma-Aldrich Chemie GmbH, Taufkirchen, Germany
Ampuwa® Rinsing Solution 1000 ml Plastipur®	1088811	Fresenius Kabi, Bad Homburg, Germany
Antipain Hydrochloride	178220	Sigma-Aldrich Chemie GmbH, Taufkirchen, Germany
Boric acid	1.00165-1000	Merck KGaA, Darmstadt, Germany
bromphenol blue	15375.01	Serva Electrophoresis GmbH, Heidelberg, Germany
Chymostatin	C-7268	Sigma-Aldrich Chemie GmbH, Taufkirchen, Germany
Dimethyl sulfoxide	D2650-100ML	Sigma-Aldrich Chemie GmbH, Taufkirchen, Germany
Dithiothreitol	20711.02	Serva Electrophoresis GmbH, Heidelberg, Germany
DMEM (1X) + GlutaMAX™-I	31966-021	Thermo Fisher Scientific Inc., Waltham, USA
DNase I 100 mg	10104159001	Roch Diagnostics GmbH, Mannheim, Germany
dNTP Mix (10 mM each)	18427013	Thermo Fisher Scientific Inc., Waltham, MA, USA
Dodecylsulfate-Na-salt in pellets	20765.03	Serva Electrophoresis GmbH, Heidelberg, Germany
Dow Corning® high-vacuum silicone grease	Z273554-1EA	Sigma-Aldrich Chemie GmbH, Taufkirchen, Germany

Materials and Methods

Dulbecco's phosphate buffered saline (commercial)	20012-019	Thermo Fisher Scientific Inc., Waltham, USA
EDTA	8043.1	CARL ROTH GMBH + CO. KG, Karlsruhe, Germany
Entellan® new	1079610500	Merck KGaA, Darmstadt, Germany
Eosin	1159350100	Merck KGaA, Darmstadt, Germany
Ethanol 99 %, denatured	ETO-5000-99-1	SAV Liquid Production GmbH, Flintsbach am Inn, Germany
Ethanol, absolute	32205-2.5L	Sigma-Aldrich Chemie GmbH, Taufkirchen, Germany
ethidium bromide	1.11608	Merck KGaA, Darmstadt, Germany
Fetal bovine serum	F7524, LOT BCCB3111	Sigma-Aldrich Chemie GmbH, Taufkirchen, Germany
Formaldehyd solution 4 %	PZN 02653025	Otto Fischar GmbH & Co. KG, Saarbrücken, Germany
Fresubin Energy Fibre	702150s/4	Fresenius Kabi, Bad Homburg, Germany
FuGene® HD Transfection Reagent	E2311	Promega, Fitchburg, WI, USA
Glycerol	G5516-100ML	Sigma-Aldrich Chemie GmbH, Taufkirchen, Germany
Glycine	23391.02	Serva Electrophoresis GmbH, Heidelberg, Germany
heparin sodium 25.000 IU/5 ml	PZN15782698	B. Braun Melsungen AG, Melsungen, Germany
HotStarTaq DNA Polymerase (250 U)	203203	Qiagen N.V., Hilden, Germany
hydrochloric acid 25 %	X897.1	CARL ROTH GMBH + CO. KG, Karlsruhe, Germany
hydrochlorid acid 1 mol/L		Pharmacy of Saarland University Hospital
Isolfuran-Piramal	PZN09714675	Piramal Critical Care Deutschland GmbH, Halbergmoos, Germany
Isopropanol	55346	Otto Fischar GmbH & Co. KG, Saarbrücken, Germany
Leupeptin	L-2023	Sigma-Aldrich Chemie GmbH, Taufkirchen, Germany
Magnesium chloride hexahydrate	M-2393	Sigma-Aldrich Chemie GmbH, Taufkirchen, Germany
Mayer's Hemalum solution	1092490500	Merck KGaA, Darmstadt, Germany
Mayer's Hematoxylin Solution	MHS32-1L	Sigma-Aldrich Chemie GmbH, Taufkirchen, Germany
methanol	1060091011	Merck KGaA, Darmstadt, Germany
N, N'-Methylenbisacrylamide 2X	29197.01	Serva Electrophoresis GmbH, Heidelberg, Germany
N,N,N',N'-Tetramethylethylenediamine	35930.02	Serva Electrophoresis GmbH, Heidelberg, Germany

Nonidet P40	11 754 599 001	Roch Diagnostics GmbH, Mannheim, Germany
PageRuler™ Prestained Protein Ladder paraffin	26616	Thermo Fisher Scientific Inc., Waltham, USA
Penicillin/Streptomycin	P4333	Sigma-Aldrich Chemie GmbH, Taufkirchen, Germany
Pepstatin A	P-4265	Sigma-Aldrich Chemie GmbH, Taufkirchen, Germany
Phenylmethanesulfonyl fluoride	10837091001	Sigma-Aldrich Chemie GmbH, Taufkirchen, Germany
Phosphat-buffered Saline	20012027	Life technologies corporation, Carlsbad, CA, USA
Protease Inhibitor Mix M	39102.01	Serva Electrophoresis GmbH, Heidelberg, Germany
Puromycin Dihydrochloride 1 mg/ml	A1113803	Thermo Fisher Scientific Inc., Waltham, USA
Quick-Laod Purple 1 kb DNA Ladder	N0552	New England Biolabs GmbH, Frankfurt am Main, Germany
Quick-Load Purple 100 bp DNA Ladder	N0551	New England Biolabs GmbH, Frankfurt am Main, Germany
Rimadyl®	400684.00.00	Zoetis Deutschland GmbH, Berlin, Germany
RIPA buffer	39244.02	Serva Electrophoresis GmbH, Heidelberg, Germany
Rompun® 2 %	PZN01320422	Elanco GmbH, Cuxhaven, Germany
ROTI®Zol RNA, 100 ml	9319.1	CARL ROTH GMBH + CO. KG, Karlsruhe, Germany
Saponin	8047-15-2	Sigma-Aldrich Chemie GmbH, Taufkirchen, Germany
SeaKem® LE Agarose	50004	Lonza, Rockland, ME, USA
sodium chloride	2438-1KG	Caesar & Loretz GmbH, Hilden, Germany
sodium hydroxide		Pharmacy of Saarland University Hospital
Sucofin Skimmed Milk Powder		cobio.de GmbH, Arnsberg, Germany
SYBR® Safe DNA gel stain	S33102	Thermo Fisher Scientific Inc., Waltham, MA, USA
Thapsigargin	T7458	Thermo Fisher Scientific Inc., Waltham, USA
Trifluoperazine dihydrochloride	T8516	Sigma-Aldrich Chemie GmbH, Taufkirchen, Germany
Tris-hydrochoride	9090.2	CARL ROTH GMBH + CO. KG, Karlsruhe, Germany
Trizma® Base	T1503-1KG	Sigma-Aldrich Chemie GmbH, Taufkirchen, Germany

Trypan Blue Stain (0,4 %)	T8154-20ML	Sigma-Aldrich Chemie GmbH, Taufkirchen, Germany
Trypsin 0,05 % EDTA	25300054	Thermo Fisher Scientific Inc., Waltham, USA
Tween®20	8.22184.0500	Merck KGaA, Darmstadt, Germany
Ursotamin® 100 mg/ml	PZN07005294	Serumwerk Bernburg AG, Bernburg, Germany
Vectashield® Antifade Mounting Medium	H-1000	Vector Laboratories, Inc., Burlingame, CA, USA
Vectashield® Antifade Mounting Medium with DAPI	H-1200	Vector Laboratories, Inc., Burlingame, CA, USA
Xylazine 20 mg/ml		WDT e.G., Garbsen, Germany
Xylene	PZN 09208831	Otto Fischar GmbH & Co. KG, Saarbrücken, Germany
β-mercaptoethanol	M3148-250ML	Life technologies corporation, Carlsbad, CA, USA

2.1.2. Buffers and solutions

Phenylmethanesulfonyl fluoride (PSMF) 1 M stock solution

- dissolve PSMF for 1 M stock in acetone
- dilute 1 M stock solution 1:10 with EtOH (100 %, v/v) → 100 mM

PLAC stock solution

Pepstatin A	25.0 mg/2.08 ml DMSO
Leupeptin	25.0 mg/2.08 ml DMSO
Antipain	25.0 mg/2.08 ml DMSO
Chymostatin	25.0 mg/2.08 ml DMSO

Lysis buffer (10X)

NaCl	100 mM
TRIS pH 8.0	100 mM
MgCl ₂	30 mM
NP40	5 % (v/v)

- ad 10 ml Aqua dest.
- store stock solution at 4 °C

Lysis buffer (1X)

Lysis buffer 10X	300 µl
10X DNase	30 µl

H ₂ O	2.7 ml	} Dissolve in 8 µl EtOH (100 %, v/v)
PMSF	0.1 mM	
PLAC	3 µl	

Laemmli buffer (5X)

TRIS 2 M pH 6.8	15 ml
SDS	10 g
Glycerine 87 % (v/v)	57.5 ml

→ aliquote in 7.5 ml

→ add 2.5 ml β-mercaptoethanol, bromphenol blue to each aliquot

2 % (w/v) Agarose

Agar-Agar	2 % (w/v)
-----------	-----------

→ ad 200 ml Aqua dest.

Electrophoresis buffer (5X)

TRIS Base	50 mM
Glycine	384 mM
SDS 10 % (w/v)	0.1 % (v/v)

→ ad 10 L Aqua dest.

Transfer buffer

TRIS Base	12.3 mM
Glycine	95.9 mM

→ ad 3 L Aqua dest.

Tris-buffered saline buffer (TBS) (10X)

NaCl	9 % (w/v)
TRIS	112 mM

→ ad 1 L Aqua dest.

→ adjust pH 7.4 with 8.3 ml HCl

→ for TBS-T (1X) dilute 100 ml of 10X stock and add 0.05 % (v/v) Tween®20

Ethylenediaminetetraacetic acid (EDTA) 0.5 M

EDTA 0.5 M	29.2 g
------------	--------

→ ad 200 ml Aqua dest.

Blocking solution

Sucofin	5 % (w/v)
1X TBS	50 ml

TBE buffer electrophoresis buffer 10x

TRIS	0.89 M
Boric acid	0.89 M
EDTA 0.5 M, pH 8.0	4 % (v/v)

Haematoxylin/eosin staining differentiator solution

EtOH 70 % (v/v)	1 L
Hydrochloric acid 25 % (v/v)	10 ml

Eosin solution

Eosin	1 %
Acetic acid	0.01 %

TE buffer

Tris/HCl pH 8.0	10 mM
EDTA	1 mM

Stopp-Solution (immunofluorescence)

Glycin	0.1 M
MgCl ₂	4 Mm
in PBS	

PSS buffer

FCS	5 %
Saponin	0.1 %
RNase	50 µg/ml
in PBS	

2.1.3. Technical equipment and disposables

Table 2 List of all used general devices.

Product	Product number	company
(spring-type) micro-scissors	FD-101R	Aesculap AG, Tuttlingen, Germany
1,5 ml Safe-Seal Tubes	72,706	SARSTEDT AG & Co. KG, Nümbrecht, Germany
2,0 ml Safe-Seal Tubes	72,695,500	SARSTEDT AG & Co. KG, Nümbrecht, Germany
24 Well Cell Culture Multiwell Plate	662160	Greiner Bio-One GmbH, Frickenhausen, Germany
340/26 BrightLine HC		AHF analysentechnik AG, Tübingen, Germany
387/11 BrightLine HC		AHF analysentechnik AG, Tübingen, Germany
48 Well Cell Culture Multiwell Plate	677180	Greiner Bio-One GmbH, Frickenhausen, Germany
6 Well Cell Culture Multiwell Plate	657160	Greiner Bio-One GmbH, Frickenhausen, Germany
9.4 T MRI animal scanner Biospec Avance III 94/20USR		Bruker Biospin GmbH, Ettlingen, Germany
Aquavive® Mouse Empty Water Bottle	M-WB-300	Innovive, San Diego, CA, USA
Autoclave		Schütt, Göttingen, Germany
Bactifuge		Heraeus Holding GmbH, Hanau, Germany
BD Plastipak™ 1 ml	300013	Beckton Dickinson S.A., Madrid, Spain
Biofuge pico		Heraeus Holding GmbH, Hanau, Germany
Biosphere® Filter Tips 2–100 µl	70,760,212	SARSTEDT AG & Co. KG, Nümbrecht, Germany
Blue Line - SEALS SAFE NEXT		Tecniplast Deutschland GmbH, Hohenpeißenberg, Germany
Mouse cage		
Bruker Skyscan 1176 system		Bruker Corporation, Billerica, USA
Cainda Digital Microscope	F210	Cainda, El Monte, CA, USA
Carl Zeiss Inverted Microscope, Axiovert Observer D1		Carl Zeiss AG, Jena, Germany
Carl Zeiss Invertoscope Inverted Microscope		Carl Zeiss AG, Jena, Germany
Cassettes, Q Path® MicroStar II	720-2075	VWR International, Radnor, PA, USA
CCD camera ORCA-D2		Hamamatsu Corporation, Bridgewater Township, NJ, USA
Cell Culture dishes (35x10 mm, 60x15 mm, 145x20 mm)	628160	Greiner Bio-One GmbH, Frickenhausen, Germany
Cellculture microplate, 96 well, PS, U-bottom	650180	Greiner Bio-One GmbH, Frickenhausen, Germany
CELLSTAR® Cell Cluture Flasks (T25, T75, T175)	690175, 658175, 660175	Greiner Bio-One GmbH, Frickenhausen, Germany

Materials and Methods

CELLSTAR® FourWell Plate™	96077307	Greiner Bio-One GmbH, Frickenhausen, Germany
Chemostar ECL & Fluorescence Imager		Intas Science Imaging Instruments GmbH, Göttingen, Germany
Classic 2 Rice Cooker	RK102815	Tefal Groupe SEB, Rumilly, France
clean bench		Gelaire Flow Laboratories, Meckenheim, Germany
Cleanisept® Wipes	00-208-D100	Dr. Schumacher GmbH, Malsfeld, Germany
Coil		Bruker Biospin GmbH, Ettlingen, Germany
companion plate 24 well	353504	Corning B.V. Life Science, Amsterdam, Netherlands
Corning® FluoroBlok™ Cell Culture Inserts	351152	Corning B.V. Life Science, Amsterdam, Netherlands
Countess™	C10227	Invitrogen, Carlsbad, CA, USA
Cover slip 24x60 mm	01-2455/x	R. Langenbrinck GmbH Labor- und Medizintechnik, Emmendingen, Germany
CryoPure Tube 1,8 ml	72,379,006	SARSTEDT AG & Co. KG, Nümbrecht, Germany
Delicate tissue forceps 1x2 110 mm	BD501R	Aesculap AG, Tuttlingen, Germany
Diagnostic Microscope Slides	ER-301B-CE24	Thermo Fisher Scientific Inc., Waltham, MA, USA
Disposable Glass Pasteur Pipettes 150 mm	9250101	Hirschmann Laborgeräte GmbH & Co. KG, Eberstadt, Germany
Durotip dissecting scissors 110 mm	BD330R	Aesculap AG, Tuttlingen, Germany
Durotip dissecting scissors 115 mm	BD333R	Aesculap AG, Tuttlingen, Germany
Electrophoresis Power Supply - EPS 601		GE Healthcare, IL, USA
e-plate 96	05 232 368 001	Acea Biosciences, Inc., San Diego, CA, USA
Eppendorf 5415C		Eppendorf AG, Hamburg, Germany
ET510/80 m Chroma		AHF analysentechnik AG, Tübingen, Germany
Falcon® Cell Culture Insert Companion Plates - 24 well	353504	Corning B.V. Life Science, Amsterdam, Netherlands
Fluosorber Filter Cannister	HARV34-0415	Harvard Apparatus GmbH, March-Hugstetten, Germany
FLUOVAC		Harvard Apparatus GmbH, March-Hugstetten, Germany
gauze swap 7,5x7,5 cm	731042	Fink & Walter GmbH, Merchweiler, Germany
glass beads, acid-washed	G8772-100G	Sigma-Aldrich Chemie GmbH, Taufkirchen, Germany
Hamilton® syringe, 701N, volume 10 µL, ga26s, 51 mm	28615-U	Hamilton Central Europe S.R.L., Ghiroda, Romania

Hamilton® syringe, 705N, volume 50 µL, ga22s, 51 mm/pst3	80565/00	Hamilton Central Europe S.R.L., Ghiroda, Romania
Hamilton® syringe, 710N, volume 100 µL, ga22s, 51 mm/pts2	80600/00	Hamilton Central Europe S.R.L., Ghiroda, Romania
HERAcell 150i CO2 Incubator		Thermo Fisher Scientific Inc., Waltham, MA, USA
Ice machine	AF103	Ziegra Eismaschinen GmbH, Isernhagen, Germany
illumination system Lambda DG-4		Sutter Instrument, Novato, CA, USA
Immobilon®-FL Transfer Membrane Pore size 0,45 µm	IPFL00005	Merck Millipore Ltd., Carrigtwohill, Co. Cork, Ireland
Injekt® 20 ml, Luer-Ansatz		B. Braun Melsungen AG, Melsungen, Germany
Innocage® Mouse Pre-Bedded Corn Cob	M.BTMC8	Innovive, San Diego, CA, USA
Innocage® Mouse Static Short	MS2	Innovive, San Diego, CA, USA
Kimtech Wipes		Kimberly-Clark Professional, Roswell, USA
Leica DFC7000 T		Leica Microsystems GmbH, Wetzlar, Germany
Leica LED3000 BLI lamp		Leica Microsystems GmbH, Wetzlar, Germany
Leica M651		Leica Microsystems AG, Heerbrugg, Switzerland
Leica MZ10F stereo microscope		Leica Microsystems GmbH, Wetzlar, Germany
Leica RM2125 RT		Leica Microsystems GmbH, Wetzlar, Germany
magnetic stirrer IKA® C-MAG HS 7	3581200	IKA®-Werke GmbH & Co. KG, Staufen, Germany
Maintenance diet for rats and mice, 1324		Altromin Spezialfutter GmbH & Co. KG, Lage, Germany
McIlwain Tissue Chopper		Ted Pella, Inc., Redding, CA, USA
Micro forceps 0,2 mm 110 mm		Aesculap AG, Tuttlingen, Germany
Microscope slides	03-0002	R. Langenbrinck GmbH Labor- und Medizintechnik, Emmendingen, Germany
Microscope slides superfrost® plus		Gerhard Menzel GmbH, Braunschweig, Germany
Microslide Box	631-1503	VWR International, Radnor, PA, USA
Microtome Blades A35		pfm medical ag, Köln, Germany
Microwave Exquisit MW 802	AAA0000760653	GGV Handelsgesellschaft mbH & Co. KG, Kaarst
Mini horizontal electrophoresis system, Owl™ B1A EasyCast™		Thermo Fisher Scientific Inc., Waltham, MA, USA
Multiply®-Pro cup 0.2 ml	72,737,002	SARSTEDT AG & Co. KG, Nümbrecht, Germany

Materials and Methods

MultiTemp III Thermostatic Circulator			GE Healthcare, IL, USA
Nalgene™ rapid-flow filter 150 mL; 0.2 µm aPES membrane	596-4520		Thermo Fisher Scientific Inc., Waltham, MA, USA
Nalgene™ straight-side wide mouth jar	2117-100		Thermo Fisher Scientific Inc., Waltham, MA, USA
NanoDrop®ND-1000 UV/Vis			Peqlab Biotechnologie GmbH, Erlangen, Germany
NEOPOINT® 26Gx1/2" 0,45x12 mm	PZN02040676		B. Braun Melsungen AG, Melsungen, Germany
Nikon Digital Sight			Nikon Corporation, Tokio, Japan
Nikon Inverted Microscope Eclipse TE-2000-S			Nikon Corporation, Tokio, Japan
Nikon transmission-light source			Nikon Corporation, Tokio, Japan
Nikon HB-10101AF Super High Pressure Mercury Lamp Power Supply			Nikon Corporation, Tokio, Japan
Nitrile Powder-Free Medical Examination Gloves	290418		Abena A/S, Aabenraa, Denmark
Objective Planapo 1,6x, 0,63x M-Series			Leica Microsystems GmbH, Wetzlar, Germany
Objektives PlanApo N 2x/0,08; UPlan FL N 4x/0,13; UPlanFI 10x/0.30; UPlanFI 40x/0,75 Ph2; UPlanFI 60x/1,25 Oil Iris			Olympus Deutschland GmbH, Hamburg, Germany
Olympus BX61 microscope			Olympus Deutschland GmbH, Hamburg, Germany
Olympus BX-UCB control			Olympus Deutschland GmbH, Hamburg, Germany
Olympus CH30			Olympus Deutschland GmbH, Hamburg, Germany
Olympus SC30 camera			Olympus Deutschland GmbH, Hamburg, Germany
Olympus U-CMAD3			Olympus Deutschland GmbH, Hamburg, Germany
Olympus U-PMTVC			Olympus Deutschland GmbH, Hamburg, Germany
Olympus U-RFL-T fluorescenct lamp			Olympus Deutschland GmbH, Hamburg, Germany
Olympus U-TV1X-2			Olympus Deutschland GmbH, Hamburg, Germany
Omnican®-F, 0,30x12 mm/G 30x 1/2", 1 ml	9161502S		B. Braun Melsungen AG, Melsungen, Germany
pfm Waterbath 1000	41010		pfm medical AG, Köln, Germany
pH meter 197			Xylem Analytics Germany Sales GmbH & Co. KG, WTW, Weilheim, Germany

pipett tips (10 µl)			Gilson Inc., Middleton, WI, USA
pipett tips (200 µl, 1000 µl)			SARSTEDT AG & Co. KG, Nümbrecht, Germany
pipetus®			Hirschmann Laborgeräte GmbH & Co. KG; Eberstadt, Germany
pluriStrainer® 20 µm	43-50020-03		pluriSelect Life Science, Leipzig, Germany
pneumatic cushion Graseby infant respiration sensor			Smiths Medical, Dublin, OH, USA
precision scales P-1200	P-1200		Mettler-Toledo GmbH, Gießen, Germany
Reagent reservoir 60 ml	703411		Brand GmbH & Co. KG, Wertheim, Germany
Roller mixer RM5			Ingenieurbüro CAT, M. Zipperer GmbH, Ballrechten-Dottingen, Germany
Sato WS4 series printer	WS24TT		SATO Europe GmbH, Heidelberg, Germany
Scienceware® cloning cylinders, polystyrene	C3983		Sigma-Aldrich Chemie GmbH, Taufkirchen, Germany
Scotsman AF103 Ice Flaker			Scotsman® Ice Systems, Milan, Italy
Screw cap tube, 15 ml, (LxØ): 120x17 mm, PP, with print	62,554,502		SARSTEDT AG & Co. KG, Nümbrecht, Germany
Screw cap tube, 50 ml, (LxØ): 114x28 mm, PP, with print	62,547,004		SARSTEDT AG & Co. KG, Nümbrecht, Germany
serological pipets (5 ml, 10 ml, 25 ml)	86.1253.001, 86.1254.001, 86.1685.001		SARSTEDT AG & Co. KG, Nümbrecht, Germany
Shandon Histocentre 2	AL.16.R.0.10675		Thermo Electron Corporation, Dreieich, Germany
SHIELDskin CHEM™ NEO NITRILE™ 300	66 9253		SHIELD Scientific B.V., Bennekom, Netherlands
Standard Feeder	M.FEED.P		Innovive, San Diego, CA, USA
StepOne™ Plus Real-Time PCR System	4376600		Applied Biosystems, Waltham, MA, USA
Tabvei Aspen Bedding			Tapvei Estonia OÜ, Harjumaa, Estonia
TC Strabismus Scissors STR 115 mm	BC256R		Aesculap AG, Tuttlingen, Germany
Thermal transfer Xylene resistant Ribbon 55 mmx74 mm	N0TC55X74C0.5-1RZ4		LabID Technologies B.V., Hertogenbosch, Netherlands
thermo shaker TS-100			Biosan, Riga, Lettland
Thermocycler PeqSTAR 96x Universal Gradient			Peqlab Biotechnologie GmbH, Erlangen, Germany
thermomixer comfort 1,5 ml			Eppendorf AG, Hamburg, Germany
Tissue-Tek II filter pads for embedding cassetts	SA-4699		VOGEL GmbH & Co. KG, Gießen, Germany
Tissue-Tek® VIP™ 5 Jr.			Sakura Finetek Europe B.V., Alphen aan den Rijn, Netherlands
U-410 Anaesthesia Unit, incl. syringe & tubing	8323101		Univentor limited, Bulebel, Malta
ultra freezer Dometic UF 755 GG			EWALD Innovationstechnik GmbH, Rodenwald, Germany

UV-gel documentation system ImaGo		B&L Systems, Maarsse, Netherland
Vasofix® Braunüle® 18G X 1 3/4 (1.3x45 mm)	4268130S-01	B. Braun Melsungen AG, Melsungen, Germany
Vortex-Genie® 2		Scientific Industries, Inc., NY, USA
VWR Light-Duty Tissue Wipers	115-0203	VWR International, Radnor, PA, USA
wacom intuos m		Wacom Europe GmbH, Düsseldorf, Germany
Whatman FP30/0.2 CA-S rottrand (0.2 µm)		Whatman GmbH, Dassel, Germany
xCELLigence® RTCA SP instrument		F. Hoffmann-La Roche AG, Basel, Switzerland
Xylene and Solvent resistant Labels 23 mmx19 mm	NOHTT-152C1-1WH	LabID Technologies B.V., Hertogenbosch, Netherlands

2.1.4. Antibodies

The listed antibodies were mainly used for quantification of protein amount in cell lysates using Western Blot analysis (Table 3). The quantitative protein amount analysis served to conclude the efficiency of genetic modifications that were generated using clustered regularly interspaced short palindromic repeats (CRISPR)/CRISPR-associated sequence (Cas) technology. Besides a quantitative evaluation of protein amount, immunofluorescence staining was performed as well using the listed antibodies in required dilution. The used primary antibodies for various applications are listed below (Table 3).

The used SEC62 antibody was designed against the C-terminus of the integral ER-membrane SEC62 protein and was produced by subcutaneous injection of synthesized *de novo* peptide into rabbits (Prof. Dr. rer. nat. M. Jung, Institute of Medical Biochemistry and Molecular Biology, Saarland University). The peptide was injected as a bioconjugate. The immunization of the rabbits, collection of blood and production of serum was carried out by Aline Herges and Sabine Pelvay (Institute of Medical Biochemistry and Molecular Biology, Saarland University).

Regarding Western Blot analysis, primary antibodies were detected using either fluorescent dye-labelled CyTM 5/CyTM 3 or HRP-linked secondary antibodies against respective host species of the primary antibody. All used secondary antibodies are listed below (Table 4).

Table 3 List of applied primary antibodies. Application is indicated in brackets together with the applied dilution. WB – western blot, IF – immunofluorescence.

Primary antibody	Clone	Clonality	Host	Dilution	Product number	Supplier
Anti-BiP (Bl. 9)		polyclonal	rabbit	1:1000 [WB]		Martin Jung, Medical Biochemistry, Homburg, Germany

Anti-CD31	SZ31	monoclonal	rat	1:100 [IF]	DIA-310	Dianova GmbH, Hamburg, Germany
Anti-E-Cadherin	4A2	monoclonal	mouse	1:1500 [WB]	ab231303	Abcam, Cambridge, United Kingdom
anti-GAPDH (FL-335)		polyclonal	rabbit	1:1000 [WB]	sc-25778	Santa Cruz
Anti-LYVE-1		polyclonal	rabbit	1:50 [IF]	ab14917	Abcam, Cambridge, United Kingdom
anti-Sec62 (Bl. 14)		polyclonal	rabbit	1:1000 [WB]		Martin Jung, Medical Biochemistry Homburg, Germany
anti-Sec62 (Bl. 14)		polyclonal	rabbit	1:500 [IF]		Martin Jung, Medical Biochemistry Homburg, Germany
anti-SNAIL-SLUG		polyclonal	rabbit	1:1000 [WB]	ab180714	Abcam, Cambridge, United Kingdom
Anti- β -actin	AC-15	monoclonal	mouse	1:5000 [WB]	A5441_5M L	Sigma-Aldrich, St. Louis, MO, USA
Anti- β -actin	AC-15	monoclonal	mouse	1:1500 [IF]	A5441_5M L	Sigma-Aldrich, St. Louis, MO, USA

Table 4 List of applied secondary antibodies. Application is indicated in brackets together with the applied dilution. WB – western blot, IF – immunofluorescence.

Secondary antibody	Clonality	Host	Dilution	Product number	Supplier
Anti-mouse Alexa Fluor™ 488	polyclonal	goat	1:2000 [IF]	A11001	Thermo Fisher Scientific Inc., Waltham, MA, USA
Anti-Mouse IgG (whole molecule) F(ab') ₂ fragment–Cy3	polyclonal	sheep	1:2500 [WB]	C2181-1ML	Sigma-Aldrich, St. Louis, MO, USA
Anti-rabbit Alexa Fluor™ 568	polyclonal	goat	1:500 [IF]	A11011	Thermo Fisher Scientific Inc., Waltham, MA, USA
Anti-Rabbit IgG (whole molecule), F(ab') ₂ fragment–Cy3	polyclonal	sheep	1:2500 [WB]	C2306-1ML	Sigma-Aldrich, St. Louis, MO, USA
ECL Plex Goat anti-Mouse IgG-Cy™ 3	polyclonal	goat	1:2500 [WB]	PA43009	Cytiva, Marlborough, MA, USA
ECL Plex Goat anti-Rabbit IgG-Cy™ 5	polyclonal	goat	1:2500 [WB]	PA45011	Cytiva, Marlborough, MA, USA
Phalloidin-FITC			1:100 [IF]	ab235137	Abcam, Cambridge, UK
Goat anti-Rat IgG (H+L) Highly Cross-Adsorbed Secondary Antibody, Alexa Fluor™ Plus 488	polyclonal	goat	1:200 [IF]	A48262	Invitrogen, Waltham, MA, USA
Goat anti-Rabbit IgG (H+L) Highly Cross-Adsorbed	polyclonal	goat	1:200 [IF]	A32732	Invitrogen, Waltham, MA, USA

Secondary Antibody, Alexa Fluor™ Plus 555								
Anti-rabbit Antibody	IgG,	HRP-linked	polyclonal	goat	1:2000	#7074	Cell Signaling Technology Europe B.V., Leiden, Netherlands	
Anti-mouse Antibody	IgG,	HRP-linked	polyclonal	goat	1:2000	#7076	Cell Signaling Technology Europe B.V., Leiden, Netherlands	

2.1.5. Rough microsomes

Rough microsomes (RM) represent vesicular fragments of the rough ER, which can be obtained directly from secretory tissue. They usually contain all components of the organelle in their original composition and are able to import proteins into the lumen and to catalyse the correct processing of these precursors. Rough microsomes obtained from dog pancreases were prepared according to established protocols (Walter and Blobel, 1983; Watts et al., 1983). The concentration of RM is given in equivalents (eq), where an eq is defined as 1 µl of an RM suspension with an OD280nm of 50. Rough microsomes were used as a positive control during the immunological detection of proteins in cell lysates by Western Blot analysis (2.4.3).

2.1.6. Oligonucleotide primers

The DNA oligonucleotides used for polymerase chain reactions (PCR), sanger- and next-generation sequencing of mutagenized DNA are listed below (Table 5).

All oligonucleotides were purchased from Microsynth AG (Balgach, Switzerland) and Sigma-Aldrich Chemie GmbH (Taufkirchen, Germany).

Table 5 List of DNA oligonucleotides used in this study. fwd: forward; rev: reverse; NGS: next generation sequencing

Primer	Sequence (5' -> 3')	Application
hU6-fwd	GAGGGCCTATTTCCCATGATT	CRISPR plasmid validation
ZC3H12C_fwd	ACA GCA GCA TTG CAG CTT C	OFF-target validation
ZC3H12C_rev	TTG CCC TTC TTT GCC TCT ATC	OFF-target validation
SMPD3_fwd	CAC AGA TGG GGG CAT GTT TC	OFF-target validation
SMPD3_rev	TGA AGT GCT CCC TGC AAC AG	OFF-target validation
SLC12A8_fwd	CCA AGC CAG GTA CTA AGT GAC	OFF-target validation

<i>SLC12A8_rev</i>	GGT AGG CAC AAA TGG GGA G	OFF-target validation
<i>FARP1_fwd</i>	CTG TGG TCC CAT GCT TTG CT	OFF-target validation
<i>FARP1_rev</i>	ACA CAT GAT CAC CTC ACC CA	OFF-target validation
<i>SEC62_fwd</i>	GTT GAG GTT TTG GGG AAC TAC	OFF-target validation
<i>SEC62_rev</i>	ATC TCC TGA CCT TGT GAT CC	OFF-target validation
<i>SEC62_NGS_fwd</i>	TCT TTC CCT ACA CGA CGC TCT TCC GAT CTG TTG AGG TTT TGG GGA ACT AC	NGS amplicon PCR
<i>SEC62_NGS_rev</i>	GTG ACT GGA GTT CAG ACG TGT GCT CTT CCG ATC TAG AGG TAC CAA AGA AAT CAG G	NGS amplicon PCR

2.1.7. Bacterial strain

E. coli Stbl3 used for the propagation of the Cas9-plasmid has the following genotype: $F^- mcrB mrr hsdS20(r_B^-, m_B^-) recA13 supE44 ara-14 galK2 lacY1 proA2 rpsL20(Str^R) xyl-5 \lambda^- leu mtl-1$ (Invitrogen™, Carlsbad, CA, USA).

2.1.8. Cell lines

For all experiments in this study, specifically all mouse studies and the targeted genetic modification of *SEC62*, the established human FaDu cell line (ATCC® HTB-43™) was used. This cell line of epithelial origin derives from a punch biopsy of an HPV-negative hypopharyngeal squamous cell carcinoma of a 56-year-old Hindu male patient (Rangan, 1972). The cells have a hypodiploid to hypertriploid karyotype with a modal number of 64 chromosomes (Supplementary Figure 9).

2.1.9. Kits

The kits used in this study are listed below (Table 6).

Table 6 List of used kits in this study.

Kit	Product number	Supplier
GeneART™ Genomic Cleavage Detection Kit	A24372	Invitrogen by Thermo Fisher Scientific Inc., Waltham, MA, USA
NucleoSpin® Tissue	740952.5	Macherey-Nagel GmbH & Co. KG, Düren, Germany

PureLink™ Quick PCR Purification Kit	K310001	Invitrogen by Thermo Fisher Scientific Inc., Waltham, MA, USA
Qiagen® Plasmid Midi Kit (100)	12143	Qiagen GmbH, Hilden, Germany
QIAquick® PCR & Gel Cleanup Kit (100)	28506	Qiagen GmbH, Hilden, Germany
SuperScript™ IV Vilo™ Master Mix with ezDNase™ enzyme	11766050	Invitrogen by Thermo Fisher Scientific Inc., Waltham, MA, USA
TGX Stain-Free™ FastCast™ Acrylamide Starter Kit, 10%	161-0182	Bio-Rad Laboratories, Inc., Hercules, CA, USA

2.1.10. Software

All used software for technical devices or data analyses is listed below (Table 7).

Table 7 List of used software in this study.

Software	Supplier
BarTender® 2016	Seagull Scientific Europe, Inc., Madrid, Spain
cellSens software	Olympus Deutschland GmbH, Hamburg, Germany
ChemoStar	Intas Science Imaging Instruments GmbH, Göttingen, Germany
CorelDraw® x6	Corel Coporation, Ottawa, Canada
Horos	Nimble Co LLC d/b/a Purview, Annapolis, MD USA
Image J/Fiji	Schindelin J et al., 2012
ISIS	MetaSystems Hard & Software GmbH, Altlußheim, Germany
LabImage 1D	Kapelan Bio-Imaging GmbH, Leipzig, Germany
LAS X Life Science	Leica Microsystems GmbH, Wetzlar, Germany
NIS Elements AR 3.0 software	Nikon Coporation, Tokio, Japan
OriginPro 2022	OriginLab Corporation, Northampton, MA, USA
ParaVision 5.1	Bruker BioSpin MRI GmbH, Ettlingen, Germany
Perseus 1.6.15.0	Max-Planck-Institute for Biochemistry, Martinsried, Germany
SigmaPlot 11.0	Systat Software GmbH, Erkrath, Germany
VisiView software	Visitron Systems GmbH, Puchheim, Germany

2.2. Animal Experiments

2.2.1. Animals

The used male mice (Janvier Lab, Le Genest-Saint-Isle, France) in this work were housed in groups in isolated ventilated cages (IVC) under specific pathogen-free conditions in a temperature- and humidity-controlled 12-hours light/dark environment in the animal facility of the Institute for Clinical and Experimental Surgery at the Saarland University (Homburg). All animals had access to tap water and standard pellet food *ad libitum*. Male mice were used because most of the head and neck cancer patients are male, to be as precise as possible to reality in experimental design. The experiments were performed in accordance with German legislation on protection of animals, the EU Directive 2010/63/EU and National Institutes of Health Guidelines for the Care and Use of Laboratory Animals (NIH Publication #85-23 Rev. 1985). All experiments were approved by the local governmental animal care committee (#68-2015, #37-2020) and were done in collaboration with Prof. med. M. D. Menger and Dr. med. vet. Christina Körbel (Institute of Clinical and Experimental Surgery, Saarland University, Homburg).

2.2.2. Orthotopic, lymphatic metastasis xenograft model

For the investigation of lymphatic metastasis, the primary tumour should be localised in the tongue to metastasise into cervical lymph nodes. Therefore, the human squamous cell carcinoma cell line FaDu (2.1.8) was injected into the tongue of male 8-week-old BALB/cAnNRj-Foxn1nu or NOD.CB17/Prkdc^{scid/scid}/Rj mice, respectively. During cell injection, animals were anaesthetised (80 mg/kg ketamine, 12 mg/kg xylazine) and received analgesic after the cell inoculation (5 mg/kg carprofen). For the tumour cell injection, mice had to be fixed with their teeth to open the mouth and getting access to the tongue. This was done on a heating plate to avoid cooling of anaesthetised mice (Figure 6A). Different cell injection strategies using a Hamilton® syringe (701N, volume 10 µL, needle size 26s ga; Hamilton company, Reno, NV, USA) as well as different cell numbers and imaging modalities with respect to the incidence and number of lymph node metastases together with the general living conditions of the animals were compared and are described in the corresponding “Results Chapter”. During the model establishing experiments, mice were weight checked once per week for the first two weeks. Until the third week, weight was controlled 3 times per week to control the exact progression of weight. When the first mouse of the whole experimental group had lost 20 % of its highest weight, all mice were sacrificed and the tongues, as well as submandibular lymph nodes, were dissected under video documentation (Figure 6B; Supplementary Video 1A). The size of the primary tumour in the tongue was measured using a calliper and the tissue was prefixed for histological analysis in 4 % (w/v)

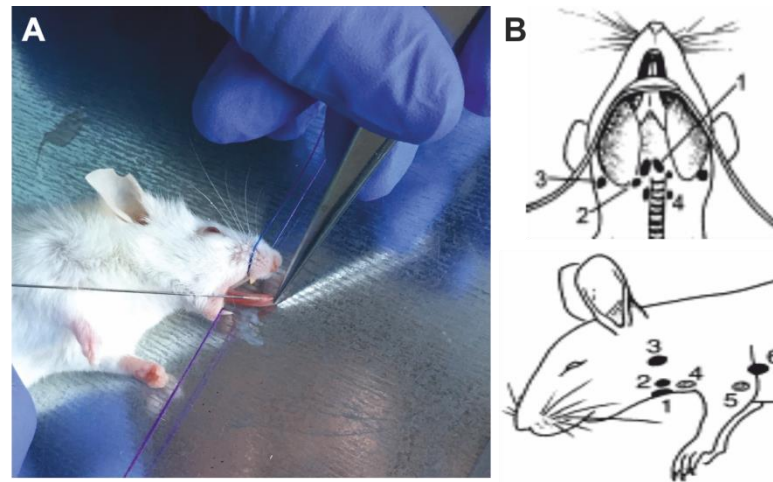


Figure 6 Tumour cell injection: (A) The mouse was fixed with its teeth on a heating plate to open the mouth and pull out the tongue. Tumour cells were injected into tongue using a Hamilton® syringe. Specific injection location and cell amount was established and is described in the “Results Chapter”. (B) When mice were sacrificed after 6-8 weeks submandibular lymph nodes (#1) as well as the primary tumour existing in the tongue were collected under video control (modified from Van den Broeck et al., 2006).

formalin for ≥ 6 hours before the resected tissue – tongue and lymph nodes - was further processed using a Tissue Tek® VIP™ 5 Jr. (Sakura Finetek Europe B.V., Alphen aan den Rijn, Netherlands).

2.2.3. Haematogenous metastasis xenograft model

For investigation of haematogenous metastasis the primary tumour was not implanted into a specific location like in the lymphatic xenograft model, but metastatic spread was mimicked at a stage when tumour cells have already invaded the blood vessels skipping the process of epithelial-mesenchymal transition (EMT). Therefore, the human squamous cell carcinoma cell line of the hypopharynx called FaDu that were also used in the lymphatic metastasis model was injected into the tail vein of male 8-week-old NOD.CB17/Prkdc^{scid/scid}/Rj mice (Janvier Labs, Le Genest-Saint-Isle, France). Here, different pre-injection treatment protocols of the cells as well as of the animals, together with various cell numbers were compared and are further described in chapter 3. For quantification after sacrifice of mice, different tissue preparation techniques were compared to each other, as well. At the endpoint metastases were identified and quantified by micro-computed tomography (μ CT; SkyScan1176; Bruker AXS, Karlsruhe, Germany), 9.4 T magnetic resonance imaging animal scanner (Biospec Avance III 94/20, Bruker Biospin GmbH, Ettlingen, Germany) and histopathological examination as gold standard. In case of the μ CT two different image acquisition properties were used which are further described in chapter 2.2.3.2. The first μ CT parameters were applied to the living animal with potential breath- and heart beating-artefacts under constant isoflurane anaesthesia with 1.5 % (v/v). After this image acquisition, the mice were sacrificed using an overdose of the volatile anaesthetic isoflurane (4 %, v/v) until the animals showed no movement of the chest anymore. Next, the second image

acquisition was done without moving artefacts generated by breathing or heartbeat. After the two image acquisitions with μ CT the lung was surgically removed and swelled by hanging at a 20 cm formalin-column for 15 min to obtain better morphological analysis in the following histological processing. The lung was then prefixed in 4 % (w/v) formalin over night before it was transferred for dehydration and fixation into the Tissue-Tek® VIP™ 5 Jr. (Sakura Finetek Europe B.V., Alphen aan den Rijn, Netherlands). Subsequently, the lung was cut into 1 mm thick slices using a tissue chopper (Ted Pella Inc., Redding, CA, USA) and each slide was finally embedded in single paraffin sections. Afterwards, paraffin blocks containing the 1 mm thick lung slices were cut into 3 μ m thick slices and stained with haematoxylin/eosin (H&E) for better identification of metastases as well as for better morphological orientation. Slices were further analysed using ImageJ/Fiji software which is described in detail in chapter 2.3.4 (Schindelin et al., 2012). All steps from tumour cell inoculation to the analysis of the lung volume and its tumour burden are shown in Figure 7.

2.2.3.1. Magnetic-resonance tomography

In this thesis, different imaging- and evaluation-techniques for lung metastases were examined. One of these techniques used for metastasis detection was the magnetic resonance imaging (MRI).

MRI is a medical technique used for imaging of inner structures of the whole body. In comparison to computed tomography (2.2.3.2) the MRI is better suited for soft tissue visualisation and is free of ionising radiation. In the MR imaging, the proton density in different tissues is displayed instead of the tissue density like in CT imaging. Therefore, the induced molecule for measurements is hydrogen which is a highly abundant component in the entire body, especially in water and fat.

The basic principle of magnetic resonance is the spin of hydrogen protons. Due to the combination of a strong magnetic field with high-frequency pulses (HF-pulses) to the long body axis hydrogen protons are resonantly induced and generate an electric signal, which is recognized and reconstructed into three-dimensional images. For the maintenance of a strong magnetic field, the MRI system consists of a superconductive magnet which has to be cooled down by liquid helium and nitrogen to set the resistance of the used coil nearly to zero (Siemens Healthcare, 2015).

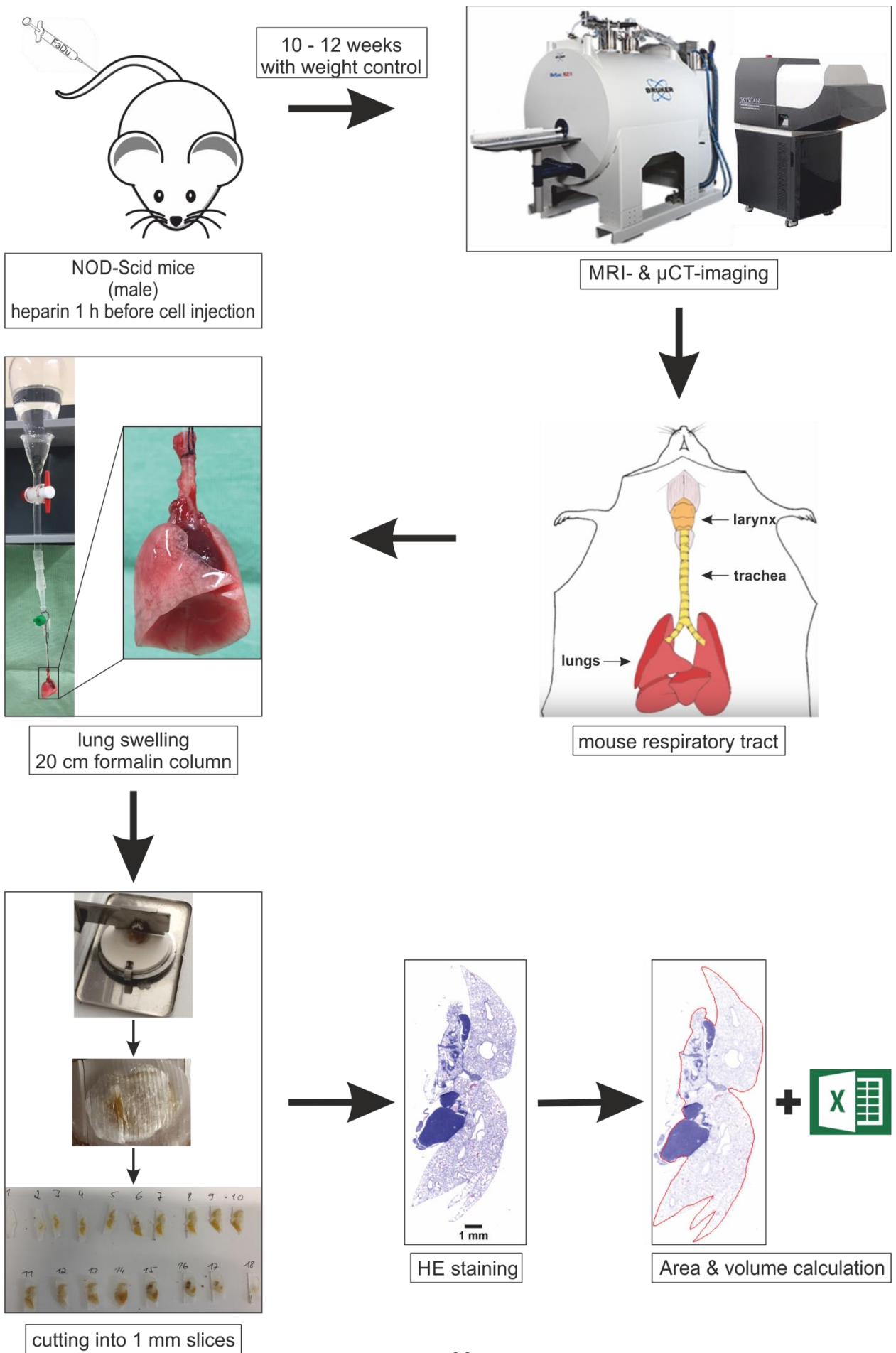


Figure 7 Workflow of haematogenous metastasis model: 8-week-old male NOD-Scid mice were prepared 1 h before cell inoculation, e.g. by intraperitoneal (i.p.) heparin application (20 U/200 μ l). During this time FaDu cells were harvested and prepared for inoculation. Mice were intravenously (i.v.) injected with FaDu cells into tail vein and were observed for the next 10 to 12 weeks. During this time constant weight control was performed. At the day of sacrifice MR imaging as well as μ CT was performed. Before the second μ CT acquisition (9 μ m) mice were killed by an overdose of isoflurane to prevent motion artefacts caused by heartbeat and breathing. After image acquisition the lung was resected and swelled for ~15 min hanging at a 20 cm formalin column. Afterwards, the lungs were prefixed in formalin over night before the tissue was further processed with dehydration and fixation. Next, the fixed lungs were cut into 1 mm thick slices and embedded into paraffin for cutting into 3 μ m thick slices, which were H&E stained. Stained sections were analysed for total slice area and lung volume as well as for total tumour burden.

The used MRI for this study is a 9.4 T MRI animal scanner (Biospec Avance III 94/20; Bruker Biospin GmbH, Ettlingen, Germany) with a BGA12A gradient system which was run with ParaVision 5.1 software (Bruker BioSpin MRI GmbH, Ettlingen, Germany). During the scan, animals were maintained under isoflurane anaesthesia with control of vital parameters including the breathing rate. Image acquisition was done using a linear polarised coil developed for imaging mouse thorax with an inner diameter of 38 mm (Bruker Biospin GmbH, Ettlingen, Germany). All MRI scans were done in collaboration with Dr. Andreas Müller (Institute of Radiology, Saarland University Hospital, Homburg) and were analysed using Horos software (Nimble Co LLC d/b/a Purview, Annapolis, MD USA). An exemplary MRI reconstruction can be seen in Supplementary Video 1B.

2.2.3.2. Micro-computed tomography

For analysis of metastasis in addition to the MRI, an *in vivo* μ CT scan was used to image the lung. The technology of CT scans is used in medicine since 1974 to generate images of the inner structures of the whole body. This method is based on X-radiation that is fanned out over the examination object lying in a donut-shaped opening. The motorized X-ray source rotates around the gantry and X-rays penetrate the examined body. Because of different organ- and tissue-densities the X-ray is diversely attenuated, which will be detected on the opposite of the X-ray source. A computer is able to calculate grey-scale images based on the measured attenuated X-ray signals by using complex algorithms. After the reconstruction, images of the examined body part can be analysed for metastasis. The μ CT was performed under isoflurane inhalation anaesthesia using a Bruker *in vivo* μ CT scanner (Skyscan 1176; Bruker Corporation, Billerica, MA, USA). The mice were positioned supine on a carbon fibre examination bed. The CT scan was started after performing an overview scan of the whole animal and defining the region of interest. For the CT scan the following experimental settings were applied: aluminium 0.5 mm/1 mm filter, averaging 2, 180° scanning, 1° steps, 9 μ m/18 μ m resolution, exposure time 800 ms/220 ms per image, source current 500 μ A, source voltage 50 kV. The obtained cross-sectional CT images were reconstructed by using the “NRecon” reconstruction software (Bruker Corporation, Billerica, MA, USA) with the following settings: Smoothing 2, ring artefacts 20 and

beam hardening 40 %. Analysis of metastasis volume was done using “CTAn” software (Bruker Corporation, Billerica, MA, USA).

2.3. Histological methods

2.3.1. Fixation and embedding of histological specimens

All specimens of sacrificed animals had to be further processed before histological sections could be made. Therefore, all specimens were fixed in 4 % formalin (w/v) for several hours. Afterwards the specimens were transferred into the Tissue Tek[®] VIP[™] 5 Jr. (Sakura Finetek Europe B.V., Alphen aan den Rijn, Netherlands) that perform a dehydration step, followed by a clearing step and end with an infiltration process of the probes (Table 8). Afterwards, the tissue samples were ready to be cut into sections and were then haematoxylin/eosin (H&E) stained or were used for immunohistological staining. Before embedding the fixed specimens into paraffin, water must be removed from the tissue and from the aqueous-based fixative (step 2-7, Table 8). For this process, the above-mentioned device was used. The Tissue Tek[®] uses a standardised protocol with accurate control of processing time and temperature. The first step is the removal of the fixative and water from the samples. Therefore, the tissue samples were gradually soaked in alcohol from 70 to 100 % (step 2-7, Table 8). In the following step, the clearing step, the used clearing agent had to be miscible with the previously used alcohol and the following infiltrating agent paraffin. In this thesis, xylene was used as clearing agent. The specimens were soaked three times in xylene to ensure a complete removal of the dehydration solution (step 8-10, Table 8). Specimens turned translucent when all the dehydrating agent was removed. In the following step, the clearing agent was replaced by paraffin as the infiltration agent (step 11-14, Table 8). During the whole embedding process, all cells and ultrastructural components remained in their functional orientation and could be visualised later by immunohistological staining methods. At this point, the specimens were ready to be removed of the Tissue Tek[®] and were embedded into molds dependent on the preferred orientation for further processing.

Table 8 Protocol of specimen embedding using Tissue Tek[®]

step	agent	duration	temperature	vacuum
1	4 % formalin/PBS	2 h	45°C	Yes
2	70 % EtOH	0.5 h	40°C	Yes
3	70 % EtOH	1 h	40°C	Yes
4	70 % EtOH	1 h	40°C	Yes
5	96 % EtOH	0.5 h	40°C	Yes

6	100 % EtOH	1 h	40°C	Yes
7	100 % EtOH	1 h	40°C	Yes
8	Xylene	1 h	40°C	Yes
9	Xylene	1 h	40°C	Yes
10	Xylene	1 h	40°C	Yes
11	Paraffin	0.5 h	60°C	Yes
12	Paraffin	0.5 h	60°C	Yes
13	Paraffin	1 h	60°C	Yes
14	Paraffin	1 h	60°C	Yes

2.3.2. Production of histological sections

For all animal experiments, histological formalin-fixed and paraffin-embedded (FFPE) sections had to be made. Therefore, a Leica RM2125 RT (Leica Microsystems GmbH, Wetzlar, Germany) rotation microtome was used. The FFPE tissue blocks were precooled, chucked into the microtome, and cut until the tissue reached a homogeneous intersection. FFPE tissue then was cut in 3 µm thick slices, that were transferred into a 40 to 50°C warm water bath to stretch the slices and to avoid wrinkle formation. The exact temperature of the water bath depended on the tissue that was cut. Tongues were mostly stretched for a few seconds in a rather cool water bath. For each FFPE tissue block 5 slices were collected onto single slides. The first and the last slices were collected onto uncoated slides for H&E staining, whereas the remaining slices were collected onto coated slides for potential immunohistochemistry (SuperFrost® plus, Gerhard Menzel GmbH, Braunschweig, Germany). As slices adhere better on coated slides, which is important for immunohistochemistry because of the heat treatment for antigen retrieval, coated slides were used for immunohistochemistry. In case of H&E staining, uncoated slides were used. To warrant consistent slice quality, the microtome blade was renewed at least after each FFPE tissue block.

2.3.3. Haematoxylin and eosin stain

Each 1st and 5th slide was H&E stained for detection of primary tumour in case of the lymphatic model, as well as for metastasis in the haematogenous model. H&E staining is the most widely used staining method and gold standard in pathology to diagnose suspected cancer in a biopsy, first introduced in 1877 by A. Wissozky. It consists of a combination of two histological stains. Haematoxylin stains nuclei in blue, eosin stains extracellular matrix and cytoplasm in pink to differentiate between nuclear and cytoplasmic parts of the cell.

Therefore, slides were incubated over night at 37 °C to ensure adherence. In the first step 3 µm thick FFPE sections were deparaffinised. Sections were immersed in three sequential xylene baths for 5 min each to remove paraffin. In the next step, sections were rehydrated by swivelling slides into a decreasing ethanol row (3x 100 % (v/v), 3x 70 % (v/v)) before the slides were immersed into purified water for at least 5 min for further rehydration. For better localization of tumour and normal tissue, slides were incubated in haematoxylin solution for about 8 min and were washed in tap water afterwards. After rinsing sections in glacial acetic acid to remove excess staining, sections were blued in tap water for 10 min. Subsequently, sections were counterstained for 20 to 30 s with eosin before they were rinsed again with tap water until no colour was washed out anymore. Sections were transferred through an increasing ethanol row (3x 70 % (v/v), 3x 100 % (v/v)) followed by three sequential xylene baths before they were embedded using Entellan® new and covered with a coverslip.

2.3.4. Microscopic evaluation

In case of the haematogenous metastasis model, from each 5th slide that was H&E stained an overview image was taken with a Leica MZ 10F stereomicroscope (Leica Microsystems GmbH, Wetzlar, Germany). These images were further analysed for metastasis using an Olympus BX61 microscope (Olympus Deutschland GmbH, Hamburg, Germany) in a later step. Images which were taken with a planapo 1.6x- respectively 0.63x-objective of the M-Series (Leica Microsystems GmbH, Wetzlar, Germany) were then evaluated by encircling the tissue borders for area calculation. For this purpose, ImageJ/Fiji was used in combination with a graphical tablet (Wacom Intuos M, Wacom Europe GmbH, Düsseldorf, Germany) (Schindelin et al., 2012). After area calculation, the whole lung volume was calculated by using the integral calculation. Therefore, each single area of one lung was multiplied with the known thickness of each lung tissue block, which was consistent with 1 mm. Afterwards, the sum of all single tissue block areas of the lung was calculated. In case of the volume calculation of metastasis, the same procedure was performed. Each metastasis was encircled for area calculation and afterwards volume was calculated by using the integral.

For lymphatic metastasis, all tongues and lymph nodes were imaged by using the microscopes as mentioned before. Also, here it was important to know if there was a primary tumour in the tongue as well as metastases in the lymph nodes plus volume calculation of the primary tumour and metastasis.

2.4. Biochemical Methods

2.4.1. Protein isolation

2.4.1.1. Protein isolation of cultured cells

For analysis of protein content in a cultured cell line cells had to be harvested. Therefore, at least 1.0×10^6 up to 2.0×10^6 cells were harvested from a 75 cm^2 cell culture flask. Culture medium was aspirated, and cells were washed with 5 ml of DPBS. After adding 1 ml Trypsin-EDTA solution, cells were incubated at $37 \text{ }^\circ\text{C}$ 5 % (v/v) CO_2 for about 10 min. Reaction was stopped by adding 4 ml DMEM GlutaMAX culture medium. After resuspending, the cell-suspension was harvested in a 15 ml falcon. Cells were counted by using a Countess™ (Invitrogen, CA, USA). At least 2.0×10^6 cells were transferred into a 1.5 ml tube and centrifuged for 2 min at 3000 rpm in an Eppendorf 5415C table centrifuge (Eppendorf AG, Hamburg, Germany). After discarding the supernatant, the remaining cell pellet was stored at -20°C .

Further sample preparation for sodium-dodecylsulfate polyacrylamid-gelelectrophoresis (SDS-PAGE) should be as harsh as possible to ensure a complete lysis of all cells and near complete protein solubilisation but should not be too destructive so that proteins become degraded. Proteins have to be protected against liberated endogenous proteases during cell disruption process. Therefore, a cocktail of protease inhibitors was added to sample buffer. To solubilise cell membranes, mild non-ionic detergents were used like NP40 to ensure a minimal denaturing of the target proteins. Later on, samples were solubilised using a mixture of RIPA buffer in addition with Proteinase Inhibitor Mix M (1:100, SERVA Electrophoresis GmbH, Heidelberg, Germany). Apart from disruption process, samples should be cleaned-up for further analysis steps. To remove nucleic acids, DNase was added. β -Mercaptoethanol (β -ME) is a strong reductant and dependent on the concentration it protects proteins from oxidation (low concentrations) or reduces disulphide bridges. Sodium-dodecylsulfate (SDS) and β -ME are also needed to ensure correct separation by size of the proteins during SDS-PAGE due to their ability to charge all proteins homogenously negative. The exact mixture of all components of the used sample buffer is listed in 2.1.2.

2.4.2. SDS-polyacrylamide gel electrophoresis (SDS-Page)

For protein separation the most commonly method in analytical protein biochemistry was used, the SDS-PAGE (Laemmli, 1970). Electrophoresis separates proteins based on size, shape, and charge. Molecules move dependent on these factors through a gel matrix with their own specific velocity. The used gel matrix is composed of a polyacrylamide gel which acts as a size-selective

sieve driven by an electric field that is generated throughout the matrix. Proteins are amphoteric compounds that are either charged positively or negatively, dependent on their amino acid residues. Because of these different residues, each protein has its own isoelectric point (pI). At this point, proteins have no net charge. Due to the fact that electrophoresis is running at a constant pH, each protein in a mixture has its own positive or negative charge and characteristics in velocity. Because all proteins in a sample have to run the same direction towards the cathode, proteins have to be forced to be negatively charged. This is ensured by adding SDS to the sample buffer. Thus, SDS is able to mask proteins by coating the amino acid residues with negatively charged detergent micelles (Weber and Osborn, 1969).

In this work, the Laemmli buffering system was used. This system consists of two distinct types of gel matrices. The first one is the stacking gel with a pH of 6.8. It deals to concentrate all proteins of all samples to a thin starting zone. Passing this zone samples run into the second gel matrix called resolving gel with a higher pH between 8 and 9. Because of relatively high pH values cysteine residues tend to form disulphide bonds which was prevented by the addition of a reducing agent to the sample like β -ME. Moreover, tertiary- and quaternary structures were split by reducing reagents and SDS, so linear polypeptide chains migrated through matrices and were separated up just by their molecular weight.

Resolving gel concentration is dependent on the molecular weights of proteins that have to be separated. It is important to choose the right concentration of acrylamide- and bisacrylamide-monomers for a good separation of samples to get properly separated protein bands. Both components were cross-linked by 2-Acrylamido-2-methylpropane sulphonic acid (APS) as an initiator and Tetramethylethylenediamine (TEMED) as a catalyser. Gel matrices were generated in between two glass plates that were clamped between two chambers filled with buffer solution during the electrophoresis process. Due to addition of SDS and the aid of heating, the denatured proteins could be separated by their specific stokes-radius (= hydrodynamic radius) based on an electric field, which is applied to the polyacrylamide gel.

Resolving gels used in this work were 12.5 % (w/v) concentrated, 11 cm x 14 cm x 1 mm sized and were sealed at the bottom with a 2 % (w/v) agarose gel (Table 9). In most of the cases a 14-lane comb was used which was filled with 20 up to 30 μ l of cell lysate containing 1x Laemmli buffer, empty lanes were filled with 20 μ l of 1x Laemmli buffer for consistence in running front. For molecular weight standard 5 μ l of "PageRuler Prestained Protein Marker" were used.

Table 9 Composition of SDS gels: 12.5 % (w/v) resolving gel was attached to 5 % (w/v) stacking gel. Single components for gel preparation were manufactured based on Laemmli (1970) and pipetted in the shown order, mixed and poured between two glass plates. Cured gels were stored at 4 °C and used at the latest after 1.5 weeks for gel electrophoresis.

Solution	Resolving gel	Stacking gel
40 % (w/v) acrylamide	4.7 ml	0.9 ml
2 % (w/v) bisacrylamide	1.25 ml	0.2 ml
H ₂ O	2.9 ml	5 ml
1.875 M Tris pH 8.8	6 ml	---
1 M Tris pH 6.8	---	0.9 ml
10 % (w/v) SDS	150 µl	72 µl
20 % (w/v) APS	45 µl	67.5 µl
TEMED	5 µl	10.5 µl
Total volume	15.05 ml	7.15 ml

2.4.3. Western Blotting and detection

After protein separation depending on their specific molecular weight using SDS-gel electrophoresis proteins were transferred and detected onto a solid support membrane that is made of chemically inert substances. This method called “Western Blot” was established by Georg Stark in 1979 at Stanford University and relies on the principle of electro mobility, which also drives the migration of proteins through gel matrix during electrophoresis (Renart et al., 1979). Proteins were immobilized at their respective migration position in the gel and were transferred onto a membrane, on which proteins could be detected by binding of specific antibodies later on (Burnette, 1981).

Therefore, the polyacrylamide gel, a membrane and two electrodes were assembled like a sandwich and proteins were transferred from gel to membrane. The main importance in this process is a uniform transfer across the whole gel to ensure a similar transfer-efficiency for small and large proteins.

In this work, the wet as well as the semidry transfer method were used. Regarding the wet transfer method, gel and membrane are fully immersed in transfer buffer. In consequence of an electric field which is applied to the transfer chamber, proteins are forced by electricity and their negative charge to move from gel to membrane towards the positively charged anode. Proteins can then bind to the membrane via a combination of hydrophobic and dipole interaction. For wet transfer, a cooling system is required because the buffer will heat up during the transfer process due to the electric field, which could lead to protein damage. Wet protein transfer method is in comparison to semidry transfer more efficient, especially for larger proteins and leads to distinct

and sharp bands. On the other hand, the used method is slower than the semidry version. If the transfer process is stopped too early, transfer might be incomplete and single proteins remain in the gel. Therefore, the time span of blotting procedure in this work was calculated between 3 and 4 h to ensure a complete protein transfer from gel to membrane. For all experiments, a polyvinylidene difluoride (PVDF) membrane was used, which consists of a porous material. The binding capacity depends on pore size; here a pore size of 0.45 μm was used. This type of membrane has a high binding capacity, which also leads to higher background, but has a mechanical strength. PVDF membranes are highly hydrophobic and must be activated by rinsing with 100 % (v/v) methanol for 10 to 20 sec. After methanol activation, the membrane has to be washed with purified water. All used utensils like membrane, gel, whatman® paper and sponges had to equilibrate for at least 10 min in blotting buffer before they were packed like a sandwich and installed in the blotting chamber (Figure 8). After the transfer, proteins of interest could be detected and localised using target-specific antibodies. Before antibody detection could start, the membrane had to be prepared to prevent non-specific interactions. In this step, spaces on the membrane which were not occupied by proteins had to be blocked. For this purpose, dried milk powder was used. The membrane was incubated in 5 % (w/v) milk-TBS solution at room temperature (RT) for around 30 min under constant agitation. After the blocking step, the membrane was incubated with the primary antibody solution at 4 °C overnight, again under constant agitation. The solution consisted of 5 % (w/v) milk powder in TBS with the specific primary antibody in its unique dilution (Table 3). Following the primary antibody incubation, the membrane had to be washed to remove remaining unbound antibodies to avoid a strong background. Therefore, the membrane was washed using TBS followed by two steps of washing with TBS-T, which was then followed by one step of TBS washing again. Each washing step was done for 5 min under constant agitation at RT. In the penultimate step, the membrane was mostly incubated with fluorescence labelled secondary antibody to visualize the protein. Due to usage of secondary antibody, there is an amplification in signal emission, also allowing detection of sparse protein amounts (Figure 9). The emitted signal is proportional to the quantity of protein that is detected. The choice of secondary antibody depended on the species of the primary antibody (Table 3). Fluorescence labelled antibodies were suitable for multiplexing to detect protein of interest together with a housekeeping protein without stripping and reprobing the membrane. Signals were detected with high sensitivity by digital imaging techniques. An additional advantage of fluorescence labelled antibodies is the signal stability for up to three months. The incubation period of 1 h at RT under constant agitation was then followed by the same washing steps as mentioned above. After the last washing step, the membrane was dried for at least 12 h before imaging and quantification. As already mentioned, in this work mainly fluorophore-conjugated secondary antibodies were used, especially Cy3- and Cy5-labelled antibodies. These were excited using a LED light source. The antibody-specific emission was detected afterwards using

a cooled charge-coupled device (CCD)-camera combined with emission filters to allow only a well-defined spectrum to reach the collector (Chemostar ECL & Fluorescence Imager; Intas Science Imaging Instruments GmbH, Göttingen, Germany). This type of camera collects photons on a chip and translates the collected charge into a digital signal. For protein quantification, β -actin was always used as an internal standard (“housekeeping protein”) because it is supposed to be expressed at a constant level regardless of external stimulation.

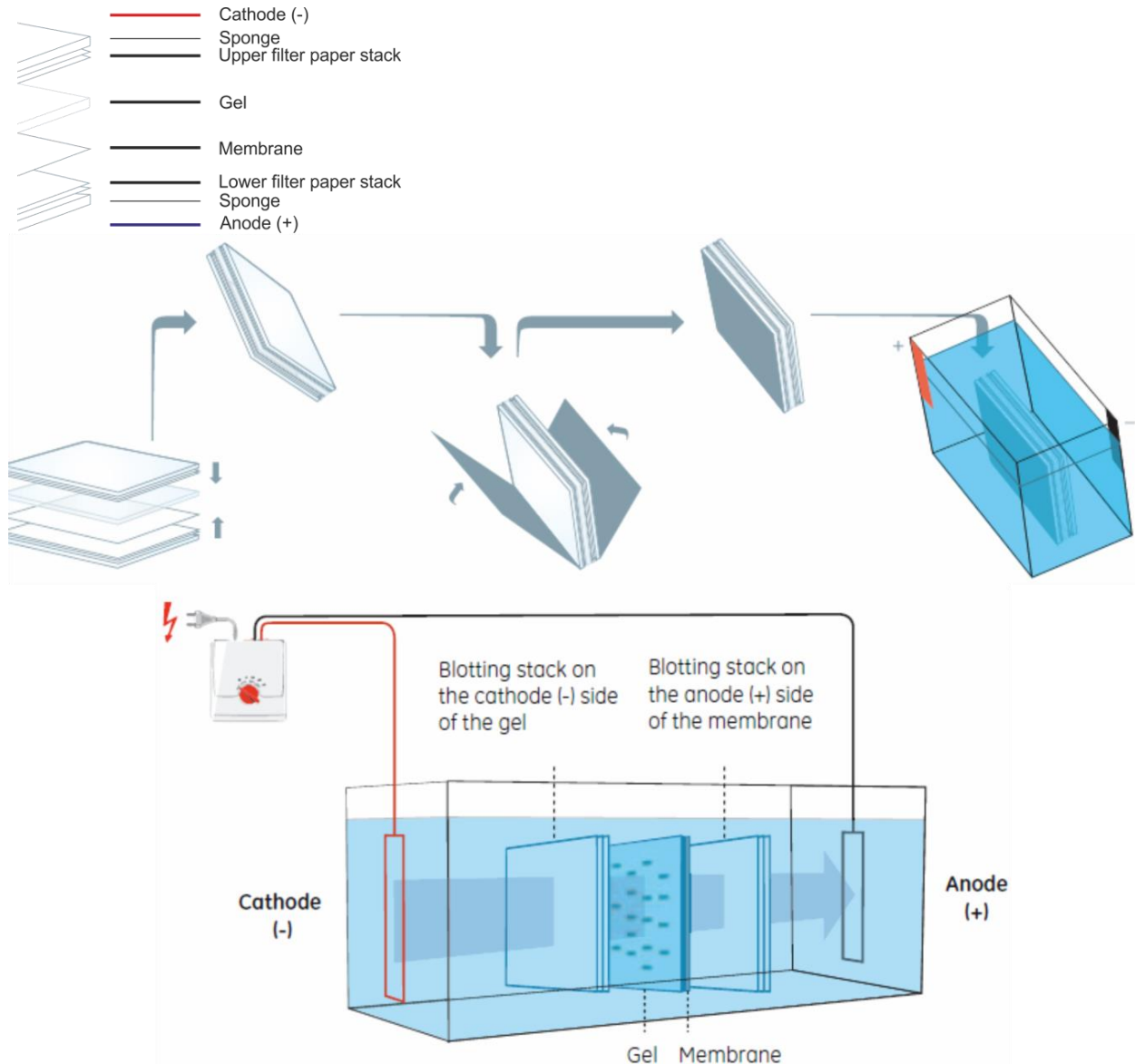


Figure 8 Constitution of wet transfer system: Assembly of wet transfer system starts after equilibration of all used components in blotting buffer for at least 10 min. The sandwich build up is started on the side facing the cathode (-) with a sponge, followed by a wetted whatman® paper, the gel, the membrane, another whatman® paper and finally a second sponge. Especially in the step when the membrane is lied down on gel it is crucial to avoid air bubbles for a uniform transfer process. The sandwich is then securely fixed and immersed into the blotting tank filled with blotting buffer. The gel is facing the cathode (-) side, the membrane is facing the anode (+) side. Proteins will migrate from the gel towards the membrane in an electric field driven by their negative charge (modified from GE Healthcare, 2011).

In some exceptions to extremely sparse protein amount also horseradish peroxidase (HRP)-conjugated secondary antibodies were used in combination with a Pierce™ ECL Western Blotting-substrate to make transferred proteins visible. Therefore, the blotted membrane was incubated for 1 h at room temperature with the HRP-labelled secondary antibody against the

required species. The membrane was washed afterwards and directly incubated with the HRP substrate solution. Membranes were also imaged using the above-mentioned imaging system from Intas in the chemiluminescence mode.

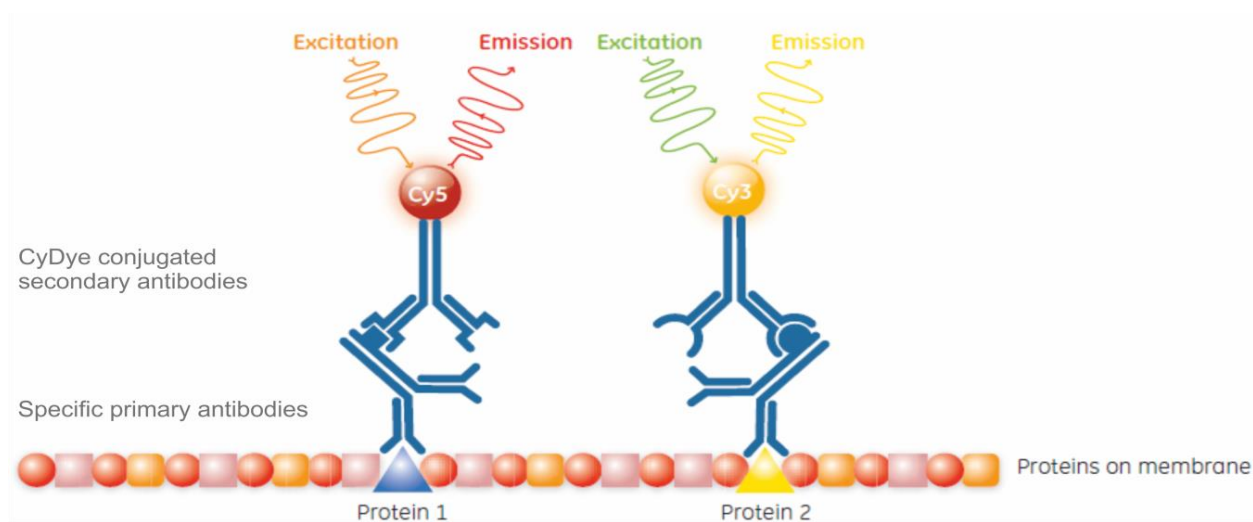


Figure 9 The principle of fluorescent Western Blot detection: Two protein-specific primary antibodies were detected by two species-specific secondary antibodies conjugated to different fluorophores. In this example the used fluorophores were Cy5 and Cy3. Each fluorophore has its own specific excitation wavelength followed by the specific emission which is detected with a CCD-camera based imager (modified from GE Healthcare, 2011).

2.5. Molecular biology and nucleic acid chemistry

2.5.1. Strategies for targeted mutagenesis

For generation of stable *SEC62* knockout mammalian cell lines, an already existing CRISPR/Cas9 plasmid was used. The design pipeline and generation of the used lentiCRISPR_v2 plasmid (catalogue# 52961, Addgene, Cambridge, MA, USA) with its specific single guide ribonucleic acid (sgRNA) directed against the *SEC62* protein is further described by Fumagalli et al. (2016).

2.5.2. Transformation of bacterial cells

For amplification, the lentiCRISPR_v2_Sec62 knockout plasmid was transformed into bacterial cells. Competent Stbl3™ *E.coli* were thawed on ice. The Stbl3™ *E.coli* were supplemented with the plasmid DNA and incubated on ice for 30 min, according to the protocol (Table 10). Next, the heat-shock transformation occurred for 45 s at 42 °C followed by an incubation on ice for 2 min. Immediately upon, pre-warmed LB medium was added to the *E.coli*-plasmid mixture and cells were incubated for 40 min at 37 °C on a rolling shaker. The transformed cells were spread out on pre-warmed LB-Agar-plates containing ampicillin for a selection of positive clones and incubated

over night at 37 °C. Colonies were picked the next day and cultivated in 100 ml LB medium before plasmid DNA was extracted the next day (2.5.4).

Table 10 Protocol for transformation of competent *E.coli*.

50 µl	Competent Stbl3™
+ 1.0 µl	Plasmid DNA (1 µg/µl)
30 min on ice	
<hr/>	
45 s 42 °C	Heat-shock
2 min on ice	
<hr/>	
+ 500 µl	LB medium
40 min 37 °C	
<hr/>	
Spreading onto selection plates (100 µg/ml ampicillin)	
Over night 37 °C	
<hr/>	
Picking colonies, 100 ml LB medium	
24 h 37°C	

2.5.3. Cultivation of bacterial cells

The Stbl3™ *E.coli* were cultivated in 100 ml LB-medium in a 1000 ml flask overnight at 37 °C with constant shaking. Depending on the resistance of the transformed plasmid, the corresponding antibiotic was supplemented to the culture medium (ampicillin 1:1000).

2.5.4. Plasmid and genomic DNA extraction and quantification

Extraction of plasmid DNA from bacterial cells was performed using Plasmid Midi kit (catalogue#12145, Qiagen, Hilden, Germany) according to the manufacturer's instructions. DNA was eluted and precipitated using isopropanol, afterwards extracted DNA was dissolved in TE buffer. Extraction of genomic DNA from cultured cells was performed using the NucleoSpin Tissue kit according to manufacturer's instructions. For quantification of nucleic acid concentrations, a NanoDrop®ND-1000 UV/Vis spectral photometer (Peqlab Biotechnologie GmbH, Erlangen, Germany) was used according to the manufacturer's instructions.

2.5.5. Sequencing of plasmid DNA and amplification

The accurate amplification of plasmid DNA was evaluated by sequencing after extraction from transformed bacterial cells. For this purpose, an aliquot of 100 ng plasmid DNA diluted in 20 µl H₂O was sent out to GATC Biotech AG (Konstanz, Germany) or Eurofins Genomics Germany GmbH (Ebersberg, Germany). The primers that were used for sequencing are listed in Table 5.

Furthermore, samples to exclude potential OFF-targets generated by CRISPR-Cas9 were sequenced by Sanger sequencing performed by GATC Biotech AG or Eurofins Genomics Germany GmbH.

2.5.6. RNA isolation

For a subsequent analysis of remaining *SEC62* on RNA level, the respective RNA was extracted from the appropriate cell line. Therefore, an adequate number of cells was harvested following the standard protocol (2.6.2), dry pelletised and blast-frozen in fluid nitrogen. Afterwards, the cell pellets were stored at -80°C until the RNA was extracted. For RNA extraction, ROTI[®]Zol RNA was used following the manufacturer's instructions. The yield and quality of extracted RNA was measured using a NanoDrop[®]ND-1000 UV/Vis.

2.5.7. Reverse transcription of RNA into cDNA

100 ng of extracted RNA per cell line was further processed into complementary DNA (cDNA) using the SuperScript[™] IV Vilo[™] Master Mix with ezDNase[™] enzyme following the manufacturer's instructions. The applied kit reverse transcribes the isolated RNA into cDNA utilizing the enzyme reverse transcriptase. The genomic DNA (gDNA) was removed by ezDNase that is included in the master mix. For verification of the absence of contaminations by gDNA in the respective template RNA, a no reverse transcriptase control (no RT control) was done.

2.5.8. Quantitative real-time PCR

The previously generated cDNA was used to perform a quantitative real-time PCR (qRT-PCR). Therefore, the respective cDNA was analysed by TaqMan[®] assays (Table 11), which were performed in technical triplicates for each used primer pair. After a pre-incubation step for enzyme activation at 95°C for 20 s, 40 circles of 95°C for 1 s and 60°C for 20 s followed.

The relative quantification of *SEC62* was done by normalisation to the used housekeeping gene (β -2-microglobulin, *B2M*). In the next step, the $2^{-\Delta\Delta CT}$ method was applied for calculation of the fold gene expression.

Table 11 Taqman assays for qRT-PCR.

Gene	RefSeq Accession	Sequence
<i>B2M</i>	NM_004048.2	Hs00187842_m1
<i>SEC62</i>	NM_003262.3	Hs00963751_m1

2.6. Cell culture and cell manipulation

2.6.1. Cultivation of mammalian cells

In order to investigate the lymphatic, as well as the haematogenous metastasis of HNSCC due to the establishment of two independent murine xenograft mouse models, the human cell line FaDu (ATCC® HTB-43™) was cultivated at 37 °C and 5 % (v/v) CO₂ in Dulbecco's modified Eagle's medium (DMEM) + GlutaMAX™-I (Gibco®, Life technologies, Carlsbad, CA, USA) supplemented with 10 % (v/v) foetal calf serum (FCS) and 1 % (v/v) penicillin/streptomycin in 75 cm² cell culture flasks.

For the generation of a stable *SEC62* knockout in mammalian cancer cells to investigate a potentially altered migration- and/or proliferation potential the FaDu cell line was used, too. The culture conditions were the same as mentioned in the previous paragraph.

For the generation of *SEC62* knockout line cells were cultured during the selection process in DMEM + GlutaMAX™-I supplemented with 20 % (v/v) FCS, 1 % (v/v) penicillin/streptomycin and 1.5 µg/ml of puromycin in varied sizes of culture vessels.

Subculturing of used FaDu cells occurred at 90 - 100 % confluence of culture flask (1:8 - 1:10 dilution). Before the next experiment cells were subcultivated for 24 h until 48 h dependent on their confluence until cells were in an exponential growth phase when starting the experiment (1:2 - 1:4 dilution). Detachment of the cells was achieved by aspiration of the culture medium, washing the cells with DPBS buffer followed by an incubation of the cells with trypsin-EDTA 0.05 % (w/v) at 37 °C and 5 % (v/v) CO₂ for 7 – 10 min. Afterwards, the enzyme reaction was inhibited by adding FCS-containing culture medium according to the required dilution.

2.6.2. Cell counting and harvesting

For cell seeding or cell inoculation, respectively, the appropriate number of cells was required prior to experiment. Cells were counted using the Countess® Automated Cell Counter (Invitrogen AG, Carlsbad, CA, USA), which additionally allows a monitoring of cell growth and viability. Cells were pre-diluted with trypan blue (Gibco®, Life technologies, Carlsbad, CA, USA) corresponding to the estimated cell number (typically 1:2).

In case of cell harvesting the respective number of cells was separated, centrifuged at 600 rpm in a Bactifuge (Heraeus Holding GmbH, Hanau, Germany) for 5 min or at 3000 rpm for 2 min in an Eppendorf 5415C table centrifuge dependent on the amount of the cell suspension. Afterwards, supernatant was discarded, and the cell pellet was stored at -20 °C until further processing.

2.6.3. CRISPR/Cas9 technology

By using the CRISPR/Cas9 technology which was discovered in 2012 stable knockout cell lines can be generated (Jinek et al., 2012). For this purpose, the wild-type cell line FaDu (2.1.8). The CRISPR/Cas9 technology was discovered as a component of the adaptive immune system of bacteria (Ishino et al., 1987; Barrangou et al., 2007). The two major components are a Cas endonuclease together with a small RNA called sgRNA (single guide RNA) (Jinek et al., 2012). This sgRNA guides the Cas endonuclease due to sequence homology to its specific cutting site within the genome. At this specific cutting site, the endonuclease causes a double strand break (DSB) that has to be repaired (Wyman and Kanaar, 2006; Garneau et al., 2010). The sgRNA consists of two components, the CRISPR-RNA (crRNA) which defines the genomic target locus for Cas-specific cutting and the trans-activating crRNA (tracrRNA) which acts as a scaffold to link the endonuclease and the crRNA (Jinek et al., 2012). The specific crRNA consists of 20 nucleotides that defines the specific cutting site inside the genome by sequence homology. This special sequence has to be in front of a protospacer adjacent motif (PAM) sequence which serves as a binding signal for the nuclease (Mojica et al., 2009; Jinek et al., 2012). This PAM sequence is nuclease-dependant. In the last few years multiple orthologs of endonucleases could be identified from different bacterial species (Kleinstiver et al., 2015; Cebrian-Serrano and Davies, 2017; Hu et al., 2018). These other endonucleases have alternative, distinct species-specific PAM sequences. The most used and first discovered endonuclease is SpCas9 with its 3'-NGG PAM sequence from *Streptococcus pyogenes* (SP) (Jinek et al., 2012). The Cas9 undergoes a conformational change after binding to the target locus to cleave the opposite target DNA strand (Palermo et al., 2017). The specific cutting site of Cas9 lies 3 – 4 nucleotides upon of the PAM sequence that defines the predicted cutting site very specifically (Shah et al., 2013). Due to generated DSBs the cell is forced to activate either non-homologous end joining (NHEJ) or homology-directed repair (HDR) to recondition the targeted DNA strand (Cong et al., 2013; Cho et al., 2014). If no DNA template is provided for restoration, the DSB will be repaired by the most active repair mechanism – the NHEJ. This mechanism is highly rapid but also highly error-prone and can induce insertion- and/or deletion-mutations (indel). These mutations are mostly small (1 – 10 nucleotides) which will call for frameshifts and finally end in an inactive protein or a non-translated mRNA (Figure 10) (Wyman and Kanaar, 2006). The sgRNAs needs to be well-designed because of possible OFF-target effects that could occur in case of a too high sequence homology of the sgRNA beside the real target site.

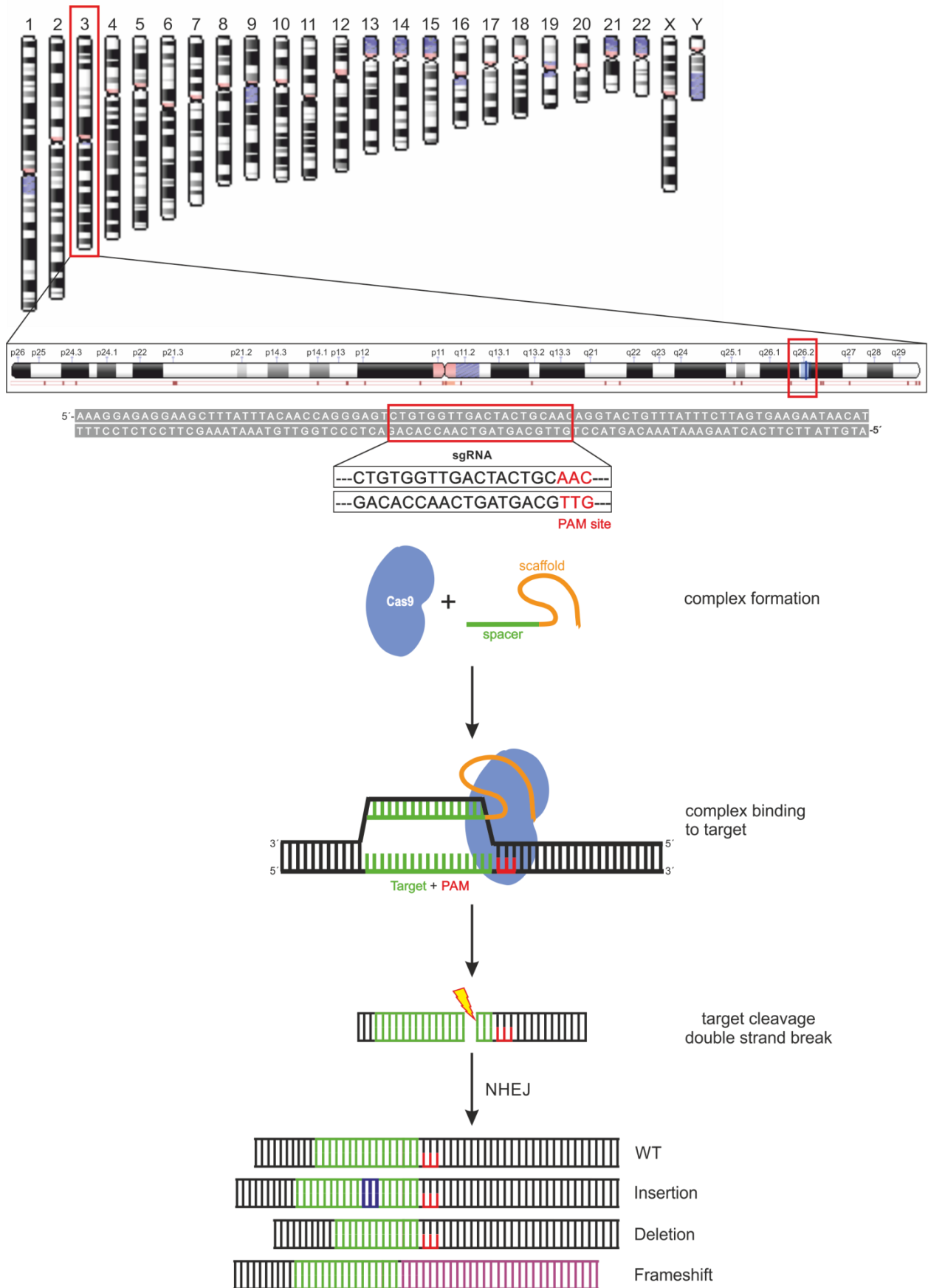


Figure 10 Principle of CRISPR/Cas9 technology: The gene of interest in this study is located on the long arm of chromosome 3 (3q). The exact location is q26.2. At this locus the protein SEC62 is coded which should be knocked-out by using CRISPR/Cas9 technology. The gRNA was chosen in this locus (3'-CTGTGGTTGACTACTGCAAC-5'). First the endonuclease Cas9 has to form its complex with the gRNA. In the next step this complex can bind to the target locus due to sequence homology of the used gRNA. After binding the Cas9-sgRNA-complex undergoes a conformational change which induces the cleavage of the double-strand. This generated break in the double helix has to be repaired either by NHEJ or HDR. The DNA-polymerase will repair the DSB but is very error-prone. The repair results in insertions, deletions, and frameshift mutations and finally in an inactivation of the gene of interest.

can result in unwanted mutations at non-target sites within the whole genome (Shen et al., 2014). Therefore, sgRNAs must be chosen cautiously and also possible OFF-targets have to be checked during clone characterization (Cho et al., 2014; Zhang et al., 2015).

In this work, an already published plasmid was used for CRISPR/Cas9 induced *SEC62*-knockout clone generation (Fumagalli et al., 2016). The sgRNA which is integrated in the plasmid for specific *SEC62* knockout consists of the following nucleotide sequence: 3'-CTGTGGTTGACTACTGCAAC-5'. This sequence was used in different software and/or online tools for OFF-target prediction within the entire genome. One of the used tools is CHOP-CHOP v3 (Labun et al., 2019). Results of the different tools that were used showed a high overlap. All potential OFF-targets within the genome, the number, and location of mismatches are listed below (Table 12).

Table 12 Potential OFF-targets for used gRNA: The listed OFF-targets were predicted using the CHOP-CHOP v3 tool (Labun et al., 2019). The genomic location, the number of potential mismatches as well as the nucleotide sequences including the predicted mismatches are shown. The mismatches are highlighted in the nucleotide sequence.

OFF-targets			
Location	Name of gene	Number of mismatches	Sequence (including mismatches)
Chr13: 98261294	FARP1	2	CTGTGG ^g TGACTAC ^a GCAACTGG
Chr3: 125155143	SLC12A8	3	CTGTGGTTGACTAC ^g G ^g AA ^a TGG
Chr11: 110147122	ZC3H12C	3	CCTGTT ^c CA ^t ITAGTCAA ^a CACAG
Chr15: 81984591	LOC105370922	3	CCAGTTGCA ^a TAGT ^g gACCACAG
Chr16: 68400823	SMPD3	3	CTGTGG ^c TGAC ^g ACTG ^t AACTGG

At the beginning (day 0) of the transfection process, FaDu cells were split in an appropriate amount so that cells were in log-growth-phase two days later. At day 2, 2.5×10^5 wild-type FaDu cells were seeded per well into a 6-well plate. Cells were transfected 24 hours after seeding (day 3) with FuGene® HD (Promega, Fitchburg, WI, USA) as transfection reagent. The used ratio between transfection reagent and plasmid was 4:1 with a plasmid amount of 2 µg. For each well with transfected FaDu wild-type cells also a mock control was included. In wells with mock control all steps were the same, especially the transfection reagent, but there was no plasmid added to cells. The next day (day 4) the selection process was started applying 1.5 µg/ml puromycin

dihydrochloride (Thermo Fisher Scientific Inc., Waltham, USA) to the transfected cells. Only successfully transfected cells which have an active plasmid were able to survive the puromycin dihydrochloride selection process because the used transfection plasmid lentiCRISPR_v2 from the Molinari group contains a puromycin dihydrochloride resistance gene. Since no plasmid was added to the mock control, these cells were dying during the selection process with puromycin dihydrochloride. The selection process was maintained during all the following steps. At day 9 of the transfection experiment, six days after the transfection step, cells were harvested and 1.0×10^4 cells were relocated into a 14.5 cm culture dish. Day 9 was chosen because at this point of time all mock control cells were dead. During this step, cell colonies should start to format. Cell culture medium containing 20 % (v/v) FCS to support proliferation was carefully changed twice per week. When colonies reached a certain size after 6 – 8 weeks of growing, they were isolated from each other. For this purpose of colony harvesting cloning cylinders (Scienceware® cloning cylinders, polystyrene, Sigma-Aldrich Chemie GmbH, Taufkirchen, Germany) were used. For harvesting the colonies, medium was aspirated and colonies were carefully washed with PBS. Now the cloning cylinder was immersed with the lower part into sterile dow corning high-vacuum silicone grease (Sigma Aldrich Chemie GmbH, Taufkirchen, Germany) and put on the colony to isolate it. Hence, colonies were shielded from each other and could be treated with Trypsin-EDTA 0.05 % (w/v) like in a normal cell culture flask. After stopping the detachment process with cell culture medium, the cells of the colony were resuspended and seeded into an appropriate well size, mostly 48-well plates. For better recovery and proliferation, cells were maintained again in cell culture medium with 20 % (v/v) FCS. Medium was changed twice per week. From now on, cells had to proliferate to gain a suitable cell amount for single cell separation. This step took up to three weeks again (week 7-10 since start of the experiment). When a K75 culture flask was confluent cells were seeded into a 96-well plate for single cell separation. For this purpose, cells were seeded in a concentration of 0.5 cells per well. After 24 h each well was analysed by microscopy to investigate the cell number in each well. Wells with more than one cell were excluded of further observation. Wells containing a single cell were further observed and harvested into a 48-well plate when single cells started to proliferate. This step of harvesting a colony which was generated out of one cell was done in weeks 10 up to 13. Now these single cell clones had to proliferate again to get enough cells for cryopreservation. 20 weeks after transfection of FaDu wild-type cells these generated clones were investigated for their SEC62 protein amount using Western Blot (see chapter 2.4) (Figure 11).

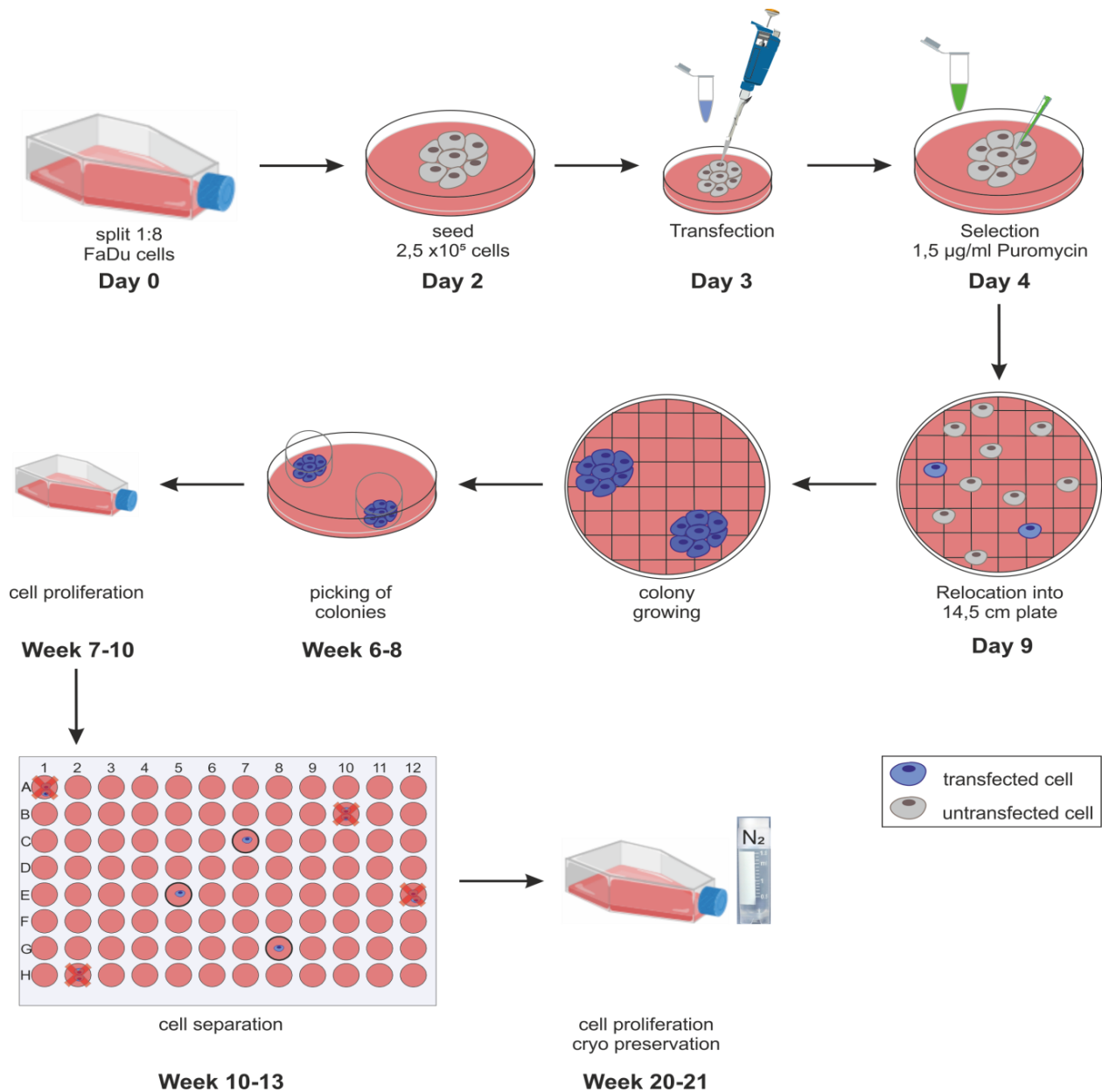


Figure 11 CRISPR/Cas9 transfection workflow of FaDu wild-type cells: At day 0 FaDu wild-type cells were split that they were in proliferation phase at day 2. At day 2 $2,5 \times 10^5$ cells were seeded into a 6-well plate. After 24 h (day 3) cells were transfected using FuGene® HD as a transfection reagent and a CRISPR/Cas9 plasmid. The used plasmid was already published by Fumagalli et al. in 2016. After 24 h (day 4) selection process was started to separate transfected cells from untransfected cells using 1.5 µg/ml puromycin as selection antibiotic. After 5 days cells were relocated into 14.5 cm culture dishes in a concentration of 1.0×10^4 cells. After 6 to 8 weeks colonies were grown, which could be harvested using cloning cylinder for separate colony picking. These colonies had to proliferate for several weeks. In week 10 to 13 after the experiment was started cells were separated for single clone selection by seeding in a 96-well plate in a concentration of 0.5 cell/well. After 7 to 11 weeks of growing, cells were able to be preserved in cryo.

2.6.4. Clone characterisation

Single cell clones which were generated using CRISPR/Cas9 technology had to be investigated for their characteristics especially abundance of the targeted *SEC62* gene,

proliferation-, migration-behaviour as well as for their potential OFF-target effects caused by the Cas9 cutting event.

In the first step SEC62 protein amount was investigated using Western Blot (chapter 2.4). Using this method different protein amounts of SEC62 were detected in various clones. Here, 2 clones with no detectable or only trace amounts of SEC62 residual protein amount were chosen for further experiments and characterisation.

After the first selection of positive clones corresponding with reduced SEC62 protein amount further investigation especially on nucleotide sequence were performed.

2.6.4.1. Next generation sequencing

2 clones which were selected by their reduced SEC62 protein amount were further investigated for their nucleotide sequence using Illumina MiSeq next-generation sequencing (NGS) to reveal the exact genetic event induced by endonuclease Cas9 cutting due to the gene-specific sgRNA. This next-generation sequencing was done in collaboration with Dr. rer. nat. Sascha Tierling (AG Prof. Dr. J. Walter – Genetic/Epigenetics, Saarland University, Saarbrücken). For this purpose, genomic DNA (gDNA) was extracted from each clone using NucleoSpin Tissue kit (Macherey-Nagel GmbH & Co.KG, Düren, Germany). A DNA fragment consisting of 300 basepair (bp) containing the potential cutting site for endonuclease Cas9 within *SEC62* gene locus was amplified using specific primers. The used primers contain universal Illumina adapters attached at the 5' end. Used primer pairs are listed above (Table 5). Using the specific NGS primer pair, a PCR was performed. This PCR was done using a Thermocycler PeqSTAR 96x Universal Gradient (Peqlab Biotechnologie GmbH, Erlangen, Germany) starting with 15 min for enzyme activation at 95°C followed by 35 cycles of 95 °C for 1 min, 60 °C for 1 min 30 s, 72 °C for 45 s and in final a 10 min extension at 72 °C. The protocol in common with used components of the PCR are listed below (Table 13, Table 14). Afterwards, an agarose gel electrophoresis was done to check amplicon size and overall performance of the previous PCR (2.6.4.2).

After the validation of the PCR product, the remaining probe of 25 µl was specifically purified for Illumina MiSeq sequencing using Agencourt Ampure XP beads (Beckman Coulter, Krefeld, Germany) following the manufacturer's instructions. Afterwards, the probes were diluted, pooled, and finally sequenced on the Illumina MiSeq platform.

Alignment of the paired end results were done using CRISPResso2 (Clement et al., 2019). Therefore, the obtained data from the NGS run was uploaded in fastq-file format to CRISPResso2 and the sgRNA sequence together with the amplicon sequence was added. In the next step, the used endonuclease was chosen as well as the sequencing design of paired end reads. After these settings, analysis request was submitted. The obtained results are further described in chapter 3.

Table 13 PCR components: All used components for PCR are listed with corresponding concentrations. Primers are listed in Table 5.

component	concentration
gDNA	25 ng/μl
10X buffer	
MgCl ₂	25 mM
dNTPs	2,5 mM
Primer for/rev	10 μM
HotStar Taq	5 U/μl
MilliQ Water	

Table 14 PCR protocol: All necessary PCR steps. First, used HotStar Taq-polymerase had to be activated. Afterwards 35 cycles of denaturation of DNA, primer annealing, and elongation took place. In the end PCR was terminated with a final step of 72°C for 10 min. PCR products were temporary stored at 4°C.

Step	temperature	time	Cycle
Enzyme activation	95 °C	15 min	
Denaturation	95 °C	1 min	} 35x
Primer-Annealing	depending (60 °C)	1 min 30s	
Elongation	72 °C	45 s	
	72 °C	10 min	
Store	4 °C	∞	

2.6.4.2. Immunofluorescence staining

The generated clones by CRISPR/Cas9 technology were also validated by an immunofluorescence staining for residual SEC62. Therefore, cells were seeded on diagnostic slides (~0.05 x 10⁴). After an attachment phase of 24 h cells were fixed by 4 % PFA. First, cells were washed once with PBS for 3 min at 4°C and afterwards fixed with 4 % PFA at 4°C for 20 min. The fixation was stopped by adding a stop solution after vacuuming off the PFA solution. This step was repeated 4 times for 5 min each at room temperature. Afterwards, cells were permeabilised, and unspecific binding sites were blocked while applying PSS buffer for 1 h at room temperature. Subsequently, the antibody was incubated and prior diluted also in PSS buffer. The specific primary antibody was incubated for 90 min at room temperature. Afterwards, the remaining primary antibody was washed away by PSS buffer twice for 10 min at room temperature. The corresponding secondary antibody was diluted also in PSS buffer in an appropriate dilution and was incubated for 1 h at room temperature. Here, an antibody that is conjugated to an immunofluorescent dye was applied. Due to that starting from this incubation step, all remaining steps must be done in a dark environment. Again, the remaining antibody was washed away by PSS buffer three times for 10 min at room temperature. Afterwards, the stained slides were immersed shortly in an increasing alcohol row (70 %, 80 %, 100 %) and subsequently embedded in DAPI antifade mounting medium. Stained slides were stored at 4°C and analysed by fluorescence microscopy using the Olympus BX61.

2.6.4.3. Agarose gel electrophoresis

To validate the generated PCR amplicon for the right amplicon size and to check the overall PCR performance, e.g. before Illumina MiSeq sequencing, an agarose gel electrophoresis was performed. Depending on the size of the generated DNA fragments, gels between 1 % and 2 % (w/v) agarose were prepared (150 ml TBE-buffer). Agarose was dissolved in TBE-buffer by heating using a microwave for approximately 3 min. Afterwards, 15 µl ethidium bromide was added to fluid agarose solution for DNA staining. Typically, 5 µl of the PCR-product was mixed with 1 µl DNA-sample buffer and loaded on the gel together with 5 µl DNA ladder. The DNA ladder was chosen depending on expected sample size (100 bp-DNA-ladder and 1 kb-DNA-ladder; New England Biolabs GmbH, Frankfurt am Main, Germany). The agarose gel was run for about 2 h at 110 V. All gels were documented using the UV-gel documentation system ImaGo (B&L Systems, Maarssen, Netherland) and were further analysed using ImageJ/Fiji.

2.6.4.4. OFF-target analysis

As mentioned before, potential OFF-targets for the specific sgRNA were predicted using the CHOP-CHOP v3 tool (Labun et al., 2019). In this step, the potential OFF-targets listed in Table 12 should be examined for their existence in the 2 generated clones. Therefore, for each predicted OFF-target a specific primer pair was generated using Primer-Blast from the National Center for Biotechnology Information (NCBI; Bethesda, MD, USA) (Ye et al., 2012). All used primers are listed with their specific annealing temperature and elongation time (Table 15). PCR was performed using PeqSTAR thermocycler. The used PCR conditions and their used components with concentrations are listed in Table 16 and Table 17. After performing the PCR, obtained amplicons were loaded on an agarose gel for confirmation of the reaction. After verification of agarose gel result, PCR products were diluted and sequenced by Sanger sequencing (Sanger et al., 1977). Probes were analysed using Sanger sequencing in collaboration with Eurofins GATC Biotech GmbH (Konstanz, Germany). Obtained results were further analysed using Tracking of Indels by DEcomposition (TIDE) tool (Brinkman et al., 2014). Therefore, chromatogram of each sequencing reaction was uploaded in accordance with naming used endonuclease Cas9 and definition of used gRNA. Results are further described in 3.5.1.1.

Table 15 List of used primer pairs for OFF-target sequencing with corresponding annealing temperature and elongation time.

OFF-target primer	Annealing temperature	Elongation time	PCR product
FARP1	60 °C	1 min 35 s	1303 bp
SLC12A8	58 °C	1 min 51 s	1852 bp
ZC3H12C	58 °C	1 min 4 s	1060 bp
SMPD3	61 °C	39 s	634 bp

Table 16 PCR components: All used components for PCR are listed with corresponding concentrations. Primers are listed in Table 5.

Component	Concentration
gDNA	25 ng/μl
10X buffer	
MgCl ₂	25 mM
dNTPs	2.5 mM
Primer for/rev	10 μM
HotStar Taq	5 U/μl
MilliQ Water	

Table 17 PCR protocol: All necessary PCR steps. First, used HotStar Taq-polymerase had to be activated. Afterwards 35 cycles of denaturation of DNA, primer annealing and elongation took place. In the end PCR was terminated with a final step of 72°C for 10 min. PCR products were temporary stored at 4°C.

Step	temperature	time	Cycle
Enzyme activation	95 °C	15 min	} 35x
Denaturation	94 °C	1 min	
Primer-Annealing	depending	1 min	
Elongation	72 °C	depending	
	72 °C	10 min	
Store	4 °C	∞	

2.6.4.5. Real-time cell analysis

For a non-invasive quantification of cell proliferation, morphology change and attachment quality the real-time cell analysis system xCELLigence (F. Hoffmann-La Roche AG, Basel, Switzerland) was used. The principle of this label-free method lies in the real-time and constant measurement of the electric resistance between electrodes also called impedance. The bottom of each well of a 96-well e-plate (Acea Biosciences, Inc., San Diego, CA, USA) is covered with gold microelectrodes that are covering nearly 70-80 % of the well surface area, representing the functional unit of this system. Within each well of the microtiter plate, the application of an electric potential across two electrodes in the well bottom causes an electron flow from the negative electrode that pass through cell culture medium to deposit onto the positive terminal. The presence of adherent cells onto the electrodes impedes the electron flow mentioned before. The measurable magnitude of impedance is dependent on cell number, size, and shape of the seeded

cells. Impedance caused by electron flow through adherent cells is reported in dimensionless cell index (CI). The used gold electrodes have no known impact on cell behaviour and viability.

Cells were prepared 48 h before the start of the experiment, ensuring that cells were in the exponential growth phase. For blank measurement, 145 μl standard culture medium was pipetted into each well of the used e-plate. After blank measurement, the e-Plate was removed from the xCELLigence unit within the CO_2 incubator and 5.0×10^4 cells per 50 μl were seeded into each well. The microtiter plate was placed back into the xCELLigence unit and cells were allowed to sink onto the bottom of the well within 30 min before the experiment was started. During the experiment, the CI was measured every 15 min. In case of studies to test the effect of different concentrations of thapsigargin and/or trifluoperazine the e-Plate was removed again from the unit within the incubator after 5–5.5 h for agent application. Within these first hours, the CI value rapidly increased because cells sank onto the electrodes and impedance increased. 5 μl of the appropriate agent was added to each well before the plate was replaced again. Now, the experiment was restarted for the next 120–148 h. During this time cells were allowed to proliferate, resulting in a continuous increase in CI. In this system, when cells have reached a 100 % confluence CI will result in a plateau phase until the CI will decrease because of cell death. This assay results in a quantitative read-out of cell number, cell proliferation rate dependent and independent of agent concentration, cell size and shape of cells.

The obtained data were analysed using the RTCA xCELLigence software (Acea Biosciences, Inc., San Diego, CA, USA).

2.6.4.6. Migration assay

For analysis of potential differences in migration behaviour between FaDu wt cells and clones generated by CRISPR/Cas9 technology, a migration assay was performed using the FluoroBlok™ 24-multiwell insert system (Corning, Inc., NY, USA). This system is based on the principle of a Boyden chamber and consist of a light-tight polyethylene terephthalate (PET) membrane at the bottom of the used cell culture inserts that efficiently blocks light transmission within 490-700 nm (BOYDEN, 1962). Cells are forced to migrate due to a chemotactic stimulus of different FCS concentrations within the insert and the well. When cells migrate through the pores of the PET-membrane (8.0 μm) they can be fixed after a certain time of migration at the bottom of the insert and be labelled by fluorescent dyes.

To perform the assay, 1.4 ml cell culture medium with 10 % (v/v) FCS was added in each well of the companion plate (Falcon® Cell culture Companion Plates – 24 well; Corning, Inc., NY, USA) before 5.0×10^4 cells were seeded into the insert containing 500 μl deficient cell culture medium (0.1 % (v/v) FCS). This gradient between 0.1% (v/v) FCS in the insert and 10 % (v/v) FCS in the well bottom provides a strong chemotactically stimulus for the seeded cells to migrate

through the membrane. Cells were allowed to migrate for 72 h before the assay was stopped. Therefore, inserts were washed using PBS before cells were fixed at the bottom of the insert using methanol for 10 min at -20°C. Afterwards the fixed cells were washed again with PBS before migrated cells were stained with 4',6-Diamidin-2-phenylindol (DAPI, 1:1000; Sigma-Aldrich Chemie GmbH, Taufkirchen, Germany) for 7 min at RT. After the last washing step with PBS, the assay can be analysed using an inverse fluorescence microscope (Nikon Eclipse TE 2000-S microscope, Nikon Corporation, Tokio, Japan). From each well three representative images were taken using NIS elements AR 3.0 software (Nikon Corporation, Tokio, Japan) and further analysed by the same software for cell counts.

2.6.4.7. Live cell calcium imaging

Before the start of the live cell Ca²⁺ imaging experiments, cells were seeded in an appropriate amount on poly-L-lysine coated coverslips (FaDu wt: 0.3 x10⁶; clone1: 0.3 x10⁶; clone2: 0.35 x10⁶) and were cultured in a humidified environment at 37°C with 5 % CO₂ for further 24 h. After 24 h of cultivation medium was discarded and cells were loaded with 4 μM Fura-2 AM for 20 min at room temperature in 1 mM Ca²⁺ containing solution (140 mM NaCl, 4 mM KCl, 1 mM MgCl₂, 1 mM CaCl₂, 10 mM Glucose, 10 mM HEPES, pH 7.4). The principle of the cytosolic Ca²⁺ amount measurement ([Ca²⁺]_{cyt}) was previously described by Lang et al. (Lang et al., 2011b). Before the measurement was started the 1 mM Ca²⁺ containing staining solution was replaced by Ca²⁺-free solution (140 mM NaCl, 4 mM KCl, 1 mM MgCl₂, 0.5 mM EGTA, 10 mM Glucose, 10 mM HEPES, pH 7.4). Using an inverted microscope (Axiovert Oberver D1, Carl Zeiss, Jena, Germany) imaging experiments were performed in combination with an illumination system (Lambda DG-4, Sutter Instrument, Novato, CA, USA), a dual CCD camera (ORCA-D2, Hamamatsu Corporation, Bridgewater Township, NJ, USA) and the data acquisition VisiView software (Visitron Systems GmbH, Puchheim, Germany). The Fura-2 AM intensities were measured by alternated excitations at 340 nm (340/26 BrightLine HC, AHF analysentechnik AG, Tübingen, Germany) and 387 nm (387/11 BrightLine HC, AHF analysentechnik AG, Tübingen, Germany). The emission was detected at 510 nm (ET510/80 m Chroma, AHF analysentechnik AG, Tübingen, Germany). For image acquisition of Fura-2 AM, both signals were recorded every 3 s with an exposure time of 10 ms and a 2 x 2 binning. Concerning the Fura-2 AM signals, background intensities at 340 nm and 387 nm were subtracted from recorded single cell ratios (R). To measure the maximal fluorescence ratio (R_{max}) 25 mM external Ca²⁺ was added in the presence of 10 μM ionomycin (IONO). For measurement of the minimal fluorescence ratio (R_{min}) 20 μM IONO in the presence of 15 mM EGTA was used. Using the equation:

$$[Ca^{2+}]_{cyt} = \beta K_{ad} \cdot (R - R_{min}) / (R_{max} - R) \quad (\text{Eq. 1})$$

measured R values were converted into [Ca²⁺]_{cyt}. βK_{ad} represents the specific apparent Ca²⁺

dissociation constant for Fura-2 AM, as previously described by Pick et al. (Pick et al., 2021). All substances (TFP, TG, IONO) for treatment and measurement of their impact on cellular Ca^{2+} levels were prepared in stock solutions dissolved in DMSO. Just before the substances were added for experimental measurements, stock solutions were diluted to a 2x greater concentration and applied to the bath solution in a further dilution of 1x. In the recording chamber, the final DMSO concentration was never larger than 0.1 % DMSO (v/v). This DMSO concentration was also used for control measurements. Based on the analysis of the background noise of the Fura-2 AM signals, differences in $[\text{Ca}^{2+}]_{\text{cyt}}$ changes that were below 25 nM were considered to be statistically not significant.

All live cell Ca^{2+} imaging experiments were performed by Tillman Pick (Institute of Experimental and Clinical Pharmacology and Toxicology, Saarland University).

2.6.4.8. RNA sequencing

RNA sequencing was done in cooperation with GENEWIZ Germany GmbH in Leipzig. Therefore, three independent fresh frozen cell pellets consisting of 2.0×10^6 cells were shipped on dry ice to GENEWIZ Germany GmbH. Upon arrival, the company extracted the total RNA from the obtained cell pellets and checked for quantity by Qubit RNA IQ Assay. The RNA integrity was checked by an Agilent Bioanalyzer. For sufficient RNA integrity, the RNA integrity number (RIN) should be above 8. The measured RIN of all samples was about 10. All samples contained sufficient and qualitatively usable RNA. Within this project, the mRNA transcriptome of FaDu wild-type cells, as well as of generated *SEC62*-ko clones should be analysed. Therefore, after the measurement of the RNA integrity and RNA quantity, the mRNA was enriched by poly(A) selection. This step was also done for mRNA enrichment and mRNA library preparation. Within this step, the enriched mRNA was converted into cDNA that was provided with specific sequencing adaptors and barcodes for a subsequent identification after NGS. The NGS was performed by an Illumina NovaSeq™ 6000 as a short-read sequencing. Short-read sequencing is useful for the quantification of a relative abundance of transcripts, as well as the identification of rare transcripts. Each cDNA fragment was sequenced by paired-end sequencing with a read configuration of 2x150 bp. This resulted in ~20 million reads per sample that were further analysed. Furthermore, the data analysis was done on the one hand by GENEWIZ Germany GmbH and on the other hand by myself using Perseus software (version 1.6.15.0) (Tyanova et al., 2016). First, the obtained raw data was pre-processed by trimming of the reads to remove the adaptor sequences and reads of low quality. Therefore, Trimmomatic v.0.36 was used. In the next step, the trimmed reads were aligned to the human reference genome (*Homo sapiens*, GRCh38) using STAR aligner v.2.5.2b to discover the genomic origin of the analysed RNA molecules. featureCounts was used for calculation of unique gene hit counts that were summarised in an

annotation file. Hereafter, the gene hit counts were transformed into TPM values (transcripts per kilobase million) that were used for further analysis using Perseus software and edgeR for a differential expression analysis. Here, the different cell lines were compared within the specific gene expressions. Genes that show a p-value <0.05 after a p-value adjustment by Benjamini-Hochberg in combination with an absolute \log_2 fold change of $>-2/2$ were called as differentially expressed genes. In addition, a gene ontology analysis was performed by using different web-based tools. The detailed steps for analysis of differential expressed genes as well as for gene ontology were described in the corresponding result section (3.5.1.2).

2.7. Statistics

Preliminary analysis of the raw data was done in Excel 2022 (Microsoft Corporation, Redmond, WA, USA). For statistical analysis and the graphical presentation of raw data the software programs OriginPro 2022 (OriginLab, Northampton, MA, USA), SigmaPlot 11.0 (Systat Software GmbH, Erkrath, Germany), and CorelDRAW X6 (Corel Corporation, Ottawa, Canada) were used. The generated data sets were tested for normal distribution according to D'Agostino and Pearson. However, since a normal distribution can normally be assumed in the context of biological data, most of the data were tested for significance using a two-sided, unpaired t-test. For this purpose, the data were previously tested for homogeneity of variances using an F-test. Differences between several independent samples were analysed using univariate, one-way analysis of variance (one-way ANOVA) followed by a test for a linear trend or Tukey's posthoc test. For linear correlation analysis, the Pearson-R was used to identify similar patterns. In case of unequal variance of the tested data sets, a Welch correction was applied. If, contrary to expectations, the data were not normally distributed, a Mann-Whitney-U-test was applied. A value of 0.05 was set as the significance level (α) whereby p-values smaller than 0.05 were considered as significant results. The p-values are displayed exactly unless <0.001 .

3. Results

3.1. Impaired migration of HNSCC cells by TG and TFP application

The results of the publication by Linxweiler et al. 2013 serve as a general basis for this work. Within this publication and also in previously and subsequently published data strong hints were found that *SEC62* has a potential oncogenic function independent of the tumour entity (Greiner et al., 2011a, 2011b; Wemmert et al., 2016; Bochen et al., 2017; Müller et al., 2021). Therefore, a knockout of *SEC62* may have a major impact on the general process of tumour cell migration and metastasis formation. The focus in this thesis lies on a functional knock-down of *SEC62* to inhibit tumour cells of the head and neck region to form lymphatic metastasis to the cervical lymph nodes as well as distant metastasis to the lung.

First, the anti-metastatic and anti-proliferative effect of two substances, TG and TFP, should be proved for their effectiveness on head and neck tumour cells. For that reason, a migration assay using TG and TFP treatment on FaDu wild-type (wt) cells was performed. Therefore, cells were seeded into FluoroBlok™ inserts and were allowed to migrate for 72 h. The basic principle of this assay relies on a boyden chamber where a concentration gradient of FCS served as a chemoattractant to urge the cells to migrate through the membrane of the FluoroBlok™ insert (BOYDEN, 1962). After 72 h cells were fixed by methanol, stained with DAPI, and analysed by a semi-automatic process. The normalised number of migrated cells are shown in Figure 12A. Treatment of FaDu wt cells with 0.1 % DMSO served as a control. The shown mean of migrated cells is based on 4 biological replicates. Each biological replicate included a technical duplicate. In each technical duplicate 3 images were taken for calculation of how many cells had migrated through the 8 µm pores. The treatment of FaDu wt cells with 5 nM TG led to a migration inhibition of almost 50 % ($\text{mean}_{5\text{nM TG}} = 0.50978 \pm 0.32612$). The treatment of FaDu wt cells with 7.5 µM TFP led to a migration inhibition of 38 % ($\text{mean}_{7.5\mu\text{M TFP}} = 0.62547 \pm 0.27579$). The combination of both substances inhibited the migratory potential of FaDu wt cells almost completely ($\text{mean}_{5\text{nM TG} + 7.5\mu\text{M TFP}} = 0.01013 \pm 0.00354$). Also, Western Blot analysis of FaDu wt cells that were treated for 72 h with 5 nM TG and/or 7.5 µM TFP was done targeting different ER stress and EMT markers. Here, a significant upregulation of BiP ($\text{mean}_{\text{BiP}} = 2.26808 \pm 0.2639$, $p = 0.011$), SNAIL-SLUG ($\text{mean}_{\text{SNAIL-SLUG}} = 1.46693 \pm 0.21868$, $p = 0.02709$), and E-cadherin ($\text{mean}_{\text{E-cadherin}} = 3.60483 \pm 2.02457$, $p = 0.0476$) expression was obvious dependent on TG treatment. No upregulation of *SEC62* protein level was detectable under TG treatment. In case of TFP treatment no significant upregulation of any of the aforementioned proteins was obvious. On the other hand, the combination of 5 nM TG and 7.5 µM TFP led to a similar upregulation of BiP but slightly lower compared to solo TG administration ($\text{mean}_{\text{BiP}} = 1.78766 \pm 0.46488$, $p = 0.0117$). Regarding *SEC62* expression there was a visible trend

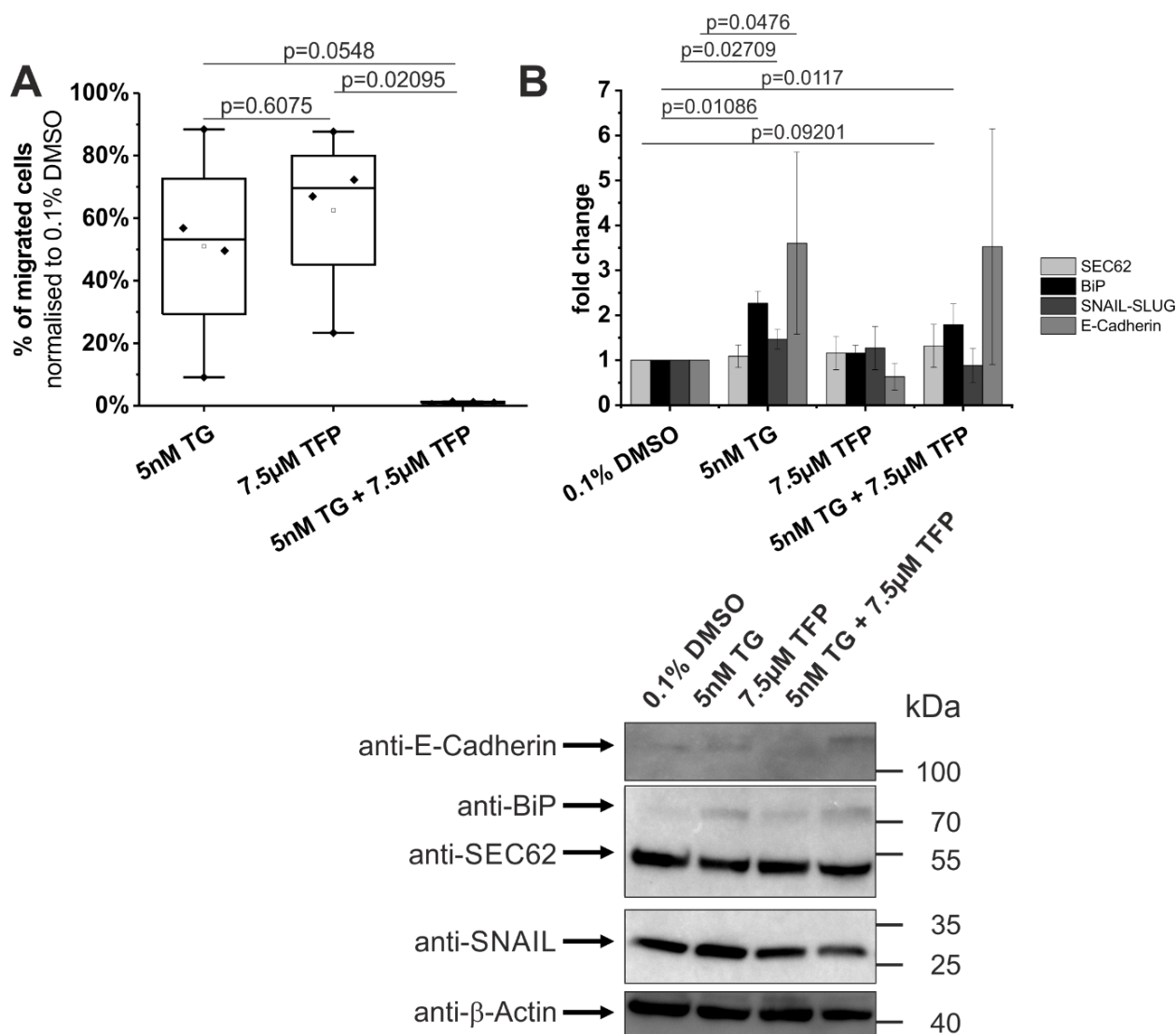


Figure 12 Impaired migration of FaDu wt cells by TG and TFP treatment: (A) FaDu wt cells were seeded in a FluoroBlok™ migration insert. Cells were allowed to migrate through 8 µm pores for 72 h before migrated cells were methanol fixed and stained by DAPI. All migrated cells were semi-automatically counted based on 3 images of each technical duplicate. Shown is the normalised mean of 4 biological replicates. (B) Western blot analysis of E-Cadherin, BiP, SEC62 and SNAIL-SLUG expression levels after TG and TFP treatment for 72 h of FaDu wt cells in relation to β-Actin expression. Shown is the calculated mean fold change for E-Cadherin, BiP, SEC62 and SNAIL-SLUG protein expression of 4 biological replicates.

for a slight upregulation, but significance was not reached ($\text{mean}_{\text{SEC62}}=1.31907\pm 0.47743$, $p=0.09201$).

3.2. Establishment of a murine orthotopic lymphatic metastasis model

One of the main goals of this work was to investigate the metastasis- and proliferation-inhibiting effect of two substances which showed promising anti-metastatic effects in *in vitro* studies. For this purpose, suitable animal models were needed for the two main forms of tumour metastasis in humans – the lymphatic and haematogenous metastasis.

First, a model for the lymphatic metastatic spread of human HNSCC cells in mice was established. During this orthotopic xenograft model establishment several steps had to be tested

until the final protocol was generated and provided reproducible results. In general, the injection site as well as the injectable cell amount were the two major challenges which were addressed in this thesis.

3.2.1. Tumour cell injection into the base of the tongue led to shorten overall survival

The process of model establishment was started with BALB/cAnNRj-Foxn1nu mice (n=6) which were injected into the base of their tongues. Therefore, mice were anaesthetised (100 mg/kg ketamin, 12 mg/kg xylazin) and positioned with a wide opened mouth on a heating plate to avoid hyperthermia during the cell inoculation process. The tongue was gently pulled out using a swab and carefully fixed at the tip of the tongue by using an anatomical forceps. For the first round a cell amount of 1×10^5 FaDu wt cells were injected and were therefore prepared by resuspending and loading into a Hamilton syringe with a cone tip. The syringe was inoculated into the bottom of the tongue and cells were injected near under the surface of the mucosa. Cells were inoculated in a volume of 5 μ l. To avoid a potential reflux of inoculated tumour cells the injection channel was carefully fixed using a forceps for a few seconds after the injection. After cell inoculation all animals received a subcutaneous analgesics depot (5 mg/kg carprofen). Two weeks after the mice received the HNSCC cells an ultrasound examination of the throat region was performed in collaboration with Dr. med. vet. Christina Körbel (Institute of Clinical and Experimental Surgery, Saarland University, Homburg). The aim of this examination was to monitor the formation as well as the growth behaviour of the originating metastases in the cervical lymph nodes. Unfortunately, this method was not suitable to detect the metastases due to their small volume and limited ultrasound resolution so that this follow up measurement was not performed in future establishing rounds. After 5 weeks (day 33) of observation 3 of 6 animals lost 20 % of their highest weight, which necessitated a sacrifice of all 6 inoculated animals (Figure 13A). The histological examination of excised tongues and cervical lymph nodes showed a 100 % take rate in primary tumours of the tongue as well as a 50 % take rate of detected lymph node metastases (Figure 13B). Interestingly, 3 mice which were sacrificed because of their rapid loss of weight showed no metastases whereas the remaining 3 animals which had an even constant till rising weight all showed metastatic spread. The primary tumours grew in the base of tongue, which led to impairments in deglutition and difficulties concerning the food intake.

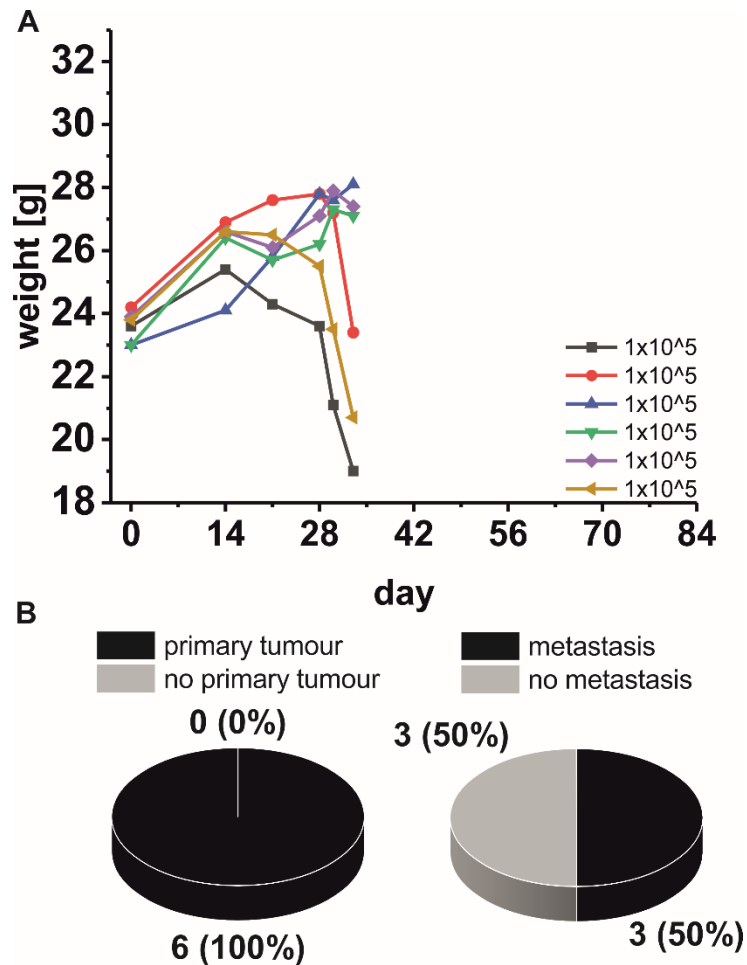


Figure 13 Summary of the first lymphatic metastasis establishing round: (A) Weight history of all mice (n=6) that were injected with tumour cells. The observation period started at the inoculation day (day 0) until individual sacrifice day. **(B)** Analysis of primary tumour take rate as well as metastasis take rate in all injected mice.

3.2.2. Tongue tip has second most lymphatic vessels - decision for injection side

Since the previous experiment led to a short overall survival of mice and could only show a minor metastasis rate of 50 % when tumour cells were injected into the base of the mouse tongue an immunofluorescence staining was done to get a better knowledge about the localisation of lymphatic vessels as a key element of lymphatic metastasis formation. The immunofluorescence staining was performed on 5 native tongues that were not previously injected with tumour cells. The markers that were further examined were CD31 to visualise the vessels in general and LYVE-1 to visualise specifically the lymphatic vessels. The immunofluorescence staining was kindly performed by Janine Becker (Institute for Clinical and Experimental Surgery, Saarland University, Homburg). Stained slides were examined by using an Olympus BX61 microscope in combination

with the ISIS software. Here, images of 10 areas distributed over the whole tongue were taken and examined for LYVE-1 and CD31 positive cells (Figure 14A).

The areas marked in the same colour were subsequently combined to form 5 main areas that were further analysed: base (grey), tip (red), inside (yellow), top (blue) and bottom (orange). The combined amount of positive stained cells in each analysed area are shown in Figure 14A. Analysing the means of LYVE-1 and CD31 positive cells in each main area display that both cell types are most equally distributed in the base of the tongue (Figure 14B). Despite the amount of LYVE-1 positive cells is the highest in the tongue base an alternative injection site was needed

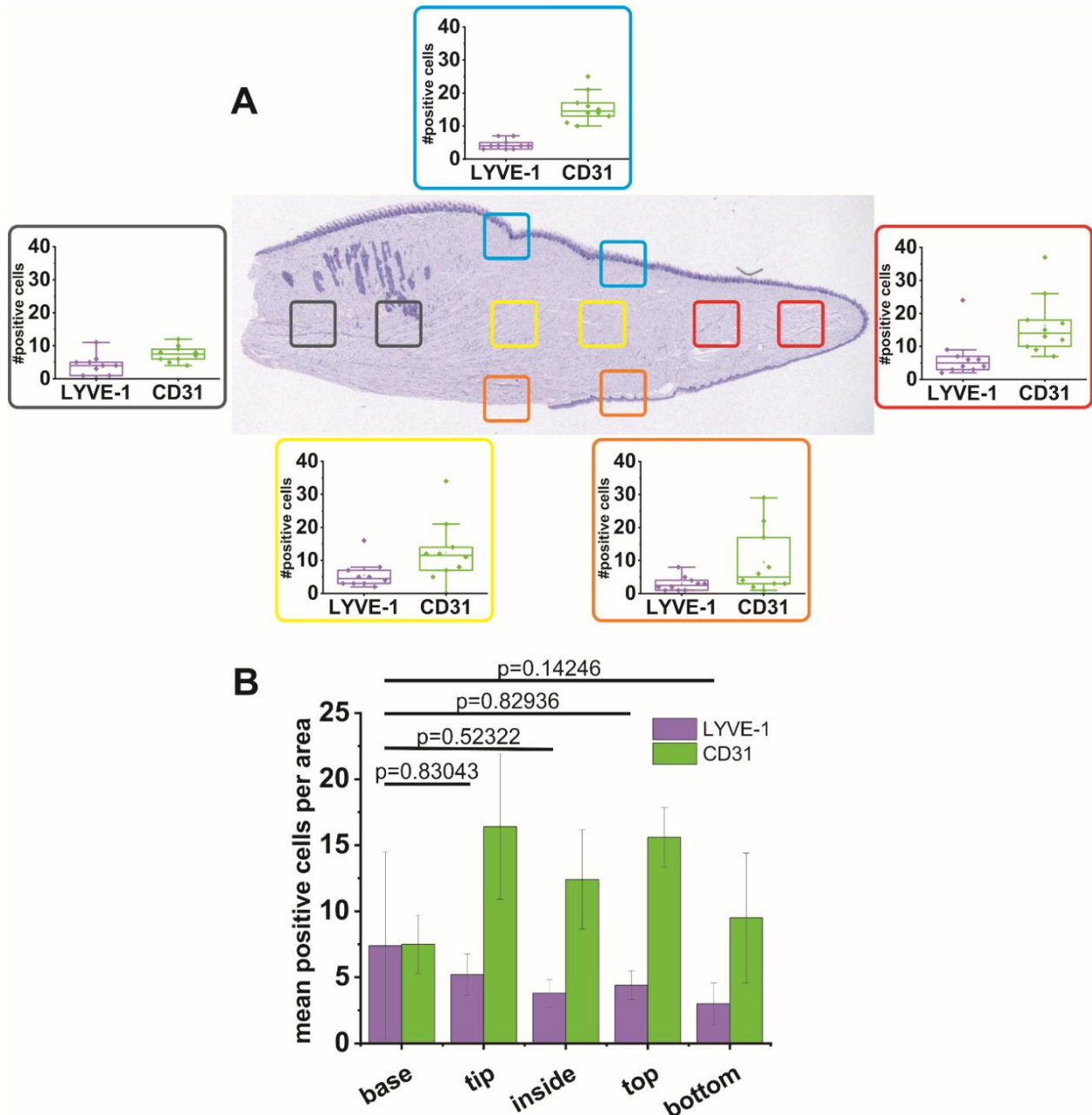


Figure 14 Distribution of LYVE-1 and CD31 positive cells: Analysis of the immunofluorescence targeting LYVE-1 and CD31. Analysed were 5 native tongues without previous tumour cell injection procedure. Images of the marked regions were made and LYVE-1 and CD31 signals were counted. Because counted cell numbers were not normally distributed a Mann-Whitney U test was performed. Immunofluorescence staining was kindly performed by Janine Becker (Institute for Clinical and Experimental Surgery, Saarland University, Homburg).

especially because of the short overall survival of mice injected into this site. The second most abundant site of LYVE-1 positive cells is the tip of the tongue. Therefore, this injection site was chosen for future experiments.

3.2.3. Tumour cell injection into the tongue tip led to prolonged overall survival

In the second establishing round HNSCC cells were inoculated into the tip of the tongue to evaluate if the injection site has an impact on originating cervical lymph node metastases. Additionally, the inoculated cell number was reduced to prolong the general observation time as well as to elongate the time for metastatic spread from the primary tumour in the tip of the tongue to the cervical lymph nodes. Therefore, again BALB/cAnNRj-Foxn1nu mice (n=6) were used. A group of 3 animals received 5×10^4 tumour cells whereas the other group of 3 animals received 8×10^4 tumour cells. The whole tumour cell injection procedure was performed as described in the previous round (chapter 3.2.1). Here, the observation time was much prolonged compared to the first establishing round (1×10^5 injected tumour cells). Mice that received just half of the tumour cell amount of the previous round were observed for almost 11 weeks (day 76) without any sign of impairment (Figure 15A). The body weight was still constant at the end of the experiment. Finally, the applied observation period was reached so that animals had to be sacrificed at this timepoint. The histological examination revealed that the injected tumour cell number of 5×10^4 cells was too low so that no primary tumour could be detected in any of the 3 injected animals. Without a primary tumour also no metastasis formation could be observed (Figure 15B). Concerning the animals that were inoculated with 8×10^4 cells into the tip of their tongues the observational period had to be stopped after about 7 weeks (day 48 till 56) due to more than 20 % loss of weight (Figure 15A). In that group 100 % of animals formed a primary tumour in the tip of the tongue, additionally 2 animals also had a second tumour formation at base of the tongue comparable to animals that were inoculated with tumour cells at the tongue base. All the three mice with 8×10^4 injected HNSCC cells also developed metastases in their cervical lymph nodes (Figure 15C).

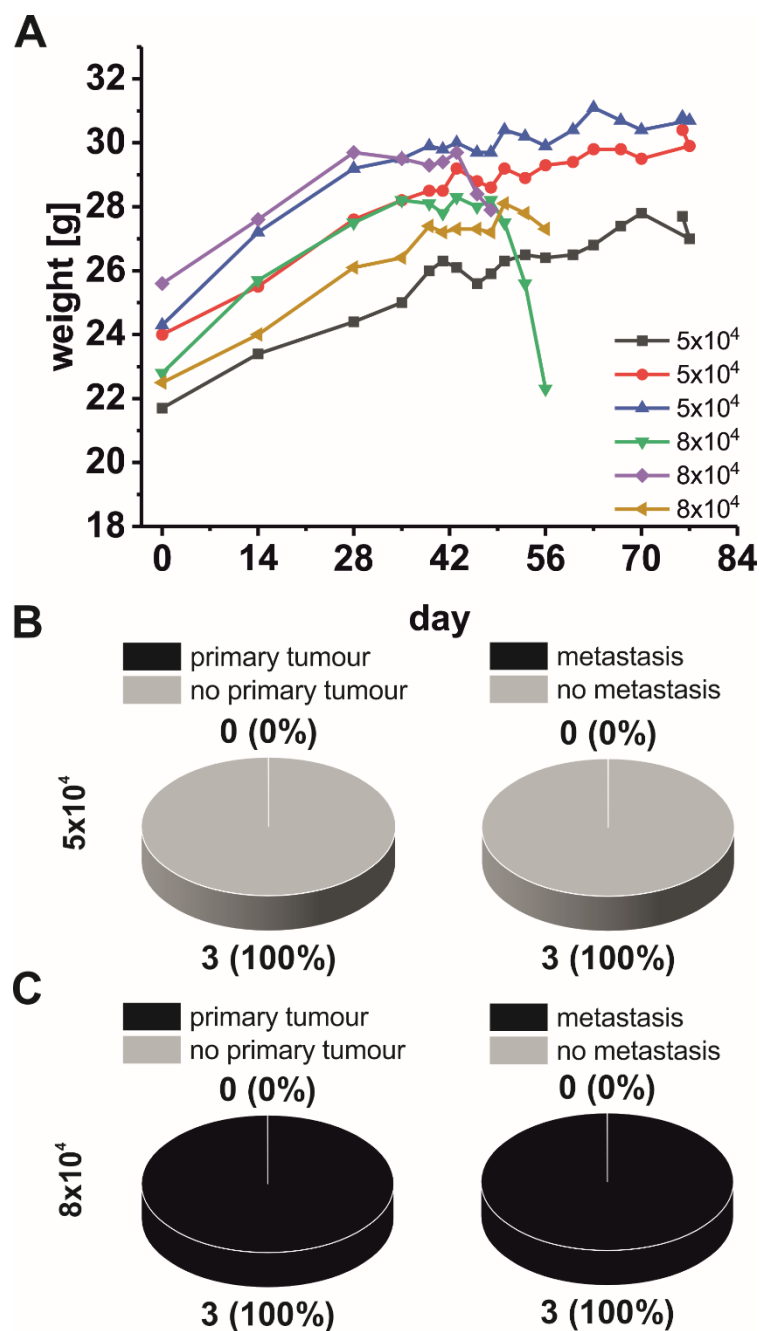


Figure 15 Summary of the second lymphatic metastasis establishing round: (A) Weight history of all mice ($n=6$) that were injected with different amounts of tumour cells. The observation period started at the inoculation day (day 0) until individual sacrifice day. **(B)** Analysis of primary tumour take rate as well as metastasis take rate in all injected mice.

3.2.4. Impact of injection side within the tongue tip on tumour growth and metastatic spread

In the third establishing round, utilized BALB/cAnNRj-Foxn1nu mice were grouped into left and right tongue tip injection sites ($n_{\text{left}}=3$; $n_{\text{right}}=5$) and received 8×10^4 HNSCC cells. 3 animals received the tumour cells into the left site of the tongue, whereas 5 animals received tumour cells

into the right site of the tongue tip. The imbalance between both groups emerged because 2 animals which were injected into the left site of the tongue died during the anaesthesia without a recognisable connection to the inoculation procedure. Due to premature weight loss one animal had to be sacrificed after 6 weeks (day 44). The overall sacrifice day after 7 weeks (day 51) was determined by 2 animals that started to lose weight (Figure 16A). All three animals that received the tumour cells into the left half of the tongue tip developed a primary tumour at the inoculation site. All these animals also developed metastases in their cervical lymph nodes within 7 weeks of observation (Figure 16B). Tumour cells that were inoculated into the right site of the mouse tongue tip developed a primary tumour in 3 of 5 animals (Figure 16C). One of these 3 animals bearing a primary tumour also developed a metastasis in a cervical lymph node. The animal that was premature sacrificed because of weight loss belonged to the right site injection group of animals. This mouse developed a primary tumour but formed no metastases. Noticeable, all generated

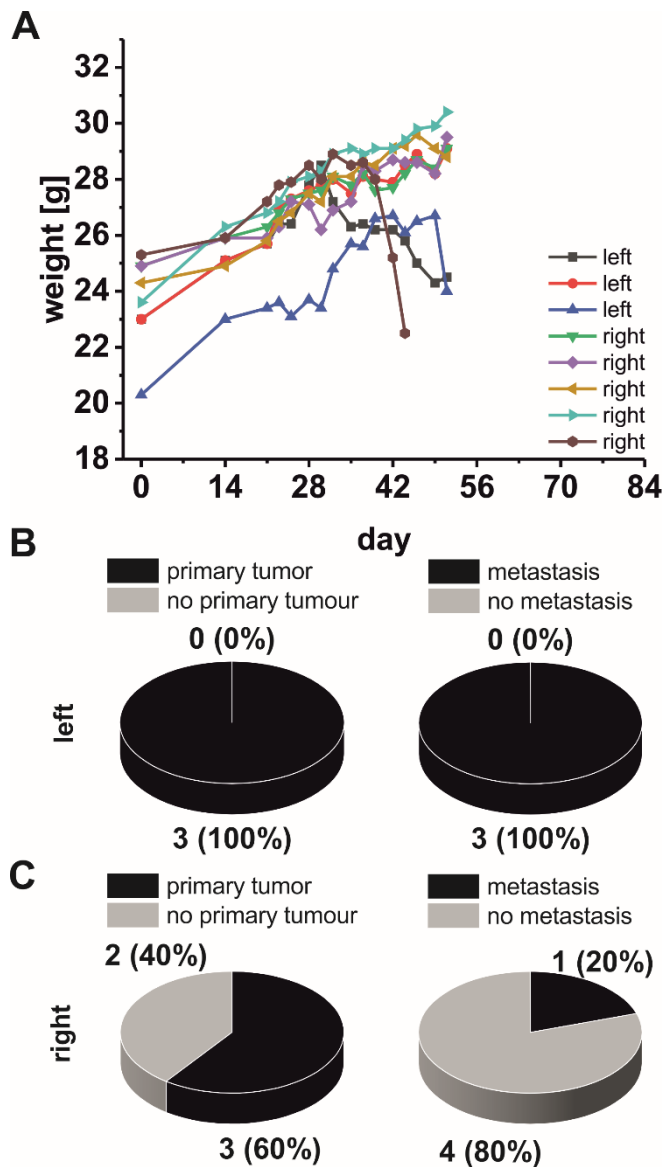


Figure 16 Summary of the third lymphatic metastasis establishing round: (A) Weight history of all mice (n=8) that were injected with 8×10^4 cells at different sites of the tongue tip. The observation period started at the inoculation day (day 0) until individual sacrifice day. **(B)** Analysis of primary tumour take rate as well as metastasis take rate in all injected mice.

metastases in the group of left injected mice showed their metastases in the left sided lymph nodes. In case of right injected mice the animal developing metastases also showed its metastases in the right sided cervical lymph nodes.

3.2.5. Increasing cell amount led to 100 % primary tumour growth in combination with 60 % metastatic spread

In the fourth round of establishing a mouse model for lymphatic metastasis formation the cell amount was increased again with intention to enhance the take rate of lymph node metastasis. In this section 1×10^5 tumour cells were inoculated into the left site of the tongue tip. Again BALB/cAnNRj-Foxn1nu mice were used (n=10). The animals reached with the higher tumour cell amount an observation time of about 6.5 weeks (day 46) (Figure 17A). Only one animal was sacrificed already after 4 weeks (day 34) because of 20 % weight loss. Of the remaining 9 animals, 2 started to lose weight after 5.5 till 6 weeks of observation that was determining the sacrifice day for all remaining animals for better comparability. The histological analysis showed a 100 % take rate for primary tumour development (Figure 17B). 2 animals showed a further primary tumour located in the base of the tongue in addition to a primary tumour located in the tongue tip at the injection site, another 2 animals showed only tumours of the tongue in its base and no tumour cells in the tongue tip. For metastasis formation 6 of 10 animals showed metastatic spread into cervical lymph nodes (Figure 17B). 50 % of detected metastases were in the right cervical lymph nodes, whereas 16.6 % developed in the left sided cervical lymph nodes. 33.3 % of detected metastases were located bilaterally located.

3.2.6. Doubling cell amount has no impact on metastasis formation in cervical lymph nodes

In the fifth round of establishing a mouse model for lymphatic metastasis formation a doubled cell amount compared to the previous round was applied. In this section 2×10^5 tumour cells were inoculated into the left site of the tongue tip. Again BALB/cAnNRj-Foxn1nu mice were used (n=10). The animals reached with the higher tumour cell amount an observation time of about 6 weeks (day 44). 1 animal was sacrificed because a 20 % loss of weight after 5 weeks (day 37) of observation. The next mouse started to lose weight after 5.5 weeks and was sacrificed at day 42. This mouse determined the sacrifice of all remaining animals that were sacrificed after 6 weeks (day 44) (Figure 18A).

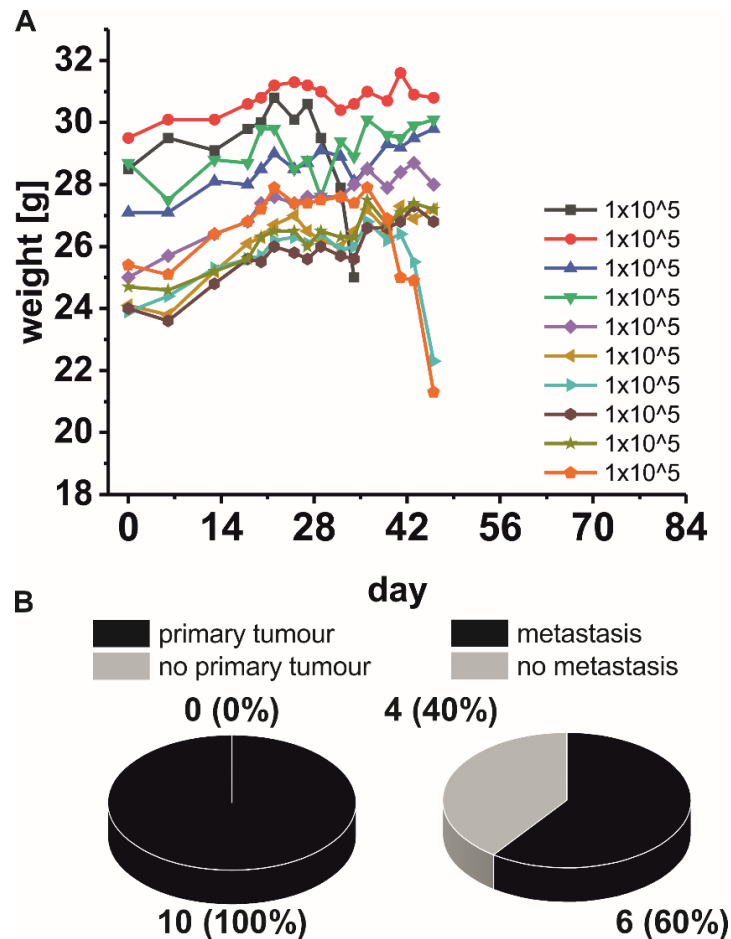


Figure 17 Summary of the fourth lymphatic metastasis establishing round: (A) Weight history of all mice (n=10) that were injected with 1×10^5 tumour cells at the tip of the tongue. The observation period started at the inoculation day (day 0) until individual sacrifice day. **(B)** Analysis of primary tumour take rate as well as metastasis take rate in all injected mice.

After the histological examination 9 of 10 animals showed a primary tumour within the tongue whereof 5 animals showed the tumour only in their tongue tip. 3 animals showed primary tumours in the tip as well as in the tongue base and 1 animal had its primary tumour only in the base of the tongue. 5 of 10 animals display metastatic spread into cervical lymph nodes. In case of 2 animals, metastases were detected in the lymph nodes located on the right side whereas 3 animals displayed metastases bilaterally.

3.2.7. Reproducibility of the new established model with another mouse strain

In the sixth round of establishing a mouse model for lymphatic metastasis formation the used mouse strain was changed. Here, NOD.CB17/*Prkdc*^{scid/scid}/Rj mice were used (n=10) to confirm the efficiency of the established model as well because of a better tolerability of later applied anti-metastatic substances. Because the high cell amount of 2×10^5 tumour cells gets no improvement in metastasis take rate but slightly shortened the observation time in this round again 1×10^5

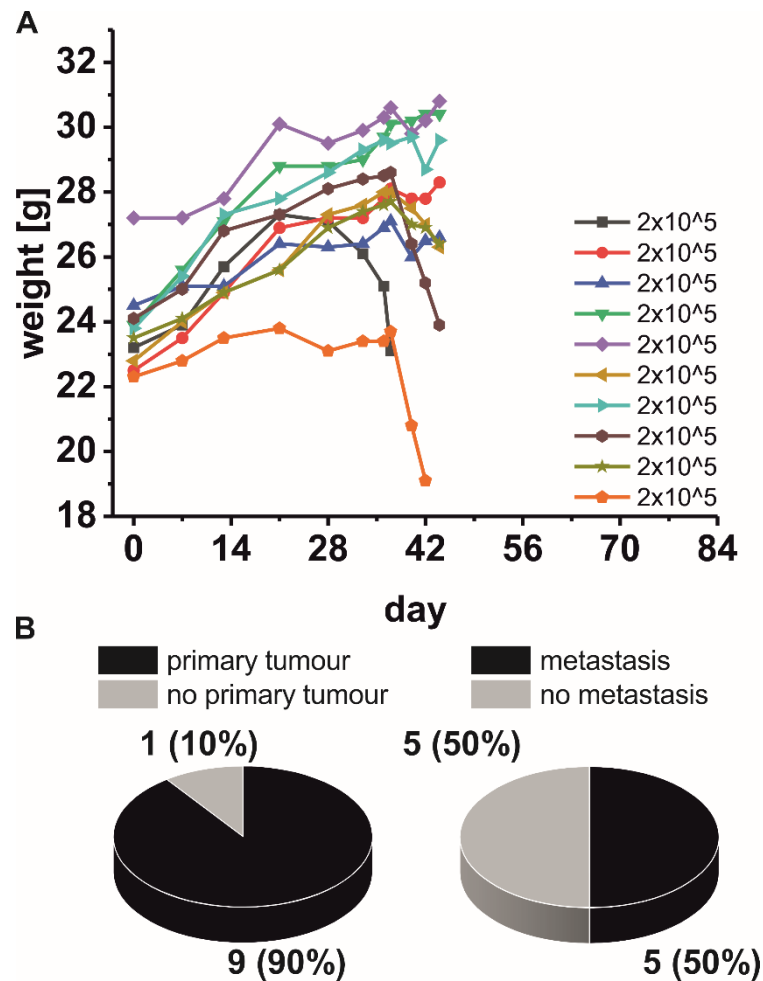


Figure 18 Summary of the fifth lymphatic metastasis establishing round: (A) Weight history of all mice ($n=10$) that were injected with 2×10^5 tumour cells at the tip of the tongue. The observation period started at the inoculation day (day 0) until individual sacrifice day. **(B)** Analysis of primary tumour take rate as well as metastasis take rate in all injected mice.

tumour cells were inoculated into the left sided tip of the tongue. The animals were observed for 6 weeks (day 44) until sacrifice because at least 3 animals started to lose weight (Figure 19A). The histological examination of excised tongues and lymph nodes revealed that all animals developed a primary tumour in the tongue. For lymph node metastasis formation 50 % of all animals showed tumour cells in the cervical lymph nodes. 3 of them showed only in the right sided lymph nodes metastases whereas 2 animals had bilateral metastases (Figure 19B).

3.2.8. Conclusion for establishing a murine orthotopic xenograft model for lymphatic metastatic spread

After 6 rounds of testing a panel of different conditions a reproducible murine orthotopic xenograft model for lymphatic metastatic spread was established (Figure 20). Within the prior

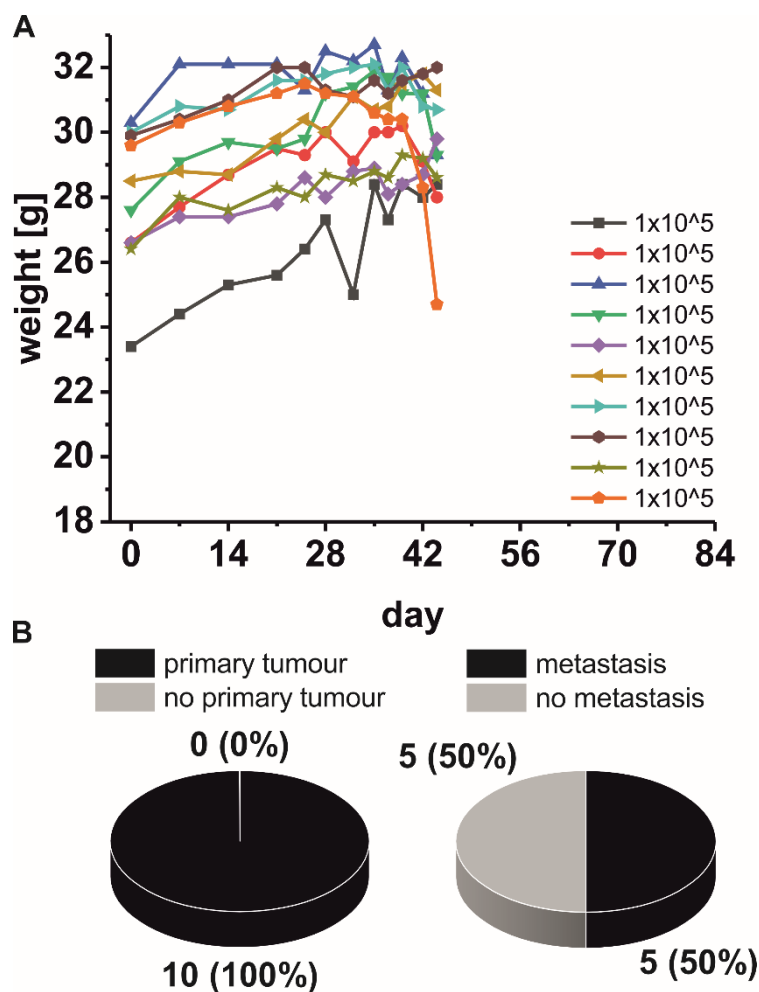


Figure 19 Summary of the sixth lymphatic metastasis establishing round: (A) Weight history of all NOD.CB17/*Prkdc^{scid/scid}/Rj* mice (n=10) that were injected with 1×10^5 tumour cells at the left side of their tip of the tongue. The observation period started at the inoculation day (day 0) until individual sacrifice day. **(B)** Analysis of primary tumour take rate as well as metastasis take rate in all injected mice.

chapters all tested conditions were shown in detail. To sum this model establishment up a tumour cell inoculation into the base of the tongue seemed to impair mice in normal deglutition and normal food intake that implicated a rapid loss of weight in combination with a forced premature sacrifice of animals (3.2.1; grey line Figure 21A). Despite the early sacrifice primary tumours were detectable but metastatic spread was rarely observed by this time (Figure 13). Using an immunofluorescence staining for LYVE-1 and CD31 the tip was chosen as the second most promising location as suitable injection site (Figure 14). Applying the tongue tip as new injection site mice were much less impaired in deglutition and observation time was able to be extended (Figure 15, Figure 21A). Another adjusting screw is the inoculated cell amount. Injecting 5×10^4 cells no primary tumours developed in the tip of tongues (Figure 15B, red line Figure 21A). This cell number was too low and was extended to 8×10^4 cells (blue line Figure 21A). Within this condition a 100 % take rate of primary tumours was achieved in combination with 100 % metastasis rate (Figure 15C, Figure 20). One has to mention that in this round only 3 animals were injected with this amount of tumour cells.

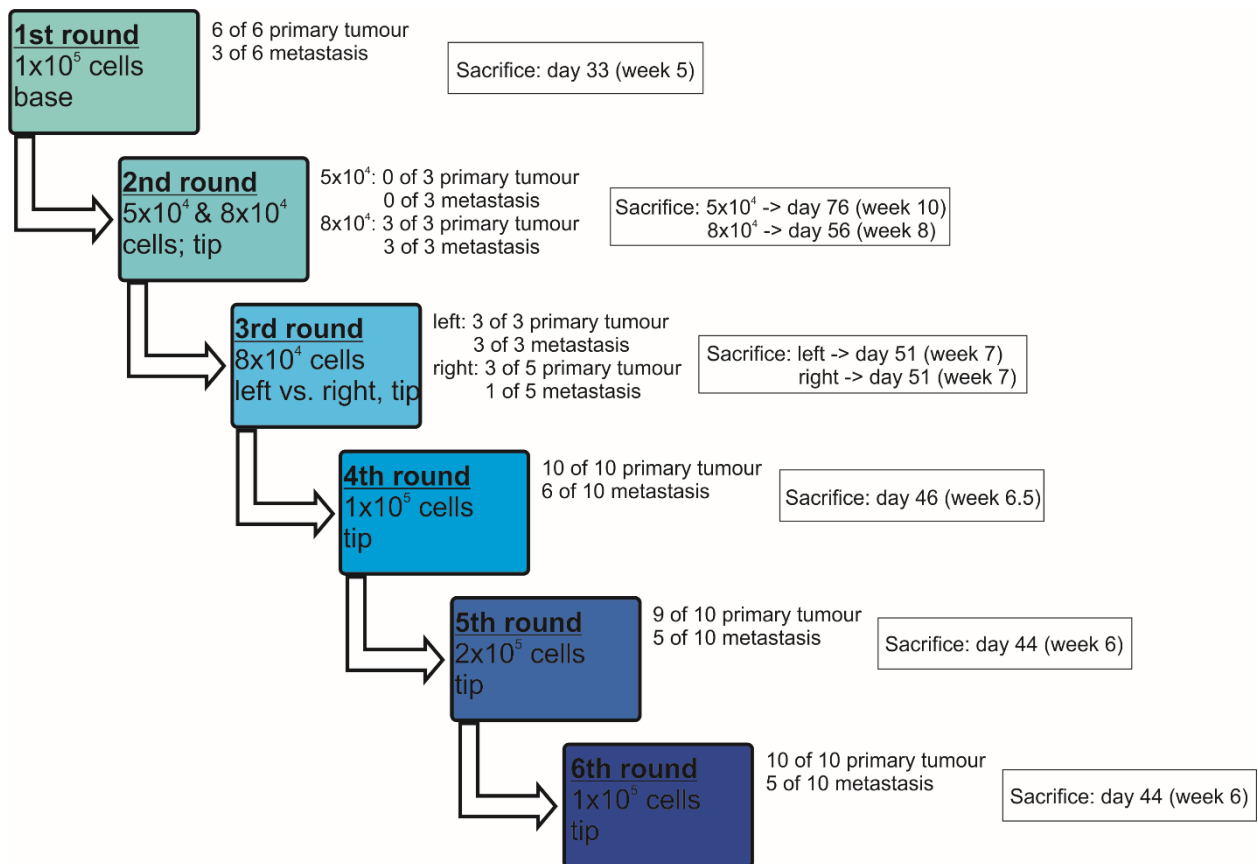


Figure 20 Schematic overview of lymphatic model establishment: In this graph all single experimental rounds are listed with information about the injected cell amount and injection site. Beside each single experiment the results concerning primary tumour and metastasis take rate are listed in combination with the duration each single round.

In the next step the injection site within the tip of the tongue was tested but revealed no clear differences depending on tumour cells being injected into the left or the right site of the tongue. Also, the survival time did not alter (Figure 16, green and purple line Figure 21A). Next, the inoculated cell amount was increased to 1×10^5 cells (Figure 17). Here, a metastasis take rate of 60 % was achieved in combination with a 100 % take rate of primary tumours (Figure 20). The overall observation time slightly decreased (dark yellow line Figure 21A). Within the next establishing round the injectable cell amount was risen again to test if a higher metastasis take rate was achievable but this was not the case (Figure 18, Figure 20). Instead, the overall survival time was again slightly shortened (cyan line Figure 21A). In the final step the established conditions were tested in another mouse strain to confirm its overall operational capability as well because the previously used mouse strain showed a low tolerance for later applied substances (Figure 19, Figure 20). In this round 1×10^5 tumour cells were injected into the left side of the tongue tip and mice developed in 100 % a primary tumour at the injection site as well as developed in 50 % of all mice metastases in their cervical lymph nodes (Figure 19, Figure 20). The overall survival was the same as in the animals injected with 2×10^5 cells (brown line Figure 21A). For comparable reasons, the tongue tumour dimensions were measured in the last three establishing rounds using a calliper (Figure 21B). The volume was calculated by using the formula

$V = (W^2 \times L) / 2$. The used formula was published for tumour volume calculation by Faustino-Rocha et al. in 2013 (Faustino-Rocha et al., 2013). Here, the injection of a doubled tumour cell amount led to a 4- till 6-fold higher tumour volume inside the tongue. Nevertheless, due to a high variance of single tumour volumes there was no significant difference of tumour volume dependent of the cell amount that was injected.

In conclusion, one must mention that a metastasis take rate of more than 50-60 % was not exceeded independent of higher tumour cell inoculation amounts. This fact must be in mind for planning future experiments using this new established model system.

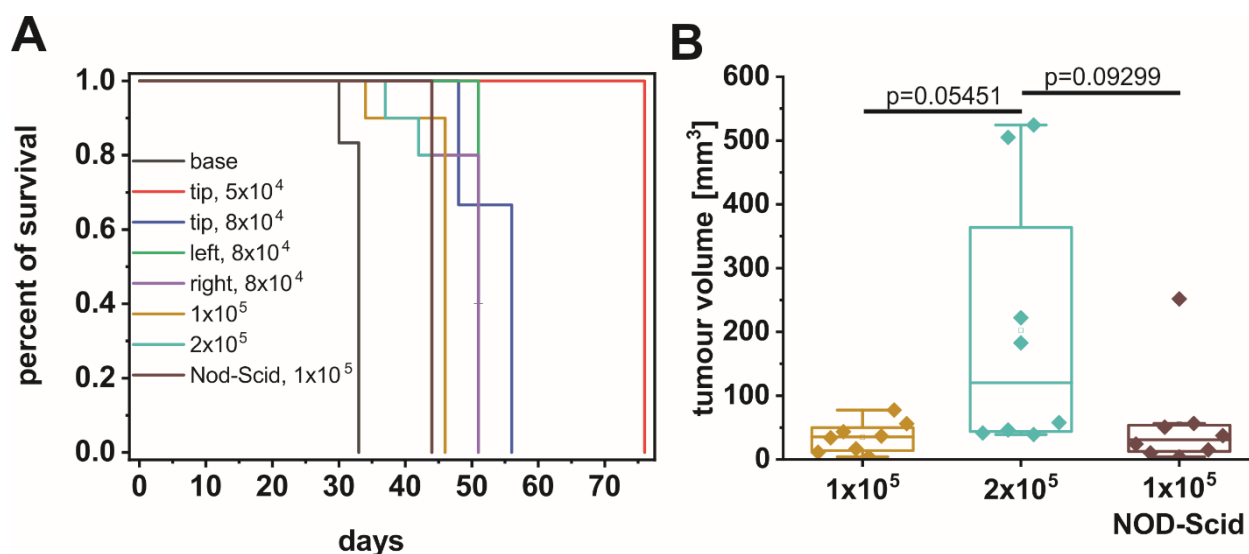


Figure 21 Kaplan Meier analysis and comparison of tumour volume calculation: (A) Summary of the overall survival of all included animals for all tested conditions in the establishment of a new orthotopic murine xenograft model for lymphatic metastasis. (B) Tumour volume was measured using a calliper and calculated by using the formula $V = (W^2 \times L) / 2$ (Faustino-Rocha et al., 2013). The p-value was calculated by a Student's t-test and the Welch-correction, because of unequal variances within the compared groups.

3.3. Establishment of a murine haematogenous metastasis model

About 10 % of HNSCC patients develop distant metastases in the lung, which significantly worsens the clinical prognosis for those patients (Takes et al., 2012). Therefore, this type of metastasis formation should also be addressed in this thesis alongside the lymphatic metastasis that has been already described previously. To be able to investigate the metastasis- and proliferation-inhibiting effect of new substances which showed promising anti-metastatic effects in *in vitro* studies, there was also the need for a reproducible murine model for the second form of metastasis – the haematogenous metastasis. In the following chapters the process of the establishment of a murine haematogenous metastasis model using immunodeficient NOD-Scid mice is described in detail.

3.3.1. First steps towards model establishment

For the formation of distant metastasis of HNSCC these metastases have to be built in lung tissue. Therefore, tumour cells must be injected into the blood vessel system of the used immunodeficient mouse strain to allow a seeding and growth of metastatic colonies in peripheral tissue. To perform an intravenous injection into mice cells have to be injected into the tail vein. This is why the tail vessels were dilated by an applied heat source for better vessel identification. While the process of tumour cell injection the process of EMT is mimicked and the injected cells were free to move with the blood flow. Because the cells were injected into the venous system the cells soon reach the heart and were forwarded into the lung where the cells got caught on the alveolar level. Here, the metastasis formation takes place. The pure process of tumour cell injection turned out to be an extremely sensitive step and had to be carefully established in this thesis especially for the used cell line in combination with the used immunodeficient mouse strain.

It is important to have in mind that cells often conglomerate with each other after the step of trypsin dependent detachment. These cell conglomerates are able to clog small blood vessels like venules or capillary vessels, which may lead to embolisms and in the worst case to death of the injected animal. Capillary vessels of mice are in average 0.3 to 4 μm in diameter and also venules are only 1 to 14 μm in diameter size (Müller et al., 2008). To avoid these cell conglomerates, cells have to be filtered after harvesting. Here, several filter pore sizes were tested. First, a filter pore size of 10 μm was used. Here, filtering of the cells with an average diameter between 10 – 15 μm experienced a too forced compression through the used 10 μm filter. This resulted in cell lysis. Therefore, a filter pore size of at least 15 μm to 20 μm was used for cell preparation. Because cells were counted after the filtering process the status of cell conglomerates could be monitored. For a better constitution of cells before injection into mice cells were allowed to recover right after harvesting for 10 min in normal growth medium including 20 % FCS instead of normal 10 % FCS amount in the standard cell culture medium at 37 C and 5 % CO_2 . However, the FCS must be washed out again before cell inoculation so that cells were washed twice with PBS.

Another critical step in tail vein injection is the stress level of the injected animals. In first tail vein injection trials mice were inserted into a restrainer for tumour cell injection. Here, the mice were highly panicked and even died within the used restrainer because of a tight fixation resulting in an extremely high stress level. Next, mice were set under a short, volatile anaesthesia using isoflurane for tumour cell injection, which led to an impairment in the general state of health. This is why tumour cell injection was still performed by setting the mouse into the restrainer, but the animal was more loosely fixed.

Nevertheless, a certain number of animals continued to die during the process of tumour cell injection. Therefore, mice were prepared with a weight-dependent i.p. heparin injection (20 IU in 200 μl) about 1 h before tumour cells were injected in order to reduce clumping of the cells with

the animals' blood. In another experiment mice were given a dose of nitroglycerine i.p. in addition to heparin shortly (~1 min) before tumour cell injection. Because this additional step gave no great advantage in survival, the tumour cell injection protocol was standardised including an i.p. dose of heparin (20 IU) 1 to 1.5 h before cell injection.

To sum up several rounds of establishment cells should be prepared most moderate to avoid cell lysis. Therefore, FaDu wild-type cells (diameter ~10-15 µm) were allowed to recover for 10 min in culture medium containing a doubled FCS amount (20 % FCS instead of 10 %) at 37°C and 5 % CO₂. Afterwards cells should be filtered using a cell strainer of 15 to 20 µm pore size with moderate pressure to avoid cell lysis. To avoid stress to injected mice the animals should be fixated more moderate using a restrainer in an appropriate size. Nevertheless, the most crucial step in cell inoculation is a pre-administration with heparin i.p. for mice that are supposed to be injected. This pre-medication should be done 1-1.5 h before the cell inoculation process. Nevertheless, even if all previous conditions are observed, there is no 100 % guarantee that all animals will survive the cell injection without further complications so that a failure rate of about 10 % per injection procedure should be calculated using this haematogenous metastasis model.

3.3.2. Establishment of metastasis formatting cell amount

Another critical step besides the already above-mentioned points in the process of distant metastasis formation was the amount and volume of injectable tumour cells. Concerning the injectable volume 200 µl seemed to be most tolerable. Regarding the injectable amount of tumour cells not to overload the blood vessel system the tested number varied between 2.5 x10⁵ up to 2 x10⁶ cells in 200 µl injection volume.

The first experiment started with an amount of 2.5 x10⁵ tumour cells. During the inoculation process 5 mice were anaesthetised by isoflurane except for 2 animals that were injected using a restrainer. Animals that were moderately fixated in the restrainer were obviously fitter compared to anaesthetised animals. Like already mentioned above it was extremely important to keep the stress to injected animals as low as possible. After the injection of 2.5 x10⁵ cells one animal was directly sacrificed after the inoculation due to neurological symptoms including a failure of the hind limbs as well as severe breathing pauses. The remaining 6 animals were monitored for at least 6 weeks. The mouse with the longest observation period of this round was able to survive 10 weeks. Starting at week 2 after cell inoculation the weight was measured once per week. After 6 weeks of observation animals started partly to lose weight rapidly, which already resulted in sacrifice of all animals until week 10. According to the guidelines that were accepted by the local governmental animal care committee and in accordance with the German legislation on protection of animals, the EU Directive 2010/63/EU and the National Institutes of Health Guidelines for the Care and Use of Laboratory Animals (NIH Publication #85-23 Rev. 1985) animals must be

sacrificed with a weight loss of 20 % of their highest measured weight. During the observation μ CT analysis was done weekly starting 6 weeks after cell inoculation. At this point of time metastasis formation was expected combined with a potential change in lung volume due to replacement of functional lung tissue by metastasis. All 6 animals received at least one prospective μ CT with 18 μ m resolution and one retrospective μ CT with 35 μ m resolution. Here, a short explanation regarding pro- and retrospective μ CT image acquisition. During prospective μ CT image acquisitions only images were acquired during a specific respiratory phase. So, the scanner waits for the right respiratory phase for taking an image. Therefore, mice with an irregular breathing rhythm during anaesthesia may have a prolonged μ CT run applying this method (Cheng et al., 2015). In contrary, a retrospective μ CT image acquisition acquires images continually throughout the breathing cycle of the mouse and compose images from the desired phase at the end of the completed scan. One animal received 5 times both categories of μ CT. However, one has to mention that 2 animals that received 4 to 5 μ CT acquisitions showed noticeable problems at their fore paws that were maybe potential radiation side effects of weekly applied μ CTs. After histological lung preparation 4 of 6 animals showed metastases in the lung.

In the next step 3 animals were injected with a doubled cell amount of 5×10^5 tumour cells in 200 μ l PBS using a restrainer for cell inoculation procedure. Starting at this point, mice always received an administration of heparin (20 IU) approximately 1 h before cell inoculation. Unfortunately, 1 animal died after cell inoculation. The remaining 2 mice received in sum 3 μ CT scans starting 4 weeks after the cell inoculation day. Again, on each scanning day 2 modi were applied, prospective with 18 μ m resolution and retrospective with 35 μ m resolution. Animals were sacrificed after 8 weeks of observation. Both remaining animals showed light fur loss that might be a result from applied μ CTs. Regarding the metastasis rate both animals showed metastases after 8 weeks of observation, but nevertheless only 2 animals survived the injected cell number.

Next, the focus lay on the applied radiation dose by μ CT acquisition during the observation period. Because possible radiation dose effects were recognised at several animals that received more than 3 μ CTs the overall radiation dose should be minimised by reducing the μ CT acquisition to one acquisition before the experimental start (35 μ m, AI 0.5 mm) and a second acquisition at the end of the observation time (35 μ m, AI 0.5 mm). Besides, we wanted to reduce the radiation dose applied to injected tumour cells as much as possible to avoid any therapeutic side effects of μ CT-originating radiation on lung metastases. The second μ CT acquisition was determined by the loss of weight of the respective animal. 5 mice were imaged using a prospective protocol one day before the tumour cell inoculation. The following day all animals were injected again with 5×10^5 cell per 200 μ l and survived the inoculation without major impairments. The first animal was sacrificed after 8 weeks of observation. The remaining 4 animals were sacrificed after 10 weeks and received another μ CT acquisition. Nearly all animals showed light fur loss at the fore

and hind legs again. A correlation with applied μ CT acquisitions was almost ruled out. After histological examination 4 out of 5 animals showed metastases in their resected lung tissue.

In the next experimental establishing round the amount of injectable tumour cells was increased. Here, 3 animals received 1×10^6 cells as well as 3 other animals received 2×10^6 cells in 200 μ l PBS. These animals were only injected for feasibility and were sacrificed again one day later. Regarding the inoculation of doubled to quadruple number of inoculated cells it could be observed that animals receiving 2×10^6 cells were in a normal state of health but nevertheless 1×10^6 cells was the new favoured cell amount because the risk was smaller compared to the other group for systemic side effects of the injection procedure. Here, one must keep in mind that only 3 animals were injected per group.

Concerning the possible injectable tumour cell amount for i.v. injection these experimental establishing rounds revealed a tolerable amount of 1×10^6 cells provided that animals received at least 1 h before the inoculation process a dose of heparin (20 IU) i.p.. Regarding the usage of prospective μ CT acquisitions the supposed decrease on calculated lung capacity was not obtained. Therefore, mice were imaged only once on sacrifice day without a further follow-up during the observation week.

3.3.3. Establishment of histological analysis of lung tissue

Besides the establishment of metastases formation also the subsequent analysis and preparation of the resected lung tissue including the metastases had to be established. The perforation of the diaphragm causes a bilateral pneumothorax during the process of animal sacrifice. In addition, lung tissue shrinks during the histological processing including formalin-based tissue fixation of approximately 40 % (Schneider and Ochs, 2014). Lung extraction of the thoracic cavity and a direct histological processing of lung tissue led to very dense tissue structures. Therefore, the lung tissue preparation had to be adapted. After surgical opening of the animals' thoracic cavity, the lung was fixed by its trachea within the thoracic cavity on a winged infusion set and was carefully resected *in toto*. In the following step the collapsed lung lobes were started to be fixed and re-expanded by instillation of formalin (4 %, v/v) via the inserted cannula with a constant pressure of approximately 30 cmH₂O. During this step, the lung hung on a column for approximately 15 min. Afterwards the trachea was ligated, and the lung filled with formalin together with the heart and the oesophagus were further fixed in formalin for several hours until the heart and oesophagus were removed. The separated lung tissue was processed using the Tissue Tek[®] VIP[™] 5 Jr.. The following fixation procedure was performed as described in 2.3.1. Finally, the lung was embedded in paraffine for storage and/or transport. First, the entire lung was cut en bloc. For this purpose, a 3 μ m thick section was collected per slide before 100 μ m were discarded between each cutting section. Due to huge effort of cutting the whole organ another

processing step was added to the protocol. After the embedding step within paraffine, the material was melted again. The fixed lung was placed dorsal on a plate and fixed using liquid paraffine. Now, the fixed lung tissue was chopped into 1 mm thick sections starting from caudal to cranial using a tissue chopper (Figure 7). Each obtained transversal lung section was embedded in paraffine for its own. Each tissue section was trimmed until the whole tissue was completely cut and ready for H&E staining. For H&E staining 3 μm slices were cut and after staining scanned using a stereo microscope (Leica MZ10F stereo microscope; Leica Microsystems GmbH, Wetzlar, Germany). The following analysis regarding area calculation was performed using a graphic tablet for encircling the lung tissue and/or metastases in combination with ImageJ/Fiji software. Because the lung sections showed a 1 mm thickness the obtained areas were multiplied by 1 mm to calculate the volume of each lung section.

3.3.4. Comparison of different imaging techniques and evaluation of metastatic burden

In this experiment different imaging techniques like μCT and MRI as well as various analysis pathways for lung volume as well as metastases evaluation were examined. For this purpose, 14 animals were injected with 1×10^6 cells i.v. in 200 μl PBS. One animal died in the context of cell inoculation; 2 more animals died in the following 5 days respectively 3.5 weeks after the inoculation. Another mouse was sacrificed due to weight loss 12 weeks after inoculation. Therefore, all remaining animals were sacrificed one week later. The overall observation time for all remaining 9 animals was 13.5 weeks after the tumour cell inoculation took place. On the sacrifice day all remaining 9 animals received first an MRI acquisition in addition to the standardised μCT acquisition (Supplementary Video 1B, C). μCT was first performed *in vivo* using an 18 μm resolution. Afterwards the animal was sacrificed inside the μCT using an isoflurane overdose and another acquisition using a 9 μm resolution was performed on the dead body without any lung and heart movement as a potential source of artefacts (Supplementary Video 1C). Subsequently, the lung was excised and re-expanded hanging on a 20 cm 4 % formalin-containing column as already described in 3.3.3. Due to prior sacrifice of 4 animals from initially 14 injected animals these 4 animals were excluded from the further analysis. Only animals that were sacrificed after at least 12 weeks of observation were included into the further analysis ($n=10$). The histological evaluation of H&E stained lung sections was defined as analytical gold standard for the detection of lung metastases. Therefore, lungs were histologically prepared and cut in 1 mm thick sections. These sections were cut using a microtome into 3 μm slices that were evaluated for the area of the whole lung as well as for metastases evaluation using a graphical tablet in combination with the ImageJ/Fiji software for calculation of the encircled areas. Obtained area was multiplied by 1 mm to calculate the respective lung and metastasis volume. For MRI

image analysis the lung and potential metastases were encircled in every obtained image using HOROS software. Afterwards the obtained areas were multiplied by 128 μm representing the resolution of MRI image acquisition. In case of μCT the lung and metastasis volume were calculated on two diverse ways. First, acquired raw images were reconstructed using “NRecon” software (Bruker Corporation, Billerica, MA, USA). Afterwards, a ROI (region of interest) was drawn around the lung in every 7th or 14th image respective to 18 μm and 9 μm resolution for better comparison to MRI resolution. In case of the automated analysis of lung and metastasis volume a previously established macro was applied to the reconstructed dataset of each mouse lung. After the reconstruction a 3D animation of the lung was exemplarily created using “CTvox” software (Bruker Corporation, Billerica, MA, USA) (Supplementary Video 1C). Several metastases were visible by multiple unfilled holes within the reconstructed lung. For an automated analysis of single μCT images the dataset was binarized to exclude structures like surrounding air around the mouse body and adipose tissue. For this purpose, a global threshold was applied to each dataset (0-65). After defining the new binary image by bitwise operations black speckles less than 99 pixel were removed from the image. All these steps were applied to the obtained 18 μm and 9 μm resolution datasets. The results display the volume of the drawn ROI i.e., the total volume of the lung, as well as the calculated volume of metastases located within the ROI (Figure 22A, B).

In case of the manual lung and metastases volume calculation by μCT analysis, the ROI was drawn again surrounding the lung tissue in general as already described previously for the automated analysis. Suspected metastases were encircled by its own in each respective slide. Referring to the analysis of H&E stained sections, every 111th image in case of 9 μm μCT resolution datasets and every 56th image in case of 18 μm resolution datasets were analysed, respectively, for the area by using ImageJ/Fiji software. The obtained areas were multiplied by factor 1 for volume calculation since the theoretical section thickness for these images should be about 1 mm like for histological sections (Figure 22A, B). Representative images of 9 and 18 μm μCT resolution, MRI in combination with a corresponding H&E staining is shown in Figure 23. An animated MRI image acquisition as well as an animated 3D reconstruction of a 9 μm μCT is shown in the Supplementary Video 1B, C.

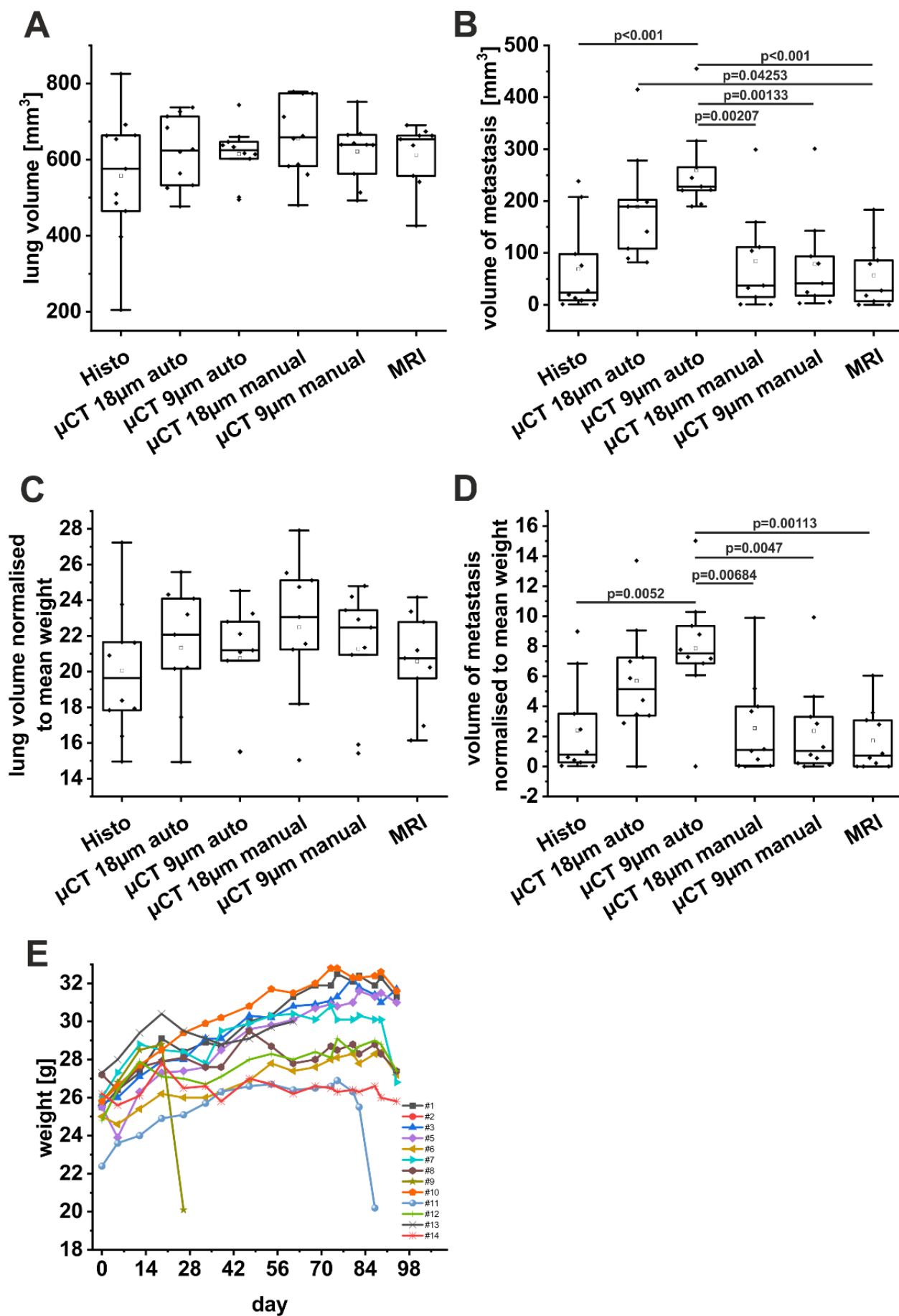


Figure 22 Summary of the first haematogenous experimental round: (A, B) Calculated raw lung and metastasis volume by different analysis methods (histology, μ CT, MRI). Histology was used as a gold standard for metastasis volume evaluation. In case of 18 and 9 μ m μ CT acquisitions the obtained images were reconstructed, and a ROI was drawn manually around the lung. Afterwards the automated evaluation of lung and metastases volume was performed by an algorithm. For manual evaluation of lung and metastases volume μ CT images in the respective resolution again a ROI was manually drawn around the lung tissue as well as the metastases and volume was calculated using ImageJ/Fiji software **(C, D)** Calculated lung and metastases volume was normalised to the mean of weight. The mean of weight was calculated between week 8 until week 10. **(E)** Weight history of all mice ($n=14$) that were injected initially with 1×10^6 tumour cells. The observation period started at the inoculation day (day 0) until individual sacrifice day. Statistical evaluation in **(A-D)** was performed by a one-way ANOVA analysis. The median is shown by the line within the boxplot, the mean is indicated by a small black square within the boxplot.

Referring to the defined gold standard based on histology in sum all 10 animals were diagnosed with metastases after at least 12 weeks of observation. For whole lung volume calculation $n=11$ injected mice were included into the analysis due to no dependence on observation time. In case of histological evaluation of the lung volume a wide volume range is visible. The smallest variability of calculated lung volumes showed the automated evaluation of 9 μ m resolution datasets ($\text{mean}_{9\mu\text{m auto}}=614.84\pm 23.08 \text{ mm}^3$; Figure 22A). An applied ANOVA showed no significant differences between calculated lung volumes of different methods. The situation is different for the calculated metastasis volume. Here, significant differences between various applied methods were obvious (Figure 22B). The largest difference between metastases volumes was seen between histologically quantified volumes of metastases ($\text{mean}_{\text{Histo}}=68.99\pm 27.69 \text{ mm}^3$) compared to automatically calculated metastasis volume of μ CT in 9 μ m resolution ($\text{mean}_{9\mu\text{m auto}}=259.38\pm 27.60 \text{ mm}^3$). Also, between 9 μ m resolution automatically calculated metastasis volume and metastasis volumes calculated based on MRI images showed a major difference ($\text{mean}_{\text{MRI}}=56.71\pm 20.89 \text{ mm}^3$). For a possibly better interpretation of the obtained raw values of lung and metastasis volume these values were normalised to the mean weight of each respective mouse (Figure 22C, D). Therefore, the mean weight of week 8 till 10 was calculated. Within this time frame all in the analysis included mice showed a constant weight. Referring to lung volumes no major differences were detectable between normalised values and corresponding means of raw data (Figure 22A, C) whereas differences were obtained concerning the calculated metastases volumes (Figure 22D). Especially, regarding the calculated values of automated volume evaluation for μ CT the prior highly significant differences between various methods were slightly compensated by normalisation to the mean of body weight. Nevertheless, an applied ANOVA analysis showed even comparable significant differences between different methods concerning the calculated metastases volumes.

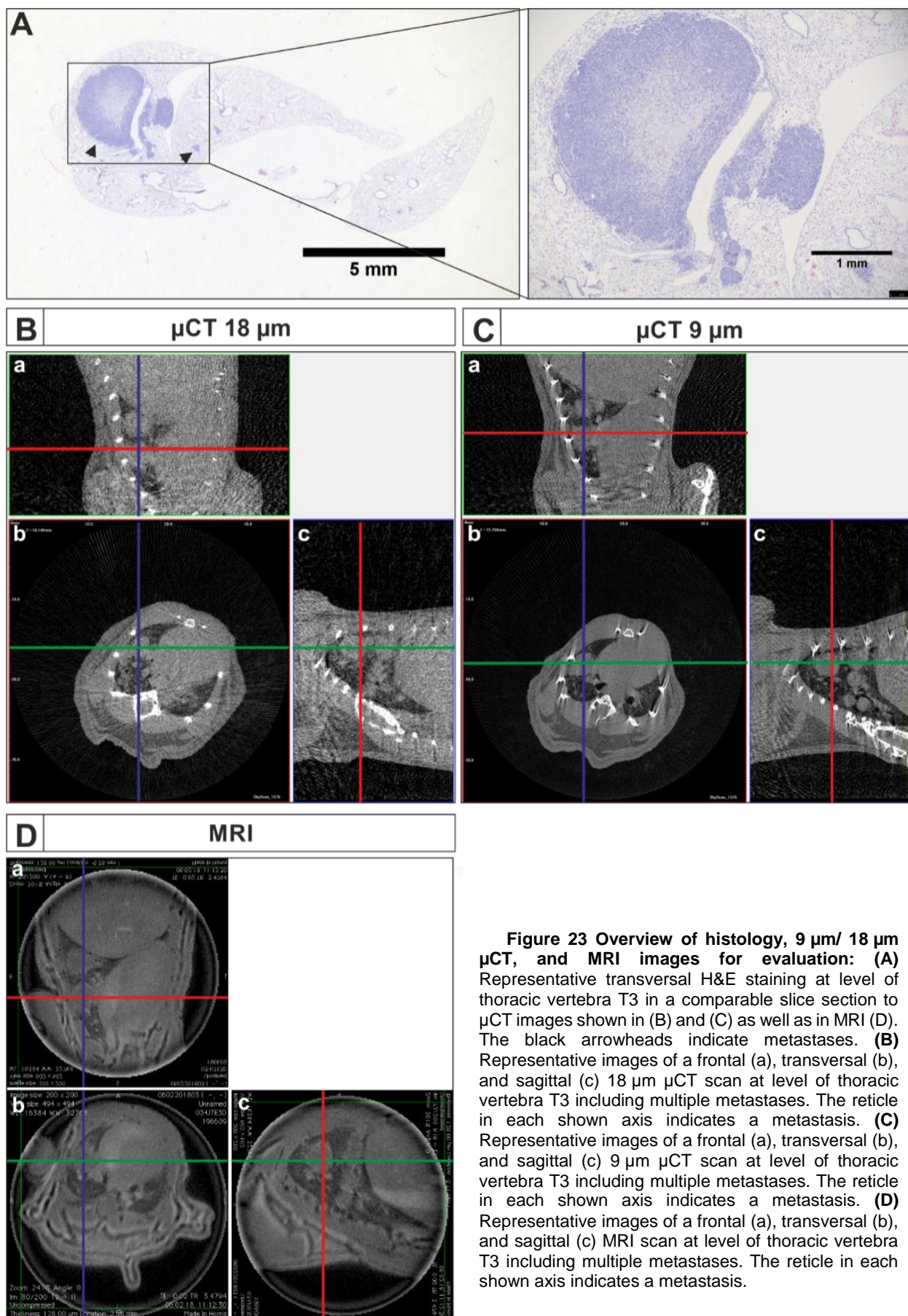


Figure 23 Overview of histology, 9 μ m/ 18 μ m μ CT, and MRI images for evaluation: (A) Representative transversal H&E staining at level of thoracic vertebra T3 in a comparable slice section to μ CT images shown in (B) and (C) as well as in MRI (D). The black arrowheads indicate metastases. **(B)** Representative images of a frontal (a), transversal (b), and sagittal (c) 18 μ m μ CT scan at level of thoracic vertebra T3 including multiple metastases. The reticle in each shown axis indicates a metastasis. **(C)** Representative images of a frontal (a), transversal (b), and sagittal (c) 9 μ m μ CT scan at level of thoracic vertebra T3 including multiple metastases. The reticle in each shown axis indicates a metastasis. **(D)** Representative images of a frontal (a), transversal (b), and sagittal (c) MRI scan at level of thoracic vertebra T3 including multiple metastases. The reticle in each shown axis indicates a metastasis.

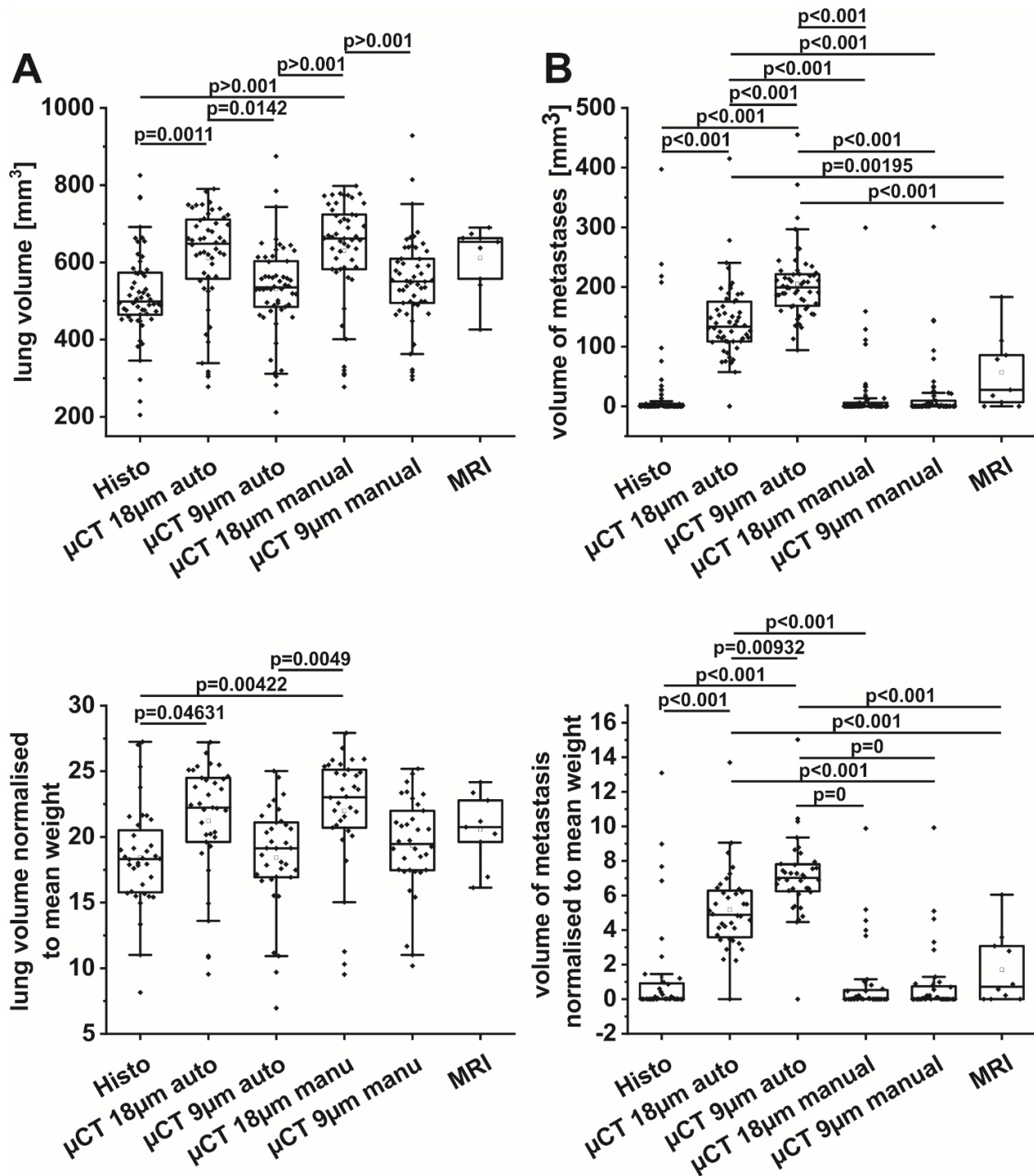


Figure 24 Comparison of all haematogenous mice included in this thesis with μ CT- and histology-analysis: (A, B) Calculated raw lung and metastasis volume by different analysis methods (histology, μ CT, MRI). Histology was used as a gold standard for metastasis volume evaluation. In case of 18 and 9 μ m μ CT acquisitions the obtained images were reconstructed, and a ROI was drawn manually around the lung. Afterwards the automated evaluation of lung and metastases volume was performed by an algorithm. For manual evaluation of lung and metastases volume μ CT images in the respective resolution again a ROI was manually drawn around the lung tissue as well as the metastases and volume was calculated using ImageJ/Fiji software. Statistical evaluation in (A, B) was performed by a one-way ANOVA analysis. The median is shown by a line within the boxplot, the mean is indicated by a small black square within the boxplot.

The previously seen trend of an overestimation of the metastases volume by an automated evaluation is still visible and comparable to the raw data (Figure 22B, D). These results showed no dependency of the measured metastasis volume with the respective mouse weight.

3.3.4.1. Comparison of the whole dataset of all investigated mice in the haematogenous metastasis model

Within the following chapter an overall comparison between the already above applied 3 imaging and analysis methods for lung and metastases volume evaluation should be made of all investigated haematogenous mice that received a μ CT on sacrifice day. In contrast to the previous chapter introducing the different methods for only a small dataset of 11 animals here the methods comparability was analysed by a larger dataset consisting of 57 animals that were all inoculated with FaDu wt cells and received at least a μ CT- and histology-based evaluation of their respective lung and metastasis volumes.

Referring to the previous chapter 3.3.4 the calculated volumes of two different μ CT resolutions (18 and 9 μ m), MRI (128 μ m), and histology (1 mm) as a gold standard were compared to each other (Figure 24). Regarding analysed total lung volumes, the overall trend differs between different applied methods. The calculated mean of histology-based lung volumes was the smallest volume value ($\text{mean}_{\text{Histo}}=515.93\pm 15.19$) of all methods (Figure 24A). Most comparable to histology-based lung volumes were volumes calculated by 9 μ m μ CT automatically ($\text{mean}_{9\mu\text{m auto}}=531.93\pm 16.25$) as well as volumes calculated by 9 μ m μ CT manually ($\text{mean}_{9\mu\text{m manu}}=550.88\pm 16.21$). Most different to histology-based lung volumes were volumes calculated by 18 μ m μ CT manually ($\text{mean}_{18\mu\text{m manu}}=630.63\pm 19.23$). The means of lung volumes calculated by MRI ($\text{mean}_{\text{MRI}}=611.64\pm 28.86$) as well as by 18 μ m μ CT automatically ($\text{mean}_{18\mu\text{m auto}}=611.13\pm 18.61$) were similar but in comparison to the histology-based gold standard also increased. One reason for these larger mean lung volumes could be the alive status of the animal during image acquisition. Due to chest movements by breathing and heart beat the lung volume could be different compared to images acquired on a dead mouse cadaver as the results of 9 μ m μ CT could show. In general, the ratio between automated and manual analysis seemed to be the same independent of the resolution of 9 μ m and 18 μ m. Additionally, the obtained raw lung volumes were normalised to the mean weight that was calculated of values between week 8 and 10 (Figure 24C). This normalisation step had no substantial impact on the obtained values. The general trends between individual measurement methods remain the same. Nevertheless, the volume differences calculated by different methods slightly assimilated.

The overall obtained volumes for metastases differ in part very much (Figure 24B). Metastases volumes calculated by the automated evaluation of 18 μ m ($\text{mean}_{18\mu\text{m auto}}=140.86\pm 8.85$) and 9 μ m μ CT ($\text{mean}_{9\mu\text{m auto}}=204.79\pm 8.04$) resolutions significantly differed from volumes calculated by all other applied methods ($\text{mean}_{\text{Histo}}=25.67\pm 9.52$). The mean metastases volume based on automated analysis of 18 μ m resolution was 5.4-fold higher compared to histology-based volumes. In case of automatically calculated volumes based on 9 μ m resolution the mean volume was even 8-fold higher compared to histology (Figure 24B). Here, one has to mention how the

automated analysis works, which is already further described in 3.3.4. In brief, the automated analysis includes all blood and lung vessels, in addition with metastases. This may lead to an overestimation of the metastases volume. Even a normalisation of the obtained raw data to mean weight between week 8 until 10 was not able to adjust these differences as already seen in the small dataset of chapter 3.3.4 (Figure 24D). The calculated differences by a one-way ANOVA analysis are indicated within the graphic (Figure 24B, D).

In the next step all applied methods should be compared regarding their calculated lung and metastases volumes among themselves using a linear correlation analysis and a Bland-Altman analysis that is best suited for method comparison (Figure 25, Figure 26, Figure 27, Figure 28). In general, the obtained Pearson correlation coefficients for lung volumes were small and gave no sign for a good comparability of lung volumes between histology and the other tested measurement methods. The best obtained Pearson correlation coefficient was calculated between histology and manual 18 μm μCT (Pearson-R=0.38998). The worst correlation was obtained between histology and MRI analysis. Here, a large dataset was compared to only 9 data points for MRI, which may explain the bad correlation (Pearson-R=0.0015). However, the correlation coefficient does not provide a good indication of the comparability of two methods. Therefore, a Bland-Altman analysis was additionally performed (Figure 25I, J). Important for the interpretation of the Bland-Altman plot is on the one hand the mean of differences. The larger this mean is the more different the measurements are, or the smaller the obtained mean, the smaller the systematic error is. The range of variation of the values should not exceed 1.96 times of the standard deviation. The zero line should be included within the confidence interval, otherwise the potential bias will be statistically significant. Applying these instructions, best results for method comparability were obtained between the histological analysis and automated 9 μm μCT analysis, followed by the manual 9 μm μCT analysis and MRI. Regarding the MRI, one must keep in mind that there is only a dataset of 9 animals available.

Comparing the obtained 9 μm and 18 μm μCT lung volumes better but not good Pearson correlation coefficients were obtained (Figure 26A-D). Regarding the Bland-Altman analysis both methods showed high means of differences combined with a significant bias. Comparing the manual and automated analysis of the μCT within the same resolution the calculated Pearson correlation coefficients were good (Figure 26E-H). Also, the Bland-Altman analysis could confirm the correlation coefficients. The means of differences were small albeit the zero line was not included into the confidence interval.

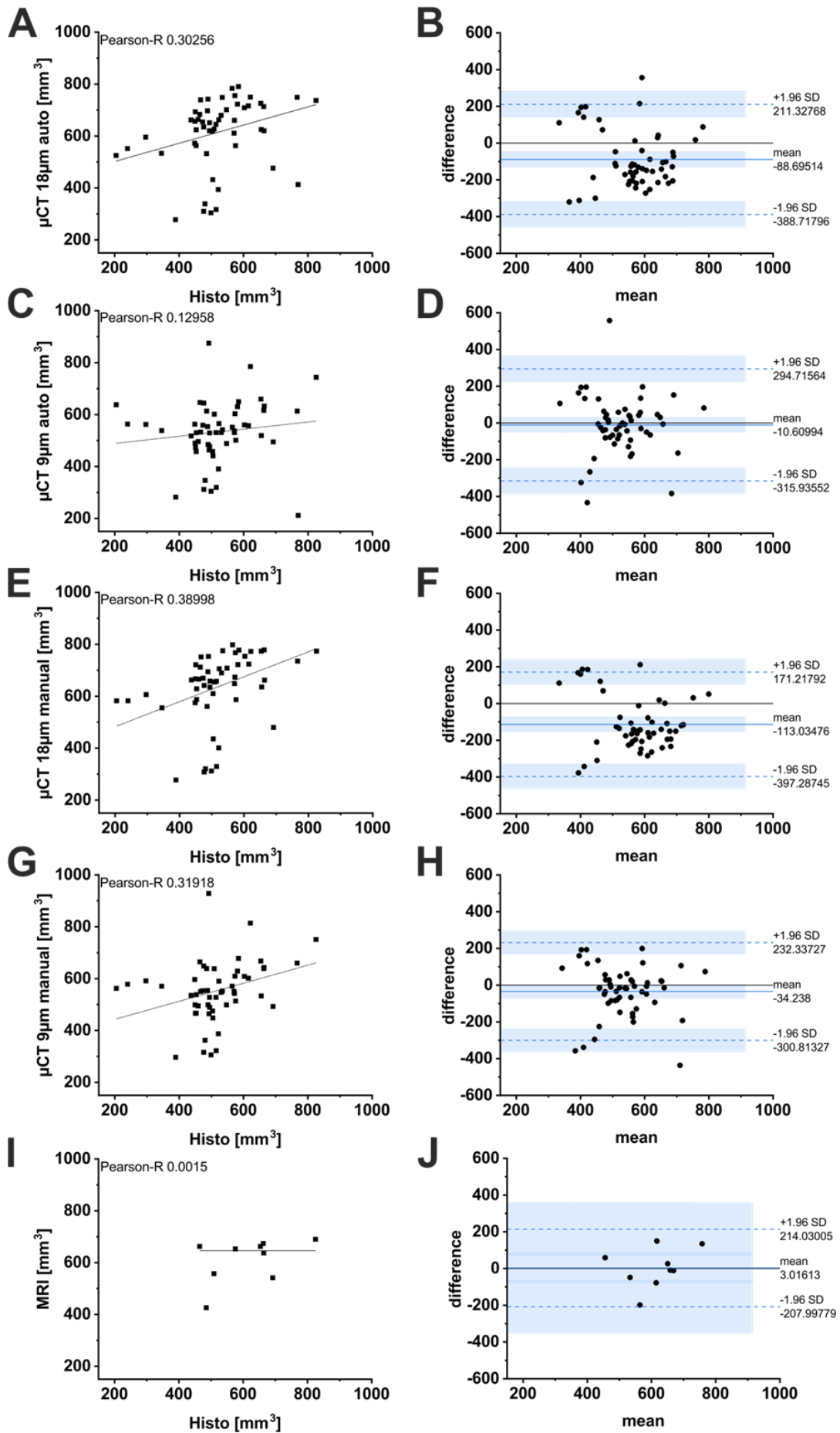


Figure 25 Linear correlation and Bland-Altman analysis of lung volumes between histology and all other applied methods for lung volume calculation: (A, C, E, G, I) Linear correlation of lung volumes based on histological sections and all remaining applied methods for lung volume evaluation. The histology-based values were set as a gold standard. (B, D, F, H, J) Bland-Altman analysis of obtained raw values for lung volume of histology and all other applied methods.

As a gold standard for metastases detection again the histological analysis was used since a reliable statement about the presence of metastases can be made. Comparing the other used methods for metastasis volume to the gold standard by linear correlation analysis the obtained correlation coefficients were optimal for manual 18 μm μCT (Pearson-R=0.95228), manual 9 μm μCT (Pearson-R=0.95167), and MRI (Pearson-R=0.93008) (Figure 27E, G, I). Also, regarding Bland-Altman analysis these methods received best conditions concerning the mean of differences (Figure 27F, H, J). Additionally, all three methods include the zero line within the respective confidence interval, which indicates a low bias regarding these methods. Regarding the automated evaluation of metastasis volume the obtained Pearson coefficients were small as well as the mean differences were really large (Figure 27A-D). Comparing the 9 μm and 18 μm μCT analysis concerning the automated versus the manual analysis the best consensus was obtained for the manual evaluation (Pearson-R=0.99138). Even the Bland-Altman analysis showed the best accordance (Figure 28C, D). All these tendencies were also visible comparing the calculated means for lung and metastases volume (Figure 24A, B).

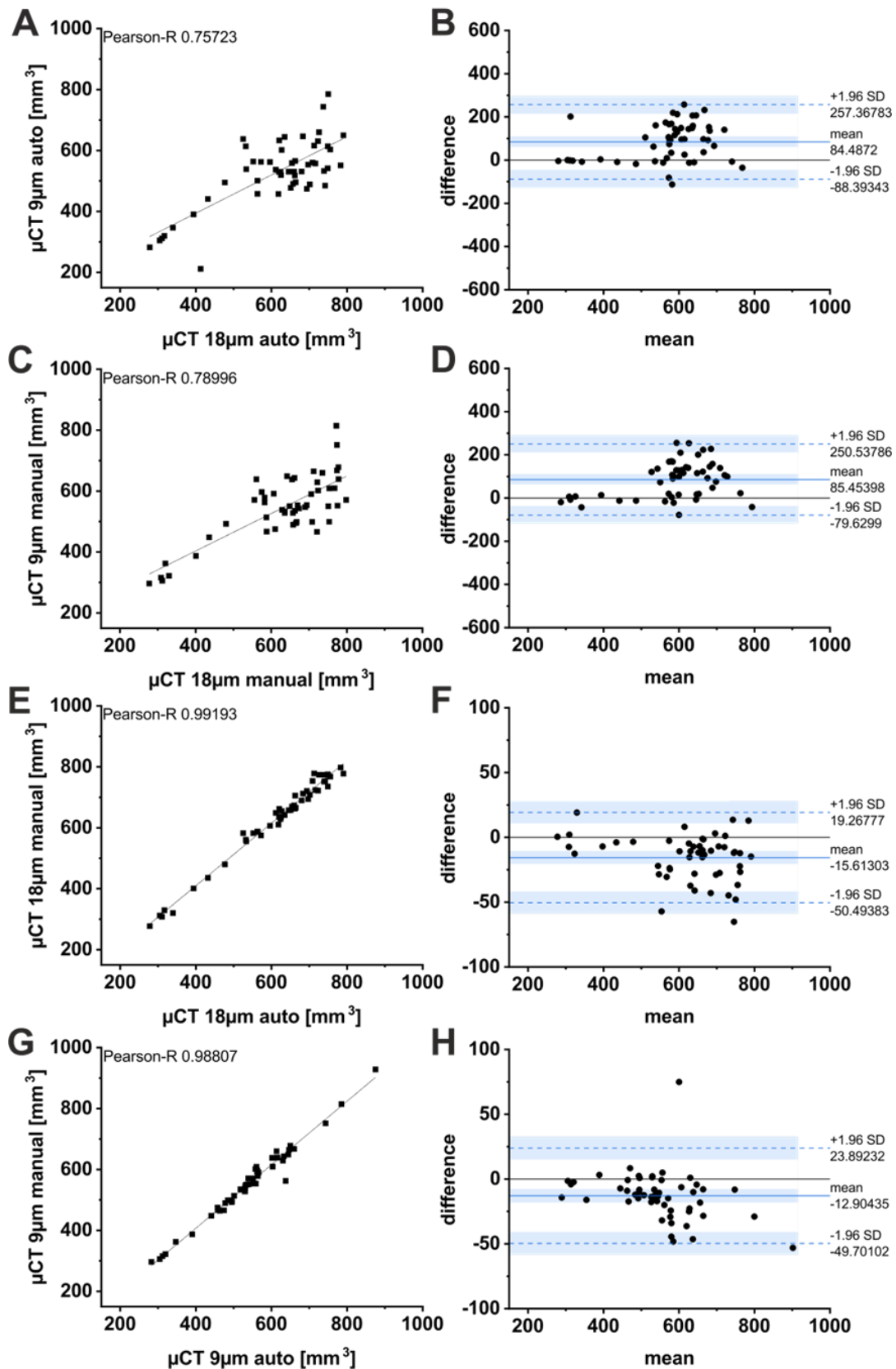


Figure 26 Linear correlation and Bland-Altman analysis of lung volumes between different μCT settings for lung volume calculation: (A, C, D, E, G, I) Linear correlation of lung volumes based on 9 μm and 18 μm μCT resolution as well as between manual and automated volume evaluation. (B, D, F, H, J) Bland-Altman analysis of obtained raw values for lung volume of different settings in μCT image acquisition and manual vs. automated evaluation.

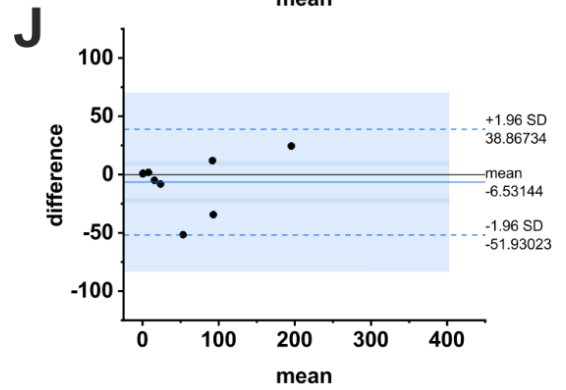
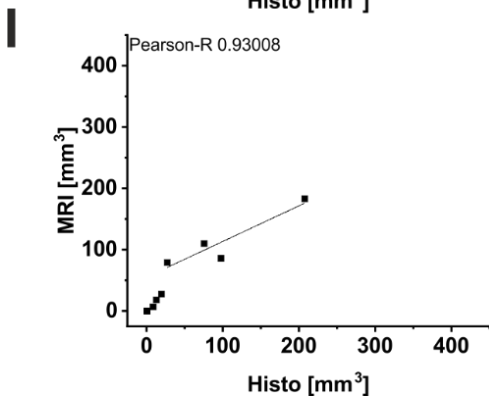
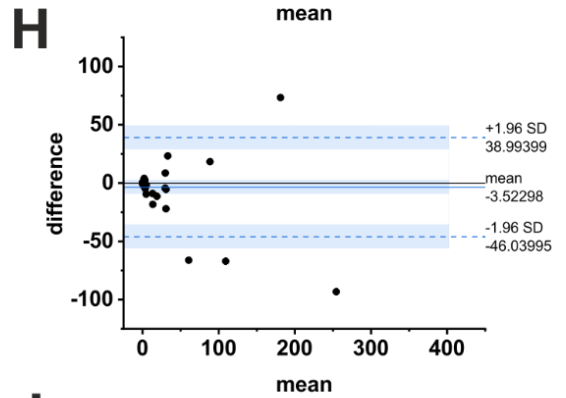
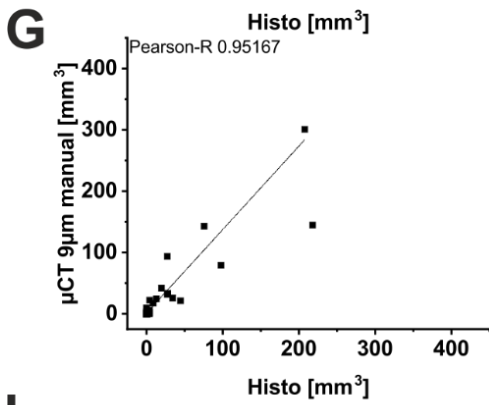
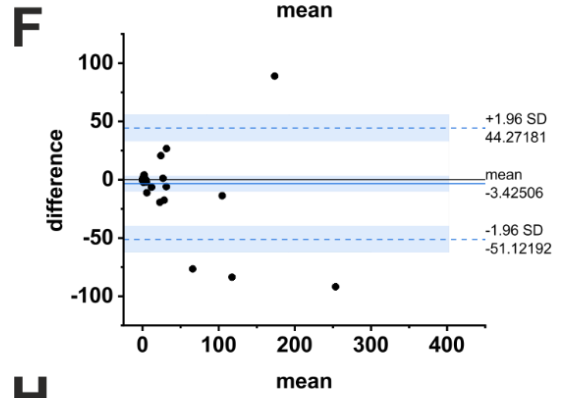
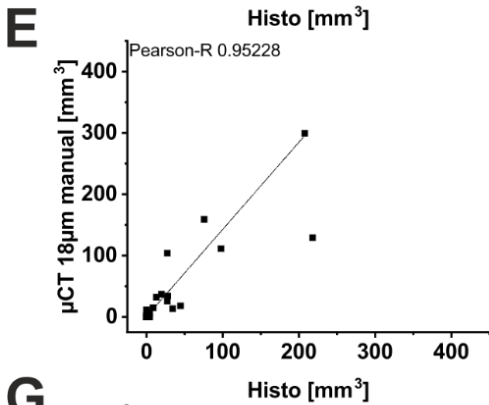
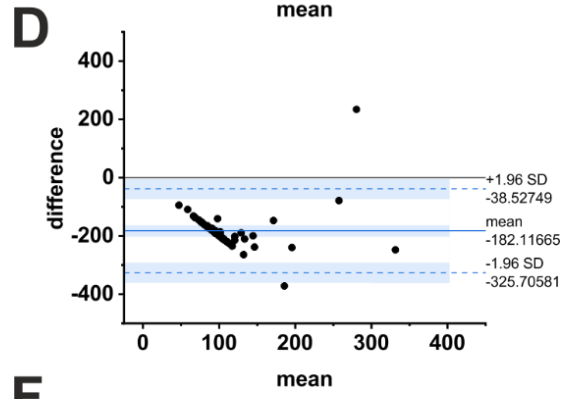
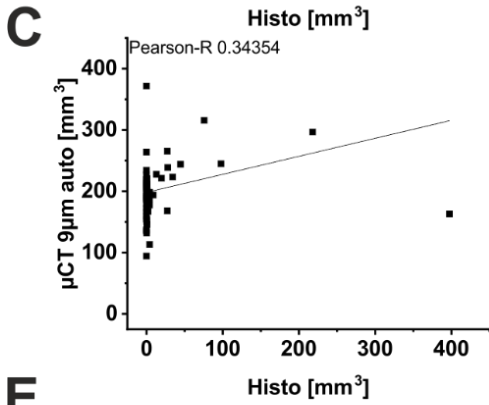
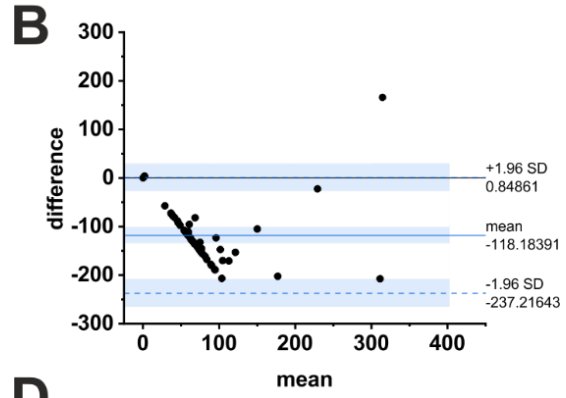
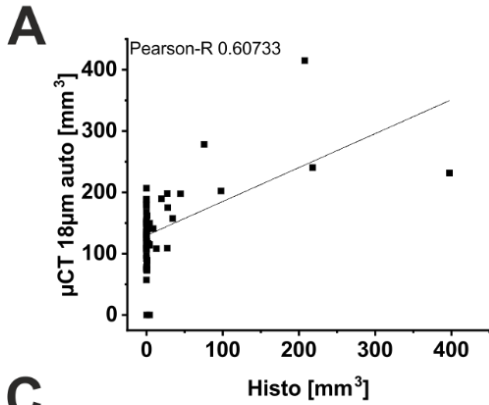


Figure 27 Linear correlation and Bland-Altman analysis of metastases volumes between histology and all other applied methods for metastases volume calculation: (A, C, D, E, G, I) Linear correlation of metastases volumes based on histological sections and all remaining applied methods for metastases volume evaluation. The histology-based values were set as a gold standard. **(B, D, F, H, J)** Bland-Altman analysis of obtained raw values for metastases volume of histology and all other applied methods.

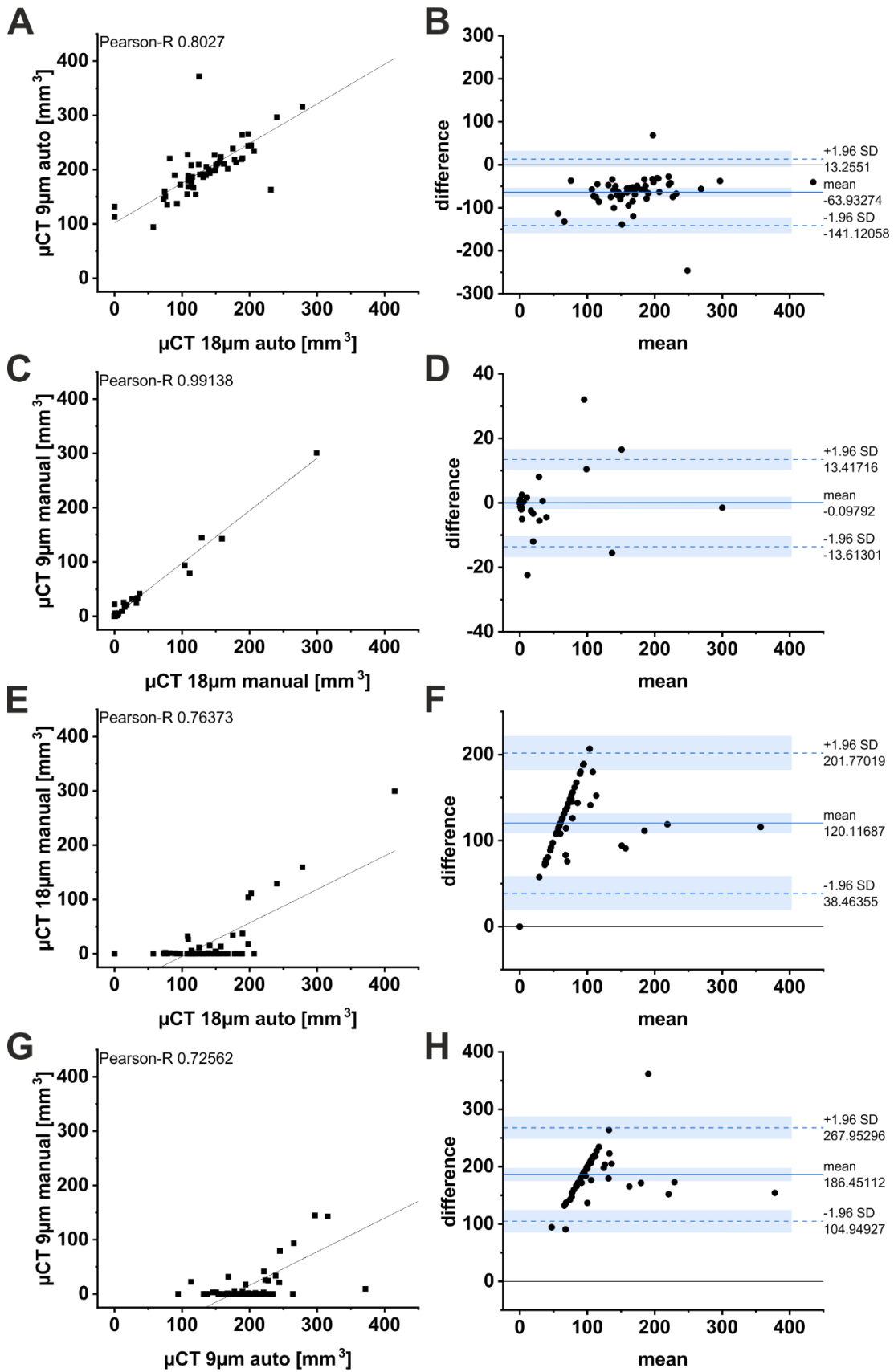


Figure 28 Linear correlation and Bland-Altman analysis of metastases volumes between different μ CT settings for metastases volume calculation: (A, C, D, E, G, I) Linear correlation of metastases volumes based on 9 μ m and 18 μ m μ CT resolution as well as between manual and automated volume evaluation. (B, D, F, H, J) Bland-Altman analysis of obtained raw values for metastases volume of different settings in μ CT image acquisition and manual vs. automated evaluation.

3.4. TFP and TG administration show a trend towards anti-metastatic effects

In vitro studies were able to show a significantly reduced migration of HNSCC cells after a siRNA mediated knockdown of *SEC62*. Unfortunately, a direct transfer of this method is unsuitable for an *in vivo* application so far. However, two substances that were further examined in this thesis were able to cause a functional knockdown of *SEC62* and showed already promising anti-migration and -proliferation effects in previous *in vitro* studies over the last years. The two substances are TG und TFP that, as in the case for TFP, are already used in clinical application, albeit with a different reason for use. For *SEC62* overexpressing tumour cells (FaDu) the combination of both substances should contribute within these specific cells to a greater ER-dependent Ca^{2+} stress compared to normal cells of the surrounding tissue. This should induce apoptosis in the *SEC62* overexpressing tumour cells, which should impair the tumour cells' ability to migrate and thus form metastases. After the introduction into the establishment of two new murine xenograft models one major aim of this thesis was to investigate the *in vivo* applicability of the aforementioned substances – TFP and TG. A summary of the experimental procedure concerning tumour cell injection, TFP and/or TG application, histological preparation, and the experimental setup of the therapeutic application of TFP and TG is summarized in Figure 29.

Main parts of this analysis were already published by Körner et al. 2022 in *Frontiers in Physiology*.

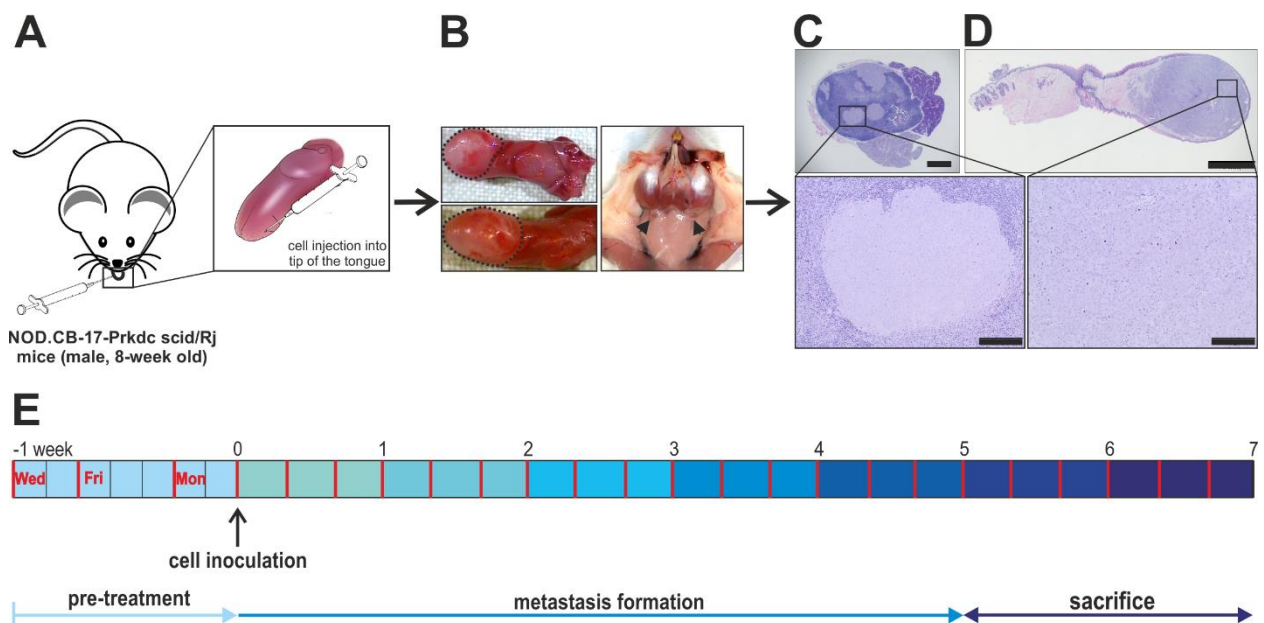


Figure 29 Summary of the experimental procedure for therapeutic approach administering the lymphatic metastasis model: (A) 8-week-old male mice were inoculated with 1×10^5 FaDu wt cells into the right side of the tip of the tongue (day 0). **(B)** During the following 5 to 7 weeks of experimental procedure primary tumours as well as lymph node metastasis developed. Shown here are two excised mouse tongues bearing a primary tumour (encircled with a dotted black line) and the location of cervical lymph nodes inside the situs. **(C, D)** For analysis and quantification of primary tumour and lymph node metastases H&E stainings were made. Shown here are samples of a lymph node including several metastatic foci and a primary tumour in the tongue tip. **(E)** Experimental procedure started at day-7 pre-treating all animals dependent on their group membership. FaDu wt cells were inoculated at day 0 and treatment was continued every 48 to 72 h until animals were sacrificed after 5 to 7 weeks. Scale bar: 1 mm (C), 2 mm (D), zoom out 200 μm .

3.4.1. Tolerance of applied substances

One main aspect of substance application is a good tolerance of the applied substances right at and shortly after the injection itself as well over the whole treatment and observation period. In the described study to test the anti-proliferative as well as the anti-metastatic effect of TFP and TG *in vivo*, 8-week-old male mice were randomly grouped in 4 different treatment groups before the experimental start. The vehicle group consisted of 9 animals, the group of animals that received the combinatory therapy of TFP and TG consisted of 11 animals, 10 animals received TFP as a solo therapy as well as another 10 animals received TG as a solo treatment. The drugs were administered i.p.. Animals that received the combinatory treatment were injected with both substances at different injection sites to exclude some complications. Over the whole experimental procedure animals showed a normal grooming behaviour combined with a normal food and water intake. Food and water intake was not separately quantified, but body weight was documented three times a week combined with each treatment application (Figure 30A). In the case that animals were not able anymore to gnaw and swallow in a normal way the food pellets showed typical food leftovers at the cage bottom. In these cases, a rapid loss of weight was mostly observable so that animals were sacrificed dependent on their body weight. In case of impaired food intake soaked food pellets or Fresubin® Energy Fibre Drink (Fresenius Kabi Deutschland GmbH, Bad Homburg, Germany) was offered to the animals. The grooming behaviour was evaluated by established scoring sheets that quantified the general state of health, the behaviour in the group, the hunching score for measurement of pain, the food intake concerning food leftovers at the cage bottom as well as the body weight. These scoring sheets also provided a basis for deciding if an animal had to be sacrificed dependent on the single score evaluation or the sum of different categories. Concerning the results of this study no long-term side effects were observed during the observation time of 5 till 7 weeks. Concerning the short-term side effects several aspects were obvious that will be further described in the following passage. First, all animals recovered from their short-term side effects within the following 6 to 8 h. Directly after any i.p. substance application animals behaved in a normal way. In case of the TFP (15 mg/kg) application animals started to move slowly about 3 - 5 min after the injection. The animals appeared exhausted, they slowed down in their movements and descended on the ground. A frequent observation was a forced pressure of the abdomen onto the ground and a rest in this position with the feet stretched backwards (Supplementary Video 1D). Animals that received both substances had a pause of 2 h between the application of both drugs to enable a recovery between both injections. In case of the TG (0.4 mg/kg) application there were similar effects visible but less abundant compared to observed side effects after TFP administration. Animals that received only a solo treatment of TG normally recovered within 10 to 20 min. After TG application animals also showed a retarded movement behaviour 5 min after the drug application.

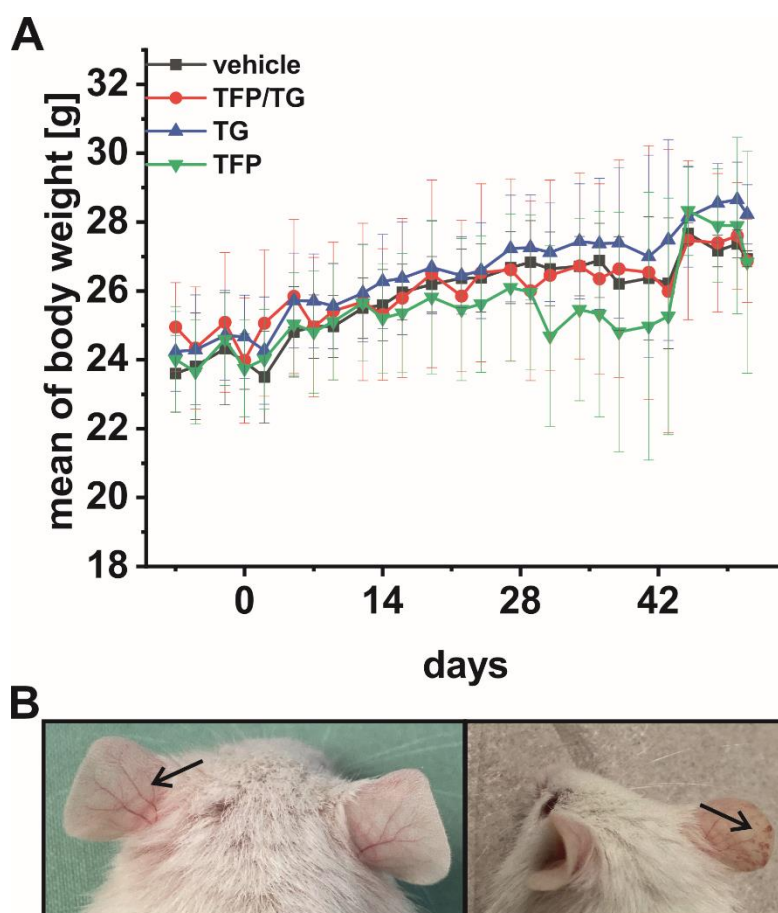


Figure 30 Weight history of all treated lymphatic NOD-Scid mice and increased ear perfusion: (A) Shown is the mean and respective standard deviation of weight of all NOD-Scid mice that were treated respective their group membership with vehicle (n=9), TFP (n=10), TG (n=10) and the combination of both substances (n=11). Mice were injected with 1×10^5 tumour cells at the right side of their tip of the tongue. The observation period started one week (day -7) before the inoculation day (day 0) due to 3 pre-treatments until individual sacrifice day. **(B)** Shown are two exemplary images of an increased ear perfusion after TG administration.

They also pressed their abdomen onto the ground and a forced defecation was observable as a sign of physical stress. In few animals a trembling in their face was observed with irregular retch-like movements (Supplementary Video 1E). Another side effect after the TG administration was a suspected decrease in body temperature due to markedly increased peripheral perfusion especially visible at the ears (Figure 30B). This parameter was not objectively quantified but was rather a subjective assessment. Therefore, and in relation to a decreased movement treated animals were positioned in front of a heating lamp right after drug administration for several hours in general.

To sum up the observed side effects after TFP and TG administration in their applied concentrations led to no severe side effects rather short- nor long-term.

3.4.2. Impact of TFP/TG administration on lymphatic metastasis

As already described in the chapter before animals tolerated the applied substances in their respective concentrations without further severe and especially long-term side effects. Therefore,

the anti-proliferative and anti-metastatic effect should be investigated using the previously new established orthotopic xenograft mouse model (chapter 3.2) in the next step. The following results show the summary of three sequentially performed experiments. In sum 46 8-week-old male NOD-Scid mice were treated with 15 mg/kg TFP, 0.4 mg/kg TG, and the respective vehicle as a solo treatment as well as a combinatory treatment consisting of TFP and TG at the already mentioned concentrations.

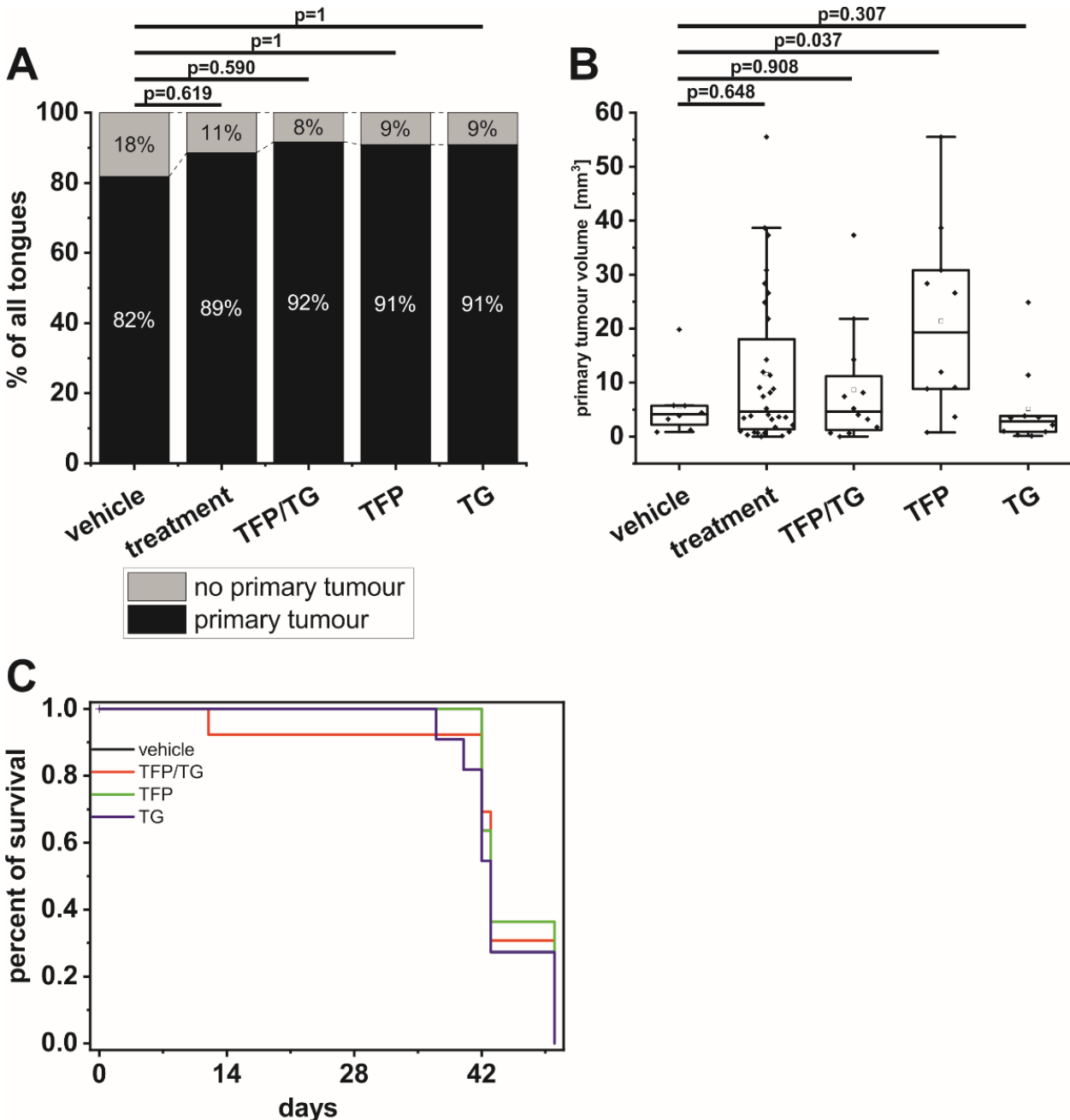


Figure 31 Primary tumour volume: (A) Shown are the relative amounts of tongues with and without a primary tumour dependent on the respective treatment group. For analysis $n=45$ animals were examined. Significance was calculated by a Fisher's exact test. (B) Comparison of calculated tumour volumes. Tumours were measured in width and length of H&E staining. The tumour volume was calculated by $V = \frac{1}{2} \times W^2 \times L$ where W is tumour width and L is the tumour length. Because raw data was not normally distributed the statistical analysis was done by Mann-Whitney-U test. The line within each box indicates the median of calculated tumour volumes, the mean by a small cube. The outliers are indicated by black dots. (C) Summary of the overall survival of all initial animals separated for every treatment condition.

Medical treatment of mice with those substances started one week prior to tumour cell inoculation (Figure 29E). For the whole experiment, all animals were allocated to four different treatment groups (vehicle $n=11$, TFP/TG $n=13$, TFP $n=11$, TG $n=11$). According to the whole observation time of 5 to 7 weeks mice were treated 3 times a week every 48 to 72 h. The pre-treatment consisted of 3 pre-tumour cell inoculation treatments for all 46 mice dependent on their respective grouping. After this pre-treatment week all mice ($n=46$) were inoculated with 1×10^5 tumour cells into the right site of the tip of their tongues under the previously described anaesthesia (chapter 3.2). In the following weeks 41 animals formed a primary tumour inside the tip of the tongue that was potentially able to spread into the cervical lymph nodes. After 5 to 7 weeks of observation including every 48 to 72 h treatment with the respective drugs mice were sacrificed using an overdose of anaesthetics. To validate the growth rate of injected tumour cells tongues of all inoculated mice were excised and histologically examined for a primary tumour. Animals that showed no signs of a primary tumour in the H&E staining were excluded from the analysis ($n=5$). One animal had to be sacrificed already at day 12 after tumour cell inoculation because of a rapid loss of weight. Hence, this animal was excluded from further analysis. A summary of the overall survival of all in the serial experimental setup included animals is shown in Figure 31C. Concerning the primary tumour growth rate 89 % of all injected animals developed a primary tumour inside the tongue tip (Figure 31A). In detail 9 out of 11 animals of the vehicle group developed a primary tumour and 31 animals of 35 treated mice developed a primary tumour. This category includes all animals that were treated either with TG or TFP as solo treatment or TG and TFP in combination. Additionally, the primary tumour size was investigated (Figure 31B). Here, only tumours that were detectable by H&E staining were considered. The primary tumours were measured by calliper on the day of sacrifice, but these measurements were rather unprecise and very small tumours were unable to be measured. Therefore, primary tumours were measured in width (W) and length (L) after tissue preparation and H&E staining. The tumour volume was calculated by using the formula $V = \frac{1}{2} \times W^2 \times L$ (Tomayko and Reynolds, 1989; Faustino-Rocha et al., 2013; Linxweiler et al., 2017a). Because the raw data was not normally distributed the statistical analysis was performed by Mann-Whitney-U testing. Here, we found a significant difference of tumour volumes between the vehicle group and mice that were treated with TFP as a solo administration. TFP-treated mice developed significantly ($p=0.0368$) larger tumours compared to vehicle animals ($\text{mean}_{\text{TFP}}=21.43 \pm 5.54 \text{ mm}^3$, $\text{mean}_{\text{vehicle}}=5.60 \pm 2.13 \text{ mm}^3$). The most equal primary tumours compared to vehicle group concerning tumour volume were detectable in animals that were treated only with TG as a solo therapy ($\text{mean}_{\text{TG}}=5.15 \pm 2.42 \text{ mm}^3$, $\text{mean}_{\text{TFP/TG}}=8.70 \pm 3.19 \text{ mm}^3$; Figure 31B).

In the next step the presence of cervical lymph node metastases was examined. Therefore, the overall existence of metastases was investigated (Figure 32A). For analysis of the amount of lymph node metastases lymph nodes were excised on sacrifice day, fixed in formalin (4 %, v/v),

and embedded in paraffin (Supplementary Video 1A). Afterwards all lymph nodes were fully cut and an H&E staining was performed every 20 µm to evaluate the overall metastatic burden. The histological specimens were further examined in a double-blind study by two investigators (Prof. Dr. Maximilian Linxweiler; MSc Sandrina Körner). The absolute numbers of excised lymph nodes per animal and respective numbers of identified metastases are listed in Table 18. Despite the total numbers of excised lymph nodes varied between mouse individuals the sum of excised lymph nodes per treatment group was comparable. Animals treated in the vehicle group showed a slight trend for the highest metastatic burden compared to the remaining treatment groups calculated on the sum of all excised lymph nodes and respective identified metastases (Figure 32A). Here, in sum 15 metastases were detected in 37 lymph nodes. Regarding animals treated with the combinatory therapy 14 metastases were identified compared to 45 resected lymph nodes. For animals treated with TFP and TG 36 respectively 37 lymph nodes were excised. Here, 9 and 11 metastases were detected. In summary no significant difference between treatment groups compared to vehicle animals were detectable. However, a slight trend could be estimated for a lower metastatic burden regarding mice treated with TFP and animals treated in general. This trend was also detectable regarding the total amount of animals that generated metastases in their cervical lymph nodes. Here, mice treated with TFP showed the lowest number of animals with detectable metastases. Under TFP treatment only 50 % of treated animals developed metastases whereas 67 % of vehicle animals developed metastases (Figure 32B). After the overall examination concerning metastatic burden the size of metastases was further categorized in micro- and macro-metastasis (Figure 32C). According to clinical parameters metastases consisting of more than 20 tumour cells were categorized as macro-metastases, respectively metastases consisting of less than 20 tumour cells were categorized as micro-metastases. All detected metastases of animals treated in the vehicle group were categorized as macro-metastases (Figure 32C). The highest amount and significant difference of micro-metastases was detected in animals treated with TG. Within this group 36 % of identified metastases were categorized as micro-metastases.

Table 18 Summary of raw data: Sum of excised lymph nodes concerning each animal and the respective amount of detectable metastasis. LN, lymph node; Met, metastasis.

	ani ma l	LN su m	Met su m		ani mal	LN sum	Met sum		ani mal	LN su m	Met su m		ani mal	LN su m	Met su m
vehicle	#1	3	0	TFP /TG	#1	4	3	TFP	#1	1	0	TG	#1	3	1
	#2	4	1		#2	4	0		#2	2	1		#2	4	1
	#3	3	1		#3	5	2		#3	4	2		#3	3	0
	#4	4	0		#4	5	2		#4	4	0		#4	2	0
	#5	6	5		#5	3	0		#5	4	0		#5	4	2
	#6	4	1		#6	5	2		#6	3	0		#6	4	1
	#7	5	3		#7	4	0		#7	4	0		#7	4	1
	#8	3	0		#8	4	1		#8	5	1		#8	6	4
	#9	5	4		#9	3	3		#9	5	2		#9	3	0
				#10	5	1	#10	4	3	#10	4	1			
				#11	3	0									

The lowest number of micro-metastases was detected within the TFP treatment group. Here, 11 % of all detected metastases were micro-metastases (Figure 32C).

Regarding the metastasis localisation most of the identified metastases were located on both sites of the neck (Figure 32D). In case of vehicle animals 80 % of all metastases were located on the left and right site. Referring to mice treated with TG the largest number of metastases (45 %) were located only on one side of the neck. All these results showed no significant difference by applying a Fisher's exact test.

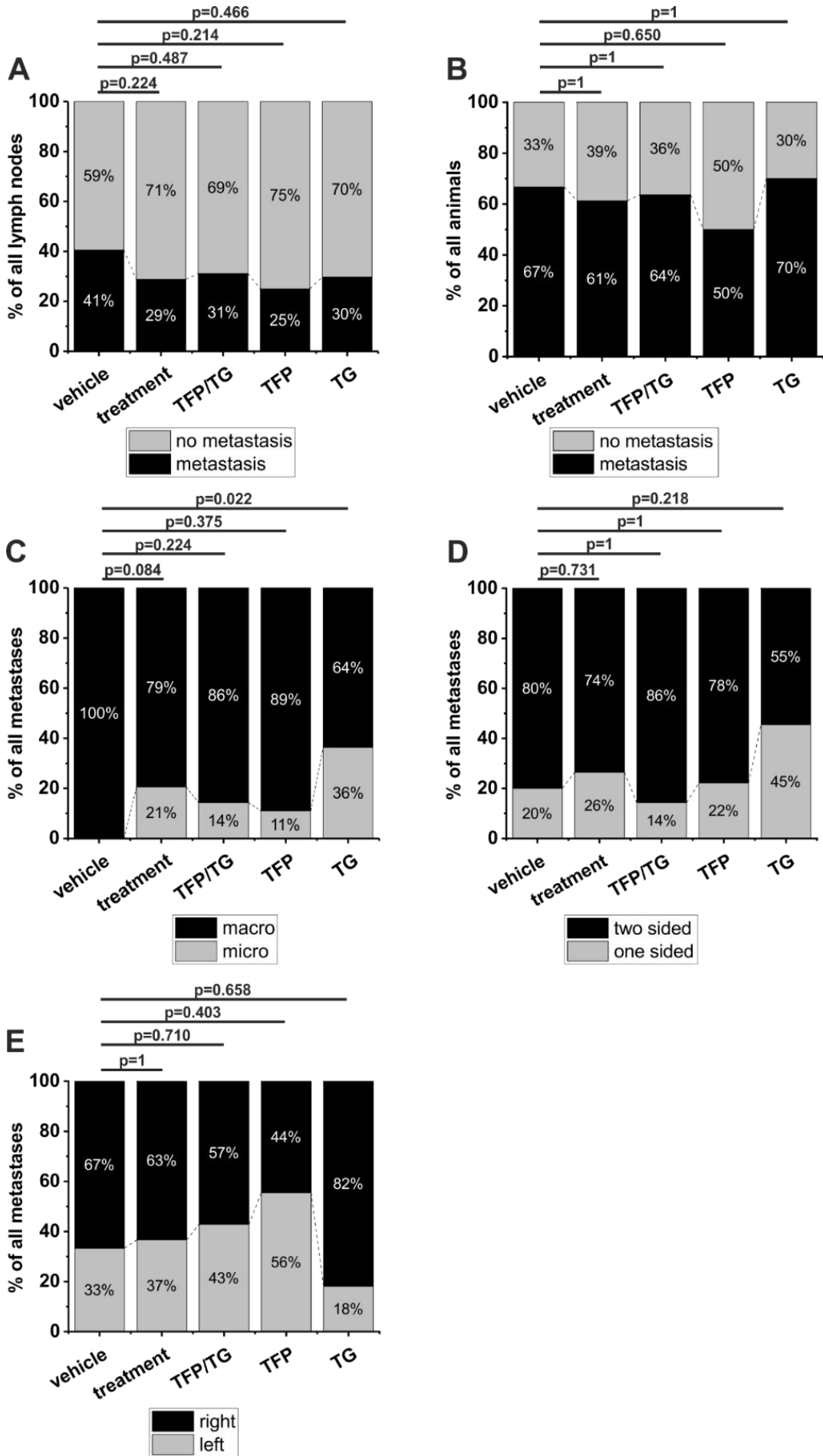


Figure 32 Analysis of metastases formation under different treatment conditions: The analysis is based on resected lymph nodes of 40 NOD-Scid mice. All excised lymph nodes were fully cut and every 20 μ m stained for H&E. Histological analysis of resected lymph nodes was performed double blinded by two investigators. **(A)** Summary of histological identified metastases dependent on the obtained treatment. **(B)** Summary of all animals identified with metastases in their cervical lymph nodes. **(C)** Summary of histological identified and categorized metastases. Metastases consisting of more than 20 tumour cells were categorized as macro-metastases respectively metastases consisting of less than 20 tumour cells were categorized as micro-metastases. **(D)** Summary of location of histological identified metastases dependent on a one or two sided metastases burden. **(E)** Summary of location of histological identified metastases dependent on left or right sided identification of the lymph node metastases. Significance was tested using a Fisher's exact test.

In the last step the distribution of metastases between left and right cervical lymph nodes was examined (Figure 32E). Again, no significant differences could be obtained regarding a preferred side for metastasis dependent on the injection site for the primary tumour. Tumour cells were initially inoculated on the right site of the tip of the tongue. Except for animals that were treated with TFP all treatment groups showed a slight preference for metastases formation in right sided cervical lymph nodes. Approximately two third of metastases regarding the vehicle treatment group as well as the general treated mice were located on the same site as tumour cells were injected. Regarding mice treated with TFP a trend towards a higher number of right sided metastases formation was visible (44 % right sided metastases). Related to mice treated with TG even 82 % of these metastases were located on the right site.

In summary the different treatments had no impact on survival of animals. Also, different treatment conditions had no impact on the general growth of the primary tumours. Concerning the size of primary tumours, a wide range was measured using histologically stained sections. Here, a significant difference was detectable in mice treated with TFP compared to vehicle animals. TFP treatment seemed to lead to larger primary tumours (Figure 31B). Next, the impact of treatment was analysed on metastases formation. Regarding all resected lymph nodes there was no significant impact of any treatment condition on the existence of metastases. A slight trend was detectable for a reduction in metastatic burden regarding TFP treatment and the general treatment of mice (Figure 32A). This trend was also visible analysing the general number of animals that developed metastases (Figure 32B). Animals treated with TFP showed a slightly reduced metastatic burden compared to vehicle animals. Regarding the size of identified metastases a significant difference was observable for animals treated with TG (Figure 32C). Here, the number of micro-metastases was significantly increased compared to vehicle animals. In case of TFP treatment the number of micro-metastases was decreased. In the next step the localisation of identified metastases was examined. No significant results were obtained but a trend for rather two-sided metastases was obviously (Figure 32D) expect for mice treated with TFP. Here, slightly more animals showed metastases in lymph nodes exclusively on one site of the neck. In the next step the preferred metastasis site was revealed. Animals treated with TFP preferred a metastasis formation on the left site that is even the opposite site where tumour cells

were inoculated (Figure 32E). Nevertheless, most of the results are not significant and can only show a vague trend in one of the given directions.

3.4.3. Impact of TFP/TG administration on haematogenous metastasis

In case of the investigation of the anti-metastatic and anti-proliferative effect of TFP and TG on the haematogenous metastasis only a first pilot study was done within this thesis.

In this first experimental setup 20 NOD-Scid mice were inoculated with FaDu wild-type cells in 200 µl PBS i.v.. The cells were prior filtered using a cell strainer with 20 µm pore size and all animals received a pre-medication of heparin i.p. (20 IU) at least 1 h before cell inoculation. All 20 animals except of one survived the cell inoculation in a good state of health. After cell inoculation all remaining 19 animals were randomly divided into a treatment group (n=11) as well as into a vehicle group (n=8) that only received the solvent control. Animals within both groups should be treated 3 times a week with a combination of TG (1.6 mg/kg) and TFP (0.5 mg/kg) or the solvent control starting 48 h after tumour cell inoculation. Regarding the concentration of both administered we used the publication of Körbel et al. 2018 as orientation guide. Here, female athymic nude mice were treated i.p. 3 times a week with 1.6 mg/kg TG in combination with 0.5 mg/kg TFP. This medication was used to treat mice that were inoculated with FaDu wild-type cells into their flanks while the medication was administered for five weeks. For mice that received the combinatory treatment an interval of 1 h was in-between both applications to ensure a valid absorption.

Concerning the remaining 19 mice that were inoculated with 1×10^6 tumour cells the treatment procedure was started 48 h after cell inoculation. The medication was started by the first application of 1.6 mg/kg TG in the case of 11 mice. Immediately after TG application all mice seemed to be very exhausted and lay down in their cages. After 1 h of recovery 0.5 mg/kg TFP should be administered. However, this medication was skipped due to the miserable state of health of all previously mice treated with TG. The corresponding vehicle animals (n=9) that received the solvent control were in a normal state of health. Approximately 3 to 4 h after the first TG application all treated mice were dead. The administered dose of 1.6 mg/kg TG was established with athymic nude mice, so that we concluded a higher sensitivity towards TG for the used NOD-Scid mice.

This hypothesis must be further considered. Therefore, a NOD-Scid mouse from the in-house breeding unit was medicated with 1.2 mg/kg TG and observed for its state of health. This mouse was in a good state of health prior to experimental start, had a normal body weight and showed a normal behaviour. Approximately 5 min after TG application the mouse slowed down in its movements, 10 min after TG application the mouse just lay in its cage. Nevertheless, the mouse was able to move when it was forced to. As already described in 3.4.1 and shown in Figure 30

the blood vessels were very impressively visible at the ears implying a potential temperature loss via vasodilation. The mouse died nearly 2.5 h after the administration of 1.2 mg/kg TG.

To be able to exclude the possibility that the supplied substance was not the correct substance, or it was used in the wrong concentration an athymic Balb/c mouse from the in-house breeding was medicated with 1.6 mg/kg TG, which should be tolerated by this mouse strain as already published by Körbel et al., 2018. The administered mouse behaved in a known way, it was attentive and curious. The mouse survived the high concentration of TG (1.6 mg/kg) so that a mistake in substance delivery was excluded.

Next, another NOD-Scid mouse of the in-house breeding unit was administered with 1.0 mg/kg TG to titrate a new tolerable concentration of TG especially for NOD-Scid mice. This mouse seemed to be not further impaired by 1.0 mg/kg TG so that this concentration was assumed as a new injectable concentration for TG. Therefore, 3 animals from the remaining vehicle group that were also inoculated with tumour cells were regrouped in a new treatment group regarding the new TG concentration. These 3 animals received 72 h after tumour cell inoculation their first treatment with TG in a 1.0 mg/kg concentration. 5 remaining animals served as vehicle animals and were administered with solvent control. All 3 animals behave like the previously treated mice that received the higher TG concentration and also died within the following 2 to 3 h after TG administration. The animals showed two differences compared to the in-house breeding NOD-Scid mouse: First, they received heparin (20 IU) i.p. 72 h before TG application and second, they received 1×10^6 tumour cells 72 h before TG, which may had a debilitating effect.

From the remaining 5 vehicle animals 2 animals were again regrouped and received for the first time 0.8 mg/kg TG one week after tumour cell inoculation. 1 animal was again treated with the higher and potential lethal dose of 1.0 mg/kg to be monitored in detail for the physiological reactions after application. Approximately, 3 min after application of TG the animal started to slow down in its movements, 10 min after application the animal showed an impressive blood vessel dilation at the ears. 20 min after application an administered electrocardiogram showed an irregular heart rate and also the body temperature was with 33°C approximately 5°C lower than normal (36.2 – 37.5°C normal body temperature of mice; (Danneman et al., 2000; Hankenson et al., 2018; Reitman, 2018)). Nevertheless, the animal survived the application of 1.0 mg/kg TG by keeping the body warm.

In the next establishing round Balb/c nude mice were used because the original used TG and TFP concentrations were established explicitly on this mouse strain (Figure 33). Because of the earlier establishing rounds NOD-Scid mice seemed to tolerate only minor concentrated treatment of TG. Therefore, 10 Balb/c nude mice received two pre-treatments administering 1.6 mg/kg TG and 0.5 mg/kg TFP i.p. prior to tail vein injection. In this case, animals received twice a pre-treatment that there was already a certain drug level before tumour cells were injected into the blood vessel system mimicking the EMT. On day 0 all mice received 1×10^6 cells i.v. into their tail

vein. The cells were prepared as already described in 3.3.1 by a 20 μm cell strainer and an incubation in 20 % FCS containing DMEM medium at 37°C and 5 % CO_2 for 10 min. 1 h before the tail vein injection took place mice were pre-treated with heparin. During cell inoculation one animal died. All remaining animals received the TG and TFP treatment in the above-mentioned concentrations every 48 to 72 h three times a week. The application was paused in between both substances for about 1 h while animals were allowed to recover in front of a heat lamp. After the 2nd administration of TG and TFP two animals died after about 2 h (Figure 33B). After the 4th TG and TFP administration another animal of the remaining two animals within the treatment group also died. Additionally, a vehicle animal was also sacrificed as a control animal (censored data, Figure 33B). The last animal of the initial treatment group of 5 animals died after the 11th administration of TG and TFP. The remaining 3 vehicle animals were sacrificed 76 days after the initial cell inoculation. Only 1 animal survived the TG and TFP treatment for 3 weeks (10 full injection days without including pre-treatment).

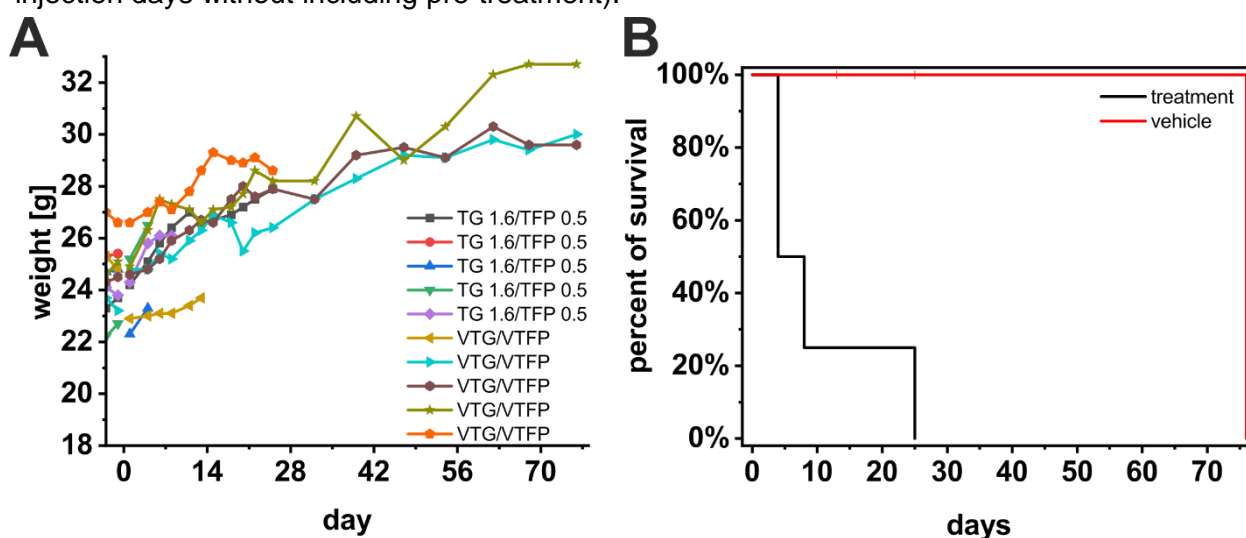


Figure 33 Summary of 1.6 mg/kg TG in combination with 0.5 mg/kg TFP treatment on Balb/c nude mice: (A) Weight history of all mice ($n=10$) injected into their tail veins with 1×10^6 cells. The observation period started at day -3 of the first treatment application until individual sacrifice day. Cells were inoculated on day 0. (B) Summary of the overall survival of all initial animals separated for treatment and vehicle.

Within the next establishing round a new minor concentration of TG was examined for its tolerability. For this purpose, the concentration of applied TG was reduced to 0.8 mg/kg. In this round in sum 4 NOD-Scid mice were initially pre-treated with 0.8 mg/kg TG in addition to 0.5 mg/kg TFP i.p. (Figure 34). The pre-treatment was done 2 times before cell inoculation of 1×10^6 took place at day 0. Again, animals were prepared with a heparin (20 IU) injection i.p. 1 h before the cell inoculation. All 4 mice survived the cell inoculation into their tail veins without any further complications. Because of an injection failure one animal died during the observation time after 12 days post cell inoculation. The cause of death were not the administered substances. The remaining animals ($n=10$) were treated with the already mentioned new concentrations every 48 to 72 h and sacrificed after 84 days. On the sacrifice day two μCT acquisitions were performed. The first μCT was done with the animal alive using a resolution of 18 μm . Before the second acquisition

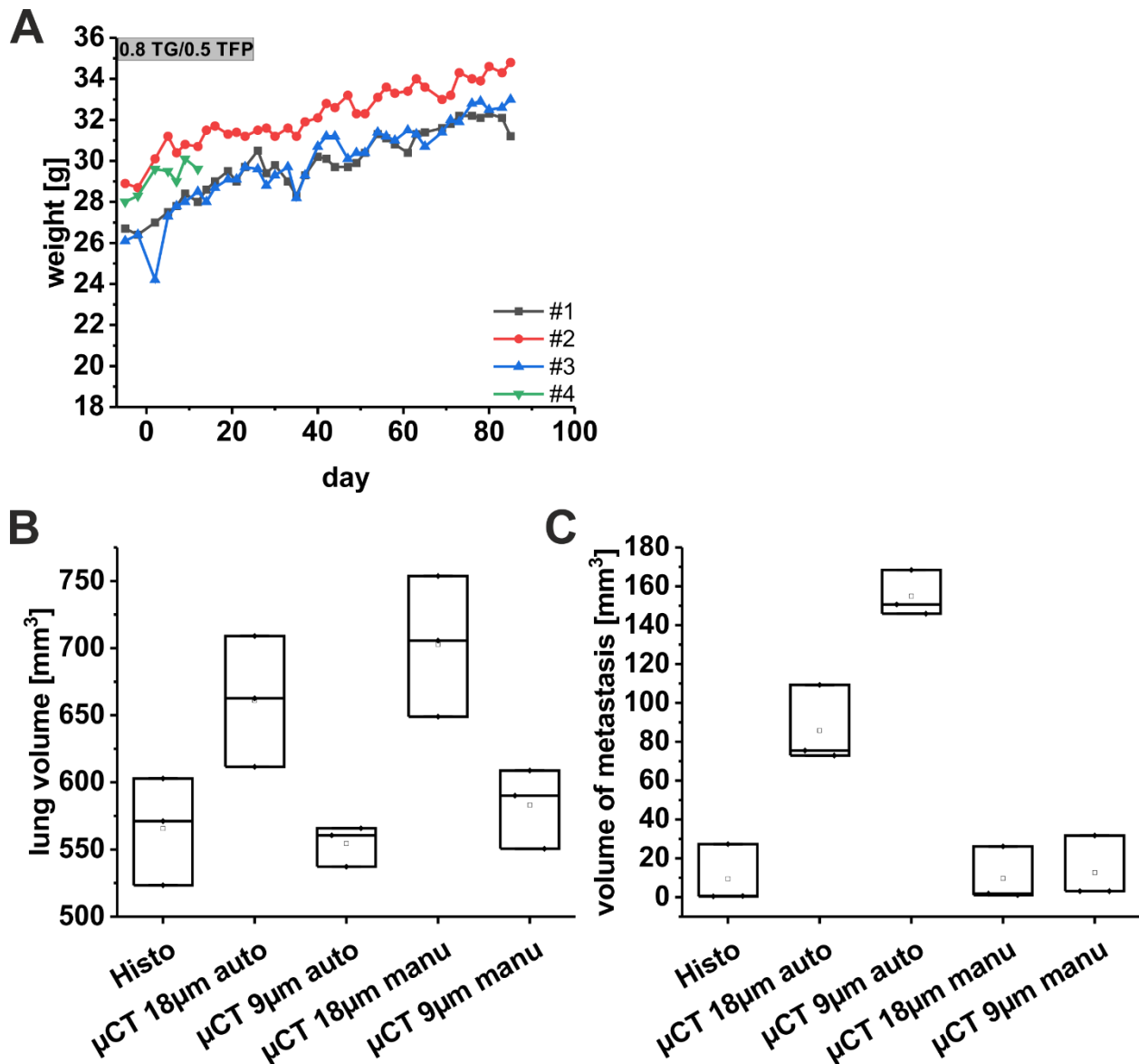


Figure 34 Summary of 0.8 mg/kg TG in combination with 0.5 mg/kg TFP treatment over 12 weeks: (A) Weight history of all mice (n=4) that were injected into their tail veins with 1×10^6 cells. The observation period started at day -5 of the first treatment application until sacrifice day. Cells were inoculated on day 0. **(B)** Calculated lung volume by histology, automated and manual μ CT evaluation based on 18 μ m and 9 μ m resolution. **(C)** Calculated metastases volume by histology, automated and manual μ CT evaluation based on 18 μ m and 9 μ m resolution. The median is shown by the line within the boxplot, the mean is indicated by a small black square within the boxplot.

the animal was sacrificed by an overdose of isoflurane inside the μ CT without changing the position of the animal. The second μ CT was acquired with a resolution of 9 μ m. Advantage of the second performed μ CT beside the higher resolution of 9 μ m was the absence of potential artefacts due to heart and breathing movements (Figure 34B, C). For the calculated lung volume similar differences were visible as already described for the whole data set in 3.3.4.1 (Figure 34B). Lung volume calculation based on histology ($\text{mean}_{\text{Histo}}=565.7 \pm 40.0 \text{ mm}^3$) and 9 μ m μ CT resolution ($\text{mean}_{9 \mu\text{m auto}}=554.5 \pm 15.2 \text{ mm}^3$; $\text{mean}_{9 \mu\text{m manu}}=583.2 \pm 29.6 \text{ mm}^3$) were most comparable independent of the manual or automated evaluation. Lung volume based on 18 μ m μ CT resolution was larger calculated ($\text{mean}_{18 \mu\text{m auto}}=661.0 \pm 48.7 \text{ mm}^3$; $\text{mean}_{18 \mu\text{m manu}}=702.8 \pm 52.5 \text{ mm}^3$). The metastases volume values obtained were very comparable

with the large dataset described above for the evaluation of different imaging techniques (3.3.4.1, Figure 34B, C). Again, the volume of metastases was overestimated by an automated calculation, especially based on 9 μm μCT resolution (Figure 34C; $\text{mean}_{\text{Histo}}=9.5\pm 15.5 \text{ mm}^3$; $\text{mean}_{18 \mu\text{m auto}}=85.8\pm 20.3 \text{ mm}^3$; $\text{mean}_{9 \mu\text{m auto}}=155\pm 11.9 \text{ mm}^3$; $\text{mean}_{18 \mu\text{m manu}}=9.7\pm 14.3 \text{ mm}^3$; $\text{mean}_{9 \mu\text{m manu}}=12.7\pm 16.5 \text{ mm}^3$). In general, the calculated volumes for metastases based on automated analysis were 9-fold to 16.3-fold higher compared to histological evaluation.

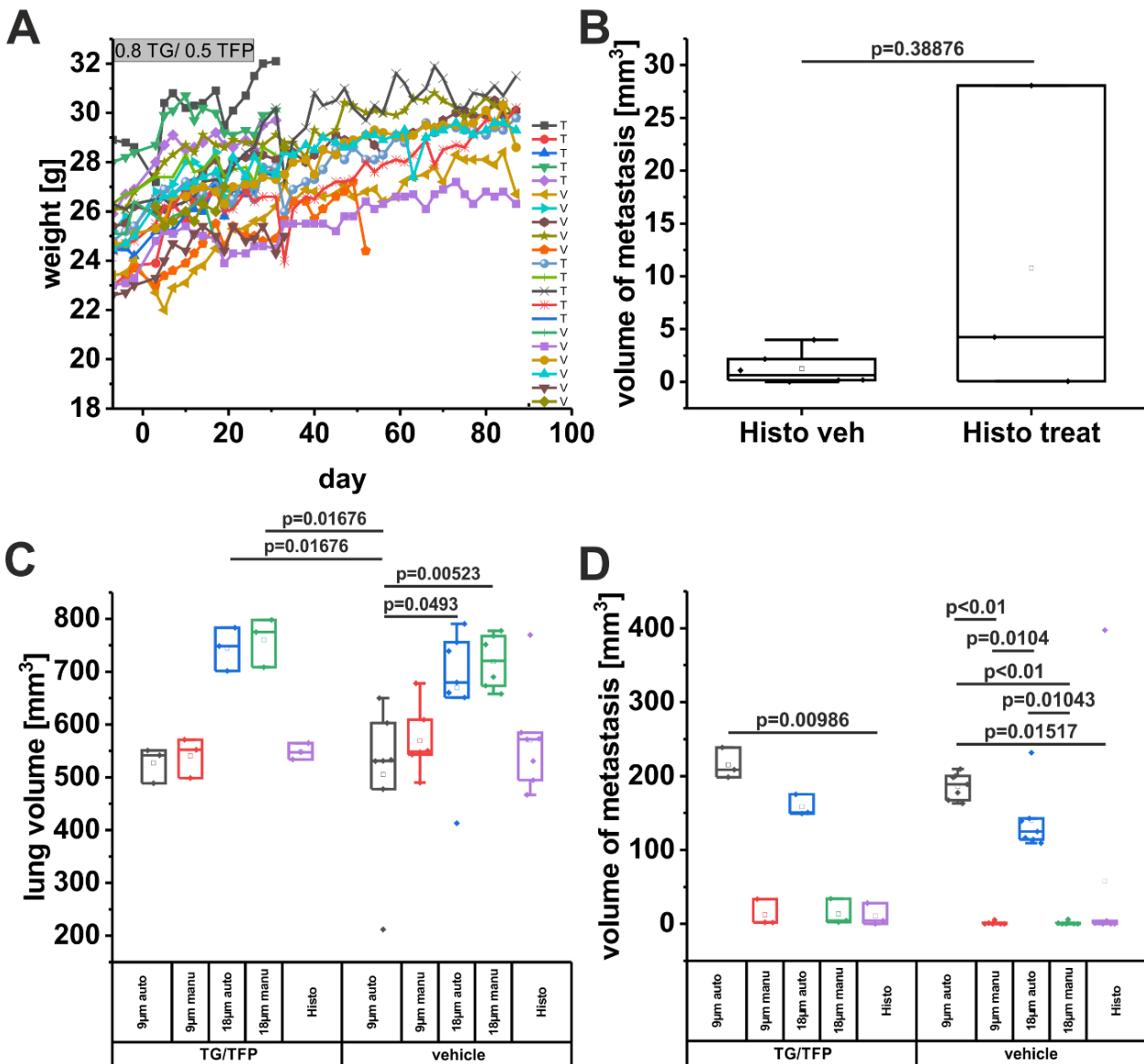


Figure 35 Summary of the first experiment of combinatory therapy containing higher animal numbers: (A) Weight history of all mice ($n=20$) that were injected into their tail veins with 1×10^6 cells. The observation period started at the day -7 of the first treatment application until the individual sacrifice day. Cells were inoculated on day 0. (B) Comparison of calculated metastases volume based on histological evaluation. Data show a normal distribution, significance was tested by a Student's t-test with Welch-correction. (C) Summary of all lung volumes calculated by different methods. Only mice with an observation time of at least 7 weeks were included into the analysis. (D) Summary of all metastases volumes calculated by different methods. Only mice with an observation time of at least 7 weeks were included. A one-way ANOVA was done for evaluation of significance. The median is shown by the line within the boxplot, the mean is indicated by a small black square within the boxplot. V – vehicle; T – treatment.

Unfortunately, the last experimental round was based only on 3 animals which survived until the end of the observation period of 12 weeks. Thus, the experimental setup was extended to 10 animals that received at least three times (one week) a pre-treatment with 0.8 mg/kg TG in combination with 0.5 mg/kg TFP prior cell inoculation of 1×10^6 cells at day 0. In addition, 10 animals were pre-treated three times with a corresponding solvent control. These animals also received 1×10^6 cells on day 0. All animals were pre-treated on inoculation day with 20 IU heparin approximately 1 h before the cells were inoculated. All animals survived the cell inoculation without further problems and received the next combinatory treatment respectively the solvent control 48 h after cell inoculation. One animal had to be sacrificed prematurely because it was limping (day 17). A μ CT acquisition was not performed in this animal as due to the early sacrifice no detectable metastases were expected. Before treatment, each single aliquot of TG and TFP was thawed for 20 min shaking in a thermomix at 37°C to guarantee a complete solubilisation of substances. Based on the observation that solved TG may crystallise during the freezing process it must be solubilised again before every injection by gentle heating and shaking. Due to a mistake during the process of substance thawing probably an overdose of TG was injected whereupon 7 treatment animals died (day 32, 4.5 weeks). From all these mice μ CT acquisitions were done in 18 μ m and 9 μ m resolution. Here, the 18 μ m acquisitions had to be done on a cadaver. Additionally, the lungs of the animals were evaluated histologically. 3 animals of the treatment group survived the incorrect preparation of substances and were sacrificed at the end of the observation period after 12 weeks (day 87). From the remaining 10 vehicle animals 3 animals were sacrificed as control animals. The remaining 7 animals were treated with solvent control until the end of the observation period of 12 weeks and were sacrificed 87 days after the initial cell inoculation. One exception within this group was an additional animal that show significant loss of weight and was already sacrificed after 52 days (7.4 weeks; orange line Figure 35A). The history of weights of all inoculated animals is shown in Figure 35A. For the evaluation of the lung as well as the metastases volume only animals that were sacrificed after at least 7 weeks of observation after the cell inoculation and received their respective therapy constantly were included. In general, the mice that were included in the analysis were at least 15 weeks old and therefore considered as adult (Flurkey et al., 2007). Concerning the overall lung volumes measured and calculated by different methods typical and already prior seen differences compared to the overall analysis were observed (Figure 35C). Again, the lung volumes calculated based on 18 μ m resolution of μ CT were slightly overestimated compared to histology and 9 μ m μ CT resolution. Regarding the differences between vehicle and treated animals no significant differences concerning the calculated lung volume were obvious expect for one mouse lung that was hard to circle in 9 μ m and 18 μ m μ CT images because of a large metastasis (Figure 35C). Referring to the outlier within the histology group this is the same mouse compared to the outlier in 9 μ m and 18 μ m automated μ CT calculation (Figure 35C). Regarding the metastases volumes

similar results concerning the different methods were obtained compared to the overall data set (Figure 35D, Figure 24). The metastases volume evaluation was overestimated by automated μ CT analysis. Referring to the histology-based gold standard for metastases evaluation there was no significant difference between treated (n=3) and vehicle animals (n=6) (Figure 35B). Nevertheless, the used animal numbers for this analysis were small and should be enlarged within further experiment.

3.4.3.1. New TG and TFP concentration

After an intensive literature research concerning TFP concentrations applied in mouse models, a new TFP concentration was chosen as a possible new standard. The previously applied concentrations relied on the mouse flank model described by Körbel et al., 2018. Here, the authors used a concentration of 1.6 mg/kg TG that was much too high for the used mouse strain within this thesis. Due to the complications described in the previous chapter in detail a new TG concentration was established. Finally, a TG concentration of 0.4 mg/kg was used within this thesis. Regarding the used TFP concentration by Körbel et al., 2018 the literature research led to a new conclusion that much higher TFP concentrations about up to 40 mg/kg were tolerated by NOD-Scid mice (Park et al., 2016; Feng et al., 2018; Kuo et al., 2019; Xia et al., 2019). Therefore, a pilot study was performed to investigate potential complications and side effects of new and much higher TFP concentrations combined with TG application. For this purpose, 5 NOD-Scid mice were treated over 6 weeks with a combinatory therapy of 15 mg/kg TFP and 0.4 mg/kg TG. These mice did not receive tumour cells because the focus was only on the applied drug concentrations and their potential side effects. Regarding TG an even lower concentration was used in combination with TFP so that animals were able to deal with the combination of both therapeutics. First, animals received 15 mg/kg TFP and got approximately 2 h for recovery before 0.4 mg/kg TG were applied. While the animals in the previous experiments did not show any considerable effect with 0.5 mg/kg TFP application, the animals now showed clear but non-severe reactions directly after the drug administration (15 mg/kg). These side effects were already described previously in detail in chapter 3.4.1.

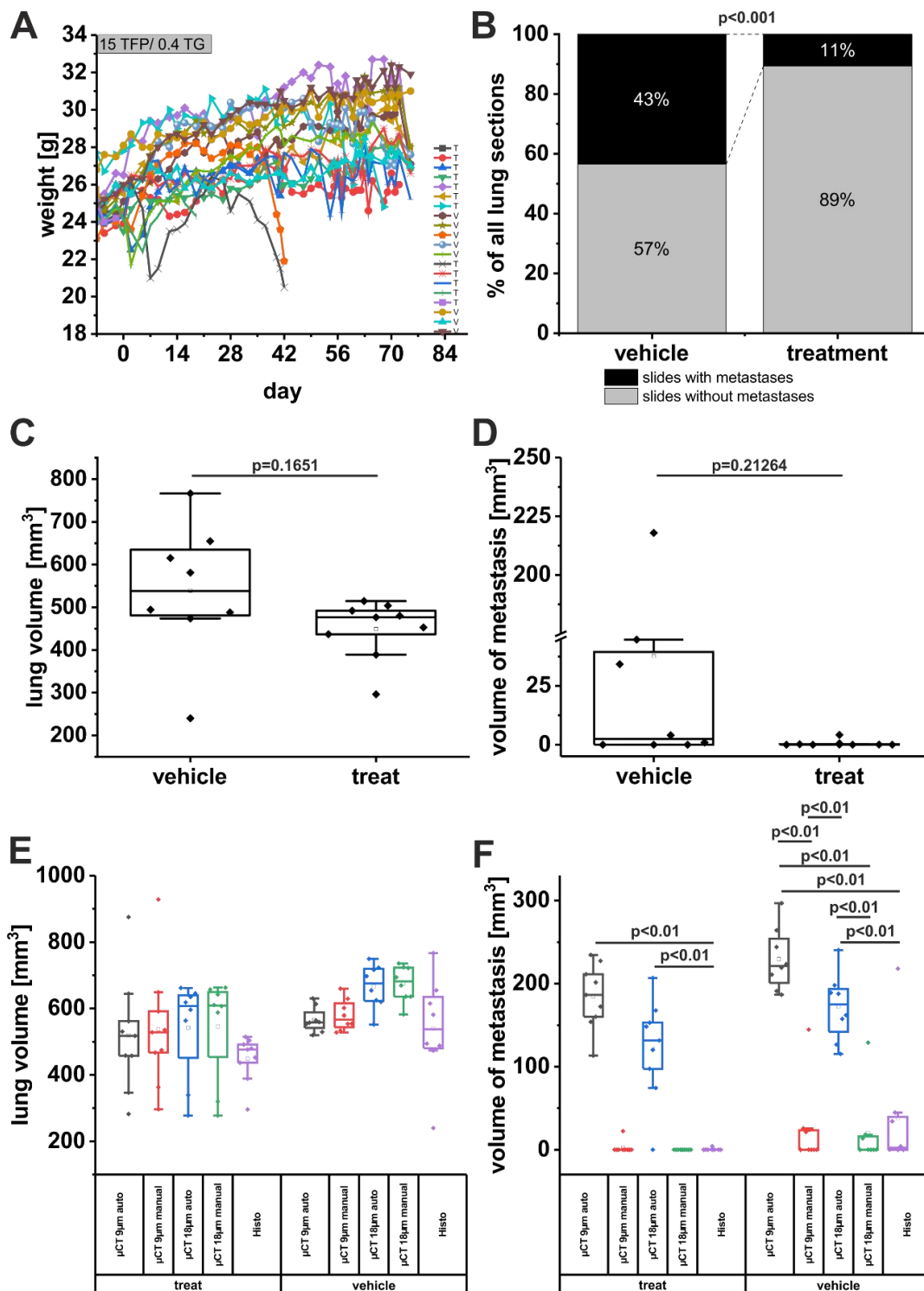


Figure 36 Summary of the new concentrations of combinatory therapy containing higher animal numbers: (A) Weight history of all mice (n=20) that were injected into their tail veins with 1×10^6 cells. The observation period started at day -7 of the first treatment application until individual sacrifice day. Cells were inoculated on day 0. (B) Summary of all investigated lung sections per animal regarding their existence of metastases independent of the metastases volume. Significance was tested using a Fisher's exact test. (C, D) Comparison of calculated lung and metastases volume based on histological evaluation between vehicle and treated animals. For this analysis only animals that survived more than 6 weeks were included. Significance for normal distributed lung volumes was tested using Student's t-test in addition with Welch-correction. Because data of metastases volumes showed no normal distribution significance was tested by Mann-Whitney U test. (E) Summary of all lung volumes calculated by different methods. Only mice with an observation time of at least 6 weeks were included in the analysis. (F) Summary of all metastases volumes calculated by different methods. Only mice with an observation time of at least 6 weeks were included. A one-way ANOVA was done for evaluation of significance concerning lung and metastases volumes. The median is shown by a line within the boxplot, the mean is indicated by a small black square within the boxplot. V – vehicle; T – treatment.

After the finished pilot experiment concerning new applied TFP and TG concentrations a group of 10 mice was pre-treated 3 times prior to cell inoculation with the above-mentioned new concentrations of TFP and TG in combination. Another 10 mice served as a control group and were treated with the respective solvent. On cell inoculation day all mice received a pre-treatment with heparin (20 IU) about 1 h prior inoculation of 1×10^6 cells. During cell inoculation 2 animals died (TFP/TG pre-treated). Within the course of the experiment 1 animal died after 19 days (2.7 weeks; 8 combinatory treatments). Another 3 animals were sacrificed after 6 weeks due to high losses of weight (2 combinatory treatment animals, 1 vehicle animal). 1 additional animal of the treatment group had to be sacrificed after 68 days (9.7 weeks). Nevertheless, all animals received 2 μ CT image acquisitions with 9 μ m and 18 μ m resolution on the individual sacrifice day and lungs were histologically processed. The remaining 13 animals of both groups were sacrificed after 10 weeks of observation and treatment with either the combinatory therapy or the solvent control. All animals received 2 μ CTs on sacrifice day and lungs were processed as previously described in 3.3.3. The final group of animals that reached the clinical endpoint consisted of 6 animals from the treatment group and 7 animals from the vehicle group. The history of weight is shown in Figure 36A. For metastases evaluation sections of the lung were investigated for the presence of metastatic tissue. Therefore, all sections containing metastases were set into ratio with the overall sections of all investigated lungs. This analysis revealed a highly significant difference of metastases bearing sections between vehicle and treatment animals by Fisher's exact test ($p < 0.001$, Figure 36B). Histologically evaluated lung volumes showed no significant differences between treated and vehicle mice but volumes showed a trend for smaller volume in treated animals ($\text{mean}_{\text{treat}} = 449.0 \pm 23 \text{ mm}^3$, $\text{mean}_{\text{vehicle}} = 539.1 \pm 55.3 \text{ mm}^3$; $p = 0.1651$, Figure 36C). Additionally, there was a slightly higher variability of lung volumes for vehicle animals. A comparison of metastases volumes between vehicle and treated animals shows no significant results due to a high range of calculated volumes ($\text{mean}_{\text{treat}} = 0.54 \pm 0.5 \text{ mm}^3$, $\text{mean}_{\text{vehicle}} = 37.7 \pm 26.5 \text{ mm}^3$, $p = 0.21234$, Figure 36D). Regarding the calculated lung and metastases volumes by different measurement methods a similar pattern as in the previous analyses was observed (Figure 36E, F). Lung volumes calculated by 18 μ m μ CT resolution seemed to be overestimated compared to histology gold standard (Figure 36E). Referring to metastases volumes as already shown the automated calculation overestimated the volumes by far compared to histology (9 μ m_{treat} - 341.6-fold, 18 μ m_{treat} - 226-fold; Figure 36F).

3.5. Generation and analysis of SEC62 knockout cells

This thesis gives an overview of the potential *in vivo* effects of a functional SEC62 knock-down by treatment with TG and TFP of orthotopically as well as i.v. inoculated HNSCC cells. This treatment is postulated to inhibit the migratory potential of tumour cells (Linxweiler et al., 2013;

Bochen et al., 2017). To study the underlying mechanisms and effects of the functional knock-down of *SEC62* by TG and TFP application a permanent knockout of *SEC62* was generated in the main cell line that was investigated in this thesis - FaDu. On that account the CRISPR-Cas9 technology was utilised to generate a stable *SEC62*-ko. For the generation of this genetically modified cell line originating from FaDu wild-type cells a plasmid already used and characterised by Fumagalli et al., 2016 was used. Because this plasmid does not contain a fluorescent protein a sorting of transfected cells was only possible by an antibiotic selection that was responsible for a several weeks lasting process. To ensure that newly generated *SEC62*-ko clones were based on a single clone these antibiotic-based selection process was done twice (Figure 11). Many potential clones did not survive these selection processes. Another critical point was the single clone selection. Transfected cells were seeded in an exceptionally low cell number (1.0×10^4) to ensure single seeded cells. After several weeks of cultivation small cell colonies were harvested as described in 2.6.3 using small cylinders and were further expanded. In an additional selection process these harvested colonies were seeded into a 96-well plate with a calculated distribution of 0.5 cells/well to ensure that a maximum of one cell is seeded per well. All wells were checked for the existence of cells. Wells that contained only one cell were further cultured and expanded to larger cell culture dishes. After this procedure generated single cell CRISPR clones were investigated for Cas9 activity, which is described in detail in the following chapter.

3.5.1. Descriptive validation of CRISPR clones

In this chapter a descriptive evaluation of a small selection of generated *SEC62*-ko clones is presented. The first method that was used to test for Cas9-activity was a western blot analysis of all generated single cell CRISPR clones. After the general screening for *SEC62*-ko clones by western blot analysis two clones were further investigated for their residual *SEC62* protein amount. Selection criteria of these two clones was no residual protein amount by western blot analysis (fold change for *SEC62* clone1: 0.04 ± 0.03 ; clone2: 0.03 ± 0.02) (Figure 38C).

In the following step an immunofluorescence staining of both clones in comparison to FaDu wild-type cells revealed a similar result as western blot analysis (Figure 38B). For western blot analysis and immunofluorescence staining the same polyclonal antibody that was generated by Martin Jung (Institute of Medical Biochemistry and Molecular biology, Saarland University, Homburg) was used. Nevertheless, the immunofluorescence staining showed a very slight *SEC62* signal for clone1. In case of clone2 no residual *SEC62* signal was detectable (Figure 38B).

Beside the validation of generated CRISPR-Cas9 clones on protein level, also nucleotide-based validation has been performed. Here, both clones were analysed by NGS as well as qRT-PCR to check the residual mRNA-level. Both experiments were performed for wt cells and both *SEC62*-ko clones. In case of qRT-PCR RNA was extracted from fresh frozen cell pellets by

ROTI[®]Zol RNA and reversely transcribed into cDNA. Afterwards, the cDNA was analysed by TaqMan[®] assays evaluating the amount of *SEC62* gene expression respectively to the used housekeeping gene *B2M* (Figure 38D). The localisation of TaqMan[®] assay was chosen behind the predicted Cas9 cutting site. A localisation of the used assay in front of the potential Cas9 cutting site would have been able to bind to an unchanged mRNA sequence. Both clones showed decreased levels of *SEC62* mRNA. In case of clone1 a reduction of 43 % ($p=0.1057$) was detectable while the calculated $2^{-\Delta\Delta Ct}$ for clone2 was decreased by 84 % ($p=0.00101$) (Figure 38D). In case of NGS, samples were sequenced in cooperation with Dr. Sascha Tierling (AG Prof. Dr. J. Walter – Genetic/Epigenetics, Saarland University, Saarbrücken) using an Illumina MiSeq. Prior to NGS an amplicon-based enrichment was done as described in 2.6.4.1. However, the sequencing did not cover the whole genomic sequence of *SEC62* as well as not the genomic sequence of *SEC62* after the predicted Cas9 cutting site. The obtained data sets were analysed by CRISPResso2 (Clement et al., 2019). The detailed procedure of data analysis is described in 2.6.4.1. Analysis results show that the Cas9 activity was not at the predicted cutting site between C-T than rather around or behind this predicted localisation. Detailed results compared to FaDu wt reference genomic sequence are shown in Figure 38A dependent on the analysed clone. Clone1 showed a rather various panel of potential mutations resulting in 5 different alleles that are also shown in Figure 37A and B. Clone1 showed a mutation panel consisting of 5 up to 15 deleted nucleotides or an insertion of a C in most of the analysed sequences (36 %). In case of clone2 only one phenotype was detected concerning an insertion of a C at the same localisation as the insertion in clone1 took place (88 %). The respective amount of reads regarding the occurred events were described in Figure 38A. Figure 37B also describes the situation over the whole amplicon sequence. The predicted cleavage site is marked by a vertically dashed line. Surrounding this site mutations were observed in both clones. In FaDu wt only a background noise was detectable. For clone1 also a various panel of mutations is obvious whereas the situation for clone2 is very distinct by an insertion directly behind the predicted cleavage site.

A

	sgRNA															PAM																											
wt	G	G	G	A	G	T	C	T	G	T	G	G	T	T	G	A	C	T	A	C	T	G	C	A	A	C	A	G	G	T	A	C	T	G	T	T	A	T	Reference				
	86.96% (440 reads)																																										
clone1	G	G	G	A	G	T	C	T	G	T	G	G	T	T	G	A	C	T	A	C	T	G	C	A	A	C	A	G	G	T	A	C	T	G	T	T	A	T	35.67% (5296 reads)				
	G	G	G	A	G	T	C	T	G	T	G	G	T	T	G	A	C	T	A	C	T	G	C	-	-	-	-	-	-	-	-	-	-	-	-	-	-	G	T	T	A	T	14.99% (2225 reads)
	G	G	G	A	G	T	C	T	G	T	G	G	T	T	G	A	C	T	A	C	T	G	C	-	-	-	-	-	G	T	A	C	T	G	T	T	A	T	13.28% (1971 reads)				
	G	G	G	A	G	T	C	T	G	T	G	G	T	T	G	A	C	T	A	C	T	G	C	A	A	C	A	G	G	T	A	C	T	G	T	T	A	T	12.77% (1896 reads)				
clone2	G	G	G	A	G	T	C	T	G	T	G	G	T	T	G	A	C	T	A	C	T	G	C	A	A	C	A	G	G	T	A	C	T	G	T	T	A	T	88.26% (11092 reads)				
	G	G	G	A	G	T	C	T	G	T	G	G	T	T	G	A	C	T	A	C	T	G	C	A	A	C	A	G	G	T	A	C	T	G	T	T	A	C	0.43% (54 reads)				
	G	G	G	A	G	T	C	T	G	T	G	G	T	T	G	A	C	T	A	C	T	G	C	A	A	C	A	G	G	T	A	C	T	G	C	T	T	A	T	0.34% (43 reads)			
	G	G	G	A	G	T	C	T	G	T	G	G	T	T	G	A	C	T	A	C	T	G	C	A	A	C	A	G	G	T	A	C	T	G	T	T	A	T	0.34% (43 reads)				
	G	G	G	A	G	T	C	T	G	T	G	G	T	T	G	A	C	T	A	C	T	G	C	A	A	C	A	G	G	T	A	C	T	G	T	T	A	T	0.34% (43 reads)				
	G	G	G	A	G	T	C	T	G	T	G	G	T	T	G	A	C	T	A	C	T	G	C	A	A	C	A	G	G	T	A	C	T	G	T	T	A	T	0.32% (40 reads)				
	G	G	G	A	G	T	C	T	G	T	G	G	T	T	G	A	C	T	A	C	T	G	C	A	A	C	A	G	G	T	A	C	T	G	T	T	A	T	0.30% (38 reads)				
	G	G	G	A	G	T	C	T	G	T	G	G	T	T	G	A	C	T	A	C	T	G	C	A	A	C	A	G	G	T	A	C	T	G	T	T	A	T	0.29% (37 reads)				
	G	G	G	A	G	T	C	T	G	T	G	G	T	T	G	A	C	T	A	C	T	G	C	A	A	C	A	G	G	T	A	C	T	G	T	T	A	T	0.29% (36 reads)				
	G	G	G	A	G	T	C	T	G	T	G	G	T	T	G	A	C	T	A	C	T	G	C	A	A	C	A	G	G	T	A	C	T	G	T	T	A	T	0.29% (36 reads)				
	G	G	G	A	G	T	C	T	G	T	G	G	T	T	G	A	C	T	A	C	T	G	C	A	A	C	A	G	G	T	A	C	T	G	T	T	A	T	0.26% (33 reads)				
	G	G	G	A	G	T	C	T	G	T	G	G	T	T	G	A	C	T	A	C	T	G	C	A	A	C	A	G	G	T	A	C	T	G	T	T	A	T	0.25% (31 reads)				
	G	G	G	A	G	T	C	T	G	T	G	G	T	T	G	A	C	T	A	C	T	G	C	A	A	C	A	G	G	T	A	C	T	G	T	T	A	T	0.24% (30 reads)				
	G	G	G	A	G	T	C	T	G	T	G	G	T	T	G	A	C	T	A	C	T	G	C	A	A	C	A	G	G	T	A	C	T	G	T	T	A	T	0.23% (29 reads)				
	G	G	G	A	G	T	C	T	G	T	G	G	T	T	G	A	C	T	A	C	T	G	C	A	A	C	A	G	G	T	A	C	T	G	T	T	A	T	0.22% (28 reads)				
G	G	G	A	G	T	C	T	G	T	G	G	T	T	G	A	C	T	A	C	T	G	C	A	A	C	A	G	G	T	A	C	T	G	T	T	A	T	0.21% (26 reads)					

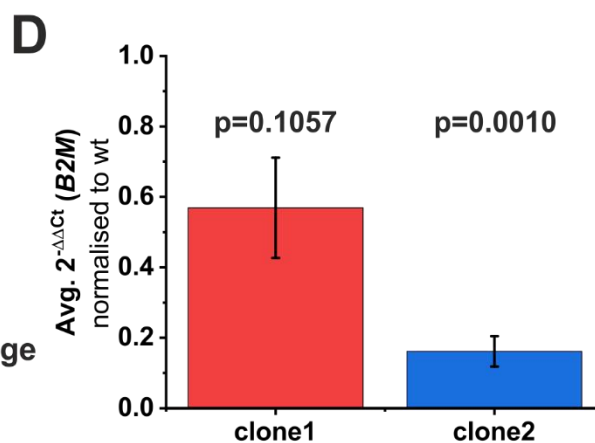
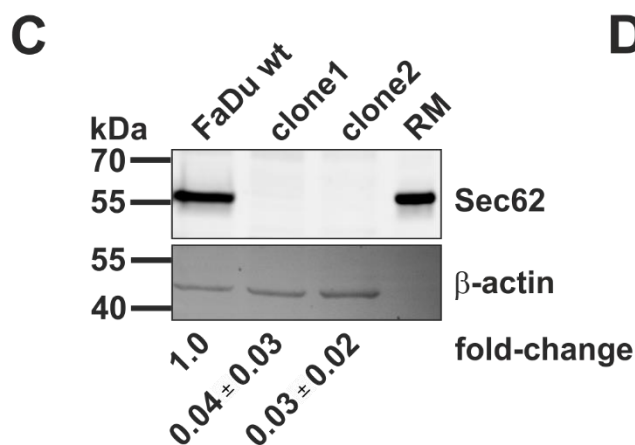
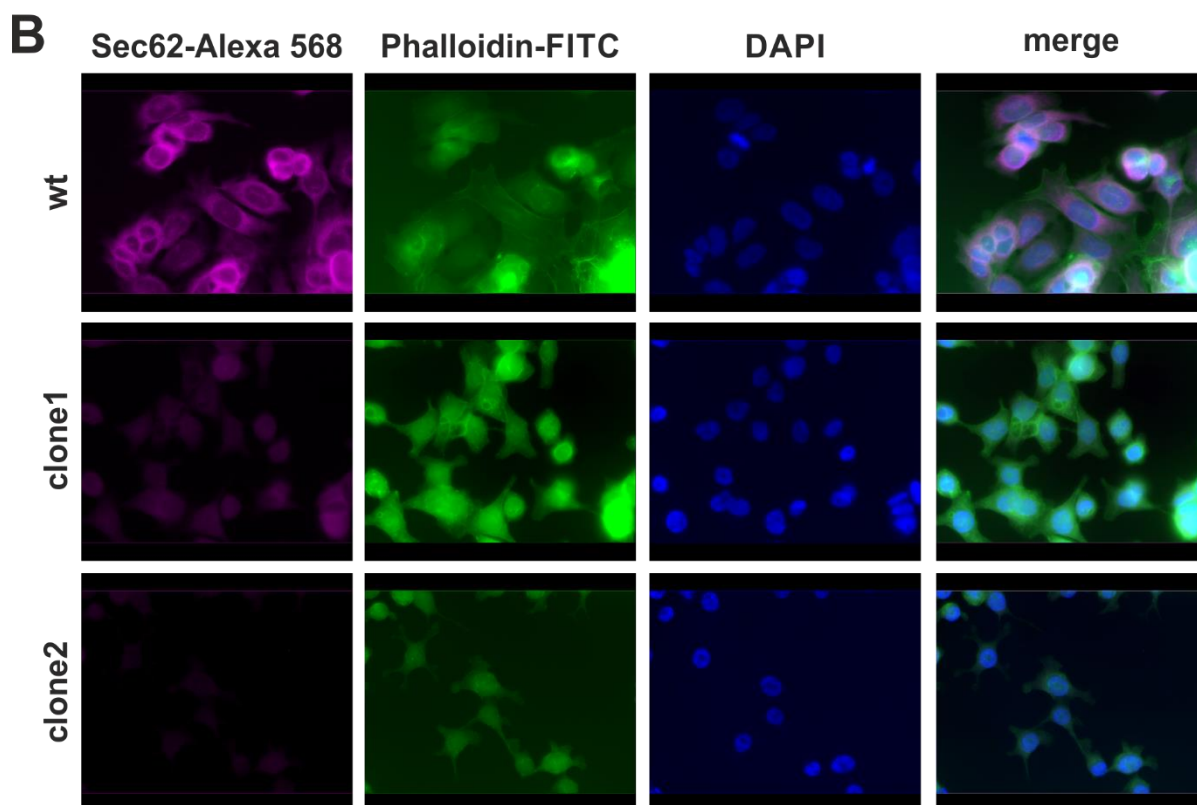


Figure 38 Characterisation of CRISPR-Cas9 generated SEC62-ko clones: (A) NGS data was analysed by using the online platform CRISPResso2 (Clement et al., 2019). In the first line the reference genomic sequence of FaDu wt is presented. Below, the sequencing results analysed with CRISPResso2 are listed of FaDu wt and both clones. The used sgRNA is marked with a blue box as well as the PAM sequence is marked with a green box within the reference sequence. Every nucleotide is marked in its specific colour: adenine – green, cytosine – orange, guanine – yellow and thymine – purple. A deletion is marked by a horizontal dash, a substitution is marked in bold, and an insertion is marked by a red box. (B) In case of immunofluorescence staining the same self-made antibody against SEC62 was used as for western blot validation. (C) Western blot analysis of FaDu wt cells and both clones. The calculated fold changes for SEC62 are indicated below the associated signal. The SEC62 fold change is indicated as a mean value (n=3) with the respective standard deviation. RM were used as a positive control for SEC62. (D) SEC62 mRNA expression relative to B2M expression that was used as a housekeeping gene. This figure was already published in a similar way in Körner et al., 2022.

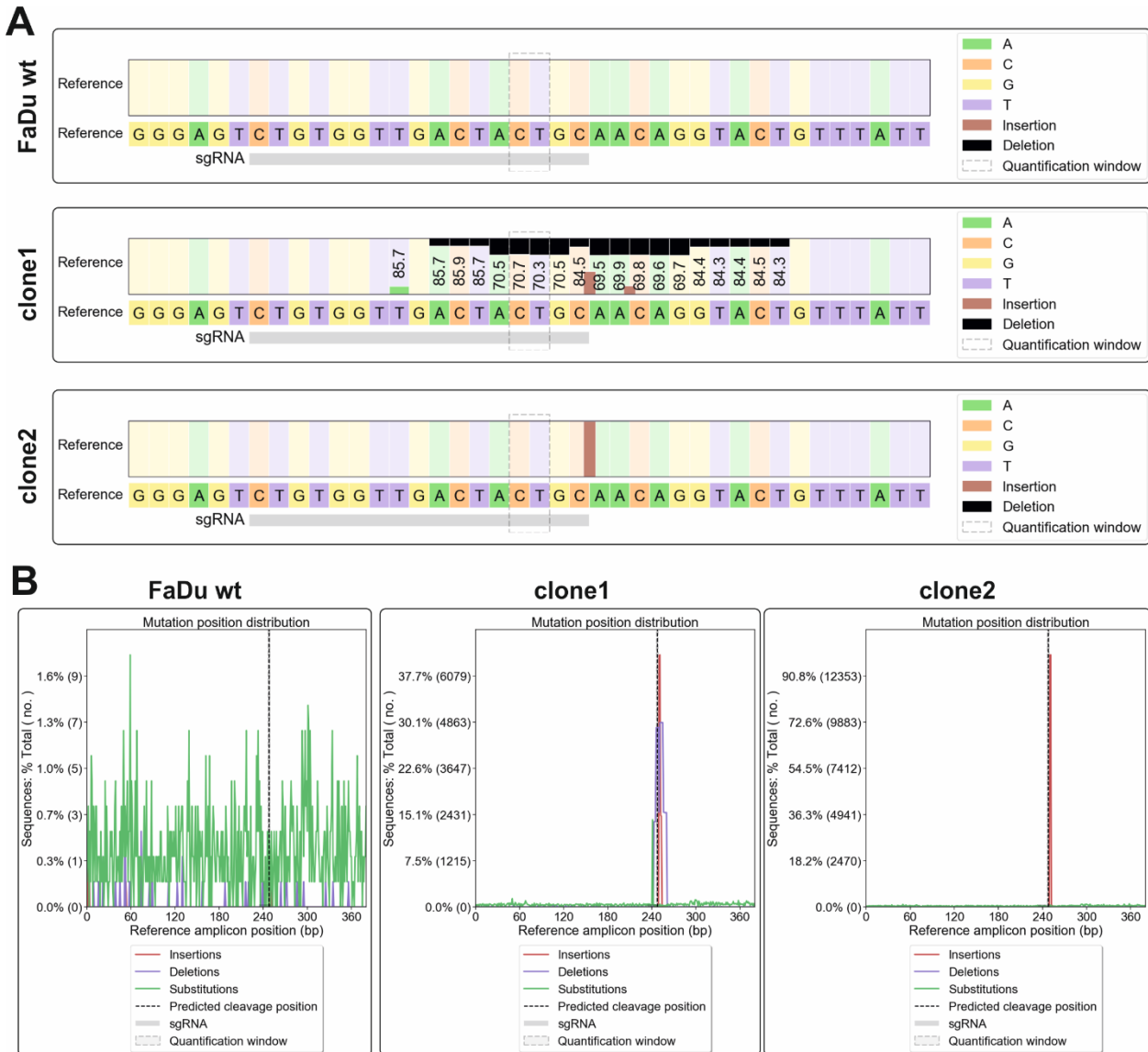


Figure 37 CRISPR-Cas9 event analysis in detail: (A) Described is the CRISPR-Cas9 event on nucleotide basis surrounding the predicted Cas9 cutting site. The sgRNA is marked in grey under the respective sequence. The predicted cutting site is highlighted with a box. Potential insertion events are marked by brown bars, potential deletions by black bars. (B) Localisation of potential mutations over the whole amplicon. Regarding FaDu wt only background was noise detectable. Clone 1 and clone 2 showed distinct mutation distribution surrounding the predicted cutting site. Insertions are marked in red, deletions were marked in blue, and substitutions were marked in green.

3.5.1.1. Potential OFF-targets

Regarding a description of two newly generated *SEC62*-ko clones also an OFF-target analysis has to be included into a full clone characterisation. OFF-targets exist due to a partial homology of the used target sequence to other segments within the genome. These potential OFF-targets are unintended genetic modifications that can occur through the usage of CRISPR-Cas9 technology. Potential OFF-targets of the used sgRNA in this thesis were predicted using the CHOP-CHOP v3 tool and are listed in Table 12 (Labun et al., 2019). Within this analysis 5 possible OFF-targets were predicted and are further described in this chapter. First, the genomic DNA was extracted from all *SEC62*-ko clones as well as from the wild-type cells (2.6.4.4). Afterwards, target-specific primer pairs were constructed for an amplicon specific PCR. All samples were shipped to GATC Biotech AG for capillary sanger sequencing. The obtained data sets were afterwards analysed using the TIDE webtool (Brinkman et al., 2014). This tool can precisely track possible indels and their frequencies by decomposition of a sequence chromatogram. Therefore, TIDE predicts the potential Cas9 cutting site between nucleotide 17 and 18 of the sgRNA that was uploaded to the tool without the PAM-sequence. In the next step a sequence chromatogram was uploaded from control sample (FaDu wt) as well as from the test sample (clone1, clone2). Here, a region for decomposition was set starting downstream of the predicted breaking site of the dsDNA. Due to low sequence quality this decomposition region had to be adjusted in some cases. As a result, the TIDE webtool gives an indel spectrum blot of the sample sequence including a calculated significance of each detected indel. The quality of the blot is indicated by R^2 . For ideal results R^2 should be >0.9 in the analysis concerning OFF-targets R^2 differs between 0.76 to 0.99. In case of smaller R^2 values the sequence quality was not perfectly fitting either from the control samples or the test sample. Keeping the R^2 values in mind the analysis was evaluated. Additionally, also a total efficiency was indicated within the indel spectrum blot. This value indicates the overall efficiency of mutations that occur around the predicted Cas9 cutting site of the total DNA amount and is calculated as $R^2 \times 100 \% \text{ wild type}$ (Brinkman and Steensel, 2019). Concerning the potential OFF-targets this total efficiency was rather negligible. As a second graph the TIDE webtool also generated an aberrant sequence signal blot for visualisation of the aligned sequences, marking the region for decomposition as well as the predicted Cas9 cutting site. Each single line stands for one nucleotide and its percentage of aberrant nucleotides of control and sample. The signal for control should be low along the whole sequence trace. A signal of 100 % indicates that the detected nucleotide does not fit to the control nucleotide at this position.

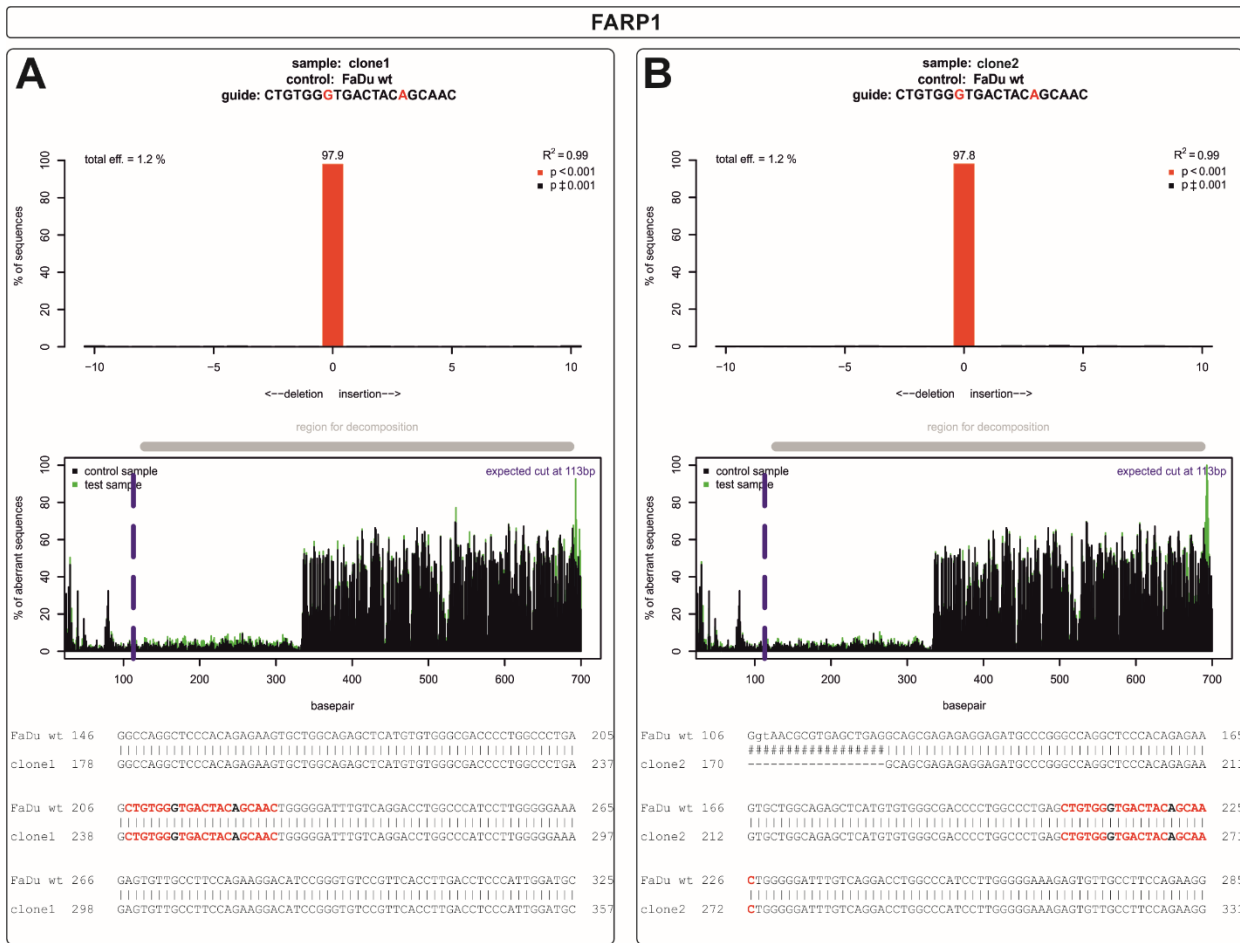


Figure 39 Potential OFF-target analysis with TIDE for FARP1: (A, B) Shown are the results of TIDE analysis for FARP1 as a potential OFF-target. For analysis sequence traces of clone1 respectively clone2 in addition to FaDu wt sequence were loaded into TIDE. Sequences were generated by Sanger sequencing. Above the first graphic the used sgRNA is shown including and highlighted the required 2 mismatches for binding to genomic FARP1 sequence. TIDE calculated a quality value represented by R^2 that is >0.9 for the mutational analysis concerning FARP1 as an OFF target. The total efficiency reveals the total amount of sequences that show mutations. Within the upper graphic the potential indel mutations are visualized regarding their frequency. The aberrant sequence blot shows the percentage of aberrant nucleotides between test and control sample. Marked is the predicted Cas9 breaking site with a dotted purple line as well as the region for decomposition (grey bar). In the lower part an alignment extract of the surrounding region of the modified sgRNA with highlighted mismatches is shown. (A) clone1, (B) clone2.

The first potential OFF-target analysed with the TIDE webtool is FARP1. For an incorrect binding of the Cas9 to FARP1-sequence 2 mismatches in the sgRNA would be required as indicated in Figure 39. Due to a high R^2 ($R^2_{clone1}=0.99$; $R^2_{clone2}=0.99$) in both analysed clones the results seemed to be rather reliable. In 97.9 % (clone1) respectively 97.8 % (clone2) of the analysed sequences no indel mutations could be found. Also, the aligned raw sequence data between each clone and the wild-type sequence revealed no undetected mutation event around the predicted cutting site. The sgRNA including its needed mismatches were marked in the sequence traces.

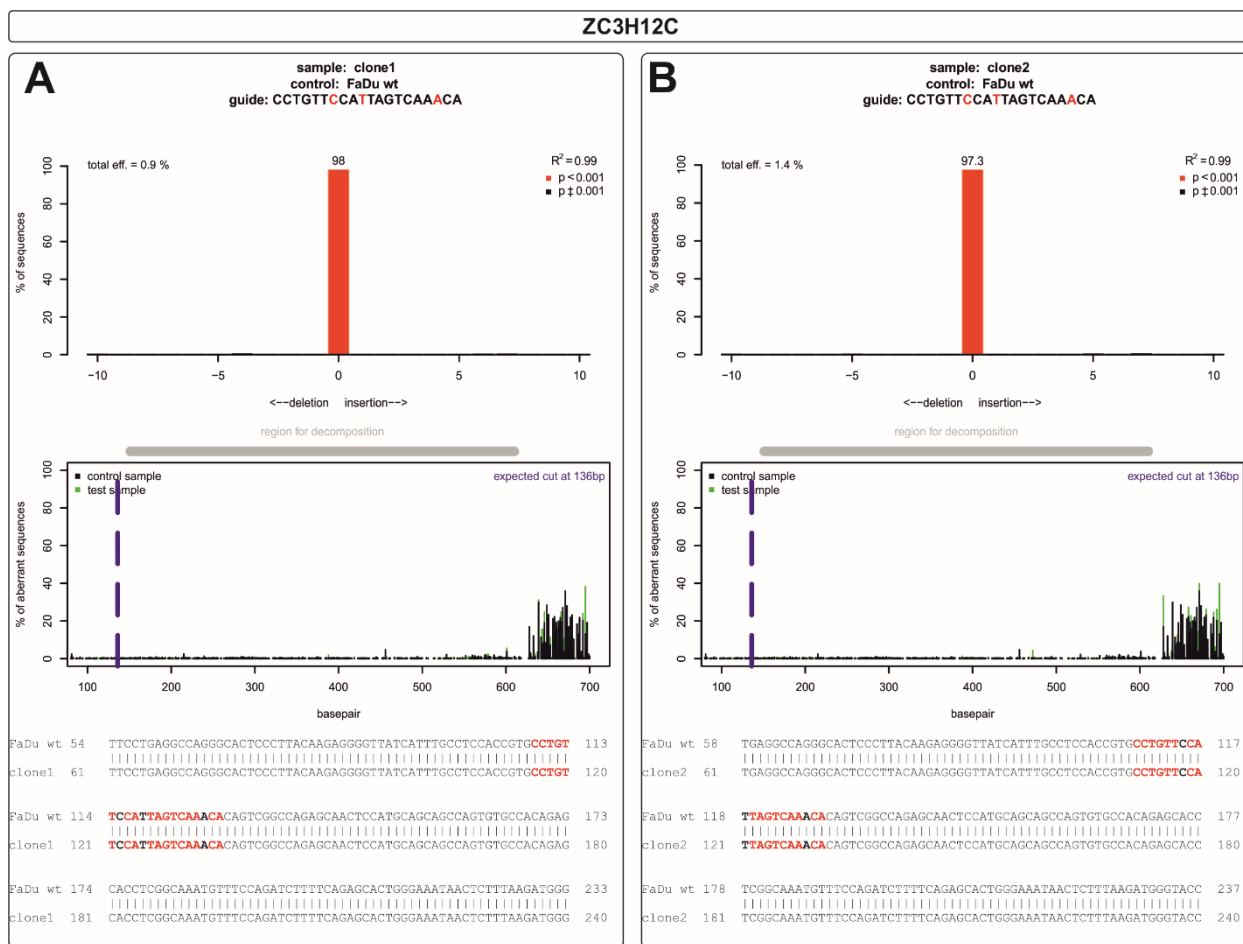


Figure 41 Potential OFF-target analysis with TIDE for ZC3H12C: (A, B) Shown are the results of TIDE analysis for ZC3H12C as a potential OFF-target. For analysis sequence traces of clone1 respectively clone2 in addition to FaDu wt sequence were loaded into TIDE. Sequences were generated by Sanger sequencing. Above the first graphic the used sgRNA is shown including and highlighted the required 3 mismatches for binding to genomic ZC3H12C sequence. TIDE calculated a quality value represented by R^2 that is >0.9 for the mutational analysis concerning ZC3H12C as an OFF target. The total efficiency reveals the total amount of sequences that show mutations. Within the upper graphic the potential indel mutations are visualized regarding their frequency. The aberrant sequence blot shows the percentage of aberrant nucleotides between test and control sample. Marked is the predicted Cas9 breaking site with a dotted purple line as well as the region for decomposition (grey bar). In the lower part an alignment extract of the surrounding region of the modified sgRNA with highlighted mismatches is shown. (A) clone1, (B) clone2.

The third analysed OFF-target that needs 3 mismatches of the used sgRNA is ZC3H12C (Figure 41). Here, the TIDE webtool could achieve highly trustful results concerning the calculated R^2 ($R^2_{clone1}=0.99$; $R^2_{clone2}=0.99$). Only in the last ~130 nucleotides of control and sample sequences the quality worsens in both clones. In this case the window for decomposition was decreased so that these regions were not included for analysis anymore. Concerning the total DNA amount only in 0.9 % (clone1) respectively 1.4 % (clone2) of the analysed sequences a mutation was detected by TIDE analysis. In 98 % (clone1) and 97.3% (clone2) no indel mutations were detectable. These results were also detectable in the original sequence trace of both clones aligned to the control sequence.

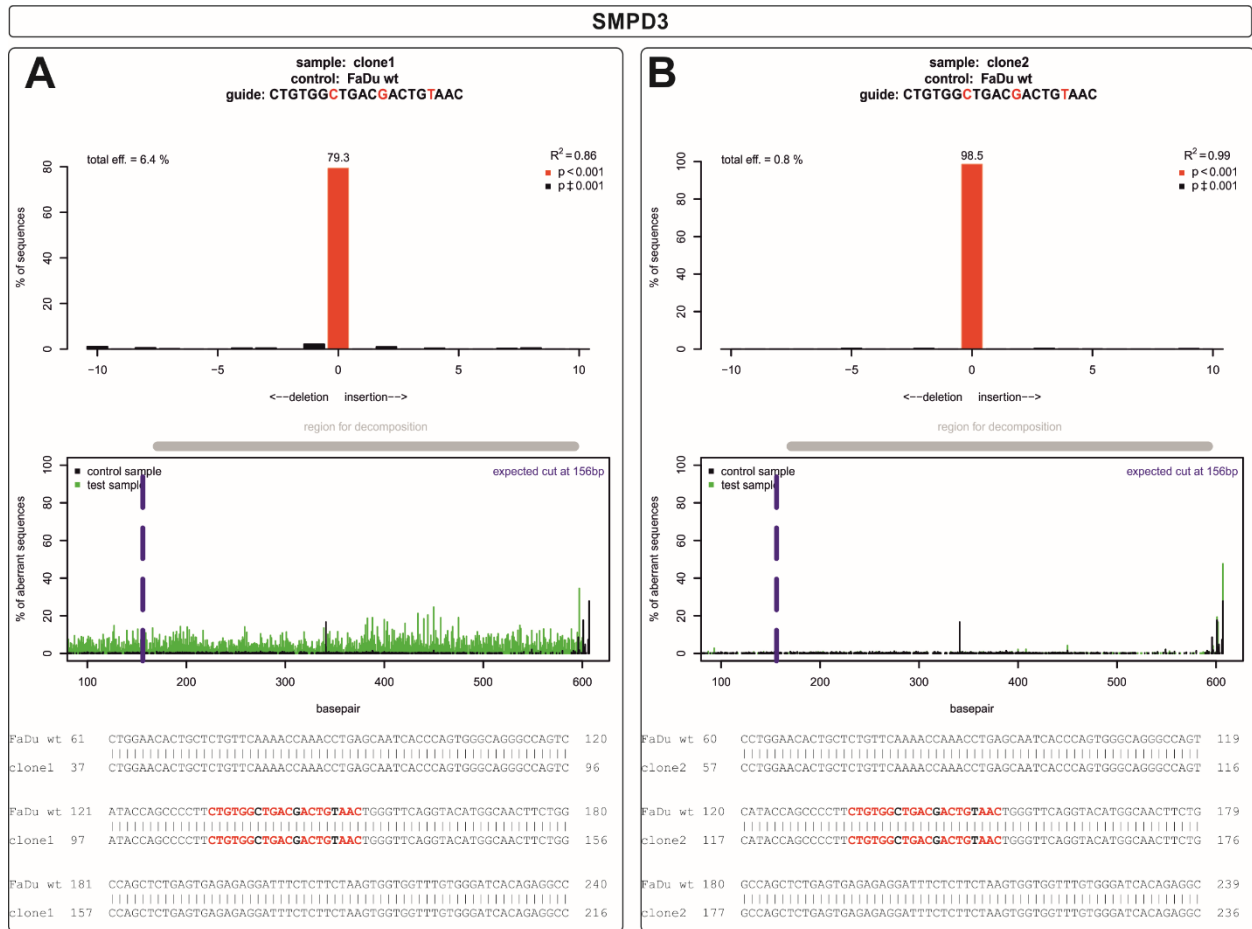


Figure 42 Potential OFF-target analysis with TIDE for SMPD3: (A, B) Shown are the results of TIDE analysis for SMPD3 as a potential OFF-target. For analysis sequence traces of clone1 respectively clone2 in addition to FaDu wt sequence were loaded into TIDE. Sequences were generated by Sanger sequencing. Above the first graphic the used sgRNA is shown including and highlighted the required 3 mismatches for binding to genomic SMPD3 sequence. TIDE calculated a quality value represented by R^2 that is in the case of clone2 >0.9 for the mutational analysis concerning SMPD3 as an OFF target. In the case of clone1 the smaller R^2 value may result from lower sequence quality. The total efficiency reveals the total amount of sequences that show mutations. Within the upper graphic the potential indel mutations are visualized regarding their frequency. The aberrant sequence blot shows the percentage of aberrant nucleotides between test and control sample. Marked is the predicted Cas9 breaking site with a dotted purple line as well as the region for decomposition (grey bar). In the lower part an alignment extract of the surrounding region of the modified sgRNA with highlighted mismatches is shown. (A) clone1, (B) clone2.

The last checked potential OFF-target was SMPD3 for which a mismatch of 3 nucleotides of the used sgRNA would have been needed for binding and therefore Cas9 breaking (Figure 42). Here, the results seemed trustworthy because of a high R^2 value of the analysed sequences ($R^2_{clone1}=0.99$; $R^2_{clone2}=0.99$). In 97.9 % (clone1) and 97.8 % (clone2) of all analysed sequences no indel mutations were detected. Even though the R^2 value was very high the calculated efficiency of Cas9 was about 6.4 % for clone1. For clone2 the total efficiency was calculated to 0.8 %. The sequence trace of clone1 showed a high background noise, which can lead to a higher total efficiency. Checking the alignments of both clones against the control sequence, no mutations surrounding the Cas9 breaking site were detectable.

To confirm the validity of the obtained results by TIDE analysis for the predicted OFF-targets this analysis was also performed for SEC62 (Figure 43). The obtained quality value R^2 was in an acceptable range ($R^2_{clone1}=0.89$; $R^2_{clone2}=0.95$). For SEC62 analysis the obtained total efficiency

was strongly different to the prior efficiencies of the OFF-targets. For clone1 about 88.8 % of the analysed sequences showed mutations whereas for clone2 even 93.8 % of all sequences showed differences to the control sequence. Also, the indel profile differed between both clones. For clone1 69.6 % of the detected mutations were confirmed as an insertion of 1 nucleotide, in 7 % of the sequences a deletion of 5 nucleotides appeared and in 12.2 % of the sequences a deletion of 7 nucleotides was detectable. For clone2 in 91.5 % of all sequences an insertion of 1 nucleotide was analysed. Additionally, in 2 % of the sequences also 2 nucleotides were inserted. That fact that there are mismatches between the clone nucleotide sequence and the control sequence was also visible in the alignments.

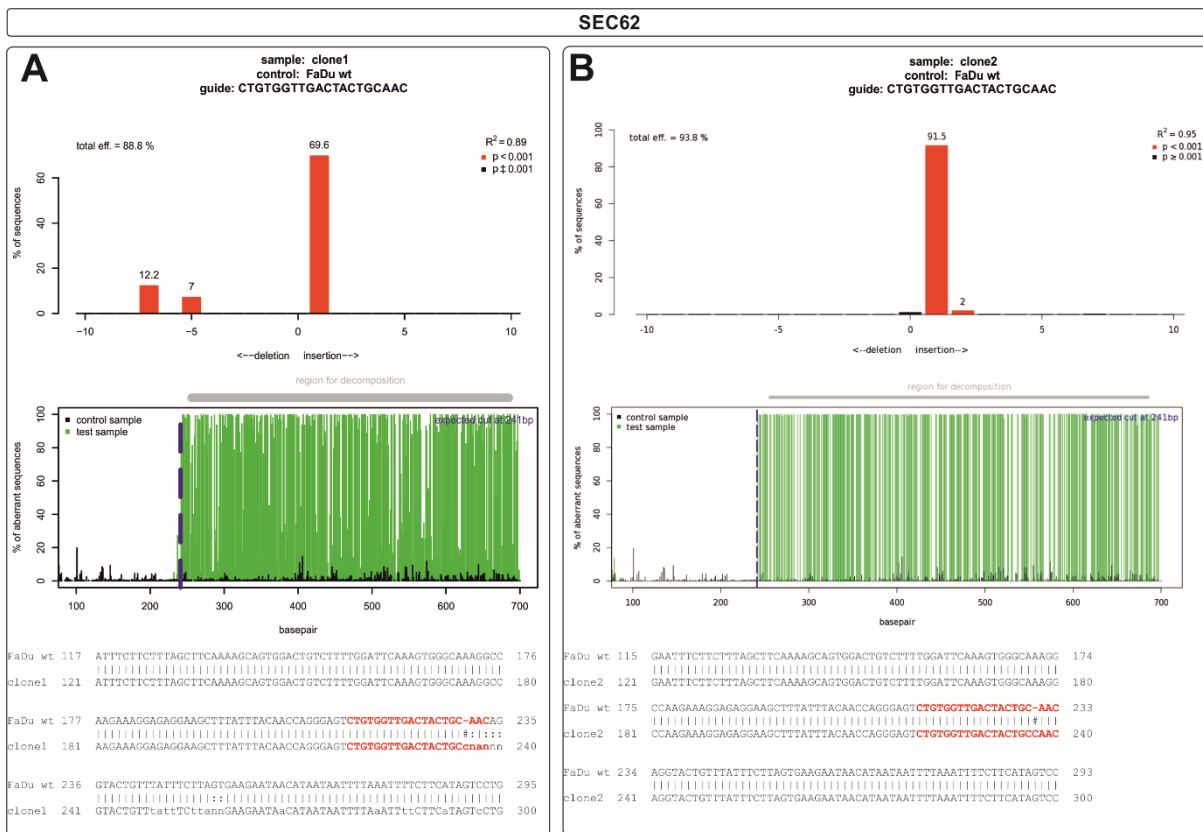


Figure 43 Confirmation of SEC62-CRISPR event with TIDE: (A, B) Shown are the results of TIDE analysis for SEC62 as the ON-target. For analysis sequence traces of clone1 respectively clone2 in addition to FaDu wt sequence were loaded into TIDE. Sequences were generated by Sanger sequencing. Above the first graphic the used sgRNA is shown for binding to genomic SEC62 sequence. TIDE calculated a quality value represented by R² that is >0.9 for the mutational analysis concerning SEC62 as an ON-target. The total efficiency reveals the total amount of sequences that show mutations. Within the upper graphic the potential indel mutations are visualized regarding their frequency. The aberrant sequence blot shows the percentage of aberrant nucleotides between test and control sample. Marked is the predicted Cas9 breaking site with a dotted purple line as well as the region for decomposition (grey bar). In the lower part an alignment extract of the surrounding region of the modified sgRNA with highlighted mismatches is shown. (A) clone1, (B) clone2.

3.5.1.2. RNA-sequencing analysis

Besides the general description concerning residual mRNA and protein level by qRT-PCR, western blot analysis and immunofluorescence staining of newly generated CRISPR-Cas9 *SEC62*-ko clones and an evaluation of potential OFF-target effects by a similar genomic sequence also a RNA-sequencing (RNA-seq) was done to get a deeper impression of targeted genes, biological processes, and molecular functions in *SEC62*-ko cells compared to wt cells. Therefore, RNA was isolated from frozen cell pellets and sequenced in cooperation with GENEWIZ Germany GmbH (Leipzig, Germany) using an Illumina NovaSeq platform with an estimated data output of ~20 M paired-end reads per sample. For analysis of the obtained sequencing data Perseus software (version 1.6.15.0) was used and loaded with TPM values as starting values after a previous quality evaluation of obtained sequencing reads and a processing step to remove adaptor sequences and nucleotides with poor quality using Trimmomatic v.0.36 (Tyanova et al., 2016). In addition, trimmed reads were mapped to the Homo sapiens GRCh38 reference genome using STAR aligner v.2.5.2b. All these pre-processing steps were already done by GENEWIZ Germany GmbH so that the obtained TPM values could be used for further analysis using Perseus software. As an initial step of the following analysis low expressed genes were removed. Therefore, used parameters were set for at least 1 count in each group, whereas groups were defined for three biological replicates of FaDu wt, clone1, and clone2. This step led to a reduction of 43,694 (76 %) genes that were too low expressed and therefore excluded from the following analysis steps. Residual TPM values (13,806 genes) were transformed for principal component analysis (PCA) and showed a harmonic distribution within each group (Figure 44C). As expected wt samples showed the largest distribution between single replicates whereas replicates of both clones showed a higher similarity. In the next step a differential expression (DE) analysis was performed using edgeR with TMM (trimmed mean of M-values) as normalisation method to calculate the fold change (FC), false discovery rate (FDR) and corresponding p-values. The DE analysis revealed all significantly regulated genes within both *SEC62*-ko clones (n=215; Figure 45A). The hierarchical analysis showed impressively the heterogeneity of FaDu wt cells in the individual heatmap pattern for each replicate. Both clones showed a more similar pattern within their individual replicates also visualised by the height of each cluster. In more detail, significantly regulated genes are presented using a volcano plot for each clone highlighting the significantly upregulated genes in orange and all significantly downregulated genes in green (Figure 44A, B). Here, *SEC62* was only significantly downregulated for clone2. In case of clone1, *SEC62* was also downregulated, but not on a significant level. Nevertheless, *SEC62* is highlighted in black in the plot. In sum DE analysis revealed for clone1 an significant regulation of 119 genes and 115 genes for clone2. The general sum of significantly regulated genes seemed very equally distributed. In detail, there were 103 upregulated genes for clone1 together with 16 significantly downregulated genes (Figure 44A). For clone2 the CRISPR-Cas9 event caused a more balanced

pattern of 58 significantly upregulated genes in combination with 57 significantly downregulated genes (Figure 44B). Based on 215 regulated genes in sum, 19 genes were regulated in both clones (Figure 45B). 4 shared regulated genes were downregulated in both, whereas 15 common genes were upregulated (Figure 46).

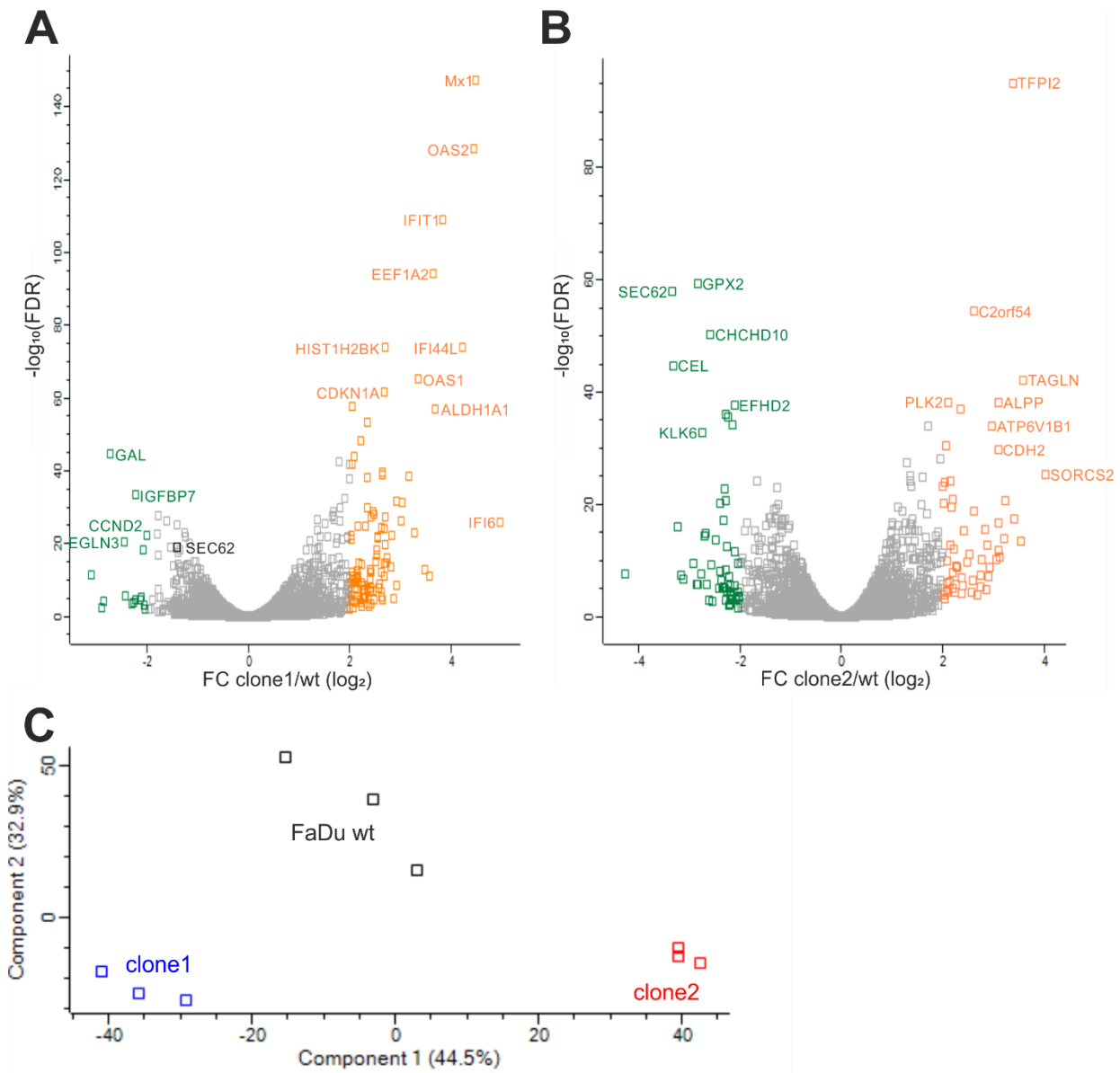


Figure 44 Significantly regulated genes upon *SEC62*-ko: (A, B) Highlighted in green and orange are all significantly regulated genes upon a *SEC62*-ko due to CRISPR-Cas9 technology in clone1 (A) and clone2 (B). Orange coloured symbols show all significantly upregulated genes, whereas significantly downregulated genes are coloured in green. *SEC62* is not significantly downregulated in clone1 but marked in black. (C) PCA plot shows the distribution of all replicates for FaDu wt cells as well as for both clones.

In a further step, these significantly regulated genes were investigated for their gene ontologies (GO). Therefore, significantly regulated genes ($n=215$; $n_{\text{clone1}}=119$; $n_{\text{clone2}}=115$) were divided into up- and downregulated genes ($n_{\text{up}}=146$; $n_{\text{down}}=69$) before datasets consisting of Ensemble gene identifiers (ENSG-number) were loaded into GO Term Finder tool to analyse correlations in biological processes, molecular functions as well as cellular components (Boyle et al., 2004). For this analysis a p-value cutoff for significantly shared GO-terms was set to 0.05. In addition, a

Bonferroni correction was done, and the FDR was calculated. Afterwards, the identified GOs were transferred to REVIGO (reduce and visualize gene ontology) for visualisation (Supek et al., 2011). Because obtained annotated results displayed very specific GO-terms additionally an analysis using Panther was performed using the Panther GO-slim annotation for more general GO-term definitions (Mi et al., 2021). In a last step also an analysis by DAVID (Database for Annotation, Visualization and Integrated Discovery) was done. Here, datasets were analysed for potential clustering, as well as potential involvement in certain pathways. In case of pathway analysis KEGG (Kyoto Encyclopedia of Genes and Genomes) was used and integrated to DAVID analysis.

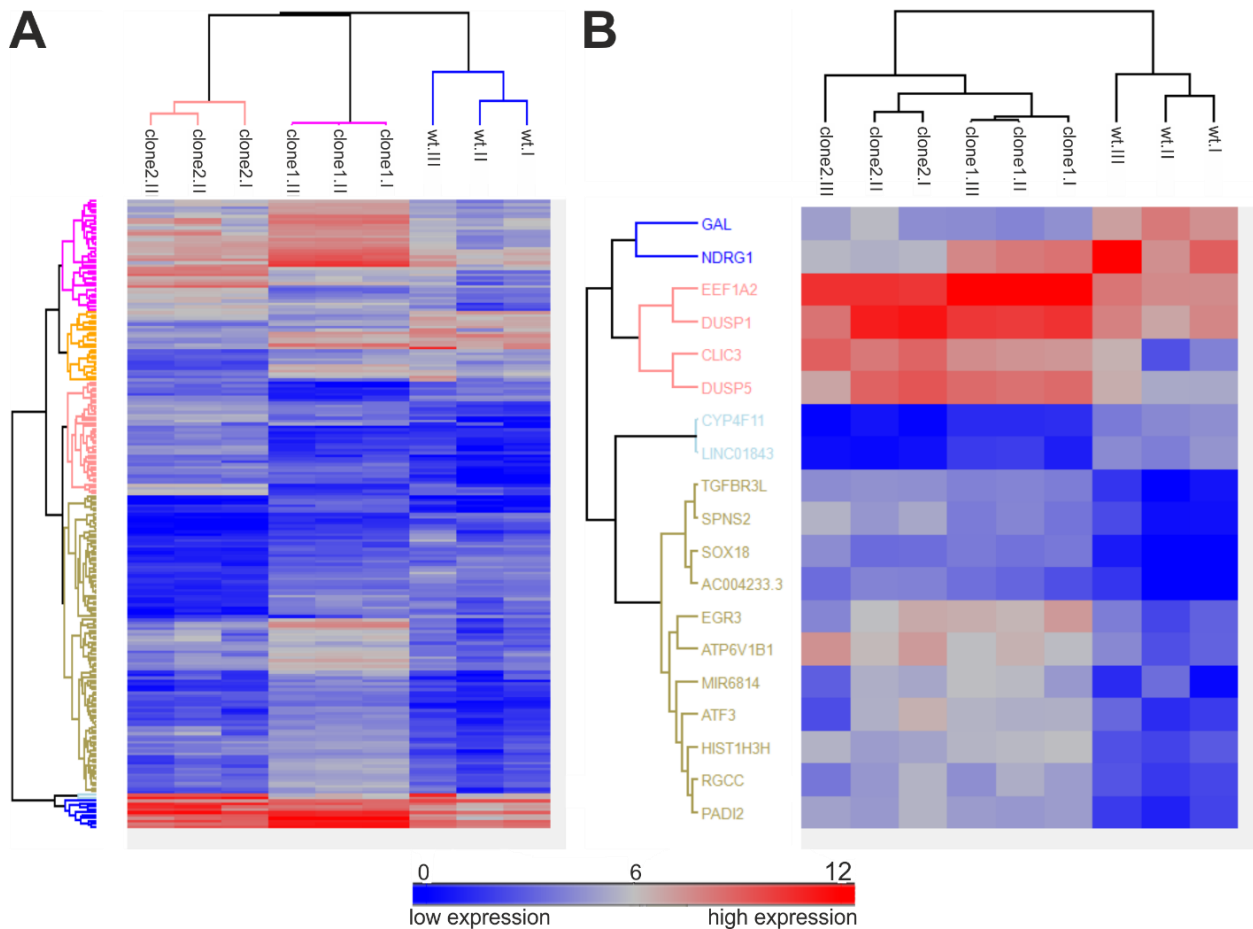


Figure 45 Heatmap of all significantly regulated genes after *SEC62*-ko: (A) Heatmap to visualise all (n=215) significantly regulated genes in both *SEC62*-ko clones compared to wt cells based on TPM values. **(B)** Heatmap to visualise regulated genes caused by *SEC62*-ko that were significantly up- or downregulated in both clones (n=19).

In case of clone1 in sum 68 significantly regulated GOs were found regarding biological processes. Only 1 GO was found in the downregulated gene dataset consisting of 16 genes, whereof 3 genes were identified as unknown. This single significantly downregulated GO was identified as “regulation of cell population proliferation” (GO:0042127) by GO Term Finder tool (Supplementary Figure 1A, marked by black circle). An analysis of affected pathways using DAVID revealed several cancer associated pathways related to downregulated genes of clone1 (Supplementary Figure 2B). In case of significantly upregulated GOs associated with biological processes the focus was on virus associated mechanisms, like defence mechanisms but also responses to general stimuli (Supplementary Figure 1A). A similar result was obtained by

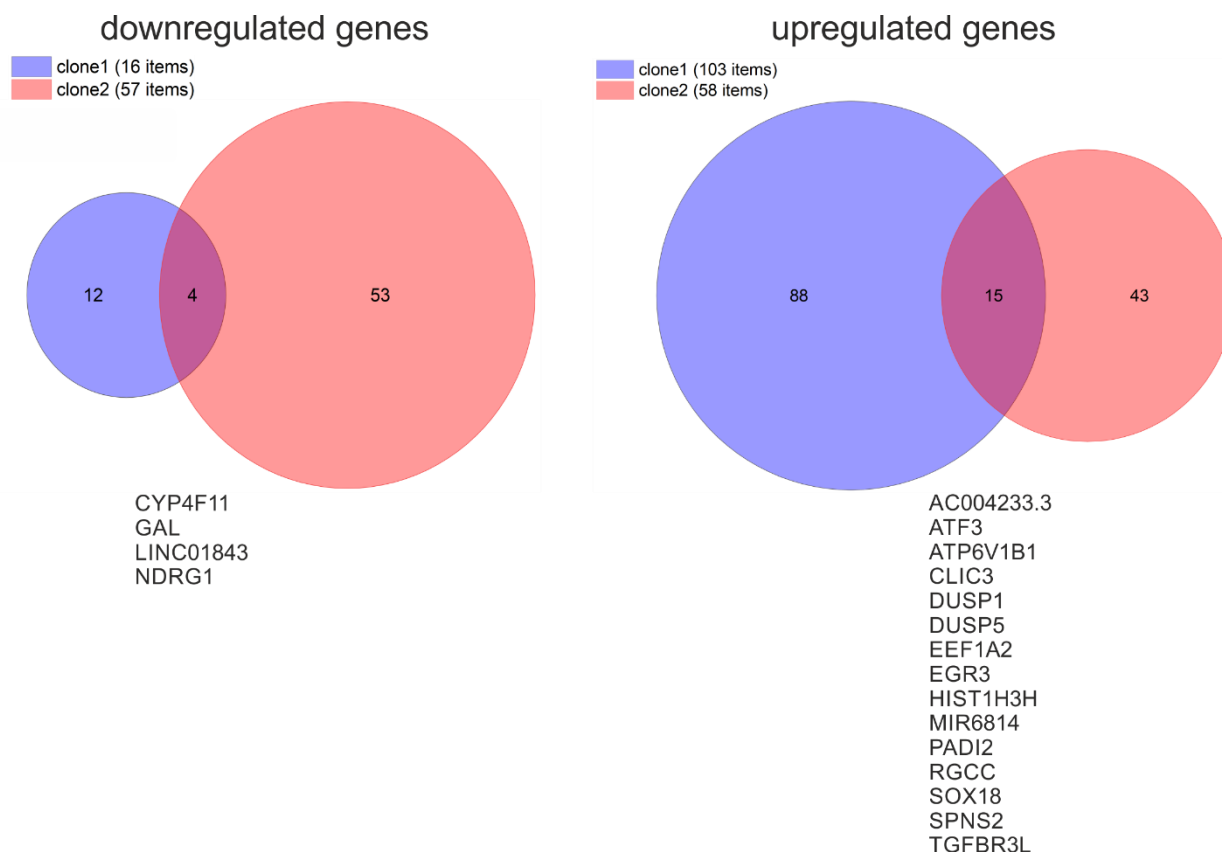


Figure 46 Comparison of significantly regulated genes within both clones: Summary of all significantly down- and up-regulated genes with a match of 4 genes that were significantly downregulated in both clones as well as 15 significantly upregulated genes in both clones. Names of matching genes within both groups are listed below the corresponding Venn diagram.

Panther-based analysis (Supplementary Figure 1B). Analysis using DAVID revealed 7 clusters (Supplementary Table 1) and several virus associated pathways (Supplementary Figure 2A). For clone2 in sum 12 significantly regulated GOs were found regarding biological processes (Supplementary Figure 3A). For the downregulated gene dataset 1 unannotated GO was found. Here, after GO Term Finder analysis the focus of biological process associated GOs in case of upregulated genes lied in developmental processes as well as in migration and locomotion (Supplementary Figure 3A). In case of Panther analysis using GO-slim similar results were obtained associated with biological processes like for clone1 (Supplementary Figure 3B, C). In detail, only gene counts varied between both clones but similar GO-slim achieved highest gene counts in both (Supplementary Figure 1B, C, Supplementary Figure 3B, C). In case of DAVID analysis 5 clusters were identified in case of upregulated genes of clone2 (Supplementary Table 2). Here, also 6 associated pathways were identified (Supplementary Figure 2C). For downregulated genes of clone2 no associated pathways were found, as well as only 1 cluster was identified (Supplementary Table 2).

For GO analysis (GO Term Finder) concerning molecular functions much less GOs were found in general. While clone1 still showed a focus in identified GOs for viral RNA defence the focus in clone2 was set on MAP kinase activity (Supplementary Figure 4A, Supplementary Figure 5A). Similar results were already described regarding the associated clusters and pathway for both

clones that include all three GO categories (Supplementary Table 1, Supplementary Table 2, Supplementary Figure 2).

Analysis (GO Term Finder) of significantly overrepresented GOs concerning cellular components revealed 6 significantly regulated GOs for all significantly regulated genes of clone1 concerning DNA and protein packaging (GO:0044815, GO:0032993), as well as “chromatin” (GO:0000785) and “nucleosome” (GO:0000786) (Supplementary Figure 6A). For clone2 only 2 GOs were identified, whereof 1 GO was unannotated. The other recognised GO was associated with “striated muscle thin filament” (GO:0005865). In case of downregulated genes of clone1 no significant GOs were found. For clone2 also just 1 unannotated GO was identified.

As a last step all shared up- and downregulated genes of both clones were analysed for their GO annotation concerning biological process, molecular function, and cellular component (GO Term Finder). Here, the analysis revealed no significantly regulated GOs for 4 commonly downregulated genes within both clones. Concerning 15 commonly upregulated genes for both clones 8 GOs (GO:0016477, GO:0035970, GO:0043534, GO:0071675, GO:0002689, GO:0048870, GO:0051674, GO:0071676) were found for biological processes and 4 GOs for molecular functions (GO:0008330, GO:0017017, GO:0033549, GO:0008138) (Supplementary Figure 8). Analysis by DAVID revealed one cluster for commonly shared upregulated genes for both clones (Supplementary Table 3).

3.5.2. Functional analysis of generated *SEC62* knockouts

After a rather descriptive evaluation of two generated *SEC62*-ko clones by CRISPR-Cas9 technology also a functional validation was performed. Here, the effect of a *SEC62*-ko should be analysed to the proliferative as well as the migratory potential.

3.5.2.1. Proliferation behaviour

First, the proliferative potential was analysed for two *SEC62*-ko clones in comparison to FaDu wt cells. The proliferation was measured with a real time cell analysis approach by using the xCELLigence system for 96 h (2.6.4.5, Figure 47A). This method is based on an electric impedance measurement. Attaching or proliferating cells generate an increasing impedance that is measured as an unitless cell index. Within the first 10 h of measurement the respective means of FaDu wt (black line) and clone 1 (red line) showed a similar behaviour in proliferation. The mean of clone 2 (blue line) showed a reduced proliferation directly after the measurement has been started, which was observed over the whole observation time. For reasons of clarity and comprehensibility the calculated standard deviations were not shown in Figure 47A. For slope calculation of the measured cell index the time range between 35 h to 60 h was chosen (marked

within dashed lines in Figure 47A). Within this time range all three analysed cell lines were in an exponential growth phase. Comparing the calculated slope of clone 1 and clone 2 both clones showed a significantly reduced proliferation rate compared to FaDu wt. Noticeable, clone 2 ($p=3.34e^{-4}$) showed a markedly stronger reduction in proliferation compared to clone 1 ($p=0.0095$, Figure 47A).

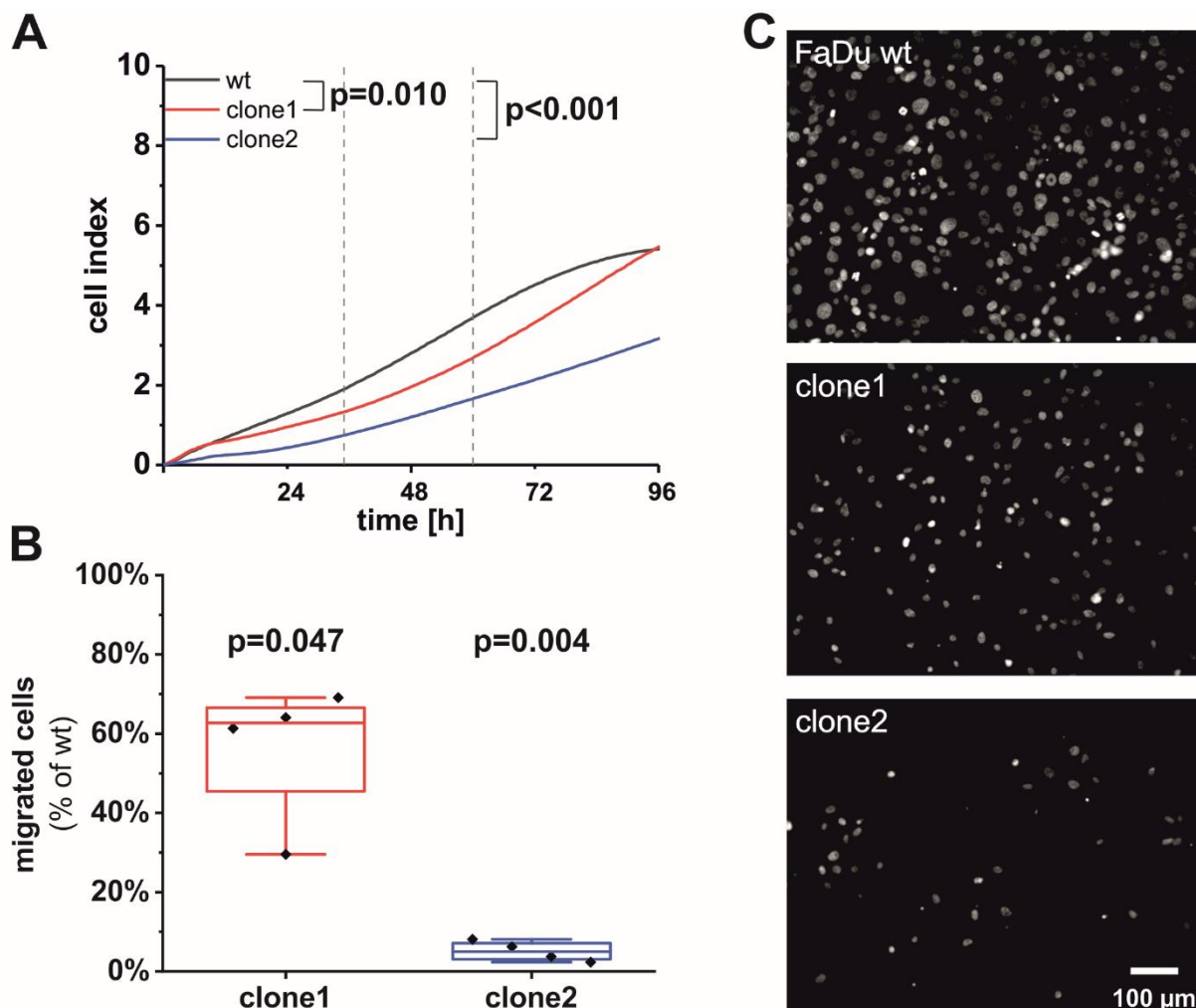


Figure 47 Functional analysis of *SEC62*-ko clones: (A) Proliferation assay using a real-time xCELLigence approach revealed a significantly impaired proliferation behaviour for *SEC62*-ko clones compared to FaDu wt. Shown are the mean cell indices ($n=12$) of all three analysed cell lines (FaDu wt – black line, clone1 – red line, clone2 – blue line). Measurements were performed in quadruplicates for each cell line. The slope of measured cell indices was calculated within the exponential growth phase that was assumed between 35 h to 60 h after cell seeding. (B) Migration behaviour of *SEC62*-ko cell clones was measured compared to FaDu wt using a FluoroBlok™ system that is based on the principal of a boyden chamber. Both clones showed a significantly reduced migration behaviour (clone1 – red, $p=0.047$; clone2 – blue, $p=0.004$). (C) Representative images of migrated cells after cell fixation using MeOH and DAPI staining. Scale bar: 100 μm .

3.5.2.2. Migration behaviour

In Figure 47B the results of a migration assay are shown. The principal of the used migration assay lies in a boyden chamber (BOYDEN, 1962). Here, cells were seeded into a transwell FluoroBlok™ insert containing 0.1 % FCS. In the lower well medium containing 10 % FCS was

added. This concentration gradient of FCS was used as a stimulus for cells to migrate through the 8 μm pores of the FluoroBlok™ insert membrane. After 72 h cells that were migrated through the pores were fixed by MeOH and stained by DAPI. The assay has been performed four times. In each single biological replicate two technical replicates were done for every cell line. For data analysis 3 representative images were taken of each insert that was analysed by a semi-automated analysis using the NIS Elements AR 3.0 software. Also, in this assay *SEC62*-ko clones showed significantly reduced migration compared to FaDu wt cells. Clone 1 showed a reduction in its migratory potential of 54 % ($p=0.047$) whereas clone 2 was reduced by even 95 % in its migratory behaviour ($p=0.004$; Figure 47B). Representative images of migrated cells are shown in Figure 47C.

3.5.2.3. Live cell Ca^{2+} imaging

In addition to functional analyses concerning the migratory and proliferative behaviour of the newly generated *SEC62*-ko clones another functional assay was performed by live cell Ca^{2+} imaging to investigate the effects on cellular Ca^{2+} homeostasis after a stable *SEC62*-ko (Figure 48). First, cells were stained with FURA-2 AM 20 min prior to measurement start and all measurements were started by quantification of the basal cytosolic Ca^{2+} content. In this experiment the basal Ca^{2+} content was estimated for 3 min before 1 μM TG was added. Concerning the basal cytosolic Ca^{2+} all three used cell lines did not show any significant differences. After the initial 3 min TG was added and the cytosolic Ca^{2+} amount was measured for additional 12 min until the basal cytosolic Ca^{2+} content was reached again (Figure 48A, B). Right after TG application the cytosolic Ca^{2+} levels strongly increased in all three cell lines, which created a cytosolic Ca^{2+} content delta of 0.69 ± 0.018 μM for FaDu wt cells, 0.56 ± 0.013 μM for clone1, and 0.510 ± 0.014 μM for clone2. Overexpressing *SEC62* FaDu wt cells showed the highest peak concerning their TG response. The estimated response of clone1 was the second highest response to TG. Clone2 showed the smallest response regarding TG application (Figure 48A, B). Nevertheless, all measured responses showed significant differences between FaDu wt cells and each *SEC62*-ko clone. Next, the total Ca^{2+} amount of all three analysed cell lines was investigated by 10 μM IONO application (Figure 48C, D). After the estimation of the initial basal Ca^{2+} amount for 1 min that was again unremarkable, IONO was added. These responses concerning IONO were estimated for 4 min in sum. Even the calculated deltas of cytosolic Ca^{2+} revealed significant differences between FaDu wt cells and clone2 as well as between *SEC62*-ko clone1 and clone2 there is no biological difference between these cell types. The estimated $\Delta[\text{Ca}^{2+}]_{\text{cyt}}$ were marginal compared to results after the combinatory treatment of TG and TFP (Figure 48E, F). As a last experiment in live cell Ca^{2+} imaging the response of all three investigated cell lines concerning the combinatory treatment consisting of TG and TFP

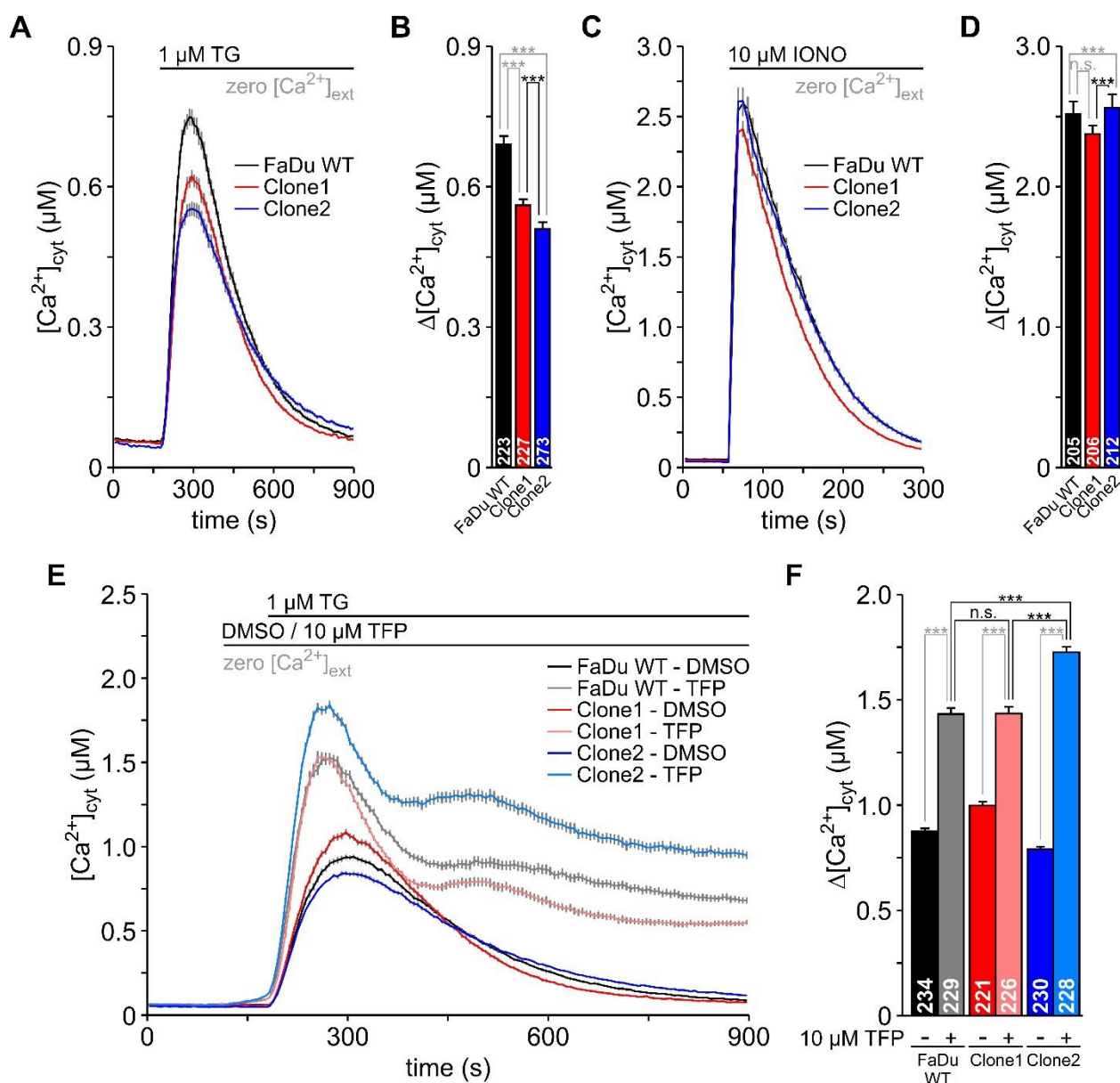


Figure 48 Live cell Ca^{2+} -imaging of FaDu wt and SEC62-ko clones: (A) Impact of TG on cytosolic Ca^{2+} concentration. The basal cytosolic Ca^{2+} level was measured within the first 3 min. Afterwards, 1 μM TG was applied and the cytosolic Ca^{2+} response was measured for further 12 min. Shown is the mean of each measured cell line over time. (B) Shown are the delta means with the respective standard deviation of each measured cell line between basal cytosolic Ca^{2+} and the reached peak after TG application. The number of measured cells is indicated at the bottom of each bar. (C) Basal cytosolic Ca^{2+} was measured for 1 min before 10 μM IONO was added. Here, the total cellular Ca^{2+} amount of the cell regarding each used cell line was measured. (D) Shown are the delta means with the respective standard deviation of each measured cell line between basal cytosolic Ca^{2+} and the reached peak after IONO application. The number of measured cells is indicated at the bottom of each bar. (E) Basal cytosolic Ca^{2+} levels were measured for 2 min before 10 μM TFP or DMSO was added. After one additional minute of measurement of the cytosolic basal Ca^{2+} level 1 μM TG was added and Ca^{2+} clearance was measured for 15 min. Shown is the mean of each measured cell line over time. (F) Shown are the delta means with the respective standard deviation of each measured cell line between basal cytosolic Ca^{2+} and the reached peak after TFP/DMSO and additional TG application. The number of measured cells is indicated at the bottom of each bar. Black – FaDu wt, red – clone1, blue – clone2.

application was examined (Figure 48E, F). Here, again the data acquisition was started with measuring the basal cytosolic Ca^{2+} amount for 2 min. After this initial measurement 10 μM TFP or in case for control DMSO (0.1 % v/v) was added for an additional minute. Within this minute the basal cytosolic Ca^{2+} amount started slightly to raise over time in all three cell lines. At minute 3 of the whole experimental setup TG (1 μM) was added and the subsequent Ca^{2+} clearance

was measured for the following 12 min (Figure 48E, F). After TG application clone2 showed the highest cytosolic Ca^{2+} content ($\Delta[\text{Ca}^{2+}]_{\text{cyt}}=1.725\pm 0.026 \mu\text{M}$). Clone1 ($\Delta[\text{Ca}^{2+}]_{\text{cyt}}=1.435\pm 0.032 \mu\text{M}$) and FaDu wt cells ($\Delta[\text{Ca}^{2+}]_{\text{cyt}}=1.432\pm 0.029 \mu\text{M}$) behave in a similar way after TG administration. Consequently, all investigated cells that were treated in combination with TFP and TG needed an exceptionally long time to decrease cytosolic Ca^{2+} levels. This phenomenon seems to be characteristic for the investigated cell line in general and is different to other human cell lines e.g., HeLa, HCT-116, RPMI 8226 or NALM-6 (Erdmann et al., 2011; Linxweiler et al., 2013; Bhadra et al., 2021; Pick et al., 2021).

3.5.2.4. Impact of TFP and TG on proliferation of *SEC62*-ko

Within this analysis the effect of a stable *SEC62*-ko was analysed on proliferative behaviour under TFP and TG treatment. Therefore, FaDu wt cells in addition to clone1 and clone2 were seeded into a 96-well e-plate for measurement of the unitless cell index using the xCELLigence system. In general, the experimental setup was similar to the previously described experiment in chapter 3.5.2.1. Substances were added in single application after initial 5 h within the cells were able to sediment. Afterwards, slope was calculated of all 3 cell lines within a time range of 35 to 60 h. Within this time range the exponential growth phase of FaDu wt cells to that slope of both clones were compared. All results were compared to solvent control (0.1 % DMSO). Regarding TFP treatment clone1 showed a higher tolerance of drug treatment compared to FaDu wt and clone2 and seemed therefore to be more resistant against TFP (Figure 49A). An impairment of proliferation by at least 50 % was first seen for FaDu wt and clone2 at a TFP concentration of 20 μM for clone2 (cell index 0.455) and 22.5 μM for FaDu wt (cell index 0.428, Figure 49A). In case of clone1 this impairment was first achieved at a concentration of 25 μM (cell index 0.298). The proliferation was further impaired by increasing TFP concentrations in all used cell types. In case of TG treatment clone1 showed comparable proliferative behaviour to FaDu wt in each tested concentration of TG (Figure 49B). Clone2 was more sensitive for TG treatment and showed a strong decrease in proliferation at 5 nM TG (cell index 0.273) whereas FaDu wt cells (cell index 1.252) as well as clone1 (cell index 1.028) showed even high levels of proliferation. FaDu wt cells (cell index 0.425) and clone1 (cell index 0.437) were decreased in their proliferative behaviour at a TG concentration of 10 nM. This impairment was further increased with increasing TG concentration. These results impressively showed a rather important impact on the severity of a *SEC62*-ko and its manifestation regarding different TFP and TG concentrations.

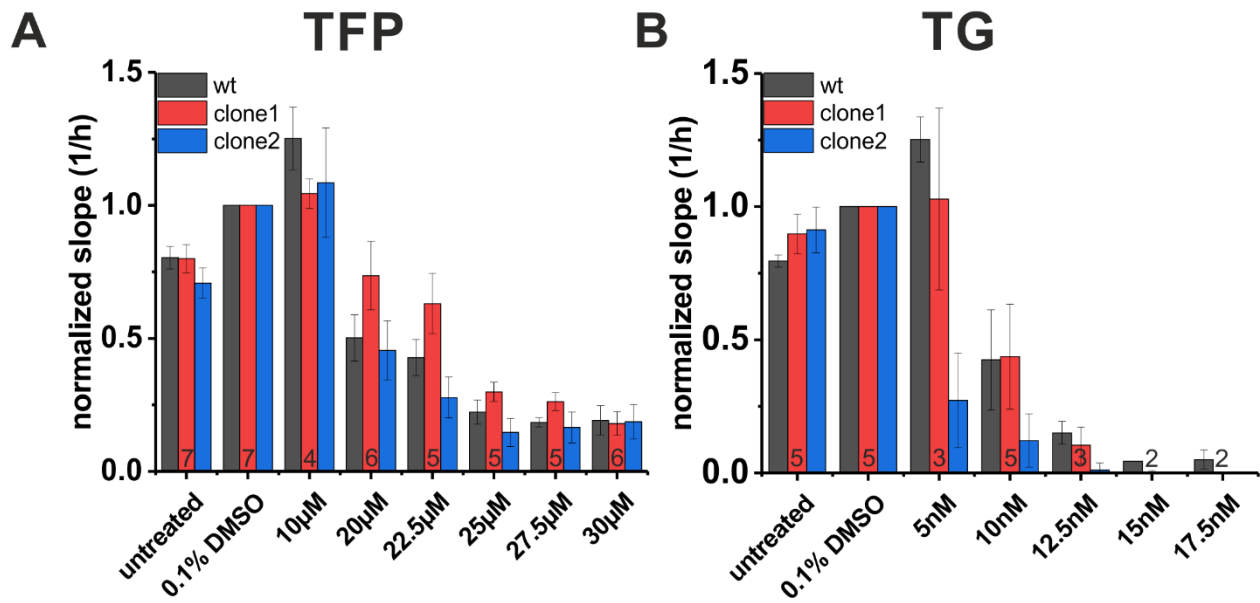


Figure 49 Effect of TFP and TG on proliferation of *SEC62*-ko clones: The slope was calculated for each cell line between 35 to 60 h due to the exponential growth phase of FaDu wt based on the unitless cell index that was calculated by the xCELLigence system. Treatment of cells was started 5 h after cell seeding. The shown data are based on technical quadruplicates. The biological replicates were indexed under each concentration. Shown is the mean of each slope (1/h) regarding each concentration normalised to solvent control. The error bars indicate the error of the mean. **(A)** Normalised slope of FaDu wt, clone1 and clone2 under different TFP concentrations. **(B)** Normalised slope of FaDu wt, clone1, and clone2 under different TG concentrations.

4. Discussion

Despite intensive research efforts, squamous cell carcinomas of the head and neck region are mostly diagnosed at advanced stages with often already pronounced lymphatic metastasis (Johnson et al., 2020). Even distant metastases are found in up to 10 % of all patients, which worsens the patients' prognosis (Wiegand et al., 2015). Which way the primary tumour chooses in general for its metastatic spread within the patients' body depends on the one hand on the site of tumour initiation and the aggressiveness of tumour cells, as well as on the other hand on various involved extrinsic and intrinsic tumour micro-environment pathways (Paduch, 2016). After tumour initiation and primary tumour growth, tumour cells may disseminate through the body either via lymphatic vessels to locoregional lymph nodes (lymphatic spread) or via blood vessels to other distant organs (haematogenous spread) (Stacker et al., 2002; Paduch, 2016). Interestingly, the lymph fluid composition even promotes survival of migrating tumour cells due to its composition and high concentrations of hyaluronic acid, as well as high level of oleic acid. The latter acid protects cancer cells from ferroptosis (Laurent and Fraser, 1992; Ubellacker et al., 2020). Even the structure of lymphatic vessels as well as the minor shear stress by larger diameter of this vessel system protects migrating tumour cells (Swartz and Skobe, 2001; Paduch, 2016). However, oxidative stress, immunosurveillance, and anoikis make circulatory systems not very hospitable to cancer cells (Hanna et al., 2015; Piskounova et al., 2015; Ubellacker et al., 2020). Nevertheless, the background how tumour cells decide either to disseminate using the blood vessel system or the lymphatic vessel system remains unclear. In addition, only a small subset of circulating tumour cells can generate metastatic tumours at all (Padmanaban et al., 2019; Tasdogan et al., 2020). Cancer cells that survived the journey to a new site of the human body and were able to settle may even die at this new location, may be cleared by immune cells, survive the step for building macro metastases or remain dormant for an unknown time period after seeding (Hanahan and Weinberg, 2011; Harper et al., 2016).

Within this thesis, both metastatic mechanisms for HNSCC were established using mouse models. After establishing these *in vivo* metastasis models, two potential new substances were examined in more detail for their effectiveness in the fight against metastasis formation. Both substances may inhibit metastasis by a functional knock-down of SEC62 that has been shown to be overexpressed in nearly 86 % of all HNSCC patients (Wemmert et al., 2016). Also, other tumour entities show an overexpression of SEC62 why this protein is considered as a potential oncogene (Jung et al., 2006; Weng et al., 2012; Hagerstrand et al., 2013; Linxweiler et al., 2016; Takacs et al., 2019; Casper et al., 2021; Müller et al., 2021; Sicking et al., 2021). Bochen et al. were able to show a significant correlation of metastatic stage with SEC62 expression level. In addition, the overall survival of patients expressing high SEC62 levels was significantly shorter compared to normal or low expressing patients (Bochen et al., 2017). These results gave impressive hints for a prognostic relevance of SEC62 level in HNSCC. First, the discussion will

focus on the establishment of two reproducible *in vivo* models before moving on to the efficacy of two potential new therapeutics targeting SEC62 function that were tested using the prior established *in vivo* models. To stay as close as possible to the clinical situation, only male mice were used (Heath et al., 2012; Ferlay et al., 2019). The second part of the discussion will deal with an artificial generation of a *SEC62*-ko by CRISPR-Cas9 technology and its functional analyses in order to investigate the molecular basis of SEC62 and its role in cancer cell proliferation and migration.

4.1. Establishment of different murine metastasis models

4.1.1. Do's and Don'ts for lymphatic metastasis model establishment

One of the main goals of this thesis was the establishment of a reproducible model for lymphatic metastasis. Therefore, all definable parameters should be as constant as possible. In this context, comparable studies used a wide variety of differently aged mice within the reported experiments. Mice with ages between 4 and 12 weeks were used for these experiments (Myers et al., 2002; Gleysteen et al., 2008; Sano et al., 2011; Heath et al., 2012). Due to different biological processes within distinct phases of life, all mice included within this thesis were delivered with an age of 7 weeks. Mice were allowed to acclimatise to their new environment for one week so that experiments were started with an age of 8 weeks.

With the goal of establishing a reproducible murine model for lymphatic metastasis, several establishing rounds were performed using those 8-week old, immunosuppressed mice who were orthotopically injected with human HNSCC cells into their tongue. One main aspect to induce lymphatic metastasis was the capability of mice to survive a sufficiently long time so that injected tumour cells can form a primary tumour that was additionally able to spread to cervical lymph nodes. This goal of sufficient lifetime was only achievable by a tumour cell injection into the tip of the tongue. Tumour cells injected into the tongue base led to a primary tumour on this site that was too large after a short period of time and impaired the animals' food intake and deglutition. Therefore, animals showed a rapid loss of weight that forced to sacrifice the animals due to animal welfare reasons. Despite the primary tumour was detectable, only 50 % of injected animals showed lymph node metastases after a tumour cell injection into the tongue base (Figure 13). For a decision support, a CD31-LYVE1 double staining was performed on 5 native tongues to detect possible preferences concerning the tumour cell injection site based on the density of detected lymphatic vessels. Here, CD31 was used as a general panvascular marker whereas LYVE-1 was used as a lymphatic vessel marker (Banerji et al., 1999). Despite the tongue base displayed the most balanced staining results of CD31- and LYVE-1-positive cells, the tip showed the most CD31-positive cells together with the second-highest number of LYVE-1-positive cells so that this

injection site was an adequate alternative (Figure 14). In general, the distribution of LYVE-1-positive cells seemed already very constantly spread over the whole tongue. This observation was also in accordance with results of Lohrberg et al. (Lohrberg and Wilting, 2016).

After the selection of the tongue tip as the favourable injection site, tumour cell amounts had to be titrated to achieve the highest number of lymph node metastases in accordance with a long survival time dependent on the primary tumour size. By injecting different cell numbers, it emerged that 5×10^4 cells were too few cells to be able to form a primary tumour at the injection site and thus no metastases may develop (Figure 15).

Although the third round of lymphatic metastasis establishment suggested that an injection into the left tip of the tongue also leads to frequent metastases in the left cervical lymph nodes, this assumption seems to have been refuted by the fourth round of establishment. Here, 1×10^5 tumour cells injected into the left site of the tongue tip led to 60 % metastasis formation. These metastases split into 50 % right sided metastases as well as 33.3 % bilaterally located metastases (Figure 17). This fact leads to the assumption that injection site of the tumour cells plays a minor role for metastatic spread. A doubling of the injected cell number did not lead to increased metastases formation in the cervical lymph nodes (Figure 18). In contrast, the higher cell amount appears to be responsible for more primary tumours located in the base of the tongue, which may lead to a premature impairment of deglutition and induces weight loss. Due to this prematurely loss of weight, mice had to be sacrificed after a shortened observation time and had no metastases formed yet. The literature shows a high variability of injected cell numbers for comparable murine orthotopic xenograft models. Concerning this purpose, injected tumour cell amounts between 2-fold up to 25-fold compared to the number used in this thesis are reported (Myers et al., 2002; Gleysteen et al., 2008; Sano et al., 2011; Heath et al., 2012). There are also large discrepancies in literature regarding the applied injection volumes. Volumes between 25 and 50 μl were reported, which is 5-10 times higher than the injection volume used in this study. We decided to inject tumour cells only in 5 μl volume to be less invasive and painful, so that mice are less impaired in their food intake the days after injection. Nevertheless, all mice received an analgesic after tumour cell injection. In summary, the reported metastasis rates in literature are comparable to the metastasis rate of 50-60 % obtained within this study (Sano et al., 2011). In general, an orthotopic model has an advantage compared to subcutaneous models because of reported biological differences dependent on the primary tumours' injection site (Sano and Myers, 2009). Additionally, Myers et al. (2002) reported differences in tumorigenicity of oral cancer injected orthotopically compared to subcutaneous injection. An orthotopic injection led to a greater tumorigenicity as well as the typical processes that are involved for local invasion (Myers et al., 2002). This led to higher rates of spontaneous metastasis and displayed a closer reflection of the clinical situation compared to a subcutaneous model. Testing potential new therapeutics then leads to a more appropriate prediction of clinical responses when primary tumours grow

orthotopically (Sano and Myers, 2009). Nevertheless, the here used model system rely on immunodeficient mice. Therefore, one must keep in mind that no contribution of the immunological tumour-microenvironment can be studied.

4.1.2. Do's and Don'ts for haematogenous metastasis model establishment

As already mentioned before, HNSCC do not only form metastases in the local lymph nodes but can also disseminate to distant organs like the lung in about 10 % of cases (Wiegand et al., 2015). Therefore, this type of metastases formation was also considered in this thesis for establishment of a murine *in vivo* model.

Referring to the first establishing rounds of the haematogenous metastasis model, several complications were observed. While cells were harvested with trypsin for tail vein inoculation, cells created conglomerates that were able to clog small blood vessels. These cell conglomerates can lead to embolization and, in the worst case, death of the animal. The used HNSCC cell line FaDu shows a size on average between 10-15 μm in diameter. Therefore, it is not surprising that the small capillary vessels of the mouse with a diameter of 0.3-4 μm can easily be clogged by the used cells. Also, venules have a diameter of only 1-14 μm (Müller et al., 2008). These facts require the mandatory presence of a single cell suspension injected i.v. into the animals' tail vein. These main requirements should be fulfilled primarily by filtering cells before inoculation. Therefore, the pore size must be selected carefully depending on the individual cell diameter of the used cell line. In this case, using a cell strainer of 10 μm pore size led to a forced compression of the cells and unfortunately to lysis of cells. A cell suspension containing a large portion of lysed cells may lead to complications in the injected mouse because of released intracellular components like toxic metabolites. Hence, the pore size of the used cell strainers was increased to 15 up to 20 μm that was still enough to split cell conglomerates.

The next adjustable screw was the method of administering the i.v. injection. While fixation of the animals in a restrainer was initially considered as too stressful, the usage of a short, volatile anaesthesia had additional negative effects on the general condition of the animals that should be inoculated with tumour cells. Hence, animals were injected using a restrainer but with a milder fixation of the animal to minimize the stress level.

Nevertheless, animals continued to die shortly after or during cell inoculation, so that further factors had to be changed to increase the success rate. For this purpose, animals were pre-treated with heparin 1-1.5 h before the cell inoculation. This preliminary treatment led to an improvement in animal survival and was adopted to the standard protocol. The additional usage of nitroglycerine (i.p.) immediately before cell inoculation led to no further improvement in survival of the injected mice and was therefore not included into the standard protocol. Indeed, one must keep in mind that a pre-treatment with heparin did not guarantee that all animals will survive the

cell injection. Albeit the usage of heparin was a key agent for animal survival in our case, it may have a putative anti-metastatic effect and contributes to a better outcome of cancer patients (Niers et al., 2007). Several studies showed that an inhibition of heparanase activity of tumour cells by heparin or other heparin derivatives correlates with lower metastatic potential of tumour cells (Parish et al., 1987; Nakajima et al., 1988; Yoshitomi et al., 2004; Niers et al., 2007). Heparanases that are secreted by tumour cells are highly important for the penetration of vascular endothelium by destroying numerous components of the extracellular matrix (Vlodavsky et al., 1999; Kurokawa et al., 2003). Various studies used a comparable single heparin administration approximately 1 h before tumour cell inoculation and registered a reduction of metastasis rate (Lee et al., 1988, 1990). Nevertheless, the used dose of heparin (40 IU) was higher compared to the used dose within this thesis (20 IU) that may have a lower impact on metastasis formation. Niers et al. (2007) also considered the timing of heparin administration and i.v. injection of the tumour cells as a critical point. The intravascular exposure of the tumour cells to heparin may influence the survival as well as the endothelial adhesion capacity of the injected tumour cells. However, heparin was used in each experimental round for each inoculated animal so that there is no comparable group that did not receive any heparin administration before the tumour cell inoculation. Thus, a potential reduction in pulmonary tumour foci as reported by other studies could not be addressed in this thesis.

During further establishing rounds, the amount of inoculating tumour cells was varied starting with 2.5×10^5 up to 2×10^6 cells per 200 μl injection volume. First, one must mention that animals developed pulmonary tumour foci independent of the previously injected cell amount. Nevertheless, the risk for animals to die during or shortly after the injection process, the amount of 2×10^6 was considered as too high so that 1×10^6 per 200 μl was used as a standard for all subsequent experiments.

In the next step, a method had to be established to monitor pulmonary tumour foci growth. Initially, tumour cell injected mice should be monitored for metastasis growth by multiple μCT image acquisitions. Therefore, mice were imaged one day before the experimental start to have a zero dataset of the lung for better detection of pulmonary tumour foci potentially growing within the following weeks of observation. Unfortunately, these regular μCT investigations led to potentially high radiation exposure indicated by visible loss of fur and wounds at the paws. In extreme cases, a possible excessive radiation exposure could also cause therapeutic irradiation effects on the metastases potentially leading to a lower number of pulmonary tumour foci. In Körner et al. (2022) we investigated the effect of different used μCT imaging protocols regarding its resolution and the resulting radiation dose (Körner et al., 2022). Using a 35 μm resolution, the lowest radiation dose was generated, but the resolution was also by far the worst. Using 18 μm resolution, the obtained resolution was much better but also the obtained radiation dose increased by 39-47 % (Körner et al., 2022). For this publication, no breath gating was used compared to the

first applied μ CT acquisitions within this thesis. Due to breathe gating, the image quality as well as the overall imaging time was increased, but the overall radiation dose might be decreased. Nevertheless, repeated μ CT acquisitions led to higher radiation doses. Dependent on the used mouse strain, the animals' age, gender and investigated tissue, there are reported life shortening effects with estimated 7.2 % per administered Gy (Ford et al., 2003; Meganck and Liu, 2017). While immune-competent mice were able to recover after low radiation doses, immunodeficient mice that were used for the reported experiments here had problems with respective recovery (Ford et al., 2003; Meganck and Liu, 2017). Unaware of whether the noticeable difficulties were really derived from excessive radiation exposure during repeated μ CT scans, the scans were reduced so that only one high- (9 μ m, 0.5Al) and medium-resolution (18 μ m, 1Al) scan was performed before sacrificing the animal.

In general, the experimental metastasis model has several advantages as well as disadvantages. On the one hand, the experimental metastasis model is a reproducible model with a comparable biology of metastasis formation in order to evaluate the capacity of tumour cells to arrest, extravasate and grow in a particular organ (Gomez-Cuadrado et al., 2017). The experimentalist can determine the exact number and type of circulating cells oneself, but cancer cell lines often fail to retain the epigenetic and genetic characteristics of the original tumour (Gomez-Cuadrado et al., 2017). In case of the FaDu cell line used within this thesis, this cell line is genetically very heterogenous which was confirmed by comparative genomic hybridization (CGH) investigations (Supplementary Figure 9). Nevertheless, a change in the epigenetic and genetic characteristics as a result of an *in vitro* cultivation since the collection in 1968 from a male patient with a hypopharyngeal squamous cell carcinoma cannot be excluded due to the lack of comparable data at the time point of excision. This impedes a valid and predictive statement about possible clinical responses and reactions of patients in a potential clinical trial phase (Singh and Ferrara, 2012; Kersten et al., 2017). For this purpose, a patient derived xenograft (PDX) model will be a possible alternative, but the engraftment rate for this model type is very low and the frequency, as well as the metastatic site, may vary from the situation in the patient (Whittle et al., 2015). Additionally, PDX models lack a competent immune system within the animal recipient, which only may be circumvented by the usage of humanized xenograft mouse model.

A further disadvantage of the experimental metastasis model used in this thesis is the circumstance that early steps in the processes of metastasis such as EMT are eliminated (Khanna and Hunter, 2005). It is assumed that tumour cells metastasise in emboli interacting with platelets and other host cells before they settle to distant tissues (Khanna and Hunter, 2005). Using the tail vein injection for distant metastases' formation, tumour cells move in high numbers as single cells that may not arrest or interact with the target tissue compared to tumour cells that spontaneously metastasise from their primary tumour host. Additionally, as already mentioned before for this model type is a lack of a host adaptive immune system because human derived

cancer cells must be injected in immune-compromised or immunodeficient mice to avoid a rejection of the host. This implies a poor clinical predictive power that is, in fact, urgently needed because only 7.5 % of potential oncological drugs successful *in vitro* were allowed for phase I clinical trials (Singh and Ferrara, 2012; Toniatti et al., 2014). Although, most preclinical mouse models only include regression of the primary tumour without consideration of effects on metastasis. Therefore, the metastasis models presented in this thesis can be considered as an effective monitoring system for testing the efficacy of anti-metastatic drugs. As most clinical trials include locally advanced and/or metastatic patients, there is the urgent need for reliable preclinical *in vivo* models (Gomez-Cuadrado et al., 2017).

4.1.3. The usage of different imaging techniques compared to the histological gold standard for lung volume evaluation

Besides, the establishment of the aforementioned metastasis model in general also different techniques were tested for metastasis analysis as well as lung volume evaluation. Here, different methods were compared to each other, beginning with histological evaluation as a gold standard including μ CT as well as MRI analysis as alternative methods. In part also automated analysis methods were tested.

Referring to the obtained results by the last establishing round of the new haematogenous metastasis xenograft model with a larger number of animals for method evaluation, additionally different imaging techniques were tested for lung volume calculation as well as for metastasis volume evaluation (3.3.4). This experimental round included initially 14 animals of that at least 10 animals were evaluated for their individual lung volume and metastasis burden via histology (gold standard), μ CT with 9 and 18 μ m resolution as well as MRI. The obtained results were additionally included within a second analysis for the evaluation of the comparability of these aforementioned imaging techniques, which we will come back to later in this discussion.

In case of the small dataset consisting of 10 animals, the here used histological gold standard showed a highly variable range of calculated lung volumes (Figure 22A). This wide lung volume range refers to the level of lung swelling after excision of the mouse body. For histological analysis, lungs were hung on a 20 cm formalin column for tissue expansion and the first step of inner fixation. Not every lung lobe was able to re-expand again to its prior dimension, also an overexpansion compared to the real vital condition inside the living animal could not be fully excluded. Reasons for an impaired re-expansion could be the possibility of a too deep inserted cannula so that only one lung lobe was inflated with formalin. Another reason for an impeded re-expansion could be a possible injury of lung tissue during the organ removal. Here, the injected formalin would directly leave the lung through the injured site without any swelling effect. For an intact lung swelling, the trachea was tied after 15 min hanging on the formalin column and the

lung was further prepared for histological examination while the tissue shrunk again (Schneider and Ochs, 2014). In the further course, the lung was cut into 1 mm thick sections that were cut in 3 μm slices. The evaluation of metastasis was done referring to the H&E stained slices independent of the swelling status. For lungs that were not completely swelled, a smaller overall lung volume was calculated due to tighter tissue structures.

Automated analysis of lung tissue refers to manually drawn borders as a ROI using the CTAn software. The volume of the drawn ROI was subsequently calculated by the software. Though minor differences in the variously calculated lung volumes were expected the obtained mean volumes were quite comparable with each other, at least in the small comparison group (3.3.4; Figure 22). Summarizing all examined mice ($n=57$) for their respective lung volume using the different imaging techniques, the previously expected minor differences are more obvious (Figure 24A). Here, the mean of lung volumes for mice analysed based on 18 μm μCT resolution showed a significant larger lung volume compared to calculated volumes of 9 μm resolution. This effect could be explained by the overall smaller lung volume in dead animals due to constant exhalation of the intrapulmonary air after the animals' death. 18 μm resolution images were acquired on a living animal that show movements of the lung and heart, whereas the 9 μm resolution images were acquired on the cadaver of the same animal. MRI analysis was also performed on the living animal that is visible in comparable means between 18 μm μCT and MRI. The mean of calculated lung volumes based on 9 μm μCT images were smaller compared to 18 μm μCT and MRI. Nevertheless, the method comparison by Bland-Altman plot shows a high comparability between histology and 9 μm μCT images (Figure 25D, H).

Concerning the calculated metastases volumes, large differences between the automatically calculated volumes compared to manual calculated volumes are obvious (Figure 22B, Figure 24B). In case of the automated volume evaluation, the metastases volumes were calculated by grey value differences based on a binary image. The differentiation between metastases and lung bronchial tubes by grey values is rather difficult, which is the reason why the automated calculation includes all of the aforementioned structures as metastases. For the manual detection of metastases, the course of suspicious structures was individually traced between different sections in order to better differentiate between metastases and bronchial tube structures that often show a path that ends up in the main bronchus. Regarding metastases detection within MRI images, the results were comparable to manually evaluated μCT acquisitions, independent of resolution, and histological sections (Figure 22B, Figure 24B). In general, the trend between the small dataset (3.3.4) and the sum of examined mice ($n=57$) for metastases burden is comparable. Concerning the Bland-Altman analysis for method comparability, most comparable with each other are the gold standard of H&E histology together with the manual analysis of 9 and 18 μm μCT images as well as the MRI images. These methods also show an acceptable Pearson correlation coefficient (Figure 27E, G, I). Volumes of metastases detected by the automated

evaluation show much larger means compared to manually detected metastases. In detail, the 9 μm μCT analysis shows even larger means of metastases volumes compared to 18 μm analysis (Figure 22B, C, Figure 24B). This effect may be explained by the doubled resolution of fine structures, referring to 9 μm μCT . Small structures will probably merge with larger structures in 18 μm resolution images, whereas these structures were single detectable within the 9 μm resolution (Figure 23B, C).

Altogether, there is no perfect method for lung and/or metastases volume calculation. Every method has its advantages and disadvantages. Maybe because of the best Bland-Altman analysis result automated 9 μm μCT analysis is the best suited method for lung volume calculation if histology analysis implies too much effort and represents a good compromise between analytical accuracy and experimental effort and time. This method seems to be the most comparable and fastest method (Figure 25D). Nevertheless, the calculated linear correlation is not convincing (Figure 25C). In case of metastases volume calculation, the fastest method without any alternative will be the automated evaluation of metastatic tissue. However, there is an enormous impact of surrounding tissue enclosed in calculation so that the obtained results were unfortunately not competitive with any other method (Figure 24B). Solely, the manual analysis of metastases in 18 μm and 9 μm μCT images as well as in MRI images were most comparable to histological analysis as shown by the linear correlation and the Bland-Altman analysis (Figure 27 E-J). Nevertheless, manual evaluation of metastases in μCT images is time-consuming and needs a trained investigator. To assure the highest accuracy for detection of metastatic tissue, histological analysis remains the gold standard compared to the presented alternative methods.

4.2. Impact of TG/TFP treatment on different murine metastasis models

After the establishment of both experimental murine xenograft metastasis models, the basis was built to apply both models to test new therapeutic approaches. As already previously described, an overexpression of *SEC62* seems to play a tumour promoting and therefore an oncogenic role in a variety of cancer entities (Bochen et al., 2017; Sicking et al., 2021). Especially, 86 % of all HNSCC patients show an overexpression of *SEC62* within the primary tumour tissue (Wemmert et al., 2016; Bochen et al., 2017). This gene-specific overexpression is associated with a highly significant shortened overall survival of these patients compared to *SEC62* normal or low expressing patients (Bochen et al., 2017). Continuing analysis also showed a significant linear correlation between a rising *SEC62* expression and the presence of local and distant metastases in HNSCC (Bochen et al., 2017). This correlation was also reported previously for lung cancer patients (Linxweiler et al., 2012). Comparing the *SEC62*-mIRS (modified immunoreactive score) of tissue originating from the primary tumour as well as from corresponding metastases of the same patient, in 60 % of all investigated cases elevated *SEC62* expression was found in the

metastatic tissue (Bochen et al., 2017). In this context, *in vitro* experiments showed a decreased ability of normally *SEC62* overexpressing HNSCC cells to migrate if *SEC62* was silenced by siRNA, otherwise an artificial overexpression of *SEC62* by plasmid transfection led to significantly increased migratory behaviour of the used cell line (Bochen et al., 2017). All these preliminary but promising results have implied the question whether *SEC62* could be considered as a potential new target for therapy of *SEC62*-overexpressing HNSCC patients. As a first step, the previous in detail described two murine, experimental xenograft metastasis models were established. In the next step, a therapeutic approach to target *SEC62* and its function had to be found. As already described, a siRNA mediated silencing of *SEC62* led to significantly reduced migratory behaviour of HNSCC cells *in vitro* (Bochen et al., 2017). However, the cell line used in this publication was not suitable for *in vivo* application because of very heterogenous tumour volumes and the early development of intratumorally cysts (Körbel et al., 2018). Mice inoculated with FaDu cells to the flank showed significantly more homogenous tumour growth in combination with none or few cysts (Körbel et al., 2018). This was convincing that this cell line was also used in this thesis. Already in 2011 Greiner et al. postulated an essential function of *SEC62* concerning cell migration and the ER stress tolerance regarding prostate cancer (Greiner et al., 2011a, 2011b). These findings were confirmed and further strengthened by Linxweiler et al. (2012) for lung and thyroid cancer. Though all of these results confirmed *SEC62* as a promising protein for targeted therapy, a direct transfer of siRNA-related silencing *in vivo* is not suitable up-to-date due to mainly delivery problems of the siRNA already mentioned in the introduction (Burnett and Rossi, 2012; Tian et al., 2021). Therefore, a functional knock-down was considered as a potential therapy approach. The main known functions of *SEC62* probably rely on the protein translocation as well as the regulation of Ca^{2+} homeostasis that is modulated by a C-terminal EF-hand motif of *SEC62* (Müller et al., 2010; Lakkaraju et al., 2012; Lang et al., 2012; Linxweiler et al., 2013). For this purpose, two substances were probably applicable to induce a functional *SEC62*-ko or at least a functional knock-down – TFP and TG.

The calmodulin-antagonist TFP belongs to the group of phenothiazines (OSBORN and WEBER, 1980). It was one of the most prescribed and oldest synthetic antipsychotic drug worldwide that was long-established and broadly used (Sudeshna and Parimal, 2010; Jaszczyszyn et al., 2012). Today it is only rarely used in the clinical practice due to possible induction of rare acute cholestatic liver injuries as well as its association with neuroleptic malignant syndrome (Kohn and Myerson, 1961; Smego, 1982; Flanagan, 2008). Besides its initial usage as an antipsychotic drug in schizophrenia patients, several studies revealed its remarkable anti-proliferative activity in various cancer cell types. Also a decreased prevalence of malignant lesions in patients treated with TFP for schizophrenia was shown (Schleuning et al., 1993; Andrew Silver et al., 1994; Mortensen, 1994; Nordenberg et al., 1999; Grinshpoon et al., 2005; Koch et al., 2014; Jeong et al., 2022). In theory, TFP is able to block cytosolic CaM as a calmodulin-

antagonist so that CaM is no longer available to be recruited by SEC62 for SEC61 channel closure. This circumstance implies an increased Ca^{2+} efflux from the intracellular Ca^{2+} -storage – the ER (Koch, 1990; Linxweiler et al., 2013). Due to elevated Ca^{2+} levels of the cytosol, cells maybe set under stress conditions. However, there is no *BiP* induction visible following 7.5 μM TFP administration (Figure 12B). In addition, CaM antagonists have been attributed an apoptosis-inducing effect, as well as a favouring of cytotoxicity by radiomimetic acting bleomycin and cisplatin (Perez et al., 1992; Kang et al., 1999; Eriksson et al., 2001; Sullivan et al., 2002; Polischouk et al., 2007).

The second promising applied substance to mimic a functional *SEC62*-knock-down was TG. TG is the most widely used irreversible inhibitor of SERCA located in the ER-membrane (Treiman et al., 1998). In a normal cellular situation, SERCAs are responsible for a coordinated back haul of Ca^{2+} ions from the cytosol into the ER lumen mainly to recover the concentration gradient between the ER and cytosol (Denmeade and Isaacs, 2005; Periasamy and Kalyanasundaram, 2007; Lang et al., 2011a). *In vitro* studies showed that TFP and TG administration is able to suppress the migratory potential of various cell lines (Linxweiler et al., 2013) (Figure 12A), which can be counteracted by *SEC62* overexpression. However, caution is probably advised when administering TG alone. Here, several studies showed that a *SEC62* overproduction protects cells against TG-induced ER-stress (Greiner et al., 2011b; Linxweiler et al., 2012). Also, previous analysis of FaDu wt cells showed significantly increased *BiP* expression after 72 h of TG administration (Figure 12B).

Keeping the molecular mechanisms of CaM-blockade by TFP administration and an irreversible SERCA inhibition by TG application in mind, the main hypotheses of this thesis is a combinatory and therefore additive effect of TFP- and TG-administration in *SEC62*-overproducing HNSCC patients to induce a functional *SEC62*-knock-down. As the solo administration of TG will probably have less effect on the migration potential of cells overexpressing *SEC62*, these cells must be pre-treated with TFP to initiate a prior cellular stress level. Previous *in vitro* analysis of FaDu wt cells showed a significant *BiP* induction after 72 h of combined treatment administration (Figure 12B).

The used FaDu cell line showed in the experiments of this thesis an impairment of its migratory behaviour by solely TG administration of 50 %, whereas a solely TFP application inhibited the migration of the same cell line by 38 % (Figure 12A). Administering the combinatory therapy approach of both substances, no residual migration was observable (Figure 12A). Especially the last observation confirmed the initial hypothesis based on previous results obtained from different cell lines. These *in vitro* results form the basis for conducting *in vivo* studies, in which the combination, as well as the single therapy, should be tested on the previously established experimental models of lymphatic and haematogenous metastasis.

4.2.1. Tolerability/toxicity of TG and TFP i.p. administration

A particularly important point in the transfer process of *in vitro* results into an *in vivo* application and further on into a possible clinical trial is the guaranteed tolerability of applied substances. In this thesis, TFP and TG were solely and in combination applied to 8-week-old NOD-Scid mice. For control, vehicle mice were also administered with an appropriate solvent control. First, all mice received a pre-treatment of one week before the actual start every 48-72 h with its individual substance upon tumour cell injection. After the initial pre-treatment week, all mice were inoculated with tumour cells and the individual treatment was continued 48 h after tumour cell inoculation. To test the tolerability of the applied substances in their respective concentration, mice were injected i.p. and were continuously observed for the next hours. As a good and easy to manage control parameter of the general state of each mouse the body weight was initially monitored before each therapeutic substance administration, also because the substances were injected according to the individual body weight (Figure 30A). All administered substances were applied for 5-7 weeks. During this experimental period, no severe side effects were evident in any of the therapy groups. In all groups, the body weight increased over time and only a small decrease in the weight course of all therapy groups could be observed directly after tumour cell inoculation (Figure 30A). However, all groups were able to recover quickly from this event. Animals treated with TFP as a solo therapy showed an additional later decrease in the weight course after 28 days but recovered again 2 weeks later (Figure 30A).

Animals administered with TFP showed an impairment in their movement 5 min after the TFP administration. Animals slowed down in their movements within the cage and started to press their abdomen onto the ground while stretching their feet out backwards (Supplementary Video 1D). Certainly, animals were able to move when they were forced to. This lethargy status slowly decreased after 2 h while mice were kept in front of a heating lamp. These observed side effects may be explained by parkinsonian-like behaviour and extrapyramidal side effects as it was reported by Kang et al. for orthotopic xenograft brain tumours (Kang et al., 2017, 2018). For these mice, doses of 5 mg or 10 mg/kg/day were used, and little signs of those reported side effects were observed that disappeared within several minutes. Investigations of Feng et al. (2018) revealed no impact of daily TFP administration (20 and 40 mg/kg i.p.) on blood routine analysis as well as no obvious pathological changes in major organs like heart, lung, liver, spleen, kidney, and brain were reported. Also, a body weight course over the period of the experiment showed no significant differences between treated animals and the respective vehicle group. In addition, several other groups monitored the body weight course that did not show any noticeable problems (Kuo et al., 2019; Qian et al., 2019; Xia et al., 2019). In some studies, animals were treated with significantly higher concentrations of TFP in combination/or more frequently compared to the treatment within this thesis. Severe side effects were not reported at all.

In case of TG administration, the “deadly carrot”, an high cytotoxicity was reported, which categorises TG as an unfavourable drug candidate (Denmeade et al., 2003; Doan et al., 2015; Jaskulska et al., 2021). Nevertheless, several groups showed impressive anti-cancer properties administering possible concentrations for *in vivo* application (Ma et al., 2016; Abdullahi et al., 2017; Körbel et al., 2018; Wu et al., 2019; Bellizzi et al., 2022). Treated mice showed forced ear perfusion by a high visibility of blood vessels in the ears 5 min after the TG application in this thesis. This phenomenon implied a possible heat loss. Additionally, the animals also tried to press their abdomens onto the ground and showed an increased defecation. In rare cases, the animals started to tremble in their face in combination with retch-like movements (Supplementary Video 1E). All these signs disappeared again within the following hour. In literature mostly a TG concentration of <1 mg/kg was chosen for *in vivo* application. In almost all studies only the body weight course of treated animals was monitored and showed no signs of toxicity. Bellizzi et al. (2022) also examined several organs like spleen, brain, heart, liver, lung, intestine, and kidney for signs of oedema, necrosis or other types of toxicity but detected no obvious alterations of tissue structures. Indeed, most studies compromised only a few days of treatment instead of several weeks as described in this thesis. Though, both applied substances had to be carefully titrated as described in detail in the single establishing rounds in the results section. Therefore, the applied substance concentrations for TFP and TG were first guided by Körbel et al. (2018). As described in 3.4.3 the used TG concentration (1.6 mg/kg) was much too high and caused death of all injected animals. TG concentration used in Körbel et al. was applied on athymic nude mice, whereas in this experimental setup NOD-Scid mice were used. This mouse strain had a significantly reduced tolerance to TG compared to athymic mice used previously in Körbel et al.. After thoroughly titration of TG, a new concentration of 0.4 mg/kg was selected for further experiments. Using this 4-fold reduced new TG concentration all mice survived the initial pre-treatment so that this concentration was also used for further procedure. The other way round, TFP concentration was explicitly increased within this thesis compared to the used TFP concentration in Körbel et al.. While this publication only used an TFP concentration of 0.5 mg/kg, the final TFP concentration applied in this thesis was 30-fold higher (15 mg/kg). Based on an intensive literature research of currently published data the new TFP concentration was chosen (Park et al., 2016; Feng et al., 2018; Kuo et al., 2019; Qian et al., 2019; Xia et al., 2019).

Körbel et al. reported high serum peak concentrations of TG resulting from i.v. injections with higher risk for toxic effects. Therefore, i.p applications were used here. Analysis of serum concentrations of both substances 48 h and 168 h after the drug application revealed equal distribution for TG and TFP in all investigated animals in combination with a slight accumulation of both substances over time. Nevertheless, all animals showed a normal movement and grooming behaviour, as also described here with adjusted concentrations for TFP and TG. Both substances in combination were previously administered only by Körbel et al. (2018). Severe side

effects were not reported at all so that repeated treatment was suggested as non-toxic and possible for further studies.

4.2.2. TG/TFP treatment and its consequences on murine lymphatic metastasis

After the initial titration of tolerable TFP and TG concentrations for *in vivo* application, the effect of both substances in combination and in solely application using the previously established lymphatic metastasis model was examined. To the best of our knowledge, there is only one study available by Körbel et al. (2018) who tested the combination of both promising substances *in vivo*. Indeed, they used quite different concentrations of both drugs, which had to be adjusted for the mouse strain used in this thesis. Additionally, the efficacy of both substances was tested on metastatic spread instead of a human derived xenograft model injecting the tumour cells into the mouse flank. The experimental procedure starting with one week of pre-treatment of animals following the tumour cell inoculation at day 0 is shown in detail in Figure 29. The shown data is based on initially 46 animals that were pre-treated. Finally, 89 % of all inoculated animals developed a primary tongue tumour after the tumour cell inoculation of 1×10^5 cells (Figure 31A). 5 animals that did not develop a primary tongue tumour were excluded for further analysis because these animals were unable to metastasise without a primary tumour. One additional animal was also excluded for further analysis because of its premature sacrifice due to a rapid loss of weight. All the following results were based on the data obtained of 40 animals divided into vehicle, TFP/TG treatment, both substances in solo therapy and the general treatment group including all treated animals except the vehicle animals. First, the primary tumour size between all mentioned groups were compared (Figure 31B). Here, animals treated with TFP significantly showed the largest primary tumour volume (Figure 31B). Animals treated with TG had the most comparable primary tumour volume like the vehicle animals (Figure 31B). In accordance to increased primary tumour volumes are the results of Wen et al. who reported a highly selective proliferation promoting effect of low TFP concentration on various cancer cell lines as well *in vivo*, especially on glioma cells (Wen et al., 2018). The same study was able to show that TFP could reduce the rate of Ca^{2+} -dependent apoptosis. In contrast, Yeh et al. reported an anti-cancer stem-like cell effect of TFP that help to overcome drug resistance in lung cancer (Yeh et al., 2012). Although the concentrations of TFP and TG are in part significantly different between the study by Körbel et al. and the doses used here, similar results were obtained regarding tumour size. Körbel et al. reported a faster increase in tumour volume of the flank model under TFP treatment, whereas TG treated mice showed the smallest tumour volume compared to vehicle mice. Both results could be partially confirmed in this study. Nevertheless, the used concentrations vary by factor 30 for TFP and 4 for TG.

Next, the amount of cervical lymph nodes containing metastases was evaluated (Figure 32A). Even though no significant results could be achieved here, there is a recognisable tendency that TFP administration suppresses lymph node metastases formation. One has to mention here, that the individual number of resected cervical lymph nodes varied between each animal, but the obtained overall sum of lymph nodes within one treatment group was comparable. This variability was caused by anatomical differences between each animal and variable observability of lymph nodes *in situ*. Vehicle animals showed the highest amount of lymph node metastases (Figure 32A). These findings were supported by the rate of animals that showed cervical lymph node metastases in general. Most metastases were built in vehicle mice. Here, 67 % of all in the analysis included animals showed metastases, whereas only 50 % of TFP treated animals also showed metastases formation (Figure 32B). Animals treated with TG even showed metastases in 70 % of all animals. Even if the proliferation rate may increase by low TFP concentration as Wen et al. reported, the metastases formation seemed to be slightly inhibited. Also, *in vitro* data showed a slight decrease in migratory potential of about 38 % (Figure 12A). These data are in accordance with an *in vivo* study by Qian et al. concerning the efficient control of colorectal tumour growth by TFP administration (Qian et al., 2019). The authors reported an impaired migratory and invasive behaviour of colorectal cancer cells by suppression of the EMT. A direct hint for EMT involvement regarding HNSCC could not be validated so far but is the subject of current research (Figure 12B).

As a next step, the size of cervical lymph node metastases was examined. Therefore, metastases were categorized in micro- and macro-metastases. Metastases consisting of less than 20 tumour cells were categorized as micro-metastases whereas metastases consisting of more than 20 tumour cells were categorized as macro-metastases. Regarding this context, all vehicle animals showed macro-metastases (Figure 32C). Due to treatment with TG, a significant reduction in metastases size was achieved. A trend for metastases size reduction was obtained for treatment in general (Figure 32C). For solo TFP treatment, most detected metastases were categorized as macro-metastases (89 %). This result may fit for the proliferation increasing effect of low TFP concentration as reported by Wen et al.. Even TFP treated mice showed the lowest metastasis rate in general, mice that still formed metastases showed predominately macro-metastases compared to other treated mice. TG treatment resulting in the smallest metastases size is in accordance with Körbel et al. where TG treatment also caused the smallest tumour within the mouse flank. However, one has to keep in mind that concentrations for TFP and TG used in Körbel et al. were significantly different from the concentrations used in this thesis.

In more detail, lymph nodes bearing metastatic foci were analysed for their location (Figure 32D, E). Vehicle mice showed 80 % two-sided metastases, whereas 20 % had only metastases within one site of the neck. Mice treated with the combinatory therapy showed the most two-sided lymph node metastases. TG treatment induced a rather balanced ratio between one- and two-

sided metastases (Figure 32D). For the localisation of metastases we also differentiated between left and right sided metastases. In this regard, TFP treated animals showed a trend for left-sided metastasis (56 %) whereas TG treated mice showed more right-sided metastases (82 %, Figure 32E). As a reminder, mice were inoculated with tumour cells on the right site of the tip of the tongue meaning that TG treated mice mostly metastasised on the same side where the inoculation took place.

In summary, the significantly largest primary tumours grew after initial tumour cell inoculation into the right site of the tip of the mouse tongue under TFP treatment (Figure 31B). Regarding this fact, the used TFP concentration may have a tumour promoting effect *in vivo*. However, the number of observed metastases after TFP treatment showed a trend for the lowest metastatic burden (Figure 32A). In addition, only few animals developed cervical lymph node metastases in general compared to TG treated animals who developed most metastases (Figure 32B). Regarding the metastases size, all vehicle animals developed macro-metastases whereas TG treated animals showed significantly more micro-metastases. This leads to the assumption that the applied TG concentration *in vivo* is able to limit metastasis growth. However, in contrast to the previously expected results of a combinatory therapy approach of TFP and TG no additive effect of TFP and TG was visible rather in number of metastasis than in size. A similar effect was expected *in vivo* as previously described based on *in vitro* results of FaDu wt cells (Figure 12A) resulting in an impairment of migration by combined application of TFP and TG. This effect was suggested because of the biological basis of less recruitment of CaM due to TFP application that blocks CaM in addition to the irreversible inhibition of SERCA by TG administration. TFP may induce a forced Ca²⁺ leakage from the ER lumen by CaM blockade, while TG inhibits the backhaul of Ca²⁺ ions. This may lead to an increasing Ca²⁺ content within the cytosol, as already seen in the live cell Ca²⁺ imaging experiments (Figure 48) that forces HNSCC cells into a Ca²⁺ stress situation compared to a single administration of both substances. Several potential explanations exist why no additive effect of both applied substances was observed. First, there is a surgical bias because very small lymph nodes may be missed during excision, which is also shown by the varying number of dissected lymph nodes between animals. Another possible bias is based on histopathological analysis. Here, tiny lymph node metastases may be missed due to the scheme for slice preparation. The next thinkable reason for no observable additive effect of the combination of both substances is the long pause of 2 h in-between substance application of two hours. During this period of time, cells may induce compensatory mechanisms like the activation of additional Ca²⁺ pumps to fight against the TFP-induced forced Ca²⁺ leakage from the ER lumen that the additional administration of TG has no additive effect anymore. Here, also the mode of action of applied TG, which was analysed and described in detail by several studies should be considered (Isaacs et al., 2021). Prostate cancer cells show within less than 5 min after TG application an inhibition of the SERCA in combination with an increase in cytosolic Ca²⁺ which is

released from the ER Ca^{2+} pool. In addition to this, TG application also induces an enhancement in CaM transcription, which is associated with a further elevation of cytosolic Ca^{2+} . The elevated cytosolic Ca^{2+} level is maintained for about 6 h by extracellular Ca^{2+} entry via SOCE (store operated Ca^{2+} entry) -dependent opening of plasma membrane calcium channels as well as via the upregulation of plasma membrane Ca^{2+} -ATPase (PMCA ATPase) pump which is the CaM client protein (Furuya and Isaacs, 1994; Furuya et al., 1994; Tombal et al., 1999). Additionally, unfolded proteins accumulate and which bind to BiP chaperone that was also significantly upregulated by TG application as well as by the combination of both substances in our own *in vitro* experiments (Figure 12B). This upregulation of BiP and other ER stress sensors induces the UPR. TG-induced apoptosis will only proceed when the initiation phase has fully run its course and could be continued by excitation phase (Tombal et al., 2002). Therefore, a CaM-dependent delayed secondary enhancement of cytoplasmic Ca^{2+} is required (>18 h post-TG application). In this context CaM plays a role in the activation of transcription factors, which leads to an enhancement of IP3 type 3 receptor (IP3R3) that moves to the plasma membrane and forms receptor-operated Ca^{2+} channels (ROC) allowing Ca^{2+} to enter the cell resulting in a second enhancement of cytosolic Ca^{2+} level about 18 h after the initial TG-application (Khan et al., 1996; Pigozzi et al., 2006). This process marks the beginning of apoptosis execution (Isaacs et al., 2021).

Setting these facts in the context of our hypothesis, initial TFP application may have an impact on CaM transcription elevation in general or enhancement of CaM may overcome the previous inhibition of CaM by TFP administration. Administering TFP a second time after the initial elevation of cytosolic Ca^{2+} may lead to a disruption of the apoptosis initiation phase, which will result in no transition into execution phase and therefore no caused cell death.

In general, experiments have to fulfil a huge step in the process from *in vitro* application to *in vivo* experiment. In the later there are much more influencing variables that could not be tested *in vitro* before e.g., the interaction of tumour cells with the tumour microenvironment including tumour associated fibroblasts.

Another explanation for no additive effect of the combinatory therapy may a suboptimal dosing of both substances. The titration showed *in vitro* an extremely small window of action for possible concentrations to see the demonstrated effects on migration *in vitro*. Therefore, a transfer from *in vitro* into *in vivo* application seems difficult, especially because of a reported and also specially seen high toxicity of applied TG *in vivo*. It is possible that applied i.p. concentrations of both substances were too low at the point of action. For future experiments, a smaller time frame should be used for substance application and the administration form may be reviewed for oral application or i.v..

4.2.3. TG/TFP treatment and its consequences on murine haematogenous metastasis

In contrast to the sequence described in this thesis, the haematogenous metastasis experiments were carried out first. Therefore, the applied doses of TG and TFP were used following Körbel et al.. Concerning the first experiment administering 1.6 mg/kg TG in combination with 0.5 mg/kg TFP, all with TG injected NOD-Scid mice died within the following 3-4 h. Searching a reason for these deaths caused by 1.6 mg/kg TG, we concluded that NOD-Scid mice have another LD₅₀ for TG compared to Balb/c nude mice that were administered with the reported dose of TG in Körbel et al.. Unfortunately, the next experiment treating Balb/c nude mice instead of NOD-Scid mice for haematogenous metastasis with the previously established 1.6 mg/kg TG revealed similar results like the experiments with NOD-Scid mice (Figure 33). However, animals did not directly die after the first administration of high TG dose like NOD-Scid mice but survived 3.5 weeks in the best case with 3 administrations per week. One difference between mice reported by Körbel et al. and mice administered with the same dose of TG in this thesis was a previous i.v. tumour cell inoculation in addition with heparin (20 IU, i.p.). An observable side effect after TG application was a visible dilation of the blood vessel system at the animals' ears (Figure 30B). While measuring the core temperature of one TG injected NOD-Scid mouse during TG concentration titration, the core temperature was 3-4 °C lower than the normal body temperature. Due to the small size of a mouse, animals transfer heat quickly and show rapid changes in core temperature. Therefore, they need a higher heat-generating capacity that was putative inhibited or decreased by TG or its side effects. Additionally, it is known that TG completely abolishes binding between sarcolipin (SLN) and SERCA in muscles (Sahoo et al., 2013). In a normal situation, SLN-SERCA binding allows ATP hydrolysis but interferes with Ca²⁺ transport so that Ca²⁺ ions remain in the cytosol, which may contribute to heat production (Toyoshima and Nomura, 2002; Sahoo et al., 2013). Therefore, TG inhibits in addition nonshivering thermogenesis by the abolishment of SLN- and SERCA-binding (Bal et al., 2012; Sahoo et al., 2013). As a conclusion, future animals were kept in front of a heating lamp for several hours to counteract the loss in thermogenesis.

Since Balb/c nude mice used here also did not tolerate 1.6 mg/kg TG over the duration of the experiment, future TG dose was reduced to 0.8 mg/kg in accordance with previous titrations. Furthermore, NOD-Scid mice were used again for haematogenous metastasis. To be cautious and to prevent unnecessary deaths if new TG concentration administered would still be too high, only 4 NOD-Scid mice were pre-treated 3x before tumour cell inoculation. As in the previous round, the pre-treatment was well tolerated by all mice. This time, all mice also survived the following treatments without severe problems and were sacrificed after 12 weeks (Figure 34A). On sacrifice day μ CT acquisitions were done in medium and high resolution. Lungs of all mice

were analysed for general lung volume and possible metastases volume by μ CT and histology (Figure 34B, C). The obtained results of lung volume were similar to the already described and discussed whole dataset in chapter 4.1.3.

Within the next experiment, the animal amount was enlarged to obtain more statistically significant results. Unfortunately, a large group of animals died prematurely due to an injection mistake (Figure 35A). Here, the main message of this experiment was a sufficient and adequate preparation of applied substances to avoid injection of too high concentrated therapeutics. This may lead to death of animals due to overdosing of not fully resuspended or solubilised substances. Therefore, the obtained results were again not convincing, but confirmed the previous estimation concerning the overall imaging modalities. A slight look regarding first results of the combinatory therapy of 0.8 mg/kg TG together with 0.5 mg/kg TFP showed no effect on metastasis volume (Figure 35B, D). However, the animal number was small for the treatment group so that no adequate prediction concerning the effectiveness of the combinatory therapy was possible. In general, only adult animals (older 15 weeks) should be included for analysis to ensure a fully developed lung for volume comparisons (Flurkey et al., 2007). Nevertheless, lungs were not always able to be fully re-expanded again, hanging on the formalin column. However, these lungs were included into analysis.

Due to probably less effect of the combinatory therapy approach *in vivo* by the used concentrations of TG and TFP so far, intensive literature research revealed new publications concerning TFP administration. Here, authors applied up to 40 mg/kg of TFP daily (Park et al., 2016; Feng et al., 2018; Kuo et al., 2019; Xia et al., 2019). Regarding TFP, the concentration was increased by factor 30 to 15 mg/kg. Because used NOD-Scid mice were extremely sensitive concerning the applied TG concentration as already described in the previous chapters, the TG concentration was reduced by factor 2. This decision was made mainly due to the small window for TG concentration adjustment during the establishment. Mice have to survive at least for 6 weeks in case of the lymphatic model, in case of the haematogenous model even 12 weeks receiving their therapeutics every 48 to 72 h. Since the TFP concentration has been increased that much, we have decided to minimise the TG dose for safety reasons hoping that the animals do not suffer too much and survive the application in any case. Therefore, a new TFP concentration was tried first on a small group of animals over 6 weeks of administration. These test-animals received no tumour cells to be fully attentive to possible complications caused by increased TFP administration. While animals showed no effect after receiving 0.5 mg/kg TFP, animals show an impairment in their movement 5 min after administering 15 mg/kg TFP as described above (chapter 4.2.1). Regarding TG application, no severe impairments were obvious in most of the applications. All animals survived the new applied substance concentrations over 6 weeks without severe side effects. As already described above, observed side effects after TFP

administration can be explained by known extrapyramidal side effects and parkinsonian-like behaviour (Kang et al., 2017, 2018; Jeong et al., 2022).

Within this experimental setup, substances were applied the other way around for the first time. Because of the severity of TG application in the previous rounds, this medication was applied first in every experiment, to see the direct effect on the animals and see if animals survive the application. However, the combinatory therapy relies on the preparatory effect of TFP that should induce the first cellular stress due to inhibited CaM recruitment by SEC62 and thus rising cytosolic Ca^{2+} concentration by an open SEC61 channel. The cellular stress level should be increased by TG application that irreversibly inhibits SERCA so that no backhaul of Ca^{2+} ions into the ER lumen is possible anymore and cytosolic Ca^{2+} levels constantly rise while the luminal Ca^{2+} decreases.

Within the next experiment, mice ($n=10$) received 3 pre-treatments of new TFP and TG concentrations prior to tumour cell inoculation. Intraperitoneal application of TFP- and TG was administered for a maximum of 10 weeks. In this experimental setup also 10 vehicle mice were included to analyse the potential effect of therapy on haematogenous metastasis. During the following weeks, several animals had to be sacrificed prematurely, mainly in the treatment group. Nevertheless, 9 animals of the treatment group were able to be included into the final analysis together with 8 vehicle animals (Figure 36). All included animals survived at least for 6 weeks and were rather categorised as adult animals (Flurkey et al., 2007). Regarding the differently calculated lung and metastases volumes, comparable results were obtained like in the previous analyses (Figure 36E, F). As a reminder, the lungs were excised on sacrifice day, re-expanded hanging on a formalin column for several minutes, formalin and paraffin embedded and then sectioned into 1 mm thick slices. Each slice was embedded for its own, the paraffin block was trimmed, and complete lung tissue was H&E stained. Based on these sections metastatic burden was evaluated and metastases volume was calculated. Presumably, not every single metastasis, especially not every micro-metastasis, could be detected by this type of lung preparation. Cutting the full lung as it was done in the first trials was also not feasible because of a huge work- and material-load with a minor result. Therefore, the applied method was a good compromise. Evaluating the metastatic burden was difficult due to the above-mentioned potential missing rate especially of micro-metastases. Hence, the sections containing metastasised tumour cells were set into ratio with the overall obtained sections of each mouse lung (Figure 36B). This analysis revealed a highly significant difference between treated and control animals. Animals belonging to the treatment group showed significantly fewer sections containing metastasised tumour cells compared to vehicle animals. This result seems to be a first hint for an inhibiting effect of the combinatory therapy in case of distant metastasis. Unfortunately, the calculated metastases volumes seemed to be not significantly different between both animal groups (Figure 36D), which may be due to the high variability in the calculated volumes. As a subjective interpretation of the obtained results, we supposed that a significant difference can be achieved with higher numbers

of treated animals per group. Nevertheless, not all vehicle animals formed lung metastases, or possible micro-/metastases were not evaluated because of an inappropriate slide section of the 1 mm thick lung sections. The analysis of lung volume based on the histological examination revealed a slight trend towards a smaller lung volume of treated mice compared to vehicle mice. Unfortunately, we have no suggestion why the combinatory treatment consisting of TFP and TG should lead to a smaller lung volume.

In summary, the analysis of a first combinatory *in vivo* application regarding haematogenous metastasis showed a divided result. On the one hand, an initial hint for an anti-metastatic effect of TFP and TG was shown, on the other hand this effect could not be proven by the following detailed analysis concerning the metastasis volume. Unfortunately, the number of used and analysable animals was restricted due to treatment associated side-effects. For this model, it would be essential to repeat the experiment with additional animals and to include groups for single substance application to reveal the sole impact of each substance as a possible anti-metastatic substance for HNSCC.

4.3. Generation of SEC62-knockout by CRISPR/Cas9 and its functional consequences for HNSCC

The final part of this discussion will provide insights into the fundamentals of the previously quite application-oriented hypothesis of functional knock-down of SEC62 and its consequences on HNSCC proliferation and metastasis. The overall basis of this thesis build the amplification of SEC62 on nucleotide- as well as on protein-level in HNSCC patients (Wemmert et al., 2016; Bochen et al., 2017). Regarding these properties, tumours overexpressing SEC62 show elevated proliferative, invasive, and migratory behaviour (Greiner et al., 2011a; Linxweiler et al., 2012; Bochen et al., 2017). Additionally, these tumours show lower sensitivity for cell death induced by ER-stress due to a generally higher tolerance for ER-stress (Greiner et al., 2011b; Linxweiler et al., 2012; Fumagalli et al., 2016). Based on the molecular background, there are 3 potential hypotheses how SEC62 overexpressing cells may benefit from this chromosomal overexpression and are able to deal better with ER-stress. First, cells with an increased amount of SEC62 are preferred to recover from stress situations due to the role of SEC62 in post-translational protein transport (Lakkaraju et al., 2012; Lang et al., 2012). Caused by perturbation of ER environment SEC62 may help cells to deal with a disturbed homeostasis of protein synthesis, folding, and ER transport by a more efficient protein transport across the ER membrane (Walter and Ron, 2011; Linxweiler et al., 2017b). The second hypothesis is strongly linked to the first one, referring to the role of SEC62 in recovER-phagy. SEC62 deals as an autophagy receptor and is supposed to deliver selectively ER-components to the autolysosomal system to recover and maintenance ER homeostasis (Fumagalli et al., 2016; Bergmann et al., 2017). This special task and the process

of recovER-phagy in general seems highly important and characteristic for *SEC62*-overexpressing tumour cells that also differentiate tumour cells from surrounding cells and generate the opportunity for a targeted therapy approach (Fumagalli et al., 2016; Bergmann et al., 2017; Linxweiler et al., 2017b). The third hypothesis is based on *SEC62*'s role in Ca^{2+} homeostasis and was already described in detail in several chapters of this thesis. Linxweiler et al. (2013) were able to show that the process of migration, as well as the stress tolerance, was inhibited by *SEC62* silencing, which implies a crucial role of *SEC62* in both mechanisms. Additionally, this study revealed the impact of *SEC62* in both processes to be Ca^{2+} dependent. Based on these findings, Ca^{2+} homeostasis was selected as a potential site of action for targeted therapy without a direct inhibition of *SEC62* itself. To understand the basis and the resulting consequences of such a functional *SEC62* knock-down, this chapter will discuss results of a real *SEC62*-ko by CRISPR-Cas9 technology.

Most of the data shown here have already been published by Körner et al. (2022) in *Frontiers in Physiology*. All the following results were based on the FaDu wt cell line that was used exclusively in this thesis.

First, *SEC62*-ko clones were generated using an already published and characterized CRISPR-Cas9 plasmid (Fumagalli et al., 2016). Based on the upper mentioned characteristics of *SEC62* chromosomal amplification it could be possible that transfection with Cas9 has to be performed for several rounds to cut and destroy every single amplified genomic copy of *SEC62*, but this was probably not the case because several *SEC62*-ko clones were successfully generated after a single transfection round. A rather big disadvantage of the used plasmid was a lack of a fluorescent protein as transfection marker. The inserted selection marker was based on an antibiotic resistance, which led to numerous time-consuming selection rounds to guarantee a new cell population originating from a single CRISPR-Cas9 *SEC62*-ko clone. To verify the Cas9-activity, a western blot analysis was performed at various time points of clone selection. Finally, 2 clones were further analysed that both showed no residual *SEC62*-amount in the western blot analysis (Figure 38Figure 37C). After the initial selection of both clones, various descriptive analyses were performed. In contrast to the western blot analysis an immunofluorescence staining revealed a slight *SEC62* signal for clone1, for clone2 no residual *SEC62* amount was detected by immunofluorescence staining (Figure 38B). In addition to protein-based analysis also an analysis based on nucleotide sequences was performed. Therefore, RNA was isolated first and checked for residual *SEC62* mRNA. The obtained results displayed the same result as the immunofluorescence staining. The used TaqMan® assay was chosen between exon 5 to 6 that was located behind the predicted cutting site of Cas9 that lies at the end of exon 3. Nevertheless, the exact cutting event was still unknown as well as its consequences on mRNA and protein level. Both clones showed in part significantly reduced levels of residual *SEC62* mRNA, but clone1 showed only a minor reduction on mRNA level compared to clone2 as it was already indicated by

immunofluorescence staining (Figure 38B, C). Both results may reveal different functional characteristics of both clones.

In a next step, both clones were analysed by NGS to display the exact cutting event and compared with the nucleotide sequence of FaDu wt cells. The analysis of obtained data was done using CRISPResso2 (Clement et al., 2019). This analysis revealed that Cas9 did not exactly cut at the predicted cutting site or that subsequent repair mechanisms repaired the real cutting site on point. The actual event based on CRISPR was rather located around or several nucleotides after the predicted site in both clones. The analysis also showed more considerable differences between both clones that also resulted in different functional behaviour as described later, but also confirmed immunofluorescence- and qRT-PCR-based results. After processing of fastq-files these files were aligned against the human genome to identify variations within the generated clones. This analysis showed a good compliance between FaDu wt and the general human genome as expected, whereas 5 different alleles were identified for clone1 and mainly one allele for clone2 (Figure 38A). For clone1, an insertion of cytosine directly in front of the PAM sequence was the most identified allele, but also deletions of 5 till 15 nucleotides were identified. Regarding clone2, the cytosine insertion was also the most abundant identified allele (88 %). An *in silico* analysis showed an altered amino acid sequence starting from amino acid 82 near the predicted cutting site of *SEC62* gene and revealed a premature stop codon at amino acid 102 caused by a shift within the open reading frame due to cytosine insertion. Only 21 % of the full-length amino acid sequence of *SEC62* (399 aa) was comparable to the wild-type sequence. The translatable mRNA for clone2 was only 25.5 % of the original mRNA wild type sequence. This will probably not be sufficient for a functional *SEC62* protein. Since the sequencing analysis was based on an amplicon based NGS, there is no data available for the full length *SEC62* sequence so that only speculations are possible regarding the resulting full-length protein. Also concerning clone1, the functional consequences of analysed deletions of 5 till 15 nucleotides were difficult to consider.

Besides the NGS analysis, potential OFF-targets were predicted *in silico* by CHOP-CHOP v3 and analysed using amplicon-based Sanger-sequencing (Labun et al., 2019). The obtained individual sequencing results were further analysed by TIDE and showed no CRISPR-Cas9 event (Figure 39, Figure 40, Figure 41, Figure 42). Furthermore, this type of analysis also confirmed the NGS-based results concerning the occurred CRISPR-events of both clones (Figure 43).

As a last step of *SEC62*-ko clone verification and also to investigate the further impact of a full *SEC62*-ko, both clones were sent for RNA-sequencing in comparison to FaDu wt cells. This sequencing was done together with GENEWIZ Germany GmbH in Leipzig and revealed comparable results as already obtained by qRT-PCR and immunofluorescence staining. Analysing the obtained sequencing datasets, *SEC62* was only significantly downregulated for clone2. In case of clone1, *SEC62* was also downregulated, but not significantly (Figure 44). The RNA-sequencing analysis also further confirmed that both clones originate from one single

transfected cell. In the hierarchical visualisation of all significantly regulated genes, FaDu wt replicates showed an obviously heterogenous pattern compared to the replicates of both *SEC62*-ko clones (Figure 45). Moreover, the length of the hierarchical branches showed a higher distance within FaDu wt cells that was already described as a very heterogenous cell line fitting well to the results of our CGH analysis (Supplementary Figure 9). Nevertheless, both clones also revealed a very heterogenous pattern of up- and downregulated genes. Only 4 genes overlapped within the group of significantly downregulated genes and 15 genes overlapped within the significantly upregulated genes (Figure 46). The 4 commonly downregulated genes within both clones include genes that are normally involved into the metabolism of endogenous substrates (*CYP4F11*, cytochrome P450 4F11), as well as display endocrine hormones themselves, like *GAL* (galanin) (López et al., 1991; Edson et al., 2013). *NDRG1* (N-myc downstream-regulated gene 1 protein) seems to play a role as a tumour suppressor and stress-responsive protein involved in processes like cell growth, differentiation, and hormone response (Kurdistani et al., 1998; Stein et al., 2004; Ellen et al., 2008). The downregulation of *NDRG1* may have an impact on reduced stress tolerance of both clones, which also may imply a minor ability to migrate. In more detail a correlation between commonly downregulated genes with observed phenotypes of *SEC62*-ko clones was not obvious.

In case of 15 commonly upregulated genes between both *SEC62*-ko clones some shared genes were involved in translational and transcriptional processes, like *ATF3* (cyclic AMP-dependent transcription factor), *EEF1A2* (elongation factor 1-alpha 2), *EGR3* (early growth response protein 3), *HIST1H3H* (histone H3.1), and *SOX18* (transcription factor SOX-18). *ATF3* acts as a transcription factor and may be induced by several stress stimuli (Chen et al., 1994; Hashimoto et al., 2002). Maybe *ATF3* was induced by CRISPR-Cas9. *EEF1A2* acts as a translational elongation factor during biosynthesis and maybe activated due to *SEC62*-depletion (Hershey, 1991). Otherwise, *EEF1A2* and its family members seems to play a role in various cancer types. In head and neck cancer *EEF1A2* was significantly downregulated in tumour tissue compared to normal tissue (Hassan et al., 2018). However, *EEF1A2* expression levels were significantly higher in high-risk groups (Hassan et al., 2018). *EGR3* is a zinc-finger protein which belongs to the early growth response (EGR) family of transcription factors and seems to be involved in cell migration and to be associated with tumour progression in gliomas (Knudsen et al., 2020). An analysis of various cancer types, especially prostate cancer, revealed a poor prognosis associated with *EGR3* downregulation, whereas an *EGR3* overexpression significantly suppressed metastasis (Shin et al., 2020). Due to *SEC62*-ko *EGR3* was significantly overexpressed in both clones that displayed both a reduced migration. In comparison to the role of *EGR3* a down-regulation of *SOX18* seems to inhibit laryngeal carcinoma cell proliferation, migration, and invasion (Xu et al., 2019). However, *SOX18* was significantly overexpressed on RNA-level. *HIST1H3H* acts as a core component of nucleosome. Here, it regulates as a key

player several transcriptional processes due to accessibility of DNA. Simultaneously, histones play an important role for epigenetic alterations (Castilho et al., 2017; Suchanti et al., 2022). *DUSP1* and *DUSP5* (dual-specificity phosphatase 1/5) belong to the class of dual-specificity phosphatases which dephosphorylate MAPK (mitogen-activated protein kinase) proteins. This class of proteins is also involved in cellular processes like proliferation, apoptosis, and differentiation (Patterson et al., 2009). Studies revealed a correlation of *DUSP1* expression level with tumour staging and tumour therapy efficacy (Shen et al., 2016). Based on these characteristics *DUSP1* may be handled as a tumour suppressor (Zhang et al., 2014; Shen et al., 2016). Another significantly regulated gene, which was significantly upregulated and handled as a tumour suppressor is *TGFBR3L* (transforming growth factor-beta receptor type 3-like). Fang et al. reported in 2020 an decrease in lymph node metastasis associated with an ectopic expression of *TGFBR3*, which will explain a decrease in migration of *SEC62*-ko clones due to significant upregulation of *TGFBR3L* (Fang et al., 2020). *PADI2* (peptidylarginine deiminase 1) is a posttranslational modifying enzyme that converts arginine residues in peptides to citrulline residues. This enzyme also modifies histones in a calcium-dependent manner (Slade et al., 2015). Here, a potential correlation between *PADI2* and *HIST1H3H* overexpression and *SEC62*-ko could be possible, which varies the cytosolic Ca^{2+} homeostasis. *SPNS2* (sphingosine-1-phosphate transporter) was also significantly overexpressed in both *SEC62*-ko clones. Here, in literature a prognostic significance of cytoplasmic *SPNS2* expression in oral squamous cell carcinoma patients as well as in CRC is reported (Lu et al., 2021; Lv et al., 2021). Oral squamous cell carcinoma patients with high levels of *SPNS2* show a significant increase in overall survival, which is in accordance with the lower migration reported for *SEC62*-ko clones (Lu et al., 2021). Lv et al. (2021) reported an EMT induction in combination with metastasis promotion for CRC by *SPNS2* downregulation via AKT signalling pathway activation. For breast cancer high *CLIC3* (chloride intracellular channel 3) expression is associated with poor patients' outcome (Macpherson et al., 2014). In case of HNSCC a previously suggested linked expression of *CLIC3* to *Rab25* could not be validated and high expression levels of *CLIC3* were determined in tumour and normal tissue (Amornphimoltham et al., 2013). The last significantly upregulated gene to look at is *ATP6V1B1* (V-type proton ATPase subunit B). This gene forms a non-catalytic subunit of vacuolar (H^+)-ATPase (V-ATPase) that are responsible for maintenance of the intracellular pH (Vasanthakumar and Rubinstein, 2020). A decrease in V-ATPase function causes a non-optimal cytoplasmic pH, which inhibits granzyme bioactivity and therefore prevents cancer cells for apoptosis induction (Nishie et al., 2021). Nevertheless, *ATP6V1B1* was significantly overexpressed in *SEC62*-ko clones that may play a role in efficacy of apoptosis induction.

In a further step, several tools for GO analysis (GO Term Finder, DAVID, Panther) were used to reveal potential functional relationships. Applying this analysis, clone1 showed a high amount of GOs that were associated with viral defence mechanisms in case of biological processes as

well as for molecular function. Furthermore, a pathway analysis, as well as a clustering by DAVID showed many virus-associated pathways for the obtained significant dataset of upregulated genes (Supplementary Figure 2, Supplementary Table 1). In case of the downregulated dataset, cancer-associated pathways revealed as significantly regulated, e.g. “p53 signalling pathway” and “cellular senescence” (Supplementary Figure 2). Nevertheless, the analysed dataset consisted of only 16 significantly downregulated genes, whereof 3 genes were not identifiable. In case of clone2, the ratio of significantly up- and downregulated genes was much more balanced compared to clone1. Here, especially MAP kinases were upregulated that are associated with many signal transduction pathways and involved in regulation of embryogenesis, cell differentiation as well as cell proliferation and programmed cell death (Supplementary Figure 3) (Theodosiou and Ashworth, 2002). The pathway analysis by KEGG revealed an impact of Hippo pathway (Supplementary Figure 2). This pathway is highly conserved as an evolutionary signalling pathway involved in tissue growth and development (Sun et al., 2021). The associated upregulated genes play a role among others as pro-proliferative and anti-apoptotic regulators. These associations seemed misleading at first glance and should be further analysed because clone2 rather showed an impaired growth behaviour as well as an inhibited migratory potential (Figure 47).

In the next step, both *SEC62*-ko clones were tested for their functional behaviour, thus validating the resulting functionality of residual *SEC62*. Therefore, clones were compared with FaDu wt concerning their general growth behaviour, as well as their ability to migrate. These analyses revealed a relevant impairment in proliferation with an impairment in migration (Figure 47). The severity of growth and migration inhibition depended on the investigated clone. As it was expected, based on the NGS results, the phenotypical effects in both functional assays were more obvious in clone2 compared to clone1. Nevertheless, both clones showed significant inhibition of proliferation and migration. Due to obtained curve shape of cell indices regarding growth behaviour, no signs of increased apoptosis in case of *SEC62*-ko clones were observed. The obtained results were in accordance with expectations about the effect of a stable *SEC62*-ko. Compared to the results of Bochen et al. (2017), a significant inhibition of migration could also be obtained in the context of a stable knockout. Regarding proliferation, Bochen et al. were unable to see any limitations induced by a transient *SEC62* knock-down. This observation was changed by a stable *SEC62*-ko. Here, both clones showed an individually different inhibition of cell proliferation, whereas clone2 was most impaired in its growth rate.

In an additional step also Ca^{2+} imaging experiments were performed in absence of extracellular Ca^{2+} to detect only ER-dependent Ca^{2+} leak. Here, results showed an overall similar cellular basal Ca^{2+} content regarding all three investigated cell types (Figure 48). In case of TG application FaDu wt cells showed the highest increase of cytosolic Ca^{2+} compared to *SEC62*-ko clones. Though, calculated differences regarding the overall cellular Ca^{2+} content reached significant

levels obtained results were considered as too small to have any biological impact. Additionally, the impact of TFP in combination with TG was measured. The combination of both substances led to a significant increase of cellular Ca^{2+} in all tested cell types whereas the increase was highest for clone2. Due to missing SEC62 there is no CaM recruitment to close the SEC61 channel in clone2, even TFP inhibits CaM anyway. Therefore, a stronger increase of cytosolic Ca^{2+} was expected in SEC62-ko clones. In general, all 3 measured cell types showed problems with Ca^{2+} clearance after the administration of both drugs. Especially cells treated with TFP were not able to remove cytosolic Ca^{2+} and did not reach basal levels again. Also control cells treated only with DMSO instead of TFP in combination with TG showed prolonged Ca^{2+} clearance, which was not observed so far for other cell lines like HeLa, HCT-116, RPMI 8226 and NALM-6 (Erdmann et al., 2011; Linxweiler et al., 2013; Bhadra et al., 2021; Pick et al., 2021). This property seemed to be highly characteristic for FaDu cells in general and should be further investigated.

For further investigation of the functional impact of SEC62-ko, both clones were compared to FaDu wt cells for their proliferative behaviour under ER-stress induction using TFP and TG in single administration (Figure 49). As it was expected based on previous results, clone2 showed an elevated sensitivity against drug-induced ER-stress, especially for TG administration. Regarding clone1 an even higher tolerance against TFP administration was registered compared to FaDu wt. In case of TG administration clone1 behaves similar to the wild-type cells. Concerning the reason for a higher tolerance against TFP some speculations there are possible several possible explanations including a faster adjustment to medication due to a more efficient UPR activation also by other possible proteins instead of SEC62. Another possible evasion mechanism and therefore increased proliferation is a forced recover-phagy induced by other proteins apart from SEC62. Even a compensatory upregulation of plasma membrane channels like NCX or PMCA are possible mechanisms to effectively regulate increasing cytosolic Ca^{2+} -levels (Mohamed et al., 2010; Chou et al., 2015).

In general, studies showed an upregulation of LC3II-b and p62 for CRC and glioblastoma cells after TFP treatment, which induced autophagy (Zhang et al., 2017; Qian et al., 2019). Overall, TFP is able to affect more targets within a cell apart from CaM. Comparably, also CaM has more cellular functions despite SEC61 channel closure to maintain cellular Ca^{2+} homeostasis. As an example, CaM deals as a multifunctional Ca^{2+} binding protein (Stevens, 1983). Studies regarding glioblastoma revealed an inhibitory effect of TFP on proliferation, migration, and invasion of model cell lines due to an increasing intracellular Ca^{2+} level in presence of extracellular Ca^{2+} but revealed no increase in survival time (Kang et al., 2018). Therefore, several TFP analogues were tested for induction of more elevated intracellular Ca^{2+} levels within this model system (Kang et al., 2018; Jeong et al., 2022). The analogue 3dc showed best results regarding probable side-effects and intracellular Ca^{2+} increase activity (Kang et al., 2018). Kang et al. (2017) previously described a potential anti-glioblastoma therapeutic mechanism because of increasing intracellular Ca^{2+} -levels

through the opening of inositol 1,4,5-trisphosphate receptor (IP₃R) by TFP administration (Kang et al., 2017). Those increased intracellular Ca²⁺-levels were also obvious in FaDu's after TFP administration, especially after an effective SEC62-ko (Figure 48). Also, NSCLC cells showed an altered ER Ca²⁺ homeostasis and an increased *ITPR* expression (Bergner et al., 2009). Especially, *ITPR3* seems to be overexpressed in HNSCC and associated with aggressiveness (Gambardella et al., 2020). Here, *ITPR3* seems to play a role also in induction of apoptosis in T lymphocytes. Due to these properties *ITPR3* may be an interesting new target for modulating immune responses in HNSCC (Gambardella et al., 2020).

As already described CaM deals as a multifunctional protein (Stevens, 1983; Chin and Means, 2000). In a bound complex with Ca²⁺ CaM is known to promote several pathways like tumour cell viability, motility, and survival by activating the AKT pathway (Dong et al., 2007; Jeong et al., 2022). Because TFP administration leads to a conformational change of CaM the binding capacity of Ca²⁺ to CaM is disturbed (Vandonselaar et al., 1994). As a consequence, AKT is no longer phosphorylated, which inhibits its subsequent actions like the ability of cells to evade cell death pathways or to promote proliferation (Cantley and Neel, 1999). Several studies were able to show an inhibition of AKT-Forkhead box protein O3 (*FOXO3*) pathway as well as an interference with autophagy and DNA repair mechanisms like homologous recombination by TFP administration (Zhang et al., 2017). TFP was able to significantly decrease levels of phosphorylated AKT, led to nuclear shuttling of FOXO3 and impairment of other associated downstream targets of both genes, which among others led to a slow-down in proliferation (Grobs et al., 2021). Interestingly, TFP also increased dose-dependent levels of LC3-II resulting in a dose-dependent accumulation of autophagosomes (Grobs et al., 2021). Further investigations revealed an promoting impact of TFP on autophagy flux in combination with increased apoptosis rate, which was explained by an unsuccessful protective mechanism in case of pulmonary arteries smooth muscle cells (PASMC) that play an important role in pulmonary arterial hypertension (Grobs et al., 2021). Here, SEC62 may also play an interactive role due to its LIR motif within the C-terminus and the resulting induction of autophagosomes formation (Birgisdottir et al., 2013; Linxweiler et al., 2017b). The exact role of SEC62, its LIR motif and the possible increase in autophagy flux as well as in apoptosis under TFP treatment should be investigated further.

4.4. Summary and perspectives

An analysis of the US Securities and Exchange Commission found an average cost of \$648.0 million to develop a single new drug to fight malignant neoplasms in 2017 (Prasad and Mailankody, 2017). A more recent systematic analysis based on literature research including articles published before March 2020 revealed research & development costs for the development of anti-cancer drugs between \$944 million and \$4.54 billion, identifying a trend of

increasing costs (Schlander et al., 2021). These immense costs may be decreased by reutilisation of already previously developed drugs with already known safety profiles, pharmacokinetics and -dynamics and newly discovered fields of application (Jeong et al., 2022).

TG and TFP are both substances that have already been used in clinical routine or at least in first clinical trials, e.g. in the case of TG. Thus, both drugs are promising candidates for reutilisation in different clinical indications. With regard to TFP, its prior application for schizophrenia treatment revealed a potential use as an anti-cancer drug for several cancer entities like lung cancer, prostate cancer, and CRC (Zacharski et al., 1990; Yeh et al., 2012; Pulkoski-Gross et al., 2015). Its required anti-proliferative, anti-invasive, and anti-migratory properties have already been shown in numerous studies (Sullivan et al., 2002; Park et al., 2016; Jiang et al., 2017; Kang et al., 2017; Grobs et al., 2021; Jeong et al., 2022). As a special add-on, the combination of chemotherapeutics and antipsychotic drugs like TFP may have a synergistic effect. Due to the antipsychotic properties like sedative, antiemetic, and analgesic effects, these substances can reduce typical side effects of chemotherapeutics. Symptoms of nausea, insomnia, and anxiety may be alleviated in general by the application of antipsychotic substances combined with anti-cancer effects as a secondary therapeutic effect e.g. by strengthening the effects of ionizing radiation via inhibition of DNA double strand repair mechanisms (Sullivan et al., 2002; Gangopadhyay et al., 2007; Yeh et al., 2012; Kuo et al., 2019).

For future experiments maybe a TFP analogue like 3dc could be used to minimise known extrapyramidal side effects of TFP administration and to strengthen the associated TFP-typical effects in combination with an increase in survival time (Kang et al., 2017; Jeong et al., 2022). Jeong et al. (2022) also postulated a possible practical dose for patients, referring to concentrations for patients with mental disorders. Therefore, Jeong et al. suggested an applicable dose of TFP for cancer patients of 100 to 150 mg/day (Marques et al., 2004; Jeong et al., 2022).

In case of TG, several potential pro-drugs were developed in order to liberate TG for therapeutic action selectively at its target site in prostate cancer (Denmeade et al., 2003, 2012). First clinical trials using TG pro-drug Mipsagargin (G202) showed promising stabilisation of clinical disease stage for locally advanced or metastasised solid tumours (Mahalingam et al., 2016, 2019).

After the establishment of two reproducible murine xenograft models for both types of metastasis, these two promising new therapeutics were investigated for the first time *in vivo* for their efficacy in HNSCC. Furthermore, the hypothesis of combining both ER-stress inducing drugs, TFP as a CaM-antagonist and TG for its irreversible SERCA-inhibition, has not been investigated in clinical trials so far. In case of lymphatic metastasis, a reproducible orthotopic xenograft mouse model was established with a metastasis induction rate of 67 %. Obtained results of combined treatment efficacy showed promising trends towards metastasis suppression and a significant reduction in metastases size in the single use situation. Regarding

haematogenous metastasis a promising trend was observed for metastases volume reduction as well.

That both models were unable to reach significant levels may be due to the fact of 3R principal related low sample size per experimental group and high inter-individual variances. Additionally, single animals died preliminary during the experiment, which further limited experimental validity. For future experiments, animal number should be critically reviewed again. Another critical point was the long pause between drug delivery of both substances. There were 2h in between both drug administrations, which can potentially lead to a significant minimisation of the expected combinatorial effect. Studies have to be performed to investigate potential cellular compensatory mechanisms to deal with induced ER-stress. Moreover, a simultaneous administration of both drugs may be a possible further step to achieve a higher level of the expected effect. Additionally, *in vivo* experiments using an HPV-positive cell line to investigate a potential therapeutic effect of TFP and TG on differently originated tumours with a different molecular background will be interesting in future experiments.

As a basement to elucidate the molecular function of SEC62 overexpression in HNSCC, SEC62-ko clones were generated based on CRISPR-Cas9 technology. These clones were already used to study the effects of a stable SEC62-ko on migration and proliferation under TFP and TG therapy, which confirmed priorly generated results of transient SEC62-knockouts by siRNA transfection (Linxweiler et al., 2013; Bochen et al., 2017). Further molecular mechanisms to adjust to ER-stress induction by TFP and TG and also the general impact and molecular function of SEC62 can be better investigated using these newly generated CRISPR-clones in future projects.

5. References

- Abdullahi A, Stanojic M, Parousis A, Patsouris D, Jeschke MG (2017) MODELING ACUTE ER STRESS in VIVO and in VITRO. *Shock* 47:506–513.
- Abou-Elhamd KEA, Habib TN (2008) The role of chromosomal aberrations in premalignant and malignant lesions in head and neck squamous cell carcinoma. *Eur Arch Oto-Rhino-Laryngology* 265:203–207.
- Ali H, Christensen SB, Foreman JC, Pearce FL, Piotrowski W, Thastrup O (1985) The ability of thapsigargin and thapsigargin to activate cells involved in the inflammatory response. *Br J Pharmacol* 85:705–712.
- Allen DG, White DJ, Hutchins AM, Scurry JP, Tabrizi SN, Garland SM, Armes JE (2000) Progressive genetic aberrations detected by comparative genomic hybridization in squamous cell cervical cancer. *Br J Cancer* 83:1659–1663.
- Amornphimoltham P, Rechache K, Thompson J, Masedunskas A, Leelahavanichkul K, Patel V, Molinolo A, Gutkind JS, Weigert R (2013) Rab25 Regulates Invasion and Metastasis in Head and Neck Cancer. *Clin Cancer Res* 19:1375–1388.
- Andrew Silver M, Wei Yang Z, Ganguli R, Nimgaonkar VL (1994) An inhibitory effect of psychoactive drugs on a human neuroblastoma cell line. *Biol Psychiatry* 35:824–826.
- Ang KK, Harris J, Wheeler R, Weber R, Rosenthal DI, Nguyen-tân PF, Westra WH, Chung CH, Jordan RC, Ph D, Lu C, Kim H, Axelrod R, Silverman CC, Redmond KP, Gillison ML, Ph D (2010) Human Papillomavirus and Survival of Patients with Oropharyngeal Cancer. *N Engl J Med* 363:24–35.
- Argiris A, Karamouzis M V., Raben D, Ferris RL (2008) Head and neck cancer. *Lancet* 371:1695–1709.
- Bagur R, Hajnóczky G (2017) Intracellular Ca²⁺ Sensing: Its Role in Calcium Homeostasis and Signaling. *Mol Cell* 66:780–788.
- Bal NC, Maurya SK, Sopariwala DH, Sahoo SK, Gupta SC, Shaikh SA, Pant M, Rowland LA, Goonasekera SA, Molkentin JD, Periasamy M (2012) Sarcosine is a newly identified regulator of muscle-based thermogenesis in mammals. *Nat Med* 18:1575–1579.
- Balmain A, Barrett JC, Moses H, Renan' MJ (1993) WORKING HYPOTHESIS How Many Mutations Are Required for Tumorigenesis? Implications From Human Cancer Data.
- Banerji S, Ni J, Wang SX, Clasper S, Su J, Tammi R, Jones M, Jackson DG (1999) LYVE-1, a new homologue of the CD44 glycoprotein, is a lymph-specific receptor for hyaluronan. *J Cell Biol* 144:789–801.
- Barrangou R, Fremaux C, Deveau H, Richards M, Boyaval P, Moineau S, Romero DA, Horvath P (2007) CRISPR Provides Acquired Resistance Against Viruses in Prokaryotes. *Science* (80-) 315:1709–1712.
- Bauer VL, Braselmann H, Henke M, Mattern D, Walch A, Unger K, Baudis M, Lassmann S, Huber

- R, Wienberg J, Werner M, Zitzelsberger HF (2008) Chromosomal changes characterize head and neck cancer with poor prognosis. *J Mol Med* 86:1353–1365.
- Bellizzi Y, Cornier PG, Delpiccolo CML, Mata EG, Blank V, Roguin LP (2022) Synergistic antitumor effect of a penicillin derivative combined with thapsigargin in melanoma cells. *J Cancer Res Clin Oncol*.
- Bergmann TJ, Fumagalli F, Loi M, Molinari M (2017) Role of SEC62 in ER maintenance: A link with ER stress tolerance in SEC62-overexpressing tumors? *Mol Cell Oncol* 4:e1264351.
- Bergner A, Kellner J, Tufman A, Huber RM (2009) Endoplasmic reticulum Ca²⁺-homeostasis is altered in small and non-small cell lung cancer cell lines. *J Exp Clin Cancer Res* 28:25.
- Bernard WS, Christopher PW (2020) World cancer report 2014.
- Bertolotti A, Zhang Y, Hendershot LM, Harding HP, Ron D (2000) Dynamic interaction of BiP and ER stress transducers in the unfolded-protein response. *Nat Cell Biol* 2:326–332.
- Bhadra P, Dos Santos S, Gamayun I, Pick T, Neumann C, Ogbechi J, Hall BS, Zimmermann R, Helms V, Simmonds RE, Cavalié A (2021) Mycolactone enhances the Ca²⁺ leak from endoplasmic reticulum by trapping Sec61 translocons in a Ca²⁺ permeable state. *Biochem J* 478:4005–4024.
- Birgisdóttir ÁB, Lamark T, Johansen T (2013) The LIR motif – crucial for selective autophagy. *J Cell Sci* 126:3237–3247.
- Bochen F, Adisurya H, Wemmert S, Lerner C, Greiner M, Zimmermann R, Hasenfus A, Wagner M, Smola S, Pfuhl T, Bozzato A, Al Kadah B, Schick B, Linxweiler M (2017) Effect of 3q oncogenes SEC62 and SOX2 on lymphatic metastasis and clinical outcome of head and neck squamous cell carcinomas. *Oncotarget* 8:4922–4934.
- Bockmühl U, Petersen I (2002) DNA ploidy and chromosomal alterations in head and neck squamous cell carcinoma. *Virchows Arch* 441:541–550.
- Bockmühl U, Schwendel A, Dietel M, Petersen I (1996) Distinct patterns of chromosomal alterations in high- and low-grade head and neck squamous cell carcinomas. *Cancer Res* 56:5325–5329.
- Bonner JA, Harari PM, Giralt J, Azarnia N, Shin DM, Cohen RB, Jones CU, Sur R, Raben D, Jassem J, Ove R, Kies MS, Baselga J, Yousoufian H, Amellal N, Rowinsky EK, Ang KK (2006) Radiotherapy plus Cetuximab for Squamous-Cell Carcinoma of the Head and Neck. *N Engl J Med* 354:567–578.
- BOYDEN S (1962) The chemotactic effect of mixtures of antibody and antigen on polymorphonuclear leucocytes. *J Exp Med* 115:453–466.
- Boyle EI, Weng S, Gollub J, Jin H, Botstein D, Cherry JM, Sherlock G (2004) GO::TermFinder-- open source software for accessing Gene Ontology information and finding significantly enriched Gene Ontology terms associated with a list of genes. *Bioinformatics* 20:3710–3715.
- Braakhuis BJM, Brakenhoff RH, René leemans C (2012) Treatment choice for locally advanced

- head and neck cancers on the basis of risk factors: Biological risk factors. *Ann Oncol* 23.
- Brana I, Siu LL (2012) Locally advanced head and neck squamous cell cancer: Treatment choice based on risk factors and optimizing drug prescription. *Ann Oncol* 23:x178–x185.
- Bray F, Ferlay J, Soerjomataram I, Siegel RL, Torre LA, Jemal A (2018) Global cancer statistics 2018: GLOBOCAN estimates of incidence and mortality worldwide for 36 cancers in 185 countries. *CA Cancer J Clin* 68:394–424.
- Bray F, Soerjomataram I (2015) The Changing Global Burden of Cancer: Transitions in Human Development and Implications for Cancer Prevention and Control. The International Bank for Reconstruction and Development / The World Bank.
- Brinkman EK, Chen T, Amendola M, van Steensel B (2014) Easy quantitative assessment of genome editing by sequence trace decomposition. *Nucleic Acids Res* 42:e168.
- Brinkman EK, Steensel B Van (2019) Chapter 3. 1961.
- Broccolo F, Ciccarese G, Rossi A, Anselmi L, Drago F, Toniolo A (2018) Human papillomavirus (HPV) and Epstein- Barr virus (EBV) in keratinizing versus non- keratinizing squamous cell carcinoma of the oropharynx. 6:1–5.
- Burnett JC, Rossi JJ (2012) RNA-Based Therapeutics: Current Progress and Future Prospects. *Chem Biol* 19:60–71.
- Burnette WN (1981) “Western Blotting”: Electrophoretic transfer of proteins from sodium dodecyl sulfate-polyacrylamide gels to unmodified nitrocellulose and radiographic detection with antibody and radioiodinated protein A. *Anal Biochem* 112:195–203.
- Burtneess B et al. (2019) Pembrolizumab alone or with chemotherapy versus cetuximab with chemotherapy for recurrent or metastatic squamous cell carcinoma of the head and neck (KEYNOTE-048): a randomised, open-label, phase 3 study. *Lancet* 394:1915–1928.
- Califano J, Van Der Riet P, Westra W, Nawroz H, Clayman G, Piantadosi S, Corio R, Lee D, Greenberg B, Koch W, Sidransky D (1996) Genetic progression model for head and neck cancer: Implications for field cancerization. *Cancer Res* 56:2488–2492.
- Cantley LC, Neel BG (1999) New insights into tumor suppression: PTEN suppresses tumor formation by restraining the phosphoinositide 3-kinase/AKT pathway. *Proc Natl Acad Sci* 96:4240–4245.
- Casper M, Linxweiler J, Weber SN (2021) SEC62 and SEC63 Expression in Hepatocellular Carcinoma and Tumor-Surrounding Liver Tissue. :110–115.
- Castilho RM, Squarize CH, Almeida LO (2017) Epigenetic modifications and head and neck cancer: Implications for tumor progression and resistance to therapy. *Int J Mol Sci* 18.
- Cebrian-Serrano A, Davies B (2017) CRISPR-Cas orthologues and variants: optimizing the repertoire, specificity and delivery of genome engineering tools. *Mamm Genome* 28:247–261.
- Chen BPC, Liang G, Whelan J, Hai T (1994) ATF3 and ATF3ΔZip. Transcriptional repression

- versus activation by alternatively spliced isoforms. *J Biol Chem* 269:15819–15826.
- Cheng JY, Zhang T, Ruangwattanapaisarn N, Alley MT, Uecker M, Pauly JM, Lustig M, Vasanaawala SS (2015) Free-breathing pediatric MRI with nonrigid motion correction and acceleration. *J Magn Reson Imaging* 42:407–420.
- Chin D, Means AR (2000) Calmodulin: a prototypical calcium sensor. *Trends Cell Biol* 10:322–328.
- Cho SW, Kim S, Kim Y, Kweon J, Kim HS, Bae S, Kim J-S (2014) Analysis of off-target effects of CRISPR/Cas-derived RNA-guided endonucleases and nickases. *Genome Res* 24:132–141.
- Chou AC, Ju Y Ten, Pan CY (2015) Calmodulin interacts with the sodium/calcium exchanger NCX1 to regulate activity. *PLoS One* 10.
- Chow LQM (2020) *Head and Neck Cancer* Longo DL, ed. *N Engl J Med* 382:60–72.
- Chujo M, Noguchi T, Miura T, Arinaga M, Uchida Y, Tagawa Y (2002) Comparative genomic hybridization analysis detected frequent overrepresentation of chromosome 3q in squamous cell carcinoma of the lung. *Lung Cancer* 38:23–29.
- Clapham DE (1995) Calcium signaling. *Cell* 80:259–268.
- Clement K, Rees H, Canver MC, Gehrke JM, Farouni R, Hsu JY, Cole MA, Liu DR, Joung JK, Bauer DE, Pinello L (2019) CRISPResso2 provides accurate and rapid genome editing sequence analysis. *Nat Biotechnol* 37:224–226.
- Cohen EEW et al. (2019) Pembrolizumab versus methotrexate, docetaxel, or cetuximab for recurrent or metastatic head-and-neck squamous cell carcinoma (KEYNOTE-040): a randomised, open-label, phase 3 study. *Lancet* 393:156–167.
- Colombo N, Carinelli S, Colombo A, Marini C, Rollo D, Sessa C, ESMO Guidelines Working Group (2012) Cervical cancer: ESMO Clinical Practice Guidelines for diagnosis, treatment and follow-up. *Ann Oncol* 23:vii27–vii32.
- Comtesse N, Keller A, Diesinger I, Bauer C, Kayser K, Huwer H, Lenhof HP, Meese E (2007) Frequent overexpression of the genes FXR1, CLAPM1 and EIF4G located on amplicon 3q26-27 in squamous cell carcinoma of the lung. *Int J Cancer* 120:2538–2544.
- Cong L, Ran FA, Cox D, Lin S, Barretto R, Habib N, Hsu PD, Wu X, Jiang W, Marraffini LA, Zhang F (2013) Multiplex genome engineering using CRISPR/Cas systems. *Science* 339:819–823.
- Cory S, Adams JM (2002) The BCL2 family: Regulators of the cellular life-or-death switch. *Nat Rev Cancer* 2:647–656.
- Daimon M, Susa S, Suzuki K, Kato T, Yamatani K, Sasaki H (1997) Identification of a human cDNA homologue to the *Drosophila* translocation protein 1 (*Dtrp1*). *Biochem Biophys Res Commun* 230:100–104.
- Danneman PJ, Suckow MA, Brayton C (2000) *The Laboratory Mouse*. CRC Press.
- Dassonville O, Formento JL, Francoual M, Ramaioli A, Santini J, Schneider M, Demard F, Milano G (1993) Expression of epidermal growth factor receptor and survival in upper aerodigestive

- tract cancer. *J Clin Oncol* 11:1873–1878.
- Denmeade SR, Isaacs JT (2005) The SERCA pump as a therapeutic target: Making a “smart bomb” for prostate cancer. *Cancer Biol Ther* 4:21–29.
- Denmeade SR, Jakobsen CM, Janssen S, Khan SR, Garrett ES, Lilja H, Christensen SB, Isaacs JT (2003) Prostate-Specific Antigen-Activated Thapsigargin Prodrug as Targeted Therapy for Prostate Cancer. *JNCI J Natl Cancer Inst* 95:990–1000.
- Denmeade SR, Mhaka AM, Rosen DM, Brennen WN, Dalrymple S, Dach I, Olesen C, Gurel B, DeMarzo AM, Wilding G, Carducci MA, Dionne CA, Moller J V., Nissen P, Christensen SB, Isaacs JT (2012) Engineering a Prostate-Specific Membrane Antigen-Activated Tumor Endothelial Cell Prodrug for Cancer Therapy. *Sci Transl Med* 4:140ra86-140ra86.
- Deshaies RJ, Schekman R (1989) SEC62 encodes a putative membrane protein required for protein translocation into the yeast endoplasmic reticulum. *J Cell Biol* 109:2653–2664.
- Deshaies RJ, Schekman R (1990) Structural and functional dissection of Sec62p, a membrane-bound component of the yeast endoplasmic reticulum protein import machinery. *Mol Cell Biol* 10:6024–6035.
- Deutsche Krebshilfe (2017) Krebs im Mund-Kiefer-Gesichtsbereich (Stiftung Deutsche Krebshilfe, ed). Bonn: Stiftung Deutsche Krebshilfe.
- Doan NTQ, Paulsen ES, Sehgal P, Møller JV, Nissen P, Denmeade SR, Isaacs JT, Dionne CA, Christensen SB (2015) Targeting thapsigargin towards tumors. *Steroids* 97:2–7.
- Dong B, Valencia CA, Liu R (2007) Ca²⁺/Calmodulin Directly Interacts with the Pleckstrin Homology Domain of AKT1. *J Biol Chem* 282:25131–25140.
- Edson KZ, Prasad B, Unadkat JD, Suhara Y, Okano T, Peter Guengerich F, Rettie AE (2013) Cytochrome P450-dependent catabolism of vitamin K: ω -hydroxylation catalyzed by human CYP4F2 and CYP4F11. *Biochemistry* 52:8276–8285.
- Ell SR, Ashman JE, Stafford ND, Greenman J (2002) Global genetic differences in squamous cell carcinoma of the head and neck. *Laryngoscope* 112:1094–1099.
- Ellen TP, Ke Q, Zhang P, Costa M (2008) NDRG1, a growth and cancer related gene: Regulation of gene expression and function in normal and disease states. *Carcinogenesis* 29:2–8.
- Erdmann F, Schäuble N, Lang S, Jung M, Honigmann A, Ahmad M, Dudek J, Benedix J, Harsman A, Kopp A, Helms V, Cavalié A, Wagner R, Zimmermann R (2011) Interaction of calmodulin with Sec61 α limits Ca²⁺ leakage from the endoplasmic reticulum. *EMBO J* 30:17–31.
- Eriksson Å, Yachnin J, Lewensohn R, Nilsson A (2001) DNA-Dependent Protein Kinase Is Inhibited by Trifluoperazine. *Biochem Biophys Res Commun* 283:726–731.
- Fang WY, Kuo YZ, Chang JY, Hsiao JR, Kao HY, Tsai ST, Wu LW (2020) The tumor suppressor TGFBR3 blocks lymph node metastasis in head and neck cancer. *Cancers (Basel)* 12.
- Faustino-Rocha A, Oliveira PA, Pinho-Oliveira J, Teixeira-Guedes C, Soares-Maia R, da Costa RG, Colaço B, Pires MJ, Colaço J, Ferreira R, Ginja M (2013) Estimation of rat mammary

- tumor volume using caliper and ultrasonography measurements. *Lab Anim (NY)* 42:217–224.
- Feng Z, Xia Y, Gao T, Xu F, Lei Q, Peng C, Yang Y, Xue Q, Hu X, Wang Q, Wang R, Ran Z, Zeng Z, Yang N, Xie Z, Yu L (2018) The antipsychotic agent trifluoperazine hydrochloride suppresses triple-negative breast cancer tumor growth and brain metastasis by inducing G0/G1 arrest and apoptosis. *Cell Death Dis* 9.
- Ferlay J, Colombet M, Soerjomataram I, Mathers C, Parkin DM, Piñeros M, Znaor A, Bray F (2019) Estimating the global cancer incidence and mortality in 2018: GLOBOCAN sources and methods. *Int J Cancer* 144:1941–1953.
- Ferlay J, Colombet M, Soerjomataram I, Parkin DM, Piñeros M, Znaor A, Bray F (2021) Cancer statistics for the year 2020: An overview. *Int J Cancer* 149:778–789.
- Ferlay J, Ervik M, Lam F, Colombet M, Mery L, Piñeros M, Znaor A, Soerjomataram I, Bray F (2020) Global Cancer Observatory: Cancer Today. *Int Agency Res Cancer*.
- Ferris RL et al. (2016) Nivolumab for Recurrent Squamous-Cell Carcinoma of the Head and Neck. *N Engl J Med* 375:1856–1867.
- Flanagan RJ (2008) Fatal toxicity of drugs used in psychiatry. *Hum Psychopharmacol Clin Exp* 23:S43–S51.
- Flurkey K, Curren JM, Harrison DE (2007) Chapter 20 Mouse Models in Aging Research. *Mouse Biomed Res*:637–672.
- Ford NL, Thornton MM, Holdsworth DW (2003) Fundamental image quality limits for microcomputed tomography in small animals. *Med Phys* 30:2869–2877.
- Friedberg EC (2003) DNA damage and repair. *Nature* 421:436–440.
- Fumagalli F et al. (2016) Translocon component Sec62 acts in endoplasmic reticulum turnover during stress recovery. *Nat Cell Biol* 18:1173–1184.
- Fung SYH, Lam JWK, Chan KCA (2016) Clinical utility of circulating Epstein-Barr virus DNA analysis for the management of nasopharyngeal carcinoma. *Chinese Clin Oncol* 5:18–18.
- Furuya Y, Isaacs JT (1994) Proliferation-dependent vs. independent programmed cell death of prostatic cancer cells involves distinct gene regulation. *Prostate* 25:301–309.
- Furuya Y, Lundmo P, Short AD, Gill DL, Isaacs JT (1994) The role of calcium, pH, and cell proliferation in the programmed (apoptotic) death of androgen-independent prostatic cancer cells induced by thapsigargin. *Cancer Res* 54:6167–6175.
- Gallagher RP, Lee TK, Bajdik CD, Borugian M (2010) Ultraviolet radiation. *Chronic Dis Can* 29 Suppl 1:51–68.
- Gamayun I, O’Keefe S, Pick T, Klein M-C, Nguyen D, McKibbin C, Piacenti M, Williams HM, Flitsch SL, Whitehead RC, Swanton E, Helms V, High S, Zimmermann R, Cavalié A (2019) Eeyarestatin Compounds Selectively Enhance Sec61-Mediated Ca²⁺ Leakage from the Endoplasmic Reticulum. *Cell Chem Biol* 26:571-583.e6.

- Gambardella J, Lombardi A, Morelli MB, Ferrara J, Santulli G (2020) Inositol 1,4,5-Trisphosphate Receptors in Human Disease: A Comprehensive Update. *J Clin Med* 9:1096.
- Gangopadhyay S, Karmakar P, Dasgupta U, Chakraborty A (2007) Trifluoperazine stimulates ionizing radiation induced cell killing through inhibition of DNA repair. *Mutat Res Toxicol Environ Mutagen* 633:117–125.
- Garneau JE, Dupuis M-È, Villion M, Romero DA, Barrangou R, Boyaval P, Fremaux C, Horvath P, Magadán AH, Moineau S (2010) The CRISPR/Cas bacterial immune system cleaves bacteriophage and plasmid DNA. *Nature* 468:67–71.
- GBD 2017 Causes of Death Collaborators (2018) Global, regional, and national age-sex-specific mortality for 282 causes of death in 195 countries and territories, 1980-2017: a systematic analysis for the Global Burden of Disease Study 2017. *Lancet (London, England)* 392:1736–1788.
- GBD 2017 Risk Factor Collaborators (2018) Global, regional, and national comparative risk assessment of 84 behavioural, environmental and occupational, and metabolic risks or clusters of risks for 195 countries and territories, 1990-2017: a systematic analysis for the Global Burden of Disease Study. *Lancet (London, England)* 392:1923–1994.
- Gleysteen JP, Newman JR, Chhieng D, Frost A, Zinn KR, Rosenthal EL (2008) Fluorescent labeled anti-egfr antibody for identification of regional and distant metastasis in a preclinical xenograft model. *Head Neck* 30:782–789.
- Gomez-Cuadrado L, Tracey N, Ma R, Qian B, Brunton VG (2017) Mouse models of metastasis: Progress and prospects. *DMM Dis Model Mech* 10:1061–1074.
- Greiner M, Kreutzer B, Jung V, Grobholz R, Hasenfus A, Stöhr RF, Tornillo L, Dudek J, Stöckle M, Unteregger G, Kamradt J, Wullich B, Zimmermann R (2011a) Silencing of the SEC62 gene inhibits migratory and invasive potential of various tumor cells. *Int J cancer* 128:2284–2295.
- Greiner M, Kreutzer B, Lang S, Jung V, Cavalié A, Unteregger G, Zimmermann R, Wullich B (2011b) Sec62 protein level is crucial for the ER stress tolerance of prostate cancer. *Prostate* 71:1074–1083.
- Grinshpoon A, Barchana M, Ponizovsky A, Lipshitz I, Nahon D, Tal O, Weizman A, Levav I (2005) Cancer in schizophrenia: is the risk higher or lower? *Schizophr Res* 73:333–341.
- Grobs Y, Awada C, Lemay S-E, Romanet C, Bourgeois A, Toro V, Nadeau V, Shimauchi K, Orcholski M, Breuils-Bonnet S, Tremblay E, Provencher S, Paulin R, Boucherat O, Bonnet S (2021) Preclinical Investigation of Trifluoperazine as a Novel Therapeutic Agent for the Treatment of Pulmonary Arterial Hypertension. *Int J Mol Sci* 22:2919.
- Gupta T, Kannan S, Ghosh-Laskar S, Agarwal JP (2018) Systematic review and meta-analyses of intensity-modulated radiation therapy versus conventional two-dimensional and/or or three-dimensional radiotherapy in curative-intent management of head and neck squamous

- cell carcinoma. *PLoS One* 13:1–15.
- Hagerstrand D et al. (2013) Systematic interrogation of 3q26 identifies TLOC1 and SKIL as cancer drivers. *Cancer Discov* 3:1044–1057.
- Hakii H, Fujiki H, Suganuma M, Nakayasu M, Tahira T, Sugimura T, Scheuer PJ, Christensen SB (1986) Thapsigargin, a histamine secretagogue, is a non-12-O-tetradecanoylphorbol-13-acetate (TPA) type tumor promoter in two-stage mouse skin carcinogenesis. *J Cancer Res Clin Oncol* 111:177–181.
- Hanahan D (2022) Hallmarks of Cancer: New Dimensions. *Cancer Discov* 12:31–46.
- Hanahan D, Weinberg RA (2000) The Hallmarks of Cancer. *Cell* 100:57–70.
- Hanahan D, Weinberg RA (2011) Hallmarks of cancer: The next generation. *Cell* 144:646–674.
- Hankenson FC, Marx JO, Gordon CJ, David JM (2018) Effects of Rodent Thermoregulation on Animal Models in the Research Environment. *Comp Med* 68:425–438.
- Hanna RN, Cekic C, Sag D, Tacke R, Thomas GD, Nowyhed H, Herrley E, Rasquinha N, McArdle S, Wu R, Peluso E, Metzger D, Ichinose H, Shaked I, Chodaczek G, Biswas SK, Hedrick CC (2015) Patrolling monocytes control tumor metastasis to the lung. *Science* (80-) 350:985–990.
- Harper KL, Sosa MS, Entenberg D, Hosseini H, Cheung JF, Nobre R, Avivar-Valderas A, Nagi C, Girnius N, Davis RJ, Farias EF, Condeelis J, Klein CA, Aguirre-Ghiso JA (2016) Mechanism of early dissemination and metastasis in Her2+ mammary cancer. *Nature* 540:588–592.
- Hashibe M et al. (2007) Alcohol Drinking in Never Users of Tobacco, Cigarette Smoking in Never Drinkers, and the Risk of Head and Neck Cancer: Pooled Analysis in the International Head and Neck Cancer Epidemiology Consortium. *JNCI J Natl Cancer Inst* 99:777–789.
- Hashimoto Y, Zhang C, Kawauchi J, Imoto I, Adachi MT, Inazawa J, Amagasa T, Hai T, Kitajima S (2002) An alternatively spliced isoform of transcriptional repressor ATF3 and its induction by stress stimuli. *Nucleic Acids Res* 30:2398–2406.
- Hassan MK, Kumar D, Naik M, Dixit M (2018) The expression profile and prognostic significance of eukaryotic translation elongation factors in different cancers. *PLoS One* 13:1–26.
- Haverty PM, Hon LS, Kaminker JS, Chant J, Zhang Z (2009) High-resolution analysis of copy number alterations and associated expression changes in ovarian tumors. *BMC Med Genomics* 2.
- Heath CH, Deep NL, Sweeny L, Zinn KR, Rosenthal EL (2012) Use of panitumumab-IRDye800 to image microscopic head and neck cancer in an orthotopic surgical model. *Ann Surg Oncol* 19:3879–3887.
- Hershey JWB (1991) TRANSLATIONAL CONTROL IN MAMMALIAN CELLS. *Annu Rev Biochem* 60:717–755.
- Hu JH, Miller SM, Geurts MH, Tang W, Chen L, Sun N, Zeina CM, Gao X, Rees HA, Lin Z, Liu DR (2018) Evolved Cas9 variants with broad PAM compatibility and high DNA specificity.

- Nature 556:57–63.
- Huang C, Lan W, Fraunhofer N, Meilerman A, Iovanna J, Santofimia-Castaño P (2019) Dissecting the anticancer mechanism of trifluoperazine on pancreatic ductal adenocarcinoma. *Cancers (Basel)* 11.
- Huang JB, Kindzelskii AL, Clark AJ, Petty HR (2004) Identification of Channels Promoting Calcium Spikes and Waves in HT1080 Tumor Cells: Their Apparent Roles in Cell Motility and Invasion. *Cancer Res* 64:2482–2489.
- International Agency for Research on Cancer (IARC), Global Cancer Observatory (2020) Germany - Globocan 2020.
- Isaacs JT, Brennen WN, Christensen SB, Denmeade SR (2021) Mipsagargin: The Beginning—Not the End—of Thapsigargin Prodrug-Based Cancer Therapeutics. *Molecules* 26:7469.
- Ishino Y, Shinagawa H, Makino K, Amemura M, Nakata A (1987) Nucleotide sequence of the *iap* gene, responsible for alkaline phosphatase isozyme conversion in *Escherichia coli*, and identification of the gene product. *J Bacteriol* 169:5429–5433.
- Issa IA, Noureddine M (2017) Colorectal cancer screening: An updated review of the available options. *World J Gastroenterol* 23:5086–5096.
- Jaskulska A, Janecka AE, Gach-Janczak K (2021) Thapsigargin—from traditional medicine to anticancer drug. *Int J Mol Sci* 22:1–12.
- Jaszczyszyn A, Gąsiorowski K, Świątek P, Malinka W, Cieślak-Boczula K, Petrus J, Czarnik-Matusiewicz B (2012) Chemical structure of phenothiazines and their biological activity. *Pharmacol Reports* 64:16–23.
- Jeong JY, Park H, Yoo H, Kim E-J, Jeon B, Lee JD, Kang D, Lee CJ, Paek SH, Roh EJ, Yi G-S, Kang SS (2022) Trifluoperazine and Its Analog Suppressed the Tumorigenicity of Non-Small Cell Lung Cancer Cell; Applicability of Antipsychotic Drugs to Lung Cancer Treatment. *Biomedicines* 10:1046.
- Jiang J, Huang Z, Chen X, Luo R, Cai H, Wang H, Zhang H, Sun T, Zhang Y (2017) Trifluoperazine Activates FOXO1-Related Signals to Inhibit Tumor Growth in Hepatocellular Carcinoma. *DNA Cell Biol* 36:813–821.
- Jin C, Jin Y, Wennerberg J, Annertz K, Enoksson J, Mertens F (2006) Cytogenetic abnormalities in 106 oral squamous cell carcinomas. *Cancer Genet Cytogenet* 164:44–53.
- Jinek M, Chylinski K, Fonfara I, Hauer M, Doudna JA, Charpentier E (2012) A programmable dual-RNA-guided DNA endonuclease in adaptive bacterial immunity. *Science* 337:816–821.
- Johnson DE, Burtness B, Leemans CR, Lui VWY, Bauman JE, Grandis JR (2020) Head and neck squamous cell carcinoma. *Nat Rev Dis Prim* 6.
- Jung V, Kindich R, Kamradt J, Jung M, Müller M, Schulz WA, Engers R, Unteregger G, Stöckle M, Zimmermann R, Wullich B (2006) Genomic and expression analysis of the 3q25-q26 amplification unit reveals TLOC1/SEC62 as a probable target gene in prostate cancer. *Mol*

- Cancer Res 4:169–176.
- Kang S, Hong J, Lee JM, Moon HE, Jeon B, Choi J, Yoon NA, Paek SH, Roh EJ, Lee CJ, Kang SS (2017) Trifluoperazine, a well-known antipsychotic, inhibits glioblastoma invasion by binding to calmodulin and disinhibiting calcium release channel IP3R. *Mol Cancer Ther* 16:217–227.
- Kang S, Lee JM, Jeon B, Elkamhawy A, Paik S, Hong J, Oh S-J, Paek SH, Lee CJ, Hassan AHE, Kang SS, Roh EJ (2018) Repositioning of the antipsychotic trifluoperazine: Synthesis, biological evaluation and in silico study of trifluoperazine analogs as anti-glioblastoma agents. *Eur J Med Chem* 151:186–198.
- Kang UG, Kim MJ, Suh PG, Ryu SH, Park JB, Kim JH, Kim YS, Lee YH (1999) Inhibition of trifluoperazine-induced DNA fragmentation by cyclic AMP mediated signaling. *Mol Cells* 9:596–602.
- Kastan MB, Bartek J (2004) Cell-cycle checkpoints and cancer. *Nature* 432:316–323.
- Kersten K, Visser KE, Miltenburg MH, Jonkers J (2017) Genetically engineered mouse models in oncology research and cancer medicine. *EMBO Mol Med* 9:137–153.
- Khan AA, Soloski MJ, Sharp AH, Schilling G, Sabatini DM, Li SH, Ross CA, Snyder SH (1996) Lymphocyte apoptosis: Mediation by increased type 3 inositol 1,4,5- trisphosphate receptor. *Science* (80-) 273:503–507.
- Khanna C, Hunter K (2005) Modeling metastasis in vivo. *Carcinogenesis* 26:513–523.
- Kian Ang K, Berkey BA, Tu X, Zhang H-Z, Katz R, Hammond EH, Fu KK, Milas L (2002) Impact of Epidermal Growth Factor Receptor Expression on Survival and Pattern of Relapse in Patients with Advanced Head and Neck Carcinoma 1.
- Kleinstiver BP, Prew MS, Tsai SQ, Topkar V V, Nguyen NT, Zheng Z, Gonzales APW, Li Z, Peterson RT, Yeh J-RJ, Aryee MJ, Joung JK (2015) Engineered CRISPR-Cas9 nucleases with altered PAM specificities. *Nature* 523:481–485.
- Knudsen AM, Eilertsen I, Kielland S, Pedersen MW, Sørensen MD, Dahlrot RH, Boldt HB, Munthe S, Poulsen FR, Kristensen BW (2020) Expression and prognostic value of the transcription factors EGR1 and EGR3 in gliomas. *Sci Rep* 10:1–13.
- Koch GLE (1990) The endoplasmic reticulum and calcium storage. *BioEssays* 12:527–531.
- Koch K, Mansi K, Haynes E, Adams CE, Sampson S, Furtado VA (2014) Trifluoperazine versus placebo for schizophrenia. *Cochrane Database Syst Rev* 2014.
- Kohn N, Myerson RM (1961) Cholestatic hepatitis associated with trifluoperazine. *N Engl J Med* 264:549–550.
- Kopp MC, Larburu N, Durairaj V, Adams CJ, Ali MMU (2019) UPR proteins IRE1 and PERK switch BiP from chaperone to ER stress sensor. *Nat Struct Mol Biol* 26:1053–1062.
- Körbel C, Linxweiler M, Bochen F, Wemmert S, Schick B, Meyer M, Maurer H, Menger MD, Zimmermann R, Greiner M (2018) Treatment of SEC62 over-expressing tumors by

- Thapsigargin and Trifluoperazine. *Biomol Concepts* 9:53–63.
- Körner S, Körbel C, Dzierma Y, Speicher K, Laschke MW, Rube C, Menger MD, Linxweiler M (2022) Micro-CT analyses of the lung in mice: Parameters influencing the radiation dose and acquisition quality. *bioRxiv*:1–27.
- Kühn JP, Schmid W, Körner S, Bochen F, Wemmert S, Rimbach H, Smola S, Radosa JC, Wagner M, Morris LGT, Bozzato V, Bozzato A, Schick B, Linxweiler M (2021) HPV Status as Prognostic Biomarker in Head and Neck Cancer—Which Method Fits the Best for Outcome Prediction? *Cancers (Basel)* 13:4730.
- Kuo KL, Liu SH, Lin WC, Hsu FS, Chow PM, Chang YW, Yang SP, Shi CS, Hsu CH, Liao SM, Chang HC, Huang KH (2019) Trifluoperazine, an antipsychotic drug, effectively reduces drug resistance in cisplatin-resistant urothelial carcinoma cells via suppressing bcl-xl: An in vitro and in vivo study. *Int J Mol Sci* 20.
- Kurdistani SK, Arizti P, Reimer CL, Sugrue MM, Aaronson SA, Lee SW (1998) Inhibition of tumor cell growth by RTP/rit42 and its responsiveness to p53 and DNA damage. *Cancer Res* 58:4439–4444.
- Kurokawa H, Katsube K, Podyma KA, Ikuta M, Iseki H, Nakajima M, Akashi T, Omura K, Takagi M, Yanagishita M (2003) Heparanase and tumor invasion patterns in human oral squamous cell carcinoma xenografts. *Cancer Sci* 94:277–285.
- Labun K, Montague TG, Krause M, Torres Cleuren YN, Tjeldnes H, Valen E (2019) CHOPCHOP v3: expanding the CRISPR web toolbox beyond genome editing. *Nucleic Acids Res* 47:W171–W174.
- Laemmli UK (1970) Cleavage of structural proteins during the assembly of the head of bacteriophage T4. *Nature* 227:680–685.
- Lakkaraju AKK, Thankappan R, Mary C, Garrison JL, Taunton J, Strub K (2012) Efficient secretion of small proteins in mammalian cells relies on Sec62-dependent posttranslational translocation. *Mol Biol Cell* 23:2712–2722.
- Lang S, Benedix J, Fedeles S V., Schorr S, Schirra C, Schäuble N, Jalal C, Greiner M, Haßdenteufel S, Tatzelt J, Kreutzer B, Edelmann L, Krause E, Rettig J, Somlo S, Zimmermann R, Dudek J (2012) Different effects of Sec61 α , Sec62 and Sec63 depletion on transport of polypeptides into the endoplasmic reticulum of mammalian cells. *J Cell Sci* 125:1958–1969.
- Lang S, Erdmann F, Jung M, Wagner R, Cavalie A, Zimmermann R (2011a) Sec61 complexes form ubiquitous ER Ca²⁺ leak channels. *Channels* 5:228–235.
- Lang S, Schäuble N, Cavalié A, Zimmermann R (2011b) Live Cell Calcium Imaging Combined with siRNA Mediated Gene Silencing Identifies Ca²⁺ Leak Channels in the ER Membrane and their Regulatory Mechanisms. *J Vis Exp*:1–7.
- Langevin SM, O'Sullivan MH, Valerio JL, Pawlita M, Applebaum KM, Eliot M, McClean MD,

- Kelsey KT (2013) Occupational asbestos exposure is associated with pharyngeal squamous cell carcinoma in men from the greater Boston area. *Occup Environ Med* 70:858–863.
- Laurent TC, Fraser JR (1992) Hyaluronan. *FASEB J* 6:2397–2404.
- Lee AE, Rogers LA, Jeffery RE, Longcroft JM (1988) Comparison of metastatic cell lines derived from a murine mammary tumour, and reduction of metastasis by heparin. *Clin Exp Metastasis* 6:463–471.
- Lee AE, Rogers LA, Longcroft JM, Jeffery RE (1990) Reduction of metastasis in a murine mammary tumour model by heparin and polyinosinic-polycytidylic acid. *Clin Exp Metastasis* 8:165–171.
- Lee EYHP, Muller WJ (2010) Oncogenes and Tumor Suppressor Genes. *Cold Spring Harb Perspect Biol* 2:a003236–a003236.
- Leemans CR, Braakhuis BJM, Brakenhoff RH (2011) The molecular biology of head and neck cancer. *Nat Rev Cancer* 11:9–22.
- Li S, Schmitz KR, Jeffrey PD, Wiltzius JJW, Kussie P, Ferguson KM (2005) Structural basis for inhibition of the epidermal growth factor receptor by cetuximab. *Cancer Cell* 7:301–311.
- Linxweiler J, Körbel C, Müller A, Jüngel E, Blaheta R, Heinzelmann J, Stöckle M, Junker K, Menger MD, Saar M (2017a) Experimental imaging in orthotopic renal cell carcinoma xenograft models: comparative evaluation of high-resolution 3D ultrasonography, in-vivo micro-CT and 9.4T MRI. *Sci Rep* 7:1–11.
- Linxweiler M, Bochen F, Schick B, Wemmert S, Al Kadah B, Greiner M, Hasenfus A, Bohle R-M, Juhasz-Böss I, Solomayer E-F, Takacs ZF (2016) Identification of SEC62 as a potential marker for 3q amplification and cellular migration in dysplastic cervical lesions. *BMC Cancer* 16:676.
- Linxweiler M, Linxweiler J, Barth M, Benedix J, Jung V, Kim Y-J, Bohle RM, Zimmermann R, Greiner M (2012) Sec62 Bridges the Gap from 3q Amplification to Molecular Cell Biology in Non-Small Cell Lung Cancer. *Am J Pathol* 180:473–483.
- Linxweiler M, Schick B, Zimmermann R (2017b) Let's talk about Secs: Sec61, Sec62 and Sec63 in signal transduction, oncology and personalized medicine. *Signal Transduct Target Ther* 2:17002.
- Linxweiler M, Schorr S, Schäuble N, Jung M, Linxweiler J, Langer F, Schäfers H-J, Cavalié A, Zimmermann R, Greiner M (2013) Targeting cell migration and the endoplasmic reticulum stress response with calmodulin antagonists: a clinically tested small molecule phenocopy of SEC62 gene silencing in human tumor cells. *BMC Cancer* 13:574.
- Lohrberg M, Wilting J (2016) The lymphatic vascular system of the mouse head. *Cell Tissue Res* 366:667–677.
- López FJ, Merchenthaler I, Ching M, Wisniewski MG, Negro-Vilar A (1991) Galanin: A hypothalamic-hypophysiotropic hormone modulating reproductive functions. *Proc Natl Acad*

- Sci U S A 88:4508–4512.
- Lu JW, Tseng YS, Lo YS, Lin YM, Yeh CM, Lin SH (2021) Prognostic significance of cytoplasmic spns2 expression in patients with oral squamous cell carcinoma. *Med* 57:1–12.
- Lv L, Yi Q, Yan Y, Chao F, Li M (2021) SPNS2 Downregulation Induces EMT and Promotes Colorectal Cancer Metastasis via Activating AKT Signaling Pathway. *Front Oncol* 11:1–14.
- Ma Z, Fan C, Yang Y, Di S, Hu W, Li T, Zhu Y, Han J, Xin Z, Wu G, Zhao J, Li X, Yan X (2016) Thapsigargin sensitizes human esophageal cancer to TRAIL-induced apoptosis via AMPK activation. *Sci Rep* 6.
- Macpherson IR, Rainero E, Mitchell LE, van den Berghe PVE, Speirs C, Dozynkiewicz MA, Chaudhary S, Kalna G, Edwards J, Timpson P, Norman JC (2014) CLIC3 controls recycling of late endosomal MT1-MMP and dictates invasion and metastasis in breast cancer. *J Cell Sci* 127:3893–3901.
- Magnano M, Bongioannini G, Lerda W, Canale G, Tondolo E, Bona M, Viora L, Gabini A, Gabriele P (1999) Lymphnode metastasis in head and neck squamous cells carcinoma: multivariate analysis of prognostic variables. *J Exp Clin Cancer Res* 18:79–83.
- Mahalingam D, Peguero J, Cen P, Arora SP, Sarantopoulos J, Rowe J, Allgood V, Tubb B, Campos L (2019) A phase II, multicenter, single-arm study of mipsagargin (G-202) as a second-line therapy following sorafenib for adult patients with progressive advanced hepatocellular carcinoma. *Cancers (Basel)* 11.
- Mahalingam D, Wilding G, Denmeade S, Sarantopoulos J, Cosgrove D, Cetnar J, Azad N, Bruce J, Kurman M, Allgood VE, Carducci M (2016) Mipsagargin, a novel thapsigargin-based PSMA-Activated prodrug: Results of a first-in-man phase i clinical trial in patients with refractory, advanced or metastatic solid tumours. *Br J Cancer* 114:986–994.
- Marques L de O, Soares B, Silva de Lima M (2004) Trifluoperazine for schizophrenia. *Cochrane Database Syst Rev*.
- Marur S, D´Souza G, Westra WH, Forastiere AA (2010) HPV-associated Head and Neck Cancer: A Virus-related Cancer Epidemic - A Review of Epidemiology, Biology, Virus Detection and Issues in Management. *Lancet Oncol* 11:781–789.
- Mason MJ, Garcia-Rodriguez C, Grinstein S (1991) Coupling between intracellular Ca²⁺ stores and the Ca²⁺ permeability of the plasma membrane. Comparison of the effects of thapsigargin, 2,5-di-(tert-butyl)-1,4-hydroquinone, and cyclopiazonic acid in rat thymic lymphocytes. *J Biol Chem* 266:20856–20862.
- Massion PP, Taflan PM, Rahman SMJ, Yildiz P, Shyr Y, Carbone DP, Gonzalez AL (2004) Role of P63 amplification and overexpression in lung cancer development. *Chest* 125:7113–7121.
- Meganck JA, Liu B (2017) Dosimetry in Micro-computed Tomography: a Review of the Measurement Methods, Impacts, and Characterization of the Quantum GX Imaging System. *Mol Imaging Biol* 19:499–511.

- Meyer HA, Grau H, Kraft R, Kostka S, Prehn S, Kalies KU, Hartmann E (2000) Mammalian Sec61 is associated with Sec62 and Sec63. *J Biol Chem* 275:14550–14557.
- Mi H, Ebert D, Muruganujan A, Mills C, Albou L-P, Mushayamaha T, Thomas PD (2021) PANTHER version 16: a revised family classification, tree-based classification tool, enhancer regions and extensive API. *Nucleic Acids Res* 49:D394–D403.
- Mohamed TMA, Baudoin-stanley FM, Cartwright E, Neyses L (2010) Membrane Transporters in Drug Discovery and Development (Yan Q, ed). Totowa, NJ: Humana Press.
- Mojica FJM, Díez-Villaseñor C, García-Martínez J, Almendros C (2009) Short motif sequences determine the targets of the prokaryotic CRISPR defence system. *Microbiology* 155:733–740.
- Moore EJ, Janus J, Kasperbauer J (2012) Transoral robotic surgery of the oropharynx: Clinical and anatomic considerations. *Clin Anat* 25:135–141.
- Mortensen PB (1994) The occurrence of cancer in first admitted schizophrenic patients. *Schizophr Res* 12:185–194.
- Mü L, Diaz De Escauriaza M, Lajoie P, Theis M, Jung M, Mü A, Burgard C, Greiner M, Snapp EL, Dudek J, Zimmermann R (2010) Evolutionary Gain of Function for the ER Membrane Protein Sec62 from Yeast to Humans. *Mol Biol Cell* 21:691–703.
- Müller B, Lang S, Dominiotto M, Rudin M, Schulz G, Deyhle H, Germann M, Pfeiffer F, David C, Weitkamp T (2008) High-resolution tomographic imaging of microvessels. In: *Developments in X-Ray Tomography VI* (Stock SR, ed), pp 70780B.
- Müller CSL, Pföhler C, Wahl M, Bochen F, Körner S, Kühn JP, Bozzato A, Schick B, Linxweiler M (2021) Expression of SEC62 Oncogene in Benign, Malignant and Borderline Melanocytic Tumors—Unmasking the Wolf in Sheep’s Clothing? *Cancers (Basel)* 13:1645.
- Müller L, de Escauriaza MD, Lajoie P, Theis M, Jung M, Müller A, Burgard C, Greiner M, Snapp EL, Dudek J, Zimmermann R (2010) Evolutionary Gain of Function for the ER Membrane Protein Sec62 from Yeast to Humans Hegde RS, ed. *Mol Biol Cell* 21:691–703.
- Myers JN, Holsinger FC, Jasser SA, Bekele BN, Fidler IJ (2002) An orthotopic nude mouse model of oral tongue squamous cell carcinoma. *Clin Cancer Res* 8:293–298.
- Nakajima M, Irimura T, Nicolson GL (1988) Heparanases and tumor metastasis. *J Cell Biochem* 36:157–167.
- Newton AC, Bootman MD, Scott JD (2016) Second Messengers. *Cold Spring Harb Perspect Biol* 8:a005926.
- Niers TMH, Klerk CPW, DiNisio M, Van Noorden CJF, Büller HR, Reitsma PH, Richel DJ (2007) Mechanisms of heparin induced anti-cancer activity in experimental cancer models. *Crit Rev Oncol Hematol* 61:195–207.
- Nishie M, Suzuki E, Hattori M, Kawaguch K, Kataoka TR, Hirata M, Pu F, Kotake T, Tsuda M, Yamaguchi A, Sugie T, Toi M (2021) Downregulated ATP6V1B1 expression acidifies the

- intracellular environment of cancer cells leading to resistance to antibody-dependent cellular cytotoxicity. *Cancer Immunol Immunother* 70:817–830.
- Noël P, Cartwright IL (1994) A Sec62p-related component of the secretory protein translocon from *Drosophila* displays developmentally complex behavior. *EMBO J* 13:5253–5261.
- Nordenberg J, Fenig E, Landau M, Weizman R, Weizman A (1999) Effects of psychotropic drugs on cell proliferation and differentiation. *Biochem Pharmacol* 58:1229–1236.
- Norup E, Smitt UW, Christensen SB (1986) The potencies of thapsigargin and analogues as activators of rat peritoneal mast cells. *Planta Med NO.* 4:251–255.
- OSBORN M, WEBER K (1980) Damage of cellular functions by trifluoperazine, a calmodulin-specific drug. *Exp Cell Res* 130:484–488.
- Padmanaban V, Krol I, Suhail Y, Szczerba BM, Aceto N, Bader JS, Ewald AJ (2019) E-cadherin is required for metastasis in multiple models of breast cancer. *Nature* 573:439–444.
- Paduch R (2016) The role of lymphangiogenesis and angiogenesis in tumor metastasis. *Cell Oncol*:397–410.
- Palermo G, Miao Y, Walker RC, Jinek M, McCammon JA (2017) CRISPR-Cas9 conformational activation as elucidated from enhanced molecular simulations. *Proc Natl Acad Sci U S A* 114:7260–7265.
- Parish CR, Coombe DR, Jakobsen KB, Bennett FA, Underwood PA (1987) Evidence that sulphated polysaccharides inhibit tumour metastasis by blocking tumour-cell-derived heparanases. *Int J Cancer* 40:511–518.
- Park SH, Chung YM, Ma J, Yang Q, Berek JS, Hu MCT (2016) Pharmacological activation of FOXO3 suppresses triple-negative breast cancer in vitro and in vivo. *Oncotarget* 7:42110–42125.
- Patkar SA, Rasmussen U, Diamant B (1979) On the mechanism of histamine release induced by thapsigargin from *Thapsia garganica* L. *Agents Actions* 9:53–57.
- Patterson KI, Brummer T, O'Brien PM, Daly RJ (2009) Dual-specificity phosphatases: Critical regulators with diverse cellular targets. *Biochem J* 418:475–489.
- Perez RP, Handel LM, Hamilton TC (1992) Potentiation of Cisplatin Cytotoxicity in Human Ovarian Carcinoma Cell Lines by Trifluoperazine, a Calmodulin Inhibitor.
- Periasamy M, Kalyanasundaram A (2007) SERCA pump isoforms: Their role in calcium transport and disease. *Muscle Nerve* 35:430–442.
- Pezzuto F, Caponigro F, Lina M (2015) Update on Head and Neck Cancer : Current Knowledge on Epidemiology , Risk Factors , Molecular Features and Novel Therapies.
- Pick T, Beck A, Gamayun I, Schwarz Y, Schirra C, Jung M, Krause E, Niemeyer BA, Zimmermann R, Lang S, Anken E van, Cavalié A (2021) Remodelling of Ca²⁺ homeostasis is linked to enlarged endoplasmic reticulum in secretory cells. *Cell Calcium* 99:102473.
- Pickering CR et al. (2013) Integrative genomic characterization of oral squamous cell carcinoma

- identifies frequent somatic drivers. *Cancer Discov* 3:770–781.
- Pigozzi D, Ducret T, Tajeddine N, Gala JL, Tombal B, Gailly P (2006) Calcium store contents control the expression of TRPC1, TRPC3 and TRPV6 proteins in LNCaP prostate cancer cell line. *Cell Calcium* 39:401–415.
- Piskounova E, Agathocleous M, Murphy MM, Hu Z, Huddlestun SE, Zhao Z, Leitch AM, Johnson TM, DeBerardinis RJ, Morrison SJ (2015) Oxidative stress inhibits distant metastasis by human melanoma cells. *Nature* 527:186–191.
- Plummer M, de Martel C, Vignat J, Ferlay J, Bray F, Franceschi S (2016) Global burden of cancers attributable to infections in 2012: a synthetic analysis. *Lancet Glob Heal* 4:e609–e616.
- Pobre KFR, Poet GJ, Hendershot LM (2019) The endoplasmic reticulum (ER) chaperone BiP is a master regulator of ER functions: Getting by with a little help from ERdj friends. *J Biol Chem* 294:2098–2108.
- Poeta ML, Manola J, Goldwasser MA, Forastiere A, Benoit N, Califano JA, Ridge JA, Goodwin J, Kenady D, Saunders J, Westra W, Sidransky D, Koch WM (2007) TP53 Mutations and Survival in Squamous-Cell Carcinoma of the Head and Neck. *N Engl J Med* 357:2552–2561.
- Polischouk AG, Holgersson Å, Zong D, Stenerlöw B, Karlsson HL, Möller L, Viktorsson K, Lewensohn R (2007) The antipsychotic drug trifluoperazine inhibits DNA repair and sensitizes non-small cell lung carcinoma cells to DNA double-strand break-induced cell death. *Mol Cancer Ther* 6:2303–2309.
- Pozzan T, Rizzuto R, Volpe P, Meldolesi J (1994) Molecular and cellular physiology of intracellular calcium stores. *Physiol Rev* 74:595–636.
- Prasad V, Mailankody S (2017) Research and Development Spending to Bring a Single Cancer Drug to Market and Revenues After Approval. *JAMA Intern Med* 177:1569.
- Pulkoski-Gross A, Li J, Zheng C, Li Y, Ouyang N, Rigas B, Zucker S, Cao J (2015) Repurposing the antipsychotic trifluoperazine as an antimetastasis agent. *Mol Pharmacol* 87:501–512.
- Qian K, Sun L, Zhou G, Ge H, Meng Y, Li J, Li X, Fang X (2019) Trifluoperazine as an alternative strategy for the inhibition of tumor growth of colorectal cancer. *J Cell Biochem* 120:15756–15765.
- Quynh Doan N, Christensen S (2015) Thapsigargin, Origin, Chemistry, Structure-Activity Relationships and Prodrug Development. *Curr Pharm Des* 21:5501–5517.
- Rahner N, Steinke V (2008) Hereditary Cancer Syndromes. *Dtsch Arztebl* 105:706–714.
- Rampias T, Sasaki C, Weinberger P, Psyrrri A (2009) E6 and E7 Gene Silencing and Transformed Phenotype of Human Papillomavirus 16 – Positive Oropharyngeal Cancer Cells. 101.
- Rangan SR (1972) A new human cell line (FaDu) from a hypopharyngeal carcinoma. *Cancer* 29:117–121.
- Rao PH, Arias-Pulido H, Lu X, Harris CP, Vargas H, Zhang FF, Narayan G, Schneider A, Terry MB, Murty VV (2004) Chromosomal amplifications, 3q gain and deletions of 2q33-q37 are

- the frequent genetic changes in cervical carcinoma. *BMC Cancer* 4:5.
- Rasmussen U, Brøgger Christensen S, Sandberg F (1978) Thapsigargin and thapsigargin, two new histamine liberators from *Thapsia garganica* L. *Acta Pharm Suec* 15:133–140.
- Rautio J, Kumpulainen H, Heimbach T, Oliyai R, Oh D, Järvinen T, Savolainen J (2008) Prodrugs: Design and clinical applications. *Nat Rev Drug Discov* 7:255–270.
- Reed AL, Califano J, Cairns P, Westra WH, Jones RM, Koch W, Ahrendt S, Eby Y, Sewell D, Nawroz H, Bartek J, Sidransky D (1996) High frequency of p16 (CDKN2/MTS-1/INK4A) inactivation in head and neck squamous cell carcinoma. *Cancer Res* 56:3630–3633.
- Reitman ML (2018) Of mice and men – environmental temperature, body temperature, and treatment of obesity. *FEBS Lett* 592:2098–2107.
- Renart J, Reiser J, Stark GR (1979) Transfer of proteins from gels to diazobenzoyloxymethyl-paper and detection with antisera: a method for studying antibody specificity and antigen structure. *Proc Natl Acad Sci U S A* 76:3116–3120.
- Roser M, Ritchie H (2020) Cancer. [OurWorldInData.org](https://ourworldindata.org).
- Rothblatt JA, Deshaies RJ, Sanders SL, Daum G, Schekman R (1989) Multiple genes are required for proper insertion of secretory proteins into the endoplasmic reticulum in yeast. *J Cell Biol* 109:2641–2652.
- Sahoo SK, Shaikh SA, Sopariwala DH, Bal NC, Periasamy M (2013) Sarcolipin protein interaction with Sarco(endo)plasmic reticulum CA 2+ ATPase (SERCA) is distinct from phospholamban protein, and only sarcolipin can promote uncoupling of the serca pump. *J Biol Chem* 288:6881–6889.
- Sanger F, Nicklen S, Coulson AR (1977) DNA sequencing with chain-terminating inhibitors. *Proc Natl Acad Sci U S A* 74:5463–5467.
- Sano D, Fooshee DR, Zhao M, Andrews GA, Frederick MJ, Galer C, Milas ZL, Morrow PKH, Myers JN (2011) Targeted molecular therapy of head and neck squamous cell carcinoma with the tyrosine kinase inhibitor vandetanib in a mouse model. *Head Neck* 33:349–358.
- Sano D, Myers JN (2009) Xenograft models of head and neck cancers. *Head Neck Oncol* 1:32.
- Sarkar S, Horn G, Moulton K, Oza A, Byler S, Kokolus S, Longacre M (2013) Cancer Development, Progression, and Therapy: An Epigenetic Overview. *Int J Mol Sci* 14:21087–21113.
- Schäuble N, Lang S, Jung M, Cappel S, Schorr S, Ulucan Ö, Linxweiler J, Dudek J, Blum R, Helms V, Paton AW, Paton JC, Cavalié A, Zimmermann R (2012) BiP-mediated closing of the Sec61 channel limits Ca²⁺ leakage from the ER. *EMBO J* 31:3282–3296.
- Schindelin J, Arganda-Carreras I, Frise E, Kaynig V, Longair M, Pietzsch T, Preibisch S, Rueden C, Saalfeld S, Schmid B, Tinevez J-Y, White DJ, Hartenstein V, Eliceiri K, Tomancak P, Cardona A (2012) Fiji: an open-source platform for biological-image analysis. *Nat Methods* 9:676–682.

- Schlender M, Hernandez-Villafuerte K, Cheng C-Y, Mestre-Ferrandiz J, Baumann M (2021) How Much Does It Cost to Research and Develop a New Drug? A Systematic Review and Assessment. *Pharmacoeconomics* 39:1243–1269.
- Schleuning M, Brumme V, Wilmanns W (1993) Growth inhibition of human leukemic cell lines by the phenothiazine derivative fluphenazine. *Anticancer Res* 13:599–602.
- Schneider JP, Ochs M (2014) Alterations of mouse lung tissue dimensions during processing for morphometry: A comparison of methods. *Am J Physiol - Lung Cell Mol Physiol* 306:341–350.
- Scorrano L, Oakes SA, Opferman JT, Cheng EH, Sorcinelli MD, Pozzan T, Korsmeyer SJ (2003) BAX and BAK regulation of endoplasmic reticulum Ca²⁺: A control point for apoptosis. *Science (80-)* 300:135–139.
- Seiwert TY, Burtneß B, Mehra R, Weiss J, Berger R, Eder JP, Heath K, McClanahan T, Luceford J, Gause C, Cheng JD, Chow LQ (2016) Safety and clinical activity of pembrolizumab for treatment of recurrent or metastatic squamous cell carcinoma of the head and neck (KEYNOTE-012): an open-label, multicentre, phase 1b trial. *Lancet Oncol* 17:956–965.
- Shah SA, Erdmann S, Mojica FJM, Garrett RA (2013) Protospacer recognition motifs: mixed identities and functional diversity. *RNA Biol* 10:891–899.
- Shen B, Zhang W, Zhang J, Zhou J, Wang J, Chen L, Wang L, Hodgkins A, Iyer V, Huang X, Skarnes WC (2014) Efficient genome modification by CRISPR-Cas9 nickase with minimal off-target effects. *Nat Methods* 11:399–402.
- Shen J, Zhang Y, Yu H, Shen B, Liang Y, Jin R, Liu X, Shi L, Cai X (2016) Role of DUSP1/MKP1 in tumorigenesis, tumor progression and therapy. *Cancer Med* 5:2061–2068.
- Sheu JJC, Lee CH, Ko JY, Tsao GSW, Wu CC, Fang CY, Tsai FJ, Hua CH, Chen CL, Chen JY (2009) Chromosome 3p12.3-p14.2 and 3q26.2-q26.32 are genomic markers for prognosis of advanced nasopharyngeal carcinoma. *Cancer Epidemiol Biomarkers Prev* 18:2709–2716.
- Shin SH, Kim I, Lee JE, Lee M, Park JW (2020) Loss of EGR3 is an independent risk factor for metastatic progression in prostate cancer. *Oncogene* 39:5839–5854.
- Shintani S, Kiyota A, Mihara M, Sumida T, Kayahara H, Nakashiro K ichi, Hamakawa H (2003) Enhancement of radiosensitivity in head and neck cancer cells by ZD1839 ('IRESSA'), a selective epidermal growth factor receptor tyrosine kinase inhibitor. *Am J Clin Oncol* 26:150–156.
- Sicking M, Lang S, Bochen F, Roos A, Drenth JPH, Zakaria M, Zimmermann R, Linxweiler M (2021) Complexity and Specificity of Sec61-Channelopathies: Human Diseases Affecting Gating of the Sec61 Complex. *Cells* 10:1036.
- Siemens Healthcare (2015) Magnetis, Spins, and Resonances. Siemens.
- Singh M, Ferrara N (2012) Modeling and predicting clinical efficacy for drugs targeting the tumor

- milieu. *Nat Biotechnol* 30:648–657.
- Slade DJ, Fang P, Dreyton CJ, Zhang Y, Fuhrmann J, Rempel D, Bax BD, Coonrod SA, Lewis HD, Guo M, Gross ML, Thompson PR (2015) Protein arginine deiminase 2 binds calcium in an ordered fashion: Implications for inhibitor design. *ACS Chem Biol* 10:1043–1053.
- Smeets SJ, Braakhuis BJM, Abbas S, Snijders PJF, Ylstra B, Van De Wiel MA, Meijer GA, Leemans CR, Brakenhoff RH (2006) Genome-wide DNA copy number alterations in head and neck squamous cell carcinomas with or without oncogene-expressing human papillomavirus. *Oncogene* 25:2558–2564.
- Smego RA (1982) The Neuroleptic Malignant Syndrome. *Arch Intern Med* 142:1183.
- Stacker SA, Baldwin ME, Achen MG (2002) The role of tumor lymphangiogenesis in metastatic spread. *FASEB J* 16:922–934.
- Stein S, Thomas EK, Herzog B, Westfall MD, Rocheleau J V., Jackson RS, Wang M, Liang P (2004) NDRG1 is necessary for p53-dependent apoptosis. *J Biol Chem* 279:48930–48940.
- Stevens FC (1983) Calmodulin: an introduction. *Can J Biochem Cell Biol* 61:906–910.
- Suchanti S, Stephen BJ, Awasthi S, Awasthi SK, Singh G, Singh A, Mishra R (2022) Harnessing the role of epigenetic histone modification in targeting head and neck squamous cell carcinoma. *Epigenomics* 14:279–293.
- Sudeshna G, Parimal K (2010) Multiple non-psychiatric effects of phenothiazines: A review. *Eur J Pharmacol* 648:6–14.
- Sullivan GF, Garcia-Welch A, White E, Lutzker S, Hait WN (2002) Augmentation of apoptosis by the combination of bleomycin with trifluoperazine in the presence of mutant p53. *J Exp Ther Oncol* 2:19–26.
- Sun X, Chen P, Chen X, Yang W, Chen X, Zhou W, Huang D, Cheng Y (2021) KIF4A enhanced cell proliferation and migration via Hippo signaling and predicted a poor prognosis in esophageal squamous cell carcinoma. *Thorac Cancer* 12:512–524.
- Supek F, Bošnjak M, Škunca N, Šmuc T (2011) Revigo summarizes and visualizes long lists of gene ontology terms. *PLoS One* 6.
- Swartz MA, Skobe M (2001) Lymphatic function, lymphangiogenesis, and cancer metastasis. *Microsc Res Tech* 55:92–99.
- Takacs ZF, Radosa JC, Linxweiler M, Kasoha M, Bohle RM, Bochen F, Unger C, Solomayer F-E, Schick B, Juhasz-Böss I (2019) Identification of 3q oncogene SEC62 as a marker for distant metastasis and poor clinical outcome in invasive ductal breast cancer. *Arch Gynecol Obstet* 299:1405–1413.
- Takes RP, Rinaldo A, Silver CE, Haigentz M, Woolgar JA, Triantafyllou A, Mondin V, Paccagnella D, De Bree R, Shaha AR, Hartl DM, Ferlito A (2012) Distant metastases from head and neck squamous cell carcinoma. Part I. Basic aspects. *Oral Oncol* 48:775–779.
- Tardy M, Dold M, Engel RR, Leucht S (2014) Trifluoperazine versus low-potency first-generation

- antipsychotic drugs for schizophrenia. *Cochrane Database Syst Rev* 10:129.
- Tasdogan A, Faubert B, Ramesh V, Ubellacker JM, Shen B, Solmonson A, Murphy MM, Gu Z, Gu W, Martin M, Kasitinon SY, Vandergriff T, Mathews TP, Zhao Z, Schadendorf D, DeBerardinis RJ, Morrison SJ (2020) Metabolic heterogeneity confers differences in melanoma metastatic potential. *Nature* 577:115–120.
- Theodosiou A, Ashworth A (2002) MAP kinase phosphatases. *Genome Biol* 3:REVIEWS3009.
- Tian Z, Liang G, Cui K, Liang Y, Wang Q, Lv S, Cheng X, Zhang L (2021) Insight Into the Prospects for RNAi Therapy of Cancer. *Front Pharmacol* 12:1–15.
- Tomayko MM, Reynolds CP (1989) Determination of subcutaneous tumor size in athymic (nude) mice. *Cancer Chemother Pharmacol* 24:148–154.
- Tombal B, Denmeade SR, Gillis JM, Isaacs JT (2002) A supramicromolar elevation of intracellular free calcium ($[Ca^{2+}]_i$) is consistently required to induce the execution phase of apoptosis. *Cell Death Differ* 9:561–573.
- Tombal B, Denmeade SR, Isaacs JT (1999) Assessment and validation of a microinjection method for kinetic analysis of $[Ca^{2+}]_i$ in individual cells undergoing apoptosis. *Cell Calcium* 25:19–28.
- Tombal B, Weeraratna AT, Denmeade SR, Isaacs JT (2000) Thapsigargin induces a calmodulin/calcineurin-dependent apoptotic cascade responsible for the death of prostatic cancer cells. *Prostate* 43:303–317.
- Toniatti C, Jones P, Graham H, Pagliara B, Draetta G (2014) Oncology drug discovery: Planning a turnaround. *Cancer Discov* 4:397–404.
- Toyoshima C, Nomura H (2002) Structural changes in the calcium pump accompanying the dissociation of calcium. *Nature* 418:605–611.
- Treiman M, Caspersen C, Christensen SB (1998) A tool coming of age: Thapsigargin as an inhibitor of sarco-endoplasmic reticulum Ca^{2+} -ATPases. *Trends Pharmacol Sci* 19:131–135.
- Tyanova S, Temu T, Sinitcyn P, Carlson A, Hein MY, Geiger T, Mann M, Cox J (2016) The Perseus computational platform for comprehensive analysis of (prote)omics data. *Nat Methods* 13:731–740.
- Tyedmers J, Lerner M, Bies C, Dudek J, Skowronek MH, Haas IG, Zimmermann R, Heim N, Nastainczyk W (2000) Homologs of the yeast Sec complex subunits Sec62p and Sec63p are abundant proteins in dog pancreas microsomes. :8–13.
- Ubellacker JM, Tasdogan A, Ramesh V, Shen B, Mitchell EC, Martin-Sandoval MS, Gu Z, McCormick ML, Durham AB, Spitz DR, Zhao Z, Mathews TP, Morrison SJ (2020) Lymph protects metastasizing melanoma cells from ferroptosis. *Nature* 585:113–118.
- Van Coppenolle F, Vanden Abeele F, Slomianny C, Flourakis M, Hesketh J, Dewailly E, Prevarskaya N (2004) Ribosome-translocon complex mediates calcium leakage from

- endoplasmic reticulum stores. *J Cell Sci* 117:4135–4142.
- van der Waal I (2009) Potentially malignant disorders of the oral and oropharyngeal mucosa; terminology, classification and present concepts of management. *Oral Oncol* 45:317–323.
- van Houten VMM, Tabor MP, van den Brekel MWM, Kumer JA, Denkers F, Dijkstra J, Leemans R, van der Waal I, Snow GB, Brakenhoff RH (2002) Mutated p53 as a molecular marker for the diagnosis of head and neck cancer. *J Pathol* 198:476–486.
- Vandonselaar M, Hickie RA, Quail W, Delbaere LTJ (1994) Trifluoperazine-induced conformational change in Ca²⁺-calmodulin. *Nat Struct Biol* 1:795–801.
- Vasanthakumar T, Rubinstein JL (2020) Structure and Roles of V-type ATPases. *Trends Biochem Sci* 45:295–307.
- Vlodavsky I, Friedmann Y, Elkin M, Aingorn H, Atzmon R, Ishai-Michaeli R, Bitan M, Pappo O, Peretz T, Michal I, Spector L, Pecker I (1999) Mammalian heparanase: Gene cloning, expression and function in tumor progression and metastasis. *Nat Med* 5:793–802.
- Vogelstein B, Fearon ER, Hamilton SR, Kern SE, Preisinger AC, Leppert M, Nakamura Y, White R, Smits AM, Bos JL (1988) Genetic alterations during colorectal-tumor development. *N Engl J Med* 319:525–532.
- Vogelstein B, Kinzler KW (2004) Cancer genes and the pathways they control. *Nat Med* 10:789–799.
- Walter P, Blobel G (1983) Preparation of microsomal membranes for cotranslational protein translocation. *Methods Enzymol* 96:84–93.
- Walter P, Ron D (2011) The Unfolded Protein Response: From Stress Pathway to Homeostatic Regulation. *Science* (80-) 334:1081–1086.
- Wang H, Mustafa A, Liu S, Liu J, Lv D, Yang H, Zou J (2019) Immune checkpoint inhibitor toxicity in head and neck cancer: From identification to management. *Front Pharmacol* 10:1–8.
- Watts C, Wickner W, Zimmermann R (1983) M13 procoat and a pre-immunoglobulin share processing specificity but use different membrane receptor mechanisms. *Proc Natl Acad Sci U S A* 80:2809–2813.
- Weber K, Osborn M (1969) The reliability of molecular weight determinations by dodecyl sulfate-polyacrylamide gel electrophoresis. *J Biol Chem* 244:4406–4412.
- Weiss BG, Ihler F, Wolff HA, Schneider S, Canis M, Steiner W, Welz C (2017) Transoral laser microsurgery for treatment for hypopharyngeal cancer in 211 patients. *Head Neck* 39:1631–1638.
- Wemmert S, Lindner Y, Linxweiler J, Wagenpfeil S, Bohle R, Niewald M, Schick B (2016) Initial evidence for Sec62 as a prognostic marker in advanced head and neck squamous cell carcinoma. *Oncol Lett* 11:1661–1670.
- Wen Y, Zhang Y, Li J, Luo F, Huang Z, Liu K (2018) Low concentration trifluoperazine promotes proliferation and reduces calcium-dependent apoptosis in glioma cells. *Sci Rep* 8.

- Weng L, Du J, Zhou Q, Cheng B, Li J, Zhang D, Ling C (2012) Identification of cyclin B1 and Sec62 as biomarkers for recurrence in patients with HBV-related hepatocellular carcinoma after surgical resection. *Mol Cancer* 11:39.
- Whittle JR, Lewis MT, Lindeman GJ, Visvader JE (2015) Patient-derived xenograft models of breast cancer and their predictive power. *Breast Cancer Res* 17.
- Wiegand S, Zimmermann A, Wilhelm T, Werner JA (2015) Survival After Distant Metastasis in Head and Neck Cancer. *5502:5499–5502*.
- Wild CP, Weiderpass E, Stewart BW (2020) *WORLD CANCER REPORT : cancer research for cancer development*. Lyon: IARC.
- Winton MJ, D'Souza G, Rettig EM, Westra WH, van Zante A, Wang SJ, Ryan WR, Mydlarz WK, Ha PK, Miles BA, Koch W, Gourin C, Eisele DW, Fakhry C (2018) Increasing prevalence of human papillomavirus-positive oropharyngeal cancers among older adults. *Cancer* 124:2993–2999.
- Wissoczky N (1877) Ueber das Eosin als Reagens auf Hämoglobin und die Bildung von Blutgefäßen und Blutkörperchen bei Säugethier- und Hühnerembryonen. *Arch für Mikroskopische Anat* 13:479–496.
- World Health Organization (2021) *World health statistics 2021: monitoring health for the SDGs, sustainable development goals*. World Health Organization.
- World Health Organization (2018) *DALY estimates, 2000-2016*.
- World Health Organization (2020) *No Title*.
- Wu CH, Bai LY, Tsai MH, Chu PC, Chiu CF, Chen MY, Chiu SJ, Chiang JH, Weng JR (2016) Pharmacological exploitation of the phenothiazine antipsychotics to develop novel antitumor agents-A drug repurposing strategy. *Sci Rep* 6.
- Wu L, Huang X, Kuang Y, Xing Z, Deng X, Luo Z (2019) Thapsigargin induces apoptosis in adrenocortical carcinoma by activating endoplasmic reticulum stress and the JNK signaling pathway: An in vitro and in vivo study. *Drug Des Devel Ther* 13:2787–2798.
- Wyman C, Kanaar R (2006) DNA double-strand break repair: all's well that ends well. *Annu Rev Genet* 40:363–383.
- Xia Y, Jia C, Xue Q, Jiang J, Xie Y, Wang R, Ran Z, Xu F, Zhang Y, Ye T (2019) Antipsychotic drug trifluoperazine suppresses colorectal cancer by inducing G0/G1 arrest and apoptosis. *Front Pharmacol* 10.
- Xu Y, Zhang Q, Zhou J, Li Z, Guo J, Wang W, Wang W (2019) Down-regulation of SOX18 inhibits laryngeal carcinoma cell proliferation, migration, and invasion through JAK2/STAT3 signaling. *Biosci Rep* 39:1–10.
- Yamamoto H, Shigematsu H, Nomura M, Lockwood WW, Sato M, Okumura N, Soh J, Suzuki M, Wistuba II, Fong KM, Lee H, Toyooka S, Date H, Lam WL, Minna JD, Gazdar AF (2008) PIK3CA mutations and copy number gains in human lung cancers. *Cancer Res* 68:6913–

6921.

- Ye J, Coulouris G, Zaretskaya I, Cutcutache I, Rozen S, Madden TL (2012) Primer-BLAST: a tool to design target-specific primers for polymerase chain reaction. *BMC Bioinformatics* 13:134.
- Yeh CT et al. (2012) Trifluoperazine, an antipsychotic agent, inhibits cancer stem cell growth and overcomes drug resistance of lung cancer. *Am J Respir Crit Care Med* 186:1180–1188.
- Yen CC, Chen YJ, Pan CC, Lu KH, Chen PCH, Hsia JY, Chen JT, Wu YC, Hsu WH, Wang LS, Huang MH, Huang BS, Hu CP, Chen PM, Lin CH (2005) Copy number changes of target genes in chromosome 3q25.3-qter of esophageal squamous cell carcinoma: TP63 is amplified in early carcinogenesis but down-regulated as disease progressed. *World J Gastroenterol* 11:1267–1272.
- Yoshitomi Y, Nakanishi H, Kusano Y, Munesue S, Oguri K, Tatematsu M, Yamashina I, Okayama M (2004) Inhibition of experimental lung metastases of Lewis lung carcinoma cells by chemically modified heparin with reduced anticoagulant activity. *Cancer Lett* 207:165–174.
- Zacharski LR, Moritz TE, Haakenson CM, O'Donnell JF, Ballard HS, Johnson GJ, Ringenberg QS, Schilsky RL, Spaulding MB, Tornyo K, Williams CC (1990) Chronic calcium antagonist use in carcinoma of the lung and colon: A retrospective cohort observational study. *Cancer Invest* 8:451–458.
- Zentrum für Krebsregisterdaten im Robert Koch-Institut (2016) Bericht zum Krebsgeschehen in Deutschland 2016. :274.
- Zhang X, Hyer JM, Yu H, D'Silva NJ, Kirkwood KL (2014) DUSP1 phosphatase regulates the proinflammatory milieu in head and neck squamous cell carcinoma. *Cancer Res* 74:7191–7197.
- Zhang X, Xu R, Zhang C, Xu Y, Han M, Huang B, Chen A, Qiu C, Thorsen F, Prestegarden L, Bjerkvig R, Wang J, Li X (2017) Trifluoperazine, a novel autophagy inhibitor, increases radiosensitivity in glioblastoma by impairing homologous recombination. *J Exp Clin Cancer Res* 36:1–13.
- Zhang XH, Tee LY, Wang XG, Huang QS, Yang SH (2015) Off-target effects in CRISPR/Cas9-mediated genome engineering. *Mol Ther - Nucleic Acids*.

6. Publications and congress contribution

Original research articles

Warth A, **Körner S**, Penzel R, Muley T, Dienemann H, Schirmacher P, von Knebel-Doeberitz M, Weichert W, Kloor M (2016) **Microsatellite instability in pulmonary adenocarcinomas: A comprehensive study of 480 cases.** *Virchows Arch* 468. Doi: 10.1007/s00428-015-1892-7

Janikovits J, Müller M, Krzykalla J, **Körner S**, Echterdiek F, Lahrmann B, Grabe N, Schneider M, Benner A, Doeberitz M von K, Kloor M (2018) **High numbers of PDCD1 (PD-1)-positive T cells and B2M mutations in microsatellite-unstable colorectal cancer.** *Oncoimmunology* 7:e1390640. Doi: 10.1080/2162402X.2017.1390640

Bochen F, Balensiefer B, **Körner S**, Bittenbring JT, Neumann F, Koch A, Bumm K, Marx A, Wemmert S, Papaspyrou G, Zuschlag D, Kühn JP, Al Kadah B, Schick B, Linxweiler M (2018) **Vitamin D deficiency in head and neck cancer patients – prevalence, prognostic value and impact on immune function.** *Oncoimmunology* 7:e1476817. Doi: 10.1080/2162402X.2018.1476817

Linxweiler M, Pillong L, Kopanja D, Kühn JP, Wagenpfeil S, Radosa JC, Wang J, Morris LGT, Al Kadah B, Bochen F, **Körner S**, Schick B (2020) **Augmented reality-enhanced navigation in endoscopic sinus surgery: A prospective, randomized, controlled clinical trial.** *Laryngoscope Investig Otolaryngol* 5:621–629. Doi: 10.1002/lio2.436

Kühn JP, Schmid W, **Körner S**, Bochen F, Wemmert S, Rimbach H, Smola S, Radosa JC, Wagner M, Morris LGT, Bozzato V, Bozzato A, Schick B, Linxweiler M (2021) **HPV Status as Prognostic Biomarker in Head and Neck Cancer—Which Method Fits the Best for Outcome Prediction?** *Cancers (Basel)* 13:4730. Doi: 10.3390/cancers13184730

Müller CSL, Pföhler C, Wahl M, Bochen F, **Körner S**, Kühn JP, Bozzato A, Schick B, Linxweiler M (2021) **Expression of SEC62 Oncogene in Benign, Malignant and Borderline Melanocytic Tumors—Unmasking the Wolf in Sheep's Clothing?** *Cancers (Basel)* 13:1645. Doi: 10.3390/cancers13071645

Linxweiler M, Körner S, Wemmert S, Rimbach H, Helfrich J, Linxweiler B, Takacs ZF, Solomayer EF, Wagner M, Morris LGT, Schick B, Kühn JP (2022) **Cytology-based Cancer Surgery of the**

Head and Neck (CyCaS-HN): a prospective, randomized, controlled clinical trial. European Archives of Oto-Rhino-Laryngology. Doi: 10.1007/s00405-022-07333-7

Körner S, Körbel C, Dzierma Y, Speicher K, Laschke MW, Rübe C, Menger MD, Linxweiler M (2022) Micro-CT analyses of the lung in mice: Parameters influencing the radiation dose and acquisition quality. bioRxiv:1–27. Doi: 10.1101/2022.04.27.489643

Körner S, Pick T, Bochen F, Wemmert S, Körbel C, Menger MD, Cavalié A, Kühn JP, Schick B, Linxweiler M (2022) Antagonizing Sec62 function in intracellular Ca²⁺ homeostasis represents a novel therapeutic strategy for head and neck cancer. Frontiers in Physiology. Doi: 10.3389/fphys.2022.880004, in press

Planned publications

Brust LA*, **Körner S***, Kühn JP, Wemmert S, Menger MD, Schick B, Holick MF, Morris LGT, Linxweiler M (2022) **The effect of Calcitriol on tumor initiation, tumor progression and anti-tumoral immune response in head and neck cancer *in vivo*.** *In preparation*

Knebel M, **Körner S**, Kühn JP, Smola S, Wagner M, Schick B, Linxweiler M (2022) **Prognostic impact of tumor infiltrating immune cell subpopulations in head and neck cancer - analysis of the TCGA-HNSC cohort and immunohistochemical validation on 105 patients.** *In preparation*

Krebs-Fleischmann HA, Linxweiler M, **Körner S**, Kühn JP, Smola S, Wagner M, Schick B, Bozzato A, Bochen F (2022) **Biological and prognostic effects of vitamin D and HPV in head and neck cancer: a focus on tumor-associated immune checkpoint molecules.** *In preparation*

Bochen F, Schmid W, Kühn JP, **Körner S**, Wagner M, Schick B, Bozzato A, Linxweiler M (2022) **Comparative analysis of current methods to determine the HPV tumor-status in head and neck cancer patients.** *In preparation*

Bochen F, Feld JM, Sterkel F, Balensiefer B, **Körner S**, Kühn JP, Wagner M, Schick B, Bozzato A, Linxweiler M (2023) **Influence of vitamin D on the lytic signature of tumorinfiltrating leukocytes in head and neck cancer.** *In preparation*

Bochen F, Sterkel F, Feld JM, Balensiefer B, **Körner S**, Kühn JP, Wagner M, Schick B,

Bozzato A, Linxweiler M (2023) **Vitamin D deficiency impacts the regulation of the tumor inflammasome in head and neck cancer.** *In preparation*

Congress contributions (only first author)

Körner S, Körbel C, Bochen F, Menger MD, Zimmermann R, Schick B, Linxweiler M. 2018. Establishment of murine xenograft models for lymphogenic and haematogenic metastatic spread of head and neck squamous cell carcinoma. Poster with short presentation. Presented at the 33rd German Cancer Congress 2018 of the Deutsche Krebsgesellschaft e. V. and Stiftung Deutsche Krebshilfe, 21th to 24th February 2018 in Berlin; doi: 10.1159/000487109

Körner S, Körbel C, Wemmert S, Menger MD, Schick B, Linxweiler M (2022) Impact of Thapsigargin and Trifluoperazine on tumor growth and lymphogenic metastasis of head and neck carcinomas in an orthotopic murine in vivo model. Presentation at the 93rd Annual Meeting of the German Society of Oto-Rhino-Laryngology, Head and Neck Surgery in Hannover, doi: 10.1055/s-0042-1746705

Experimentally supervised MD candidates

Helge Anand Krebs-Fleischmann	medical doctorate	2017-2019
Meike Vorschel	medical doctorate	since 2019
Moritz Knebel	medical doctorate	since 2019
Jana Schnatman	medical doctorate	since 2019
Lukas Alexander Brust	medical doctorate	since 2021
Sebastian Hass	medical doctorate	since 2022

7. Acknowledgement

At the end of my PhD thesis, I would like to thank all of those who have contributed to the success and completion of this work.

First, I would like to thank Prof. Dr. Maximilian Linxweiler for providing me the interesting topic and his pleasing supervision at any time. Our discussions and brainstormings for new ideas were important for my motivation and were one of the main driving motors for this work. Prof. Bernhard Schick I would like to thank for provision of the laboratories and the laboratory equipment.

I want to thank Prof. Dr. Martin Jung for being the first corrector of my thesis and for supporting me with his great network over the whole campus for all matters.

Prof. Richard Zimmermann and Dr. Sven Lang, Dr. Mark Sicking and Monika Lerner of the Institute of Medical Biochemistry and Molecular Biology I want to give a special thank for providing me their laboratories, their equipment, and their knowledge especially with questions concerning the cell culture and western blot techniques, as well as having an open ear at any time.

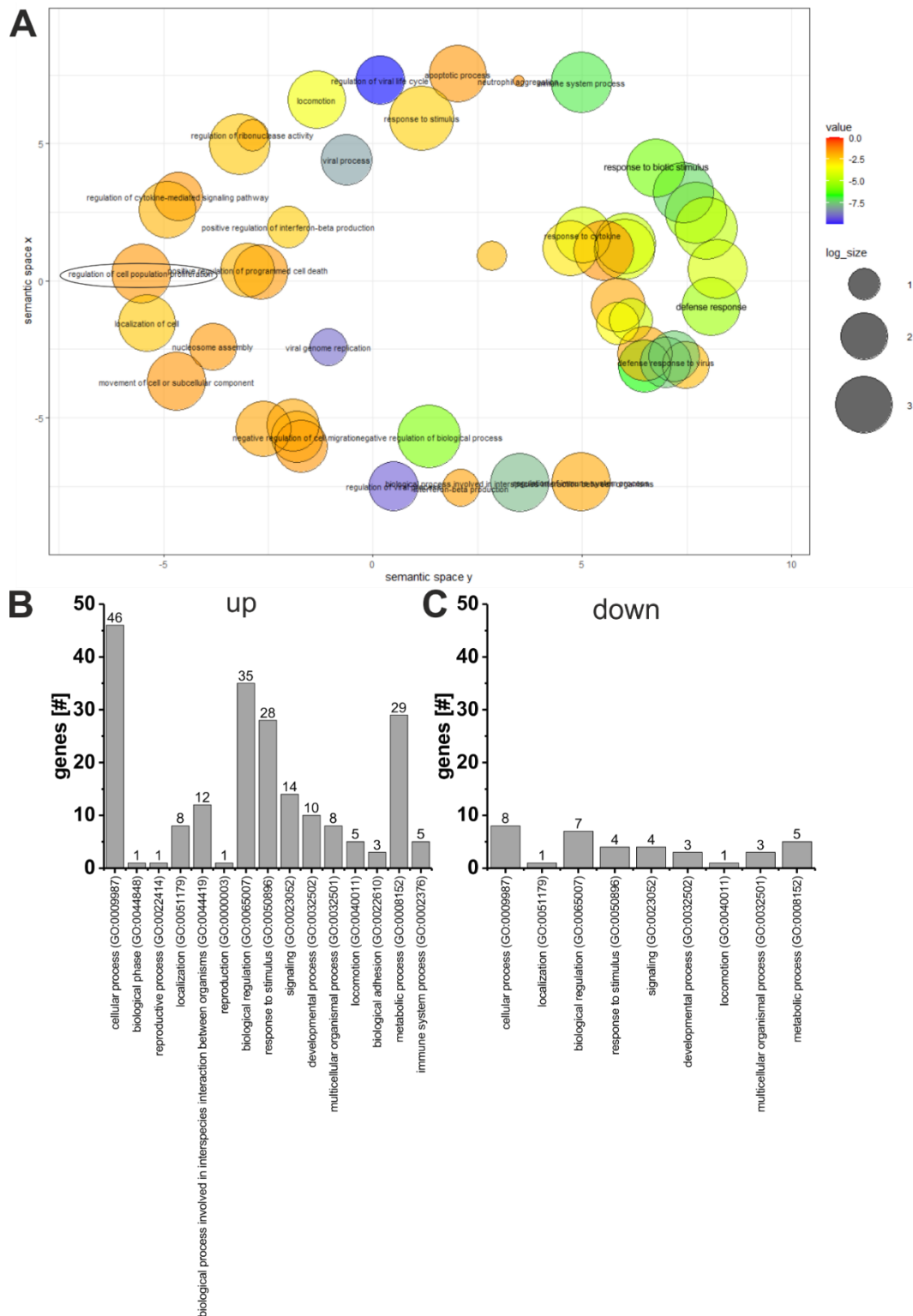
A great and special thank I want to give to Dr. Florian Bochen who helped me during this work very much, introduced me in many of the applied methods and analytical skills I had to use and who introduced me in general into the topic of this thesis.

Special thanks also go to Dr Silke Wemmert, Carolin Bick, Ulrike Bechtel, Katharina Sorg and Monika Hoffmann for your constant helpfulness and support, as well as your numerous encouragements.

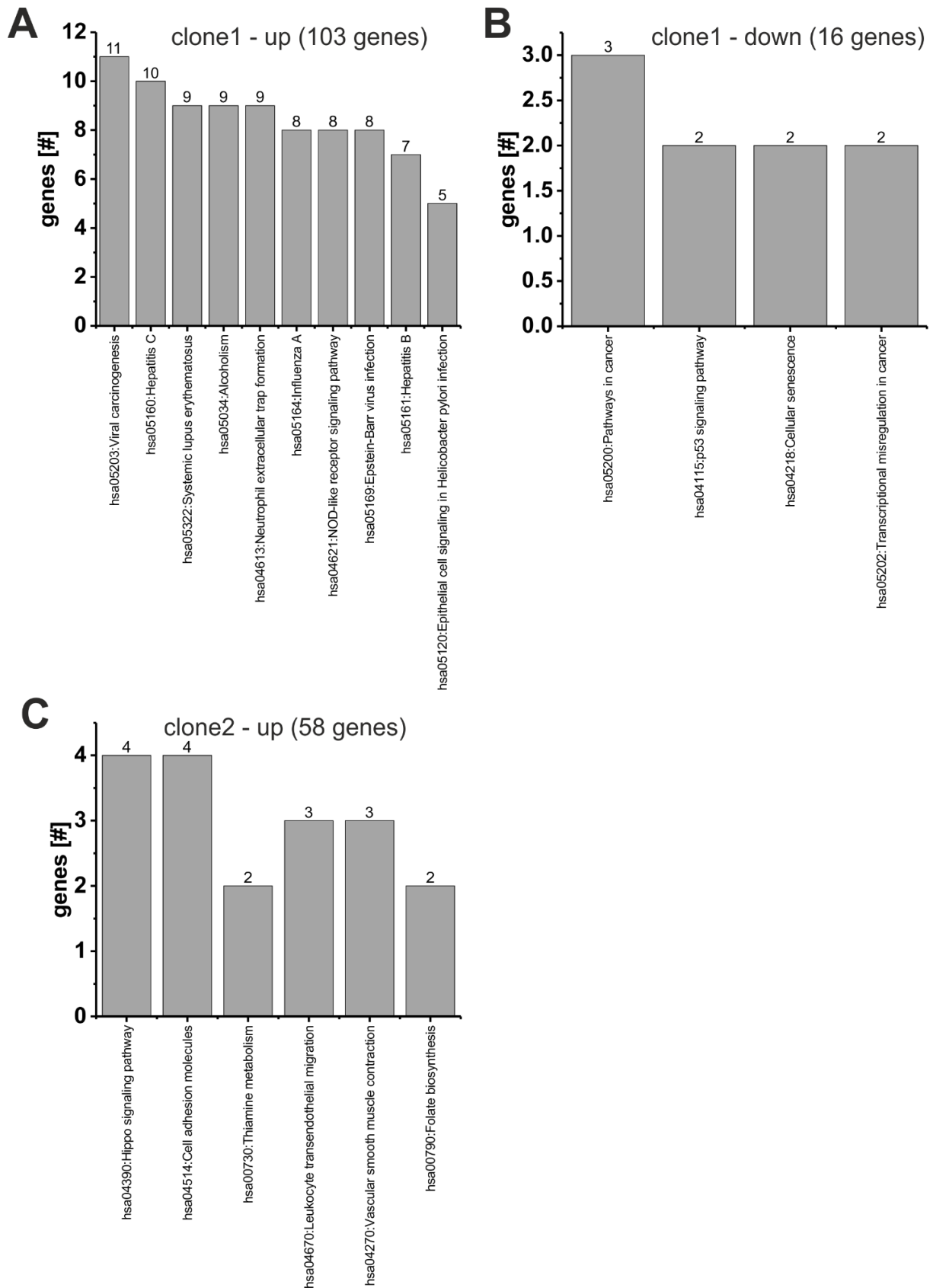
Prof. Michael Menger, Prof. Matthias Laschke, Dr. Christina Körbel, Janine Becker, Ruth Nickels, and all animal keepers of the Institute for Clinical and Experimental Surgery I want to thank for the provision of the animal husbandry as well as their technical support in any questions concerning the animal handling and sample preparation.

I would like to express my deep and sincere gratitude to my family and friends for their never-ending support. I would like to thank my parents, Jürgen and Carmen, for always giving me the freedom to make my own decisions. Due to their permanent support, they gave me all opportunities and helped me to get to where I am now. From the bottom of my heart, I would like to thank Fabian for all his encouraging advice both biologically and personally, his patience and hugs when I really needed them.

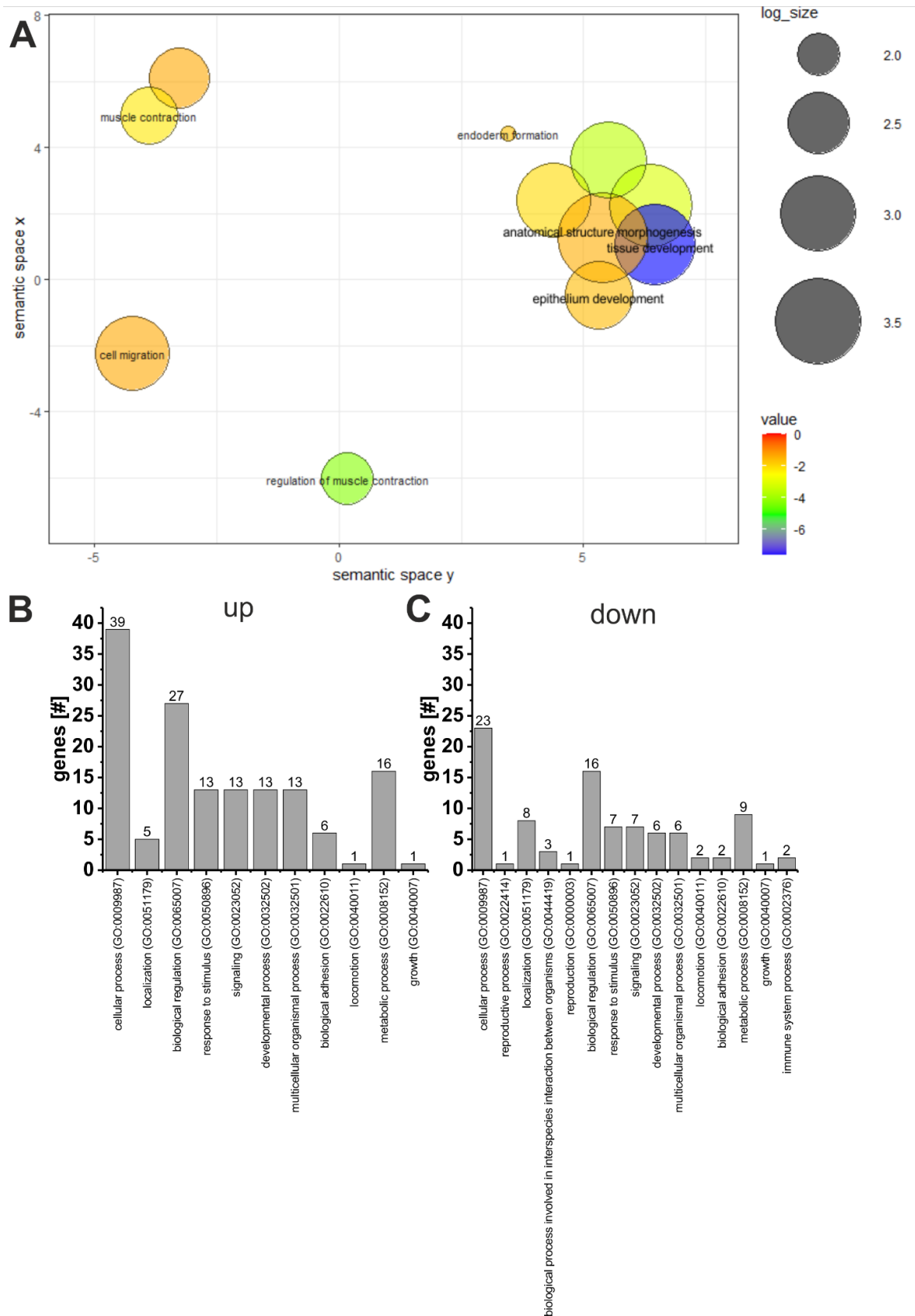
8. Supplement



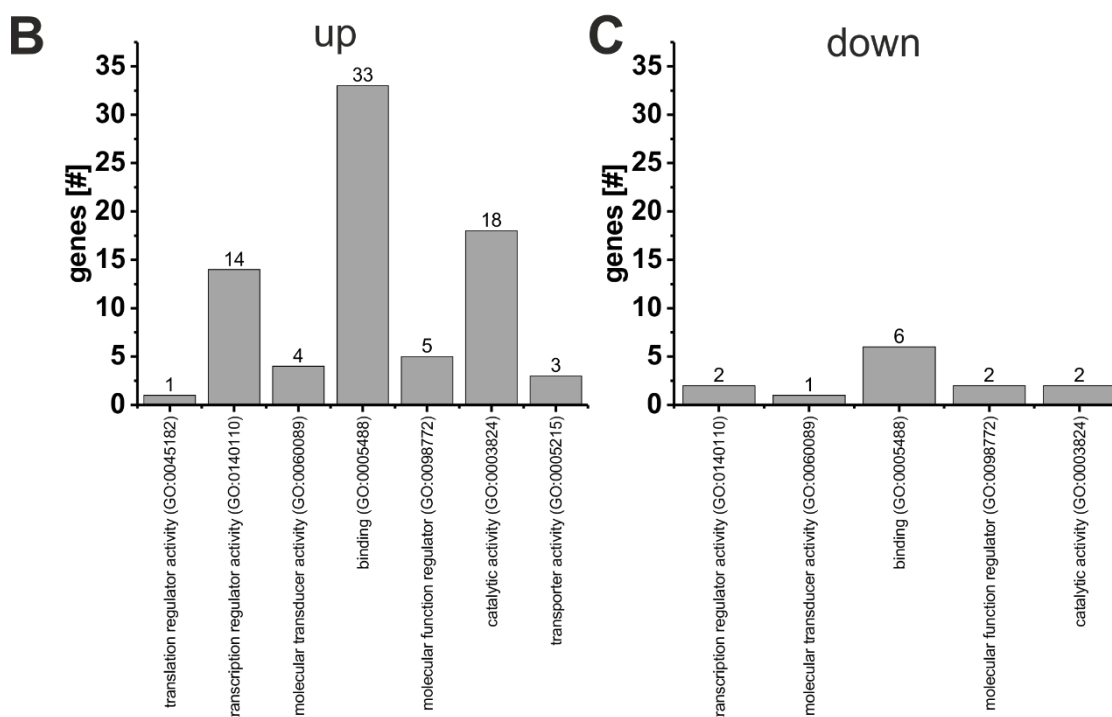
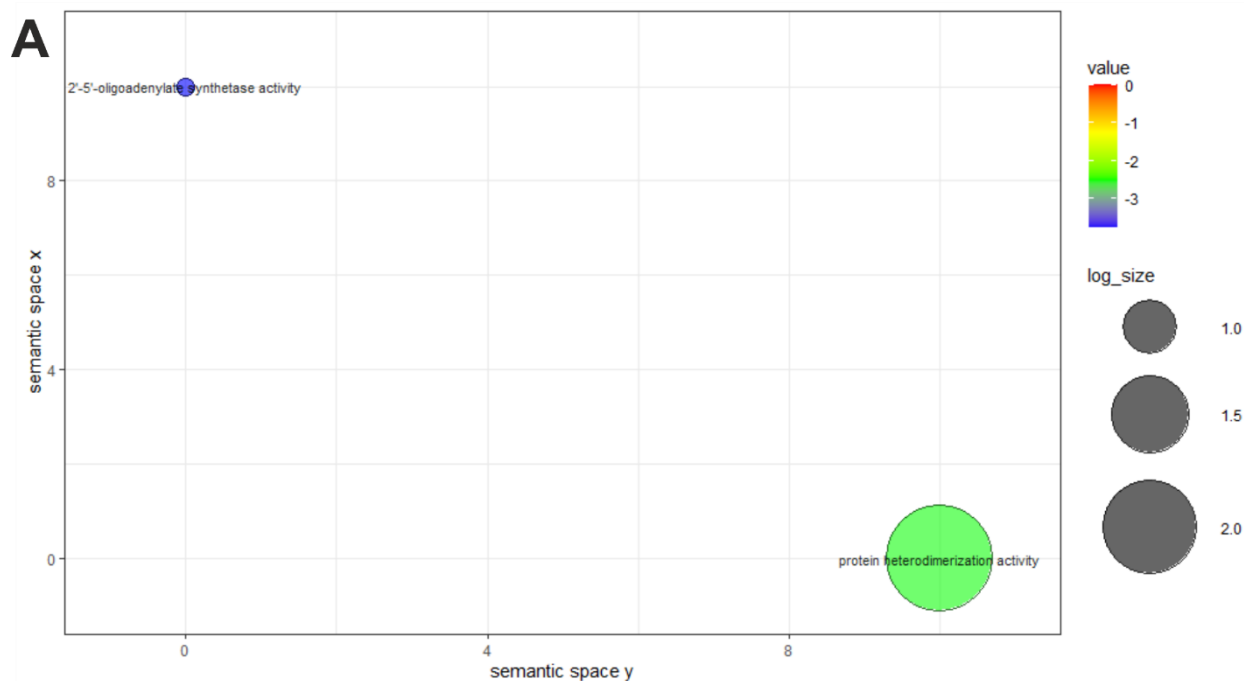
Supplementary Figure 1 GO analysis for biological processes of clone1: (A) All significantly regulated genes of clone1 were analysed using GO Term Finder tool and visualised by REVIGO. Displayed are all associated GOs for biological processes. The analysis revealed 68 GOs, whereas only upregulated genes were associated with 65 GOs and all downregulated GOs were associated with 1 GO. This single GO for downregulated genes of clone1 is marked by a black circle. Bubble size displays the log-transformed gene count and colour indicates the calculated p-value. **(B, C)** All significantly regulated genes of clone1 either up (B) or down (C) were analysed using Panther. Here, the associated genes were analysed using the GO-slim subset to obtain more parental categories of associated GOs. Numbers indicate the corresponding gene count for each found GO.



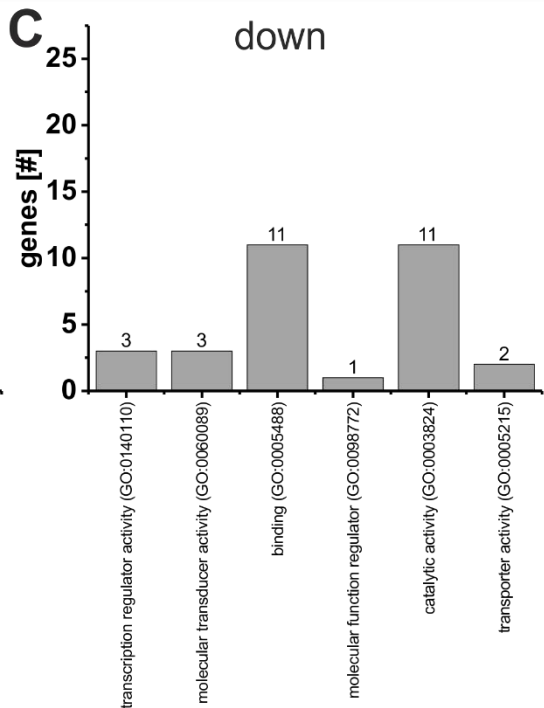
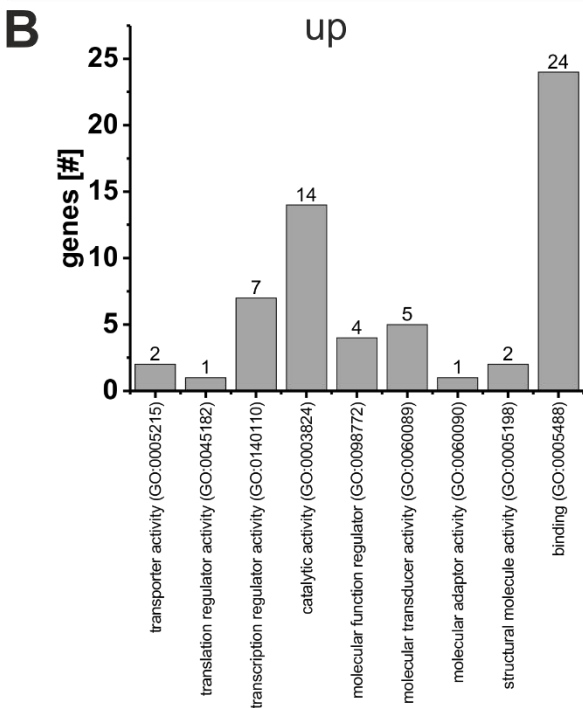
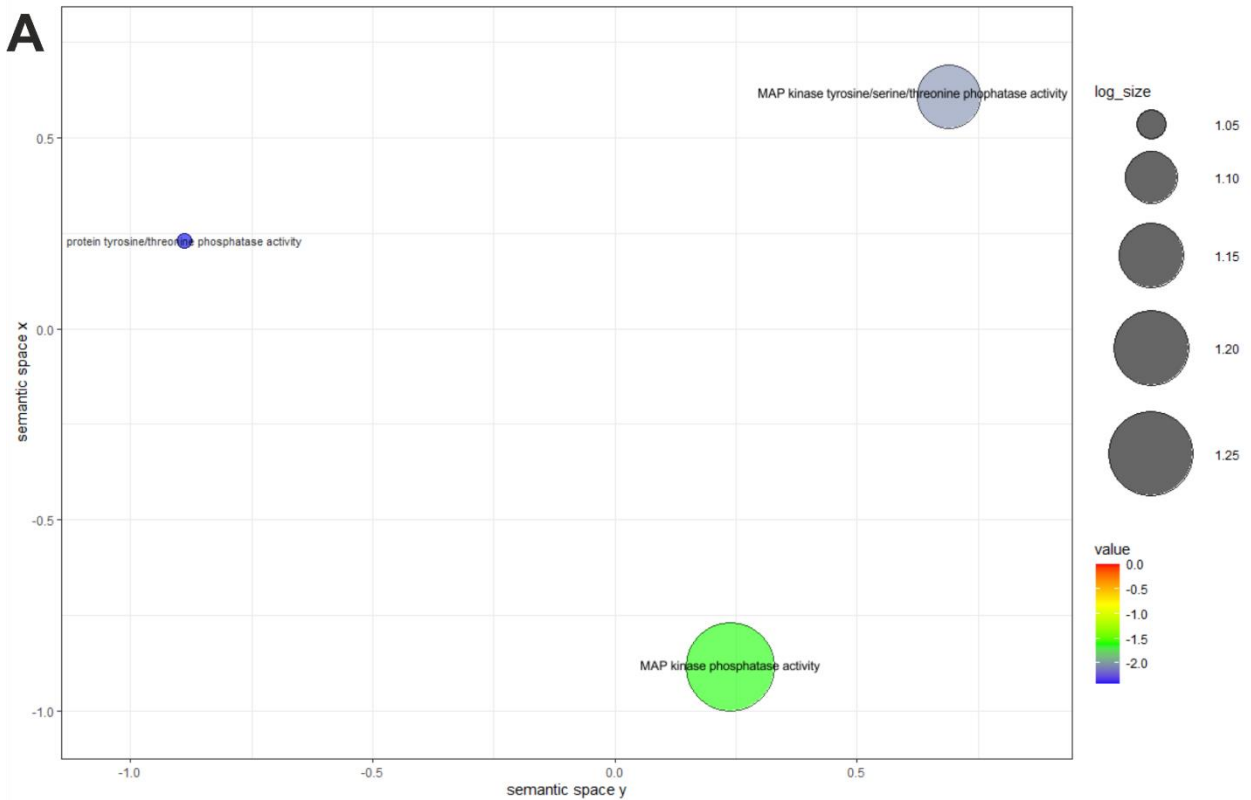
Supplementary Figure 2 KEGG analysis for associated pathways: Significantly up- and down-regulated genes of both clones using DAVID. This platform was able to analyse associated pathways by comparing gene datasets with the KEGG tool. Shown are the 10 most significantly associated pathways for clone1 and clone2 either for up- or downregulated genes. The numbers indicate the corresponding gene count. In brackets the sum of analysed genes is indicated.



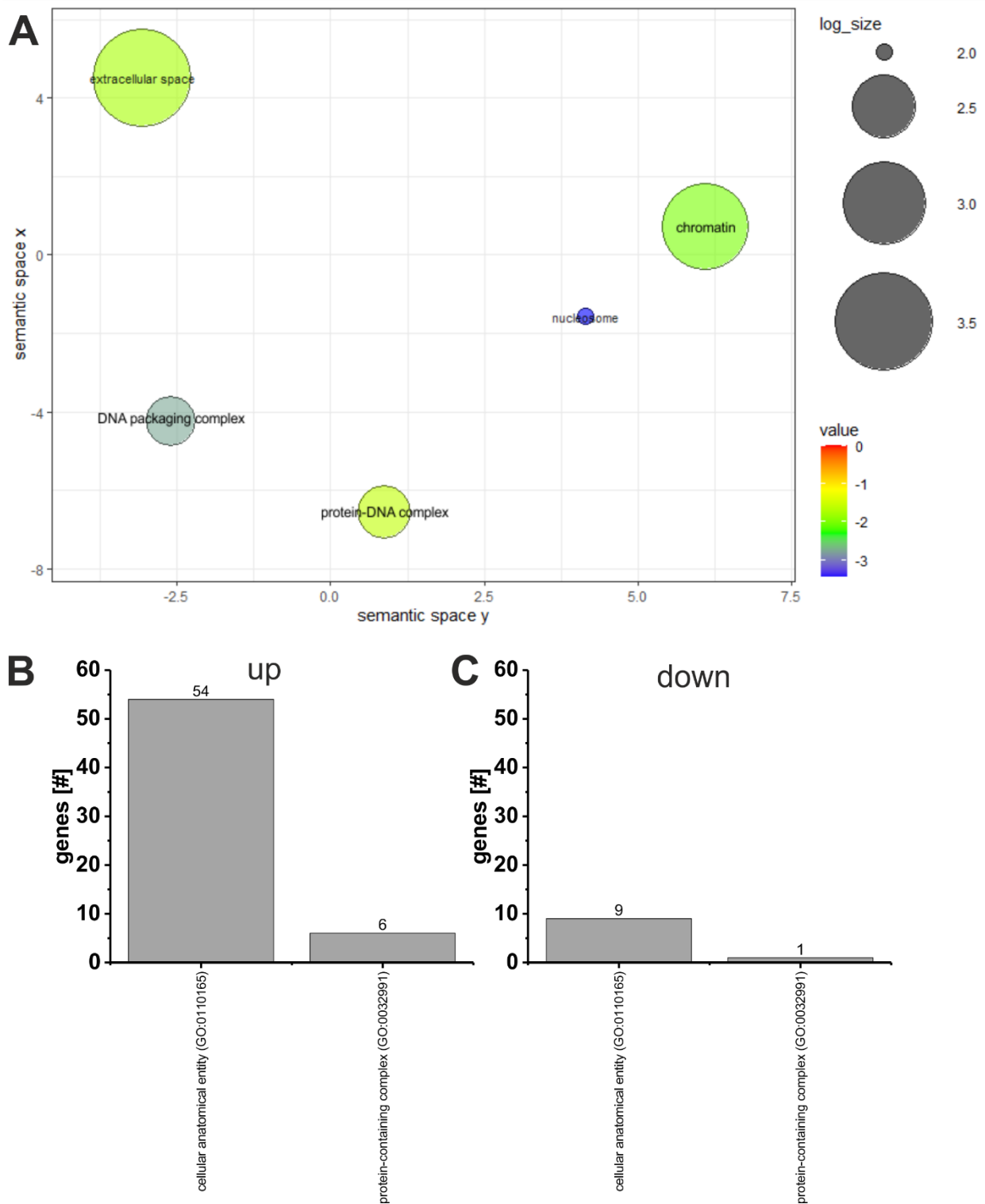
Supplementary Figure 3 GO analysis for biological processes of clone2: (A) All significantly regulated genes of clone2 were analysed using GO Term Finder tool and visualised by REVIGO. Displayed are all associated GOs for biological processes. The analysis revealed 12 GOs, whereas only upregulated genes were associated with 24 GOs and all downregulated GOs were associated with 1 GO. Bubble size displays the log-transformed gene count and colour indicates the calculated p-value. (B, C) All significantly regulated genes of clone2 either up (B) or down (C) were analysed using Panther. Here, the associated genes were analysed using the GO-slim subset to obtain more parental categories of associated GOs. Numbers indicate the corresponding gene count for each found GO.



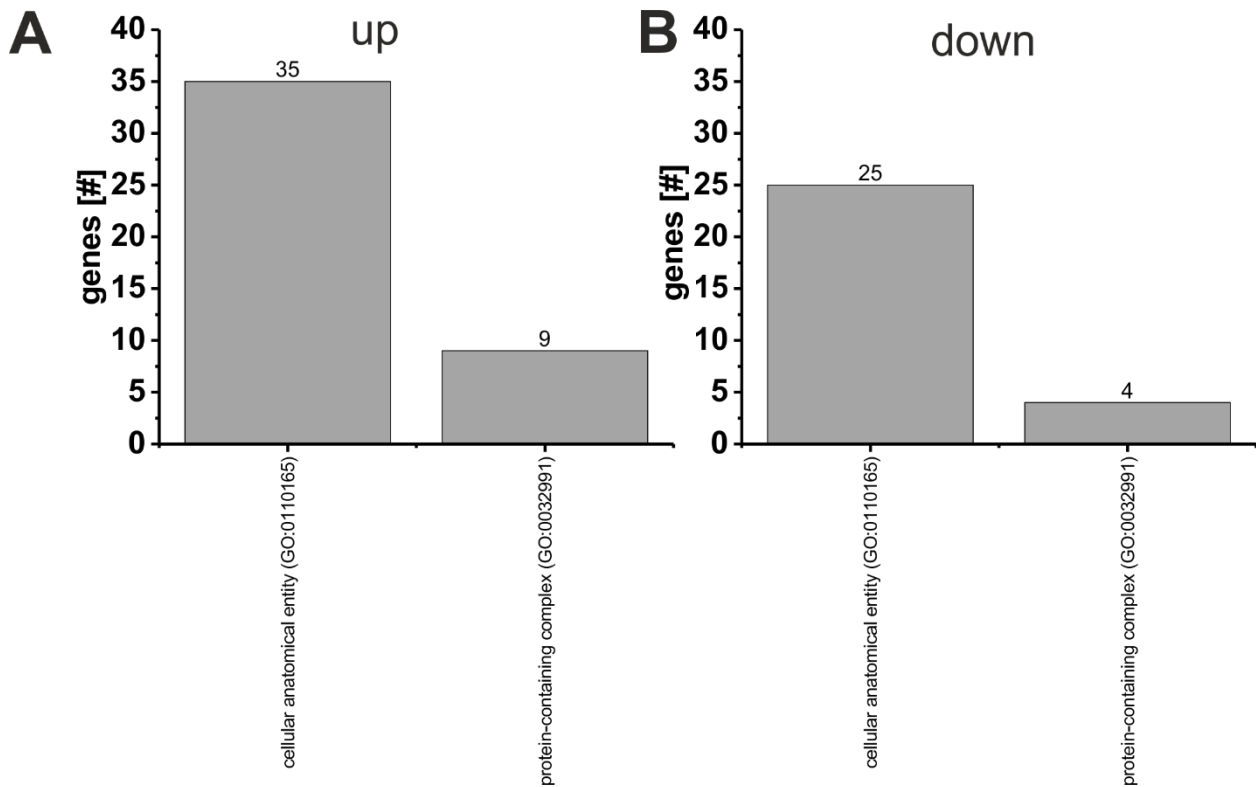
Supplementary Figure 4 GO analysis for molecular function of clone1: (A) All significantly regulated genes of clone1 were analysed using GO Term Finder tool and visualised by REVIGO. Displayed are all associated GOs for molecular function. The analysis revealed 2 GOs, whereas only upregulated genes were associated with 5 GOs and all downregulated GOs were associated with 1 GO. Bubble size displays the log-transformed gene count and colour indicates the calculated p-value. **(B, C)** All significantly regulated genes of clone1 either up (B) or down (C) were analysed using Panther. Here, the associated genes were analysed using the GO-slim subset to obtain more parental categories of associated GOs. Numbers indicate the corresponding gene count for each found GO.



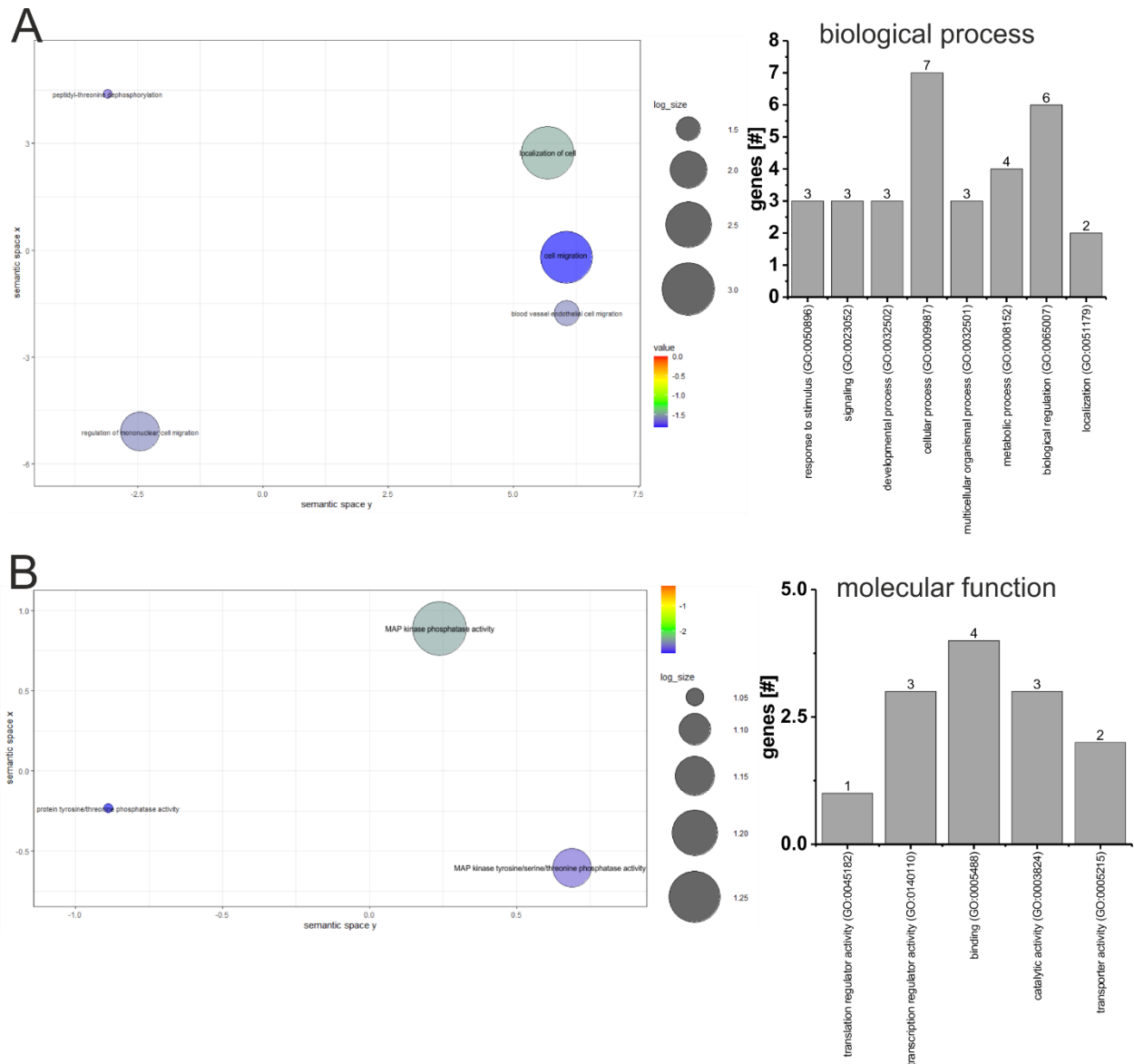
Supplementary Figure 5 GO analysis for molecular function of clone2: (A) All significantly regulated genes of clone2 were analysed using GO Term Finder tool and visualised by REVIGO. Displayed are all associated GOs for molecular function. The analysis revealed 4 GOs, whereas only upregulated genes were associated with 6 GOs and all downregulated GOs were associated with 1 GO. Bubble size displays the log-transformed gene count and colour indicates the calculated p-value. (B, C) All significantly regulated genes of clone2 either up (B) or down (C) were analysed using Panther. Here, the associated genes were analysed using the GO-slim subset to obtain more parental categories of associated GOs. Numbers indicate the corresponding gene count for each found GO.



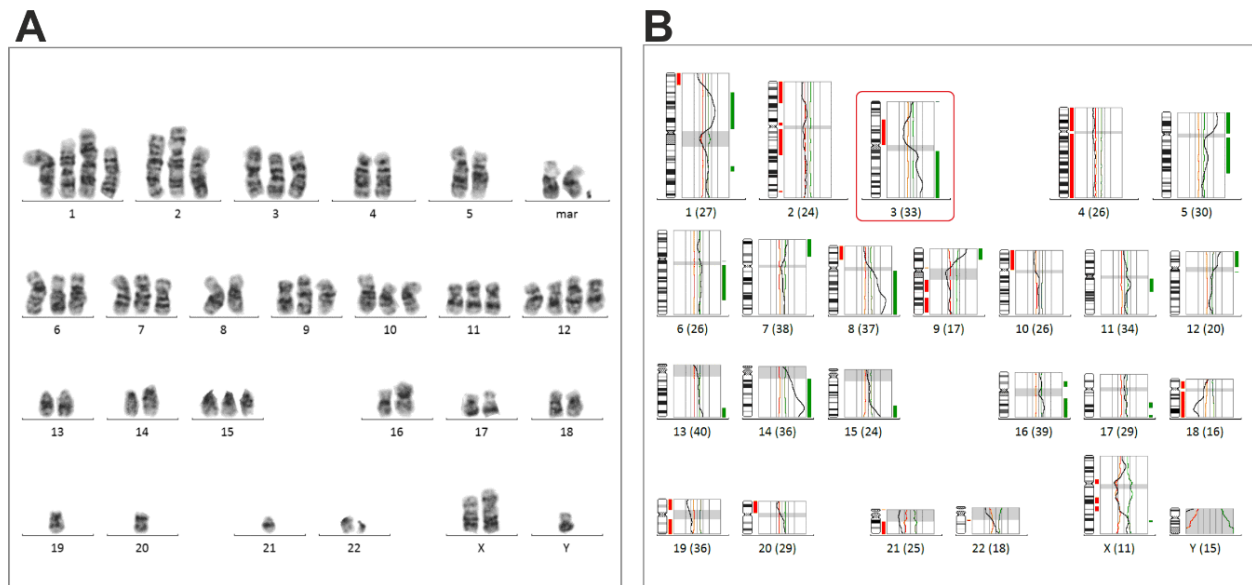
Supplementary Figure 6 GO analysis for cellular component of clone1: (A) All significantly regulated genes of clone1 were analysed using GO Term Finder tool and visualised by REVIGO. Displayed are all associated GOs for cellular component. The analysis revealed 6 GOs, whereas only upregulated genes were associated with 4 GOs and no GO was associated with all downregulated genes. Bubble size displays the log-transformed gene count and colour indicates the calculated p-value. (B, C) All significantly regulated genes of clone1 either up (B) or down (C) were analysed using Panther. Here, the associated genes were analysed using the GO-slim subset to obtain more parental categories of associated GOs. Numbers indicate the corresponding gene count for each found GO.



Supplementary Figure 7 GO analysis for cellular component of clone2: (A, B) All significantly regulated genes of clone2 either up (A) or down (B) were analysed using Panther. Here, the associated genes were analysed for using the GO-slim subset to obtain more parental categories of associated GOs. Numbers indicate the corresponding gene count for each found GO.



Supplementary Figure 8 Analysis of 15 shared upregulated genes of clone1 and clone2: (A) Significantly regulated genes of clone1 and clone2 were analysed using GO Term Finder tool and visualised by REVIGO. Displayed are all associated GOs for biological processes (A) and molecular function (B). The analysis revealed 8 GOs for biological processes and 4 GOs for molecular function. Bubble size displays the log-transformed gene count and colour indicates the calculated p-value. On the right side corresponding Panther analysis results are displayed using GO-slim categories.



Supplementary Figure 9 G-banding and comparative genomic hybridization of FaDu wt cells: (A) G-banding of FaDu wt cells for identification of each chromosome by its specific band pattern. FaDu wt cells show a very heterogenous chromosome set consisting of multiple triploid and tetraploid chromosomes. **(B)** Comparative genomic hybridization (CGH) of FaDu wt cells shows various chromosomal gains and losses on multiple chromosomes. Chromosome 3 (highlighted in red) that is bearing the SEC62 gene on its long arm (q) shows gains on the whole chromosomal 3q-section. This chromosomal gain might be due to SEC62 amplification. Figure modified from Körbel et al., 2018.

Supplementary Table 1 Clustering results after DAVID analysis for all upregulated genes of clone1

Annotation Cl Enrichment Score: 11.118086113386633											
Category	Term	Count	%	PValue	List Total	Pop Hits	Pop Total	Fold Enrichment	Bonferroni	Benjamini	FDR
GOTERM_BP	GO:0045071~	11	10.78	1.05E-14	91	46	19256	50.60	8.32E-12	8.29E-12	8.15E-12
GOTERM_BP	GO:0051607~	16	15.69	2.01E-13	91	231	19256	14.66	1.58E-10	7.91E-11	7.77E-11
GOTERM_BP	GO:0009615~	11	10.78	1.04E-10	91	111	19256	20.97	8.23E-08	2.74E-08	2.69E-08
GOTERM_BP	GO:0045087~	17	16.67	1.53E-08	91	597	19256	6.03	1.21E-05	3.01E-06	2.96E-06
Annotation Cl Enrichment Score: 6.21489943645515											
Category	Term	Count	%	PValue	List Total	Pop Hits	Pop Total	Fold Enrichment	Bonferroni	Benjamini	FDR
GOTERM_CC	GO:0000786~	13	12.75	2.28E-12	97	139	20472	19.74	3.35E-10	3.35E-10	3.26E-10
GOTERM_MF	GO:0046982~	16	15.69	4.53E-10	95	371	18811	8.54	1.00E-07	1.01E-07	9.97E-08
GOTERM_MF	GO:0030527~	10	9.80	1.57E-09	95	99	18811	20.00	3.48E-07	1.75E-07	1.73E-07
GOTERM_BP	GO:0006334~	9	8.82	1.10E-07	91	123	19256	15.48	8.70E-05	1.74E-05	1.71E-05
GOTERM_MF	GO:0003677~	23	22.55	2.63E-07	95	1286	18811	3.54	5.81E-05	1.94E-05	1.93E-05
GOTERM_CC	GO:0000228~	5	4.90	1.20E-04	97	54	20472	19.54	0.02	0.01	0.01
GOTERM_BP	GO:0032200~	4	3.92	2.66E-04	91	27	19256	31.35	0.19	0.02	0.02
GOTERM_BP	GO:0006335~	4	3.92	4.44E-04	91	32	19256	26.45	0.30	0.03	0.02
GOTERM_CC	GO:0032991~	9	8.82	0.02	97	703	20472	2.70	0.92	0.32	0.31
Annotation Cl Enrichment Score: 2.384482733318418											
Category	Term	Count	%	PValue	List Total	Pop Hits	Pop Total	Fold Enrichment	Bonferroni	Benjamini	FDR
GOTERM_BP	GO:0032728~	5	4.90	4.36E-05	91	42	19256	25.19	0.03	0.00	0.00
GOTERM_MF	GO:0001730~	3	2.94	1.47E-04	95	4	18811	148.51	0.03	0.01	0.01
GOTERM_BP	GO:0060700~	3	2.94	2.14E-04	91	5	19256	126.96	0.16	0.02	0.02
GOTERM_BP	GO:0060339~	3	2.94	0.00	91	20	19256	31.74	0.95	0.13	0.13
GOTERM_BP	GO:0042742~	6	5.88	0.00	91	234	19256	5.43	0.98	0.16	0.16
GOTERM_MF	GO:0003725~	3	2.94	0.05	95	75	18811	7.92	1.00	0.64	0.64
GOTERM_BP	GO:0032760~	3	2.94	0.09	91	108	19256	5.88	1.00	0.92	0.91
GOTERM_MF	GO:0005524~	8	7.84	0.66	95	1544	18811	1.03	1.00	1.00	1.00
Annotation Cl Enrichment Score: 2.3525134257047418											
Category	Term	Count	%	PValue	List Total	Pop Hits	Pop Total	Fold Enrichment	Bonferroni	Benjamini	FDR
GOTERM_BP	GO:0061844~	6	5.88	1.59E-04	91	109	19256	11.65	0.12	0.01	0.01
GOTERM_BP	GO:0019731~	4	3.92	0.00	91	59	19256	14.35	0.88	0.11	0.11
GOTERM_BP	GO:0002227~	3	2.94	0.01	91	28	19256	22.67	1.00	0.21	0.21
GOTERM_BP	GO:0050830~	3	2.94	0.12	91	129	19256	4.92	1.00	1.00	0.98
Annotation Cl Enrichment Score: 2.1880693123562427											
Category	Term	Count	%	PValue	List Total	Pop Hits	Pop Total	Fold Enrichment	Bonferroni	Benjamini	FDR
GOTERM_BP	GO:0030593~	6	5.88	4.10E-05	91	82	19256	15.48	0.03	0.00	0.00
GOTERM_BP	GO:0006935~	5	4.90	0.00	91	123	19256	8.60	0.88	0.11	0.11
GOTERM_BP	GO:0006954~	8	7.84	0.00	91	411	19256	4.12	0.92	0.12	0.12
GOTERM_MF	GO:0008009~	3	2.94	0.03	95	50	18811	11.88	1.00	0.58	0.57
GOTERM_BP	GO:0070098~	3	2.94	0.04	91	70	19256	9.07	1.00	0.70	0.68
GOTERM_BP	GO:0006955~	5	4.90	0.20	91	492	19256	2.15	1.00	1.00	0.98
Annotation Cl Enrichment Score: 1.7095825208190085											
Category	Term	Count	%	PValue	List Total	Pop Hits	Pop Total	Fold Enrichment	Bonferroni	Benjamini	FDR
GOTERM_BP	GO:0035970~	3	2.94	0.01	91	25	19256	25.39	0.99	0.19	0.18
GOTERM_MF	GO:0004721~	3	2.94	0.02	95	46	18811	12.91	0.99	0.55	0.54
GOTERM_MF	GO:0017018~	3	2.94	0.06	95	76	18811	7.82	1.00	0.64	0.64
Annotation Cl Enrichment Score: 1.52318369736157											
Category	Term	Count	%	PValue	List Total	Pop Hits	Pop Total	Fold Enrichment	Bonferroni	Benjamini	FDR
GOTERM_MF	GO:1990837~	11	10.78	4.58E-04	95	556	18811	3.92	0.10	0.02	0.02
GOTERM_MF	GO:0001228~	10	9.80	5.98E-04	95	473	18811	4.19	0.12	0.02	0.02
GOTERM_BP	GO:0045944~	14	13.73	0.00	91	1201	19256	2.47	0.95	0.13	0.13
GOTERM_BP	GO:0000122~	11	10.78	0.01	91	967	19256	2.41	1.00	0.35	0.34
GOTERM_CC	GO:0000785~	11	10.78	0.03	97	1057	20472	2.20	0.98	0.35	0.34
GOTERM_MF	GO:0000976~	5	4.90	0.03	95	238	18811	4.16	1.00	0.58	0.58
GOTERM_MF	GO:0000981~	12	11.76	0.05	95	1279	18811	1.86	1.00	0.64	0.64
GOTERM_MF	GO:0003700~	7	6.86	0.06	95	554	18811	2.50	1.00	0.64	0.64
GOTERM_MF	GO:0000978~	11	10.78	0.08	95	1207	18811	1.80	1.00	0.67	0.67
GOTERM_CC	GO:0005667~	4	3.92	0.09	97	231	20472	3.65	1.00	0.83	0.81
GOTERM_BP	GO:0006366~	4	3.92	0.10	91	240	19256	3.53	1.00	0.97	0.96
GOTERM_MF	GO:0043565~	4	3.92	0.23	95	328	18811	2.41	1.00	1.00	1.00
GOTERM_BP	GO:0045893~	6	5.88	0.24	91	716	19256	1.77	1.00	1.00	0.98
GOTERM_BP	GO:0006357~	11	10.78	0.28	91	1721	19256	1.35	1.00	1.00	0.98

Supplementary Table 2 Clustering results after DAVID analysis for all up- and downregulated genes of clone2. The first 5 clusters belong to upregulated genes, whereas the last cluster results from downregulated genes.

Annotation Cluster 1 Enrichment Score: 2.4419171207269526											
Category	Term	Count	%	PValue	List Total	Pop Hits	Pop Total	Fold Enrichme	Bonferroni	Benjamini	FDR
GOTERM_MF_DIRECT	GO:0008330~	3	5.56	0.00	52	10	18811	108.53	0.05	0.04	0.04
GOTERM_BP_DIRECT	GO:0001706~	3	5.56	0.00	52	13	19256	85.46	0.23	0.12	0.12
GOTERM_MF_DIRECT	GO:0017017~	3	5.56	0.00	52	13	18811	83.48	0.08	0.04	0.04
GOTERM_BP_DIRECT	GO:0000188~	3	5.56	0.00	52	20	19256	55.55	0.47	0.16	0.16
GOTERM_BP_DIRECT	GO:0035970~	3	5.56	0.00	52	25	19256	44.44	0.63	0.20	0.20
GOTERM_MF_DIRECT	GO:0051019~	3	5.56	0.00	52	30	18811	36.18	0.36	0.15	0.15
GOTERM_BP_DIRECT	GO:0035335~	3	5.56	0.00	52	38	19256	29.23	0.90	0.30	0.30
GOTERM_BP_DIRECT	GO:0043409~	3	5.56	0.01	52	43	19256	25.84	0.95	0.32	0.32
GOTERM_MF_DIRECT	GO:0004721~	3	5.56	0.01	52	46	18811	23.59	0.64	0.26	0.25
GOTERM_MF_DIRECT	GO:0017018~	3	5.56	0.02	52	76	18811	14.28	0.93	0.34	0.33
GOTERM_MF_DIRECT	GO:0004725~	3	5.56	0.03	52	107	18811	10.14	0.99	0.56	0.55
GOTERM_BP_DIRECT	GO:0006470~	3	5.56	0.06	52	155	19256	7.17	1.00	1.00	0.99
Annotation Cluster 2 Enrichment Score: 2.1256785159884326											
Category	Term	Count	%	PValue	List Total	Pop Hits	Pop Total	Fold Enrichme	Bonferroni	Benjamini	FDR
GOTERM_CC_DIRECT	GO:0009986~	8	14.81	0.00	52	638	20472	4.94	0.12	0.12	0.12
GOTERM_BP_DIRECT	GO:0098742~	3	5.56	0.00	52	39	19256	28.49	0.91	0.30	0.30
GOTERM_BP_DIRECT	GO:0098609~	3	5.56	0.09	52	190	19256	5.85	1.00	1.00	0.99
Annotation Cluster 3 Enrichment Score: 1.9600158292724732											
Category	Term	Count	%	PValue	List Total	Pop Hits	Pop Total	Fold Enrichme	Bonferroni	Benjamini	FDR
GOTERM_BP_DIRECT	GO:0007160~	4	7.41	0.00	52	107	19256	13.84	0.76	0.24	0.24
GOTERM_MF_DIRECT	GO:0005178~	4	7.41	0.01	52	161	18811	8.99	0.76	0.27	0.26
GOTERM_BP_DIRECT	GO:0007155~	6	11.11	0.02	52	557	19256	3.99	1.00	0.60	0.60
GOTERM_BP_DIRECT	GO:0016477~	4	7.41	0.03	52	268	19256	5.53	1.00	0.81	0.80
Annotation Cluster 4 Enrichment Score: 1.5965727112192358											
Category	Term	Count	%	PValue	List Total	Pop Hits	Pop Total	Fold Enrichme	Bonferroni	Benjamini	FDR
GOTERM_BP_DIRECT	GO:0045109~	3	5.56	0.01	52	66	19256	16.83	1.00	0.55	0.55
GOTERM_CC_DIRECT	GO:0045095~	3	5.56	0.03	52	105	20472	11.25	0.97	0.74	0.74
GOTERM_CC_DIRECT	GO:0005882~	3	5.56	0.04	52	133	20472	8.88	1.00	0.74	0.74
Annotation Cluster 5 Enrichment Score: 0.8912130431700016											
Category	Term	Count	%	PValue	List Total	Pop Hits	Pop Total	Fold Enrichme	Bonferroni	Benjamini	FDR
GOTERM_MF_DIRECT	GO:1990837~	6	11.11	0.02	52	556	18811	3.90	0.92	0.34	0.33
GOTERM_BP_DIRECT	GO:0045944~	8	14.81	0.04	52	1201	19256	2.47	1.00	0.86	0.86
GOTERM_CC_DIRECT	GO:0000785~	7	12.96	0.05	52	1057	20472	2.61	1.00	0.74	0.74
GOTERM_BP_DIRECT	GO:0000122~	6	11.11	0.11	52	967	19256	2.30	1.00	1.00	0.99
GOTERM_MF_DIRECT	GO:0003677~	7	12.96	0.13	52	1286	18811	1.97	1.00	1.00	0.99
GOTERM_MF_DIRECT	GO:0001228~	4	7.41	0.14	52	473	18811	3.06	1.00	1.00	0.99
GOTERM_MF_DIRECT	GO:0000981~	6	11.11	0.26	52	1279	18811	1.70	1.00	1.00	0.99
GOTERM_BP_DIRECT	GO:0030154~	4	7.41	0.27	52	680	19256	2.18	1.00	1.00	0.99
GOTERM_MF_DIRECT	GO:0000978~	5	9.26	0.42	52	1207	18811	1.50	1.00	1.00	0.99
GOTERM_BP_DIRECT	GO:0006357~	5	9.26	0.68	52	1721	19256	1.08	1.00	1.00	0.99
Annotation Cluster 1 Enrichment Score: 0.27540810904522											
Category	Term	Count	%	PValue	List Total	Pop Hits	Pop Total	Fold Enrichme	Bonferroni	Benjamini	FDR
GOTERM_MF_DIRECT	GO:0001228~	3	5.88	0.25	39	473	18811	3.06	1.00	1.00	1.00
GOTERM_MF_DIRECT	GO:0003700~	3	5.88	0.31	39	554	18811	2.61	1.00	1.00	1.00
GOTERM_MF_DIRECT	GO:1990837~	3	5.88	0.31	39	556	18811	2.60	1.00	1.00	1.00
GOTERM_BP_DIRECT	GO:0045944~	4	7.84	0.48	42	1201	19256	1.53	1.00	1.00	1.00
GOTERM_CC_DIRECT	GO:0000785~	3	5.88	0.65	43	1057	20472	1.35	1.00	1.00	1.00
GOTERM_MF_DIRECT	GO:0000978~	3	5.88	0.71	39	1207	18811	1.20	1.00	1.00	1.00
GOTERM_MF_DIRECT	GO:0000981~	3	5.88	0.74	39	1279	18811	1.13	1.00	1.00	1.00
GOTERM_BP_DIRECT	GO:0006357~	3	5.88	0.89	42	1721	19256	0.80	1.00	1.00	1.00
GOTERM_CC_DIRECT	GO:0005654~	5	9.80	0.97	43	3939	20472	0.60	1.00	1.00	1.00

Supplementary Table 3 Clustering results after DAVID analysis for all upregulated genes of clone1 and clone2.

Annotation Cl Enrichment Score: 1.1725708229522174											
Category	Term	Count	%	PValue	List Total	Pop Hits	Pop Total	Fold Enrichme	Bonferroni	Benjamini	FDR
GOTERM_BP	GO:0045944~	4	30.77	0.03	12	1201	19256	5.34	0.99	0.73	0.73
GOTERM_MF	GO:0001228~	3	23.08	0.03	12	473	18811	9.94	0.75	0.23	0.22
GOTERM_MF	GO:1990837~	3	23.08	0.04	12	556	18811	8.46	0.85	0.26	0.24
GOTERM_CC	GO:0000785~	3	23.08	0.11	12	1057	20472	4.84	0.98	1.00	1.00
GOTERM_MF	GO:0000978~	3	23.08	0.15	12	1207	18811	3.90	1.00	0.62	0.58
GOTERM_MF	GO:0000981~	3	23.08	0.17	12	1279	18811	3.68	1.00	0.62	0.58

Supplementary Video 1: QR code or link to indicated video examples. **(A)** Neck dissection of an exemplary mouse bearing a lymph node metastasis in the right sided lymph node. **(B)** MRI reconstruction in sagittal, transversal and frontal of a mouse thorax bearing multiple metastases. **(C)** 3D μ CT reconstruction of the same metastases bearing mouse as in (B). **(D)** Reactions 5 min after TFP administration. Please have a focus on the two mice on the right, because they show most the described behaviour like pressing down the abdomen. **(E)** Reactions 5 min after TG administration. Please have a focus especially on the mouse on the left in the foreground, because it shows most the described behaviour like pressing down the abdomen and irregular retch-like movements.



Neck dissection:

https://www.dropbox.com/s/7z7oo4ide9036fp/Video1_%2019.08.2021_Neck%20dissection.mp4?dl=0



MRI reconstructions:

https://www.dropbox.com/sh/exs78i618h2sbo2/AACQ_KTgkC6dhVuSZrMO7XGSa?dl=0



3D μ CT reconstruction:

https://www.dropbox.com/s/jzb5covn6gunwr9/Video3_3D%20including%20reconstruction%20including%20metastasis_AI05%209%C2%B5m%20dead.avi?dl=0



Reaction after TFP administration:

https://www.dropbox.com/s/t5pibw001exath4/Video4_22.07.20%20Pressing%20down%20the%20abdomen%20after%20TFP%20administration.MOV?dl=0



Reaction after TG administration:

https://www.dropbox.com/s/k54v6o6rvyire0l/Video5_30.07.21%20Reaction%20after%20TG%20administration.MOV?dl=0

9. Curriculum vitae

Aus datenschutzrechtlichen Gründen wird der Lebenslauf in der elektronischen Fassung der Dissertation nicht veröffentlicht.

